Doctoral Thesis

Multipurpose Solid Additives for Efficient and Stable Organic Solar Cells

Jiyeon Oh

School of Energy and Chemical Engineering
(Energy Engineering)

Ulsan National Institute of Science and Technology

2023

Multipurpose Solid Additives for Efficient and Stable Organic Solar Cells

Jiyeon Oh

School of Energy and Chemical Engineering
(Energy Engineering)

Ulsan National Institute of Science and Technology

Multipurpose Solid Additives for Efficient and Stable Organic Solar Cells

A thesis/dissertation submitted to
Ulsan National Institute of Science and Technology
in partial fulfillment of the
requirements for the degree of
Doctor of Philosophy

Jiyeon Oh

11.29.2022 of submission

Approved by

Changduk Yang

Multipurpose Solid Additives for Efficient and Stable Organic Solar Cells

Jiyeon Oh

This certifies that the thesis/dissertation of Jiyeon Oh is approved.

11.29.2022 of submission

Advisor: Changduk Yang

Tae-Hyuk Kwon: Thesis Committee member #1

Jin Young Kim: Thesis Committee member #2

Hyesung Park: Thesis Committee member #3

Ji-Wook Jang: Thesis Committee member #4

Abstract

Organic solar cells (OSCs) are one of the efficient and practical ways to use solar energy as a green energy source. Based on several advantages of organic materials, organic solar cells have attracted great attention as next-generation solar cells. However, many researchers are still needed for commercialization of organic solar cells. There are three key points to fabricate efficient solar cell systems: efficiency, stability, and reproducibility. With these three keywords, researchers are conducting various studies such as the introduction of a new donor or acceptor, and interlayer engineering. Among several approaches for efficient solar cells, the introduction of additive (only small amounts) into the active layer is one of the facile methods owing to low-cost, easy processing, and unique property. In addition, this promising approach is expected to improve the power conversion efficiency together with several kinds of stability. Thereby, in this dissertation, I look at the role of additives in OSCs by applying newly synthesized donor materials using the commonly used solvent additive. Based on this, I design the multipurpose solid additives for organic solar cells based on each characteristic by categorizing additives into three types (nonvolatile polymer additives, nonvolatile small molecule additives, and volatile small molecule additives). Furthermore, I investigate the influence of solid additives on performance, stability, and reproducibility. In the first study, with the increasing concern for discovering a new processing additive, the effects of polymer additives (polystyrene, poly(styrene-*b*-pentafluorostyrene) and poly(pentafluorostyrene)) on the bulk heterojunction blend system were thoroughly investigated to obtain a direct comparison with the widely used volatile solvent 1,8-diiodooctane solvent additive. In the second study, dibutylhydroxytoluene (BHT)-based nonvolatile antioxidant additives with polar cyanide (CN) and perfluorinated alkyl chains (designated as BHT–CN and BHT–PF) are developed, demonstrating that the OSCs will have significantly improved long-term stability by using them when exposed to the H_2O, O_2. In particular, the use of BHT–PF in the various given test-bed OSC systems can remarkably enhance the long-term stability, as well as the high initial PCEs similar to the maximized values obtained from the highly optimized OSCs with each well-known suitable solvent additive. Last study, I carry out a comprehensive investigation into the effect of benzothiadiazole (BT) and its fluorinated analogs (FBT and 2FBT) as solid additives on the device performance of layer-by-layer (LBL) platform. The use of FBT in the donor layer results in a suitable morphology that ensures efficient charge transport/generation properties and suppresses recombination loss, boosting the photovoltaic performance of the LBL device. These findings are not only invaluable in shaping our understanding of OSCs, but also provides the possibility of development of next-generation solar cell technologies.

Contents

1. Introduction

2. Solvent Additive

3. Solid Additives

[Nonvolatile Solid Additives]

3.2 Nonvolatile Antioxidant Additives for High Photo-Oxidative Stabilization OSCs

[Volatile Solid Additives]

3.3 Benzothiadiazole-Based Volatile Additives for Favorable Interfacial Component Distribution in Layer-by-Layer OSCs

4. Experimental Section

5. Acknowledgement

6. Appendix

List of Schemes

List of Figures

List of Tables

Technical Terms and Abbreviations

μ	Mobility
AFM	Atomic force microscopy
ATRP	Atom transfer radical polymerization
CB	Chlorobenzene
CCL	Crystalline coherence length
CF	Chloroform
CN	1-chloronaphthalene
CT	Charge transfer
CV	Cyclic voltammetry
D-A	Donor-Acceptor
DFT	Density functional theory
DIM	Diiodomethane
DIO	1,8-diiodooctane
DPE	Diphenyl ether
DSC	Differential scanning calorimeter
EA	Elemental analysis
EH	2-ethylhexyl
E_{loss}	Energy loss
ETL	Electron transport layer
EQE	External quantum efficiency
$\mathrm{EQE}_{\mathrm{EL}}$	Electroluminascence external quantum efficiency
FF	Fill factor
FT-IR	Fourier transform infrared spectroscopy
FTPS-EQE	Fourier-transform photocurrent spectroscopy EQE
GIWAXS	Grazing-incidance wide-angle X-ray scattering
GPC	Gel-permeation chromatography
HOMO	Highest occupied molecular orbital
HTL	Hole transport layer
***i*BDD**	Benzo[1,2-b:4,5-c′]dithiophene-4,8-dione
ICT	Intramolecular charge transfer
ITO	Indium tin oxide
J_{ph}	Photocurrent density
J_{SC}	Short-circuit current density
J-V	Current density-Voltage
LUMO	Lowest unoccupied molecular orbital
M_{n}	Number average molecular weight
M_{w}	Weight average molecular weight
NBS	N-bromosuccinimide
NFAs	Non-fullerene acceptor

NMR	Nuclear magnetic resonance
NOESY	Nuclear overhauser effect spectroscopy
OSCs	Organic solar cells
PCE	Power conversion efficiency
PDI	Polydispersity index
PDIN	Amine functionalized perylene-diimide
PDINO	Perylenediimide functionalized with amino N-oxide
PDINN	Perylenediimide functionalized with aliphatic amine
PEDOT:PSS	Poly(3,4-ethylenedioxythiophene):poly(styrenesulfonate)
PL	Photo luminescence
PMMA	Poly(methyl methacrylate)
PS	Polystyrene
PSCs	Polymer solar cells
RMS	Root mean square
SCLC	Space charge limited current
SEM	Scanning electron microscopy
TA	Transient absorption
TEM	Transmission electron microscopy
TGA	Thermogravimetric analysis
THF	Tetrahydrofuran
TIPS	Triisopropylsilyl
UV–Vis	Ultravolet-visible
V_{eff}	Effective voltage
V_{OC}	Open-circuit voltage
XPS	X-ray photoelectron spectroscopy

CHAPTER 1 Introduction

1.1 Organic Solar Cells

1.1.1 Historical Background

Research and development in renewable energy sources is motivated by environmental concerns regarding the use of fossil fuels, such as air pollution and climate change. Particularly, solar energy, in the form of easily accessible radiation light, has the potential to produce more energy than the projected global energy demand, even according to conservative estimates.[1-5] In 1839, Edmond Becquerel experimented with an electrolytic cell consisting of two metal electrodes placed in an electricity-conducting solution, demonstrating the 'photovoltaic effect' in which electricity generation increased when exposed to light.[6] In 1884, Charles Fritts experimented with the first solar cell, which consisted of a selenium layer covered with a thin gold film.[7] The device's efficiency was only about 1%. This invention sparked a movement for the production of solar energy. In 1950, three scientists, Gerald Pearson, Calvin Fuller, and Daryl Chapin, designed a silicon solar cell capable of 6% of energy conversion efficiency in direct sunlight. Based on the development of silicon-based inorganic solar cells, people have also begun to pay attention to organic-based solar cells. Pochettino reported the first finding of photoconductivity in an organic compound in 1906.[8] Organic semiconductors are inexpensive than their inorganic counterparts. During the 1970s and 1980s, several efforts were conducted in the field of OSCs, but relatively low efficiencies were attained due to the low concentration and mobility of free charge carriers.[5, 9-11] Since the turn of the century, OSCs have garnered a fresh and significant amount of attention.[12-14]

1.1.2 Fundamental Principles

Architecture

In 1986, Tang group was the first to successfully use dyes in OSCs based on a planar construction that produced 1 % PCE in sunshine (**Figure 1.1.1**).[11, 15, 16] Planar solar cells are mady by sandwiching an organic active materials between two metallic conductors. After the first success with OPVs, the notion of the bulk heterojunction was introduced to address the limiting exciton (tightly bound electron-hole pair) within the diffusion length of planar OSCs (less than 10 nm).[5] In 1995, Yu et al. proposed the BHJ OSCs, in which the photo-active donor and acceptor materials are generated from a homogeneous solution for a bi-continuous interpenetrating architecture with large donor and acceptor interfacial surfaces for effective dissociation.[17-21] The BHJ structure had an improved D/A interface and a shorter diffusion distance for exciton separation, resulting in a considerable improvement in device performance. Nonetheless, as a result of its great potential to circumvent the infamous problems associated with the BHJ approach, such as the consideration of domain size and mixed phase, the strong morphological sensitivity of the blend solution, and the limited construction of desirable vertical component distribution, the LBL approach has reemerged as a promising alternative.[22-26] LBL fabrication enables the integration of single layer deposition processes with enhanced interfacial contact made possible by BHJ design. LBL entails the successive deposition of OSC active layers by solution processing for the first layer (typically the donor in a device configuration) followed by evaporation or solution deposition of the second layer (the acceptor). Numerous features make sequential deposition a feasible approach to commercialisation of OSCs. Each material is deposited separately, allowing for the control and optimization of distinct layers. Understanding the relationship between physical processes and morphology and device performance is facilitated by the simplicity of interface characterization. The manufacturing procedure yields effective vertical phase separation, which may be modified to enhance exciton dissociation and decrease charge carrier recombination. In addition, several research have indicated that the improved stability and environmentally friendly construction of LBL OSCs over BHJ OSCs may be more advantageous for the industrial use of large-scale PSCs.[27-31] Ternary OSCs using acceptor-acceptor or donor-acceptor-donor materials in the active layer also have been studied to increase OSC performance because they combine three materials with complimentary absorption spectra.

A typical OSC consists of an active layer positioned between two transport layers that carry holes or electrons and two electrodes (cathode and anode). The electrodes are responsible for collecting charge carriers and delivering the resulting current to an external electrical circuit. The ETL conducts the electron to the cathode (negative electrode), whereas the HTL conducts the holes to the anode (positive electrode). OSCs can be classified as conventional (anode directly on substrate) or inverted (cathode directly on substrate) based on which side is closest to the substrate (**Figure 1.1.1**). Despite structural differences, the underlying operating principle of OSCs is same. After thirty years of research, the PCE of OSC devices has surpassed 19 %, quickly approaching that of their inorganic counterparts.[32-34]

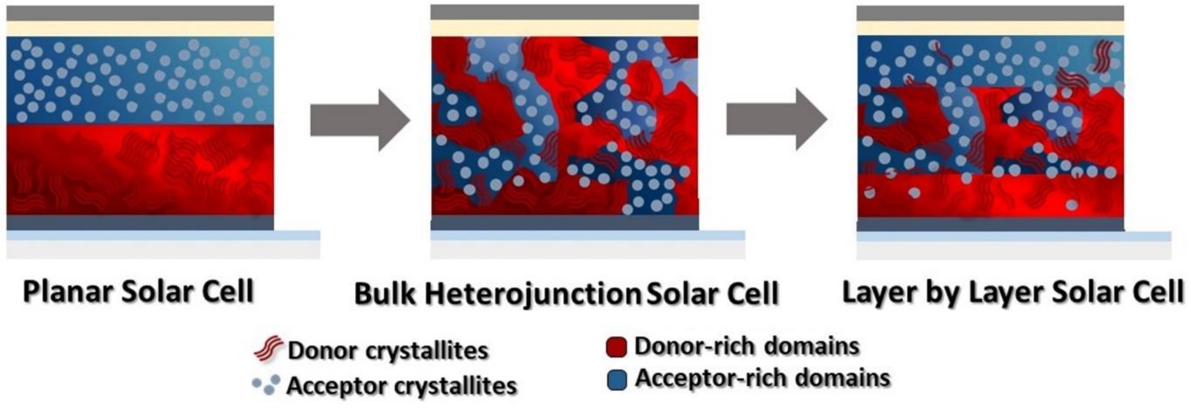

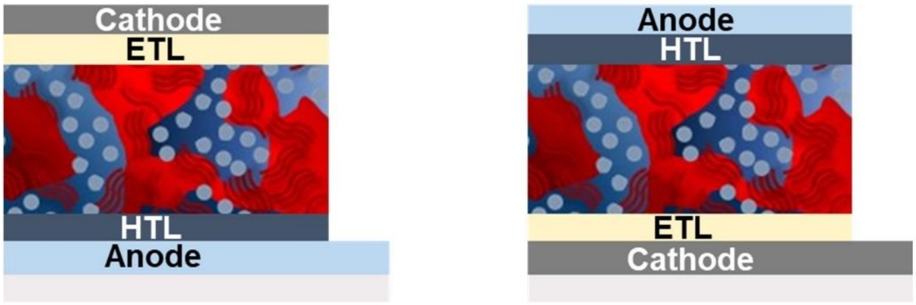

[Conventional Organic Solar Cell] [Inverted Organic Solar Cell]

Figure 1.1.1. Schematic of OPV device architectures.

Basic Parameters

The solar cell performance is expressed through a parameter called PCE, described as the ration of output power form device to incident sunlight energy. The PCE of the solar cell can be expressed as following equation:

$$\text{PCE} = J_{\text{SC}} \times V_{\text{OC}} \times \text{FF} / P_{\text{in}}$$

J_{SC} is the current density when the voltage applied to the devices is 0. JSC is determined by the light absorption range and the EQE for each wavelength. EQE is a value calculated as the product of absorption efficiency, exciton diffusion efficiency, charge-transfer efficiency, and charge collection efficiency. Therefore, the EQE means the efficiency at which incident light is charged collection.

V_{OC} is the open-circuit voltage when the current density is 0. V_{OC} is determined by subtracting the energy loss from the energy gap of semiconductor. It corresponds to the forward bias at which the dark current density compensates for the photocurrent density.

FF is another parameter that determines the output maximum of the solar cell along with J_{SC} and V_{OC}. It is expressed as: maximum power/(V_{OC} x J_{SC}). It is derived from the largest rectangular area that may be accommodated by the *J*-*V* characteristic. (**Figure 1.1.2**).

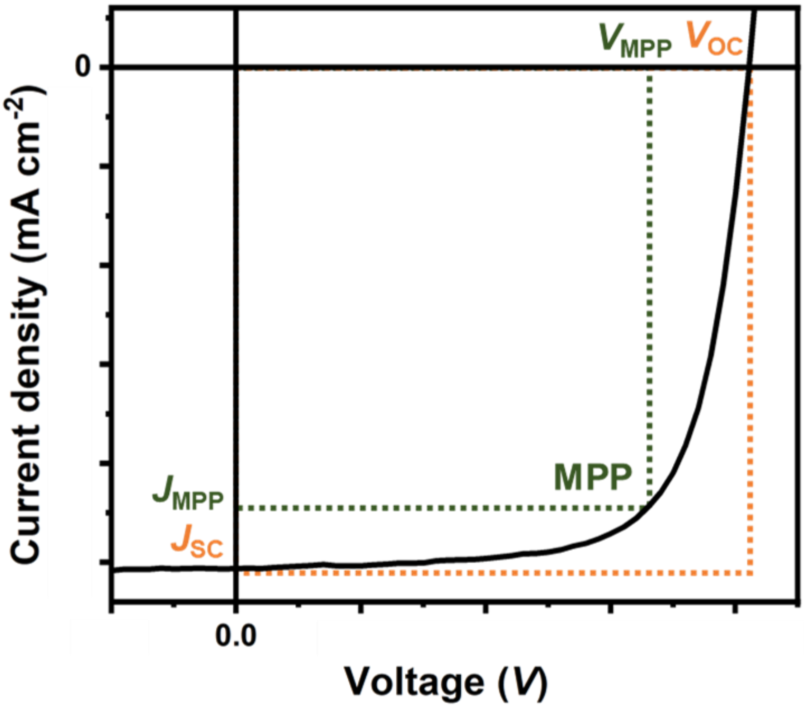

Figure 1.1.2. Archetypal *J-V* characteristic of the solar cells.

Working Mechanism

The Photovoltaic process begins with the absorption of light and ends with the transport of charges to electrodes. This is accomplished in the following 4 steps: (1) light absorption and exciton generation, (2) exciton diffusion, (3) charge separation, and (4) charge extraction (**Figure 1.1.3**). Upon light absorption in the active layer, an electron is excited from the HOMO level to the LUMO level, leaving an empty state called 'hole' in the HOMO. Because their charge is the opposite, the excited electron and hole are coulombically bound, which known as an 'exciton'. Then, generated exciton diffuses from the bulk of the film to the donor/acceptor boundaries and separated into free charges. Finally, electrons are transferred through the acceptor material to the anode, and holes are move through the donor material to the cathode to produce electrical power-this step is contributed by built-in and applied electric fields.

In the OSCs process, system undergo two main types, that is, geminate recombination and non-geminate recombination. **Figure 1.1.4** shows geminate pair recombination and non-geminate recombination.[35-39] The extracted charges at steady state are equal to the generated charges minus the recombined charges. $J = q \times (G - R)$ where G is the generation rate and R is the recombination rate. R is proportional to the charge carrier density n in the device. $R = \beta n \gamma$ where β is the recombination constant and γ is the order of recombination. The recombination of an electron-hole pair created by a single photon is called geminate recombination. The recombination of excitons that relax to the ground state before dissociating to CT excitons, and CT exciton relaxation before separating into free charge carriers are geminate, which are also considered as monomolecular recombination. Geminate recombination is a first order process, $\gamma = 1$, as R is proportional to the number of excitons in the device and thus is proportional to the illumination intensity and the dissociation rate of excitons. Accordingly, recombination between an electron and a hole created by different photons are non-geminate, which include bimolecular, trap-assistant, surface and auger recombination. Bimolecular recombination, also called Langevin recombination, is a second order process ($\gamma = 2$), which mainly occurs at the donor/acceptor interfaces via CT. Therefore, reducing the donor/acceptor interfaces would reduce the likelihood that opposite charge carriers will meet each other thereby suppressing the bimolecular recombination.

Trap-assistant recombination, also named as Shockley-Read-Hall recombination, is a first-order process where free charges recombine with the trapped opposite charges resident in trap states. Trap-assistant recombination usually originates from impurities present in organic semiconductors, creating energy levels inside the forbidden band gaps. Energy states at the tail of DOS could also act as traps in organic materials. The current generated by surface recombination, or more accurately, the collection of diffusion-driven charges at the opposite electrode owing to a non-selective contact, is anti-parallel to the drift photocurrent and is thus not a true recombination. However, it results in a reduced collected photocurrent just as does recombination. All non-geminate recombination depends on the densities of free charge carriers and the charge carrier generation rate. The carrier density upper limit is determined by light intensity. Therefore, the light intensity and temperature-dependent current-voltage measurements will provide information to differentiate between geminate and non-geminate recombination.

Under short circuit conditions, most generated charge carriers can be extracted from the bulk under a high enough built-in field. The relationship between J_{SC} and light intensity I can be found as $J_{\mathrm{SC}} \propto I^{\alpha}$, where α ranges typically from 0.85 to 1. Thus, the deviation from α = 1 has been conjectured to arise from a small loss of carriers via bimolecular recombination. The results show that high-intensity photocurrents are space-charge restricted when the electron and hole transport rates are significantly different. Thus, space charge effects will reduce the α value.

Under open circuit conditions, all photo-generated charges will be recombined. The dominating type of recombination can be distinguished by the dependence of V_{OC} on the natural logarithm of the light intensity. Bimolecular recombination has a slope of 1 kT/q, while trap-assisted recombination has a slope of 2 kT/q. A slope less than 1 kt/q may be due to surface recombination.

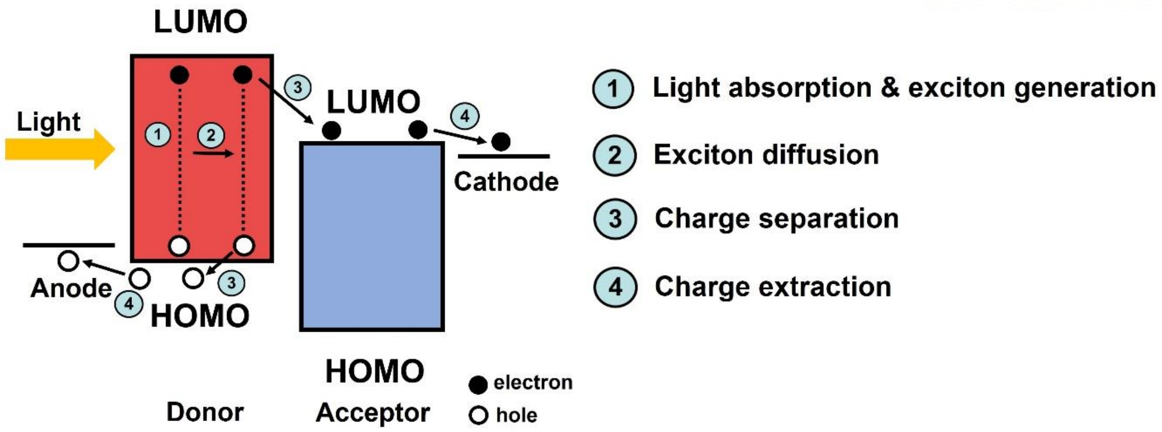

Figure 1.1.3. Working mechanism of OSCs.

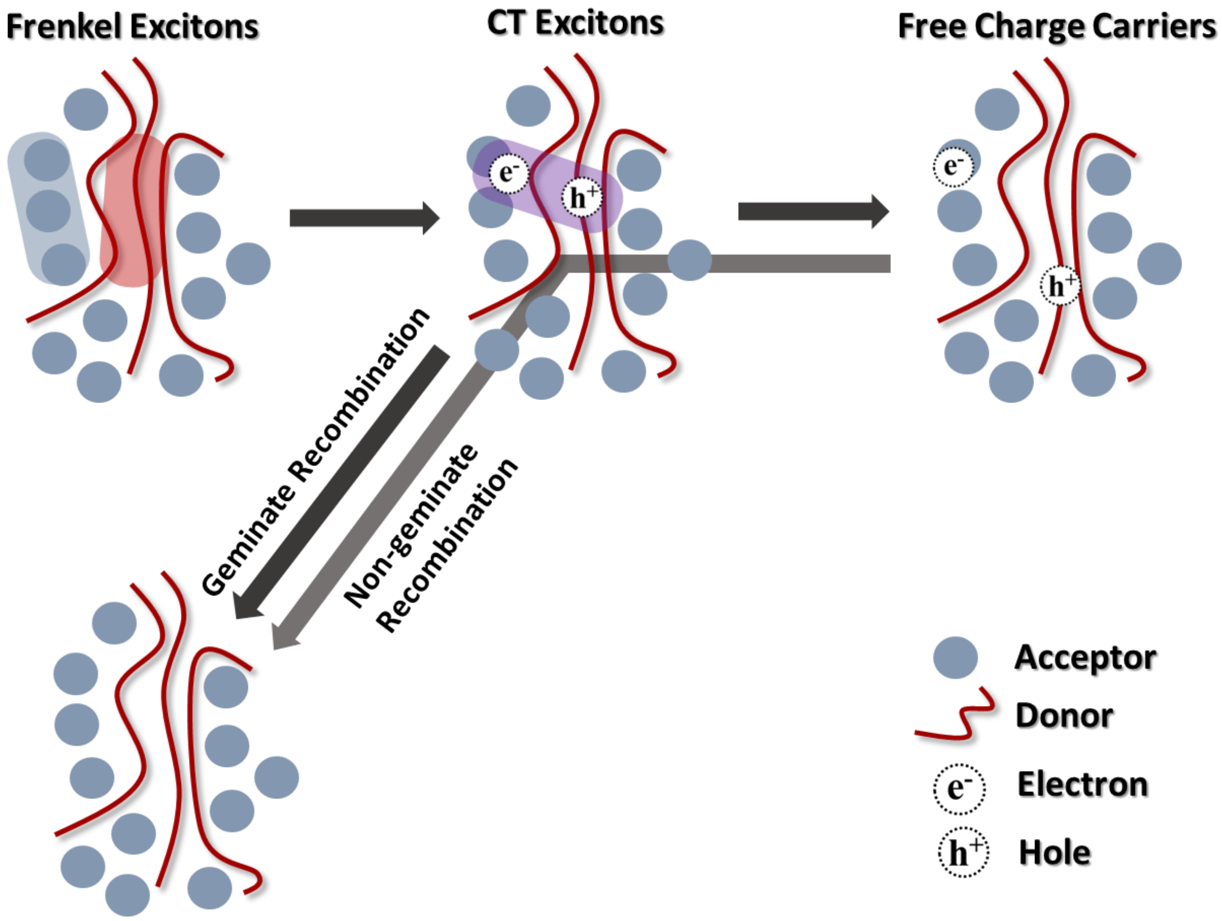

Figure 1.1.4. Illustration of geminate and non-geminate recombination process.

1.2 Strategies for efficient OSCs

1.2.1 Active layer modification

In OSCs, photoactive layer materials have always been the key factors for achieving high PCE. Donor/acceptor materials, in general, should have (i) matching absorption spectrum; (ii) adequate molecular energy level alignment; (iii) nanoscale phase separation; and (iv) high charge carrier mobility.[40-45]

Donor Materials

Donor materials are one of the crucial elements in the advancement of OSCs, as illustrated above (**Figure 1.2.1**). Electron-rich donor polymers are used to donate electrons in the absorber layer of OSCs. Polythiophenes, thienthiopene, and 2,1,3-benzothiadiazole are typical donor polymers utilized in the formulation of the absorber medium in OSCs. Polythiophenes and their derivatives have enhanced the scientific interest in solar applications. P3HT, PTB7, and PTB7-Th are frequently used to assemble OSCs. The combination of polymer donors and fullerene counterparts has developed efficient and stable organic semiconductor-based devices on both glass and flexible substrates.[46-55] Furthermore, to provide complementary absorption with narrow-bandgap NFAs, several wide-bandgap polymer donors, such as the *J*-series, PBDB-series, PTQ10, and D18, are devised and synthesized.[56-63] In 2012, Hou's group designed the PBDBT material for the first time. The PBDB-T:$PC_{61}BM$-based OSCs yielded a PCE of 6.67 %, which was not exceptional among fullerene-based OSCs. When incorporated into NFA-based OSCs, PBDB-T began to demonstrate its immense potential for high-performance device development. Hou’s group found that PBDB-T:ITIC showed a broader absorption and a more suitable energy level alignment. With the combination of PBDB-T and ITIC, the device presented a PCE as high as 11.21%. On the basis of PBDB-T, Hou's group modified its optical and electrical characteristics in order to make it a more effective donor material. After that, two conjugated polymers were formed: PBDB-T-2F (PM6) and PBDB-T-2Cl (PM7). In PBDB-T-2F, the thiophene side groups were fluorinated, whereas in PBDB-T-2Cl, they were chlorinated. PBDB-T-2Cl exhibited comparable optoelectronic and morphological properties to PBDB-T-2F resulting in a high PCE in OSCs. In 2012, Li's group designed J51, a conjugated side-chain-isolated D-A copolymer. J51 was formed of the donor unit of BDT with a thiophene-conjugated side chain, a thiophene bridge, and the acceptor unit of benzotriazole with fluorine substitution, exhibiting well-defined absorbance and strong hole mobility. With continual alteration of the thiophene side chain of BDT, Li's group discovered more efficient donor materials, J71, J81, and J91, with increased absorption, higher hole mobility, and reduced energy loss. Later, Ding's group developed a more effective copolymer, D18, using a fused-ring acceptor unit, dithieno[3′,2′:3,4;2″,3″:5,6]benz[1,2-c][1,2,5]thiadiazole (DTBT). DTBT has a broader molecular plane than DTTP, resulting in a greater hole mobility.[63]

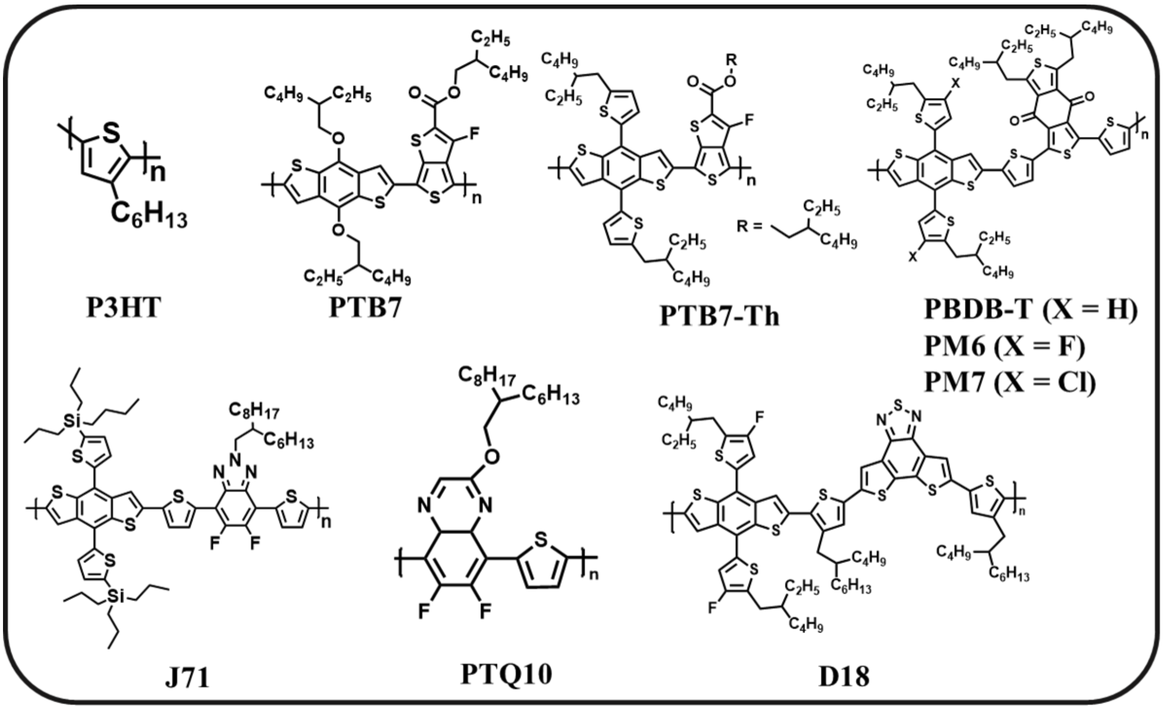

Figure 1.2.1. Representative donor for OSCs.

Acceptor Materials

Before to 2015, the most common acceptors in OSCs were fullerene derivatives, such as $PC_{61}BM$ and $PC_{71}BM$.[64-68] Although fullerene derivatives are the most commonly used materials as the main acceptors in OSCs, they have disadvantages such as high manufacturing cost, poor mechanical flexibility, low light absorption in the infrared to ultraviolet range of the electromagnetic spectrum, and, in the longterm, the OSC's morphology and stability can be compromised by the fullerenes' propensity to diffuse and aggregate. The PCE of OSCs, whose active layer comprises polymer and fullerene, is limited due to the low charge carrier mobility in comparison to the short exciton diffusion length. These limitations, together with the benefits of NFA such as strong solubility (important for large-scale manufacturing), processing in halogen-free (less hazardous) solvents, and good thermal stability, have prompted research on NFAs, resulting in the fast development of PCE generated by NFAs. In 2015, Lin and coworkers reported the NFA, ITIC, which had superior visual absorbance, increased electron mobility, and enhanced D/A miscibility in comparison to fullerene acceptors.[69] Later, Yuan and co-workers revealed a new class of NFA, Y6, which utilized a ladder-type electron-deficient-core-based central fused ring, dithienothiophen[3,2-b]-pyrrolobenzothiadiazole (TPBT). The joined TPBT unit in Y6 retained the conjugation over the length of the molecule, allowing for the adjustment of the electron affinity. In addition, the introduction of lengthy alkyl side chains to the core unit's terminal enhanced the solubility of Y6. With the assistance of Y6, the PCE of NFA-based OSCs has been significantly enhanced. The exceptional photovoltaic performance of Y6 and its derivatives drew great interest. Recently, Cui et al. conducted a new "Y-series" NFA, BTP-4Cl, by replacing the halogen atoms of the fluorinated Y6.[70] In comparison to Y6, the chlorinated acceptor BTP-4Cl displayed a redshift in optical absorption and a downshift in the LUMO energy level. In order to achieve a compromise between the processability of BTP-4Cl and the efficiency of the device, the alkyl chains on the pyrrole rings were extended to 2-bultyloctyl (BO), which improved the solubility. In addition, the optimization of alkyl chains on the edge of BTP-4Cl was conducted by shortening the n-undecyl (C11) to n-nonyl (C9). With the modifications of BO and C9, a new NFA namely, BTP-eC9 was developed.[70-73] In recent years, the field of NFA-based OSCs has shown extraordinary growth, and the efficiency record of NFA-based OSCs has been continuously updated **(Figure 1.2.2).**[74-77]

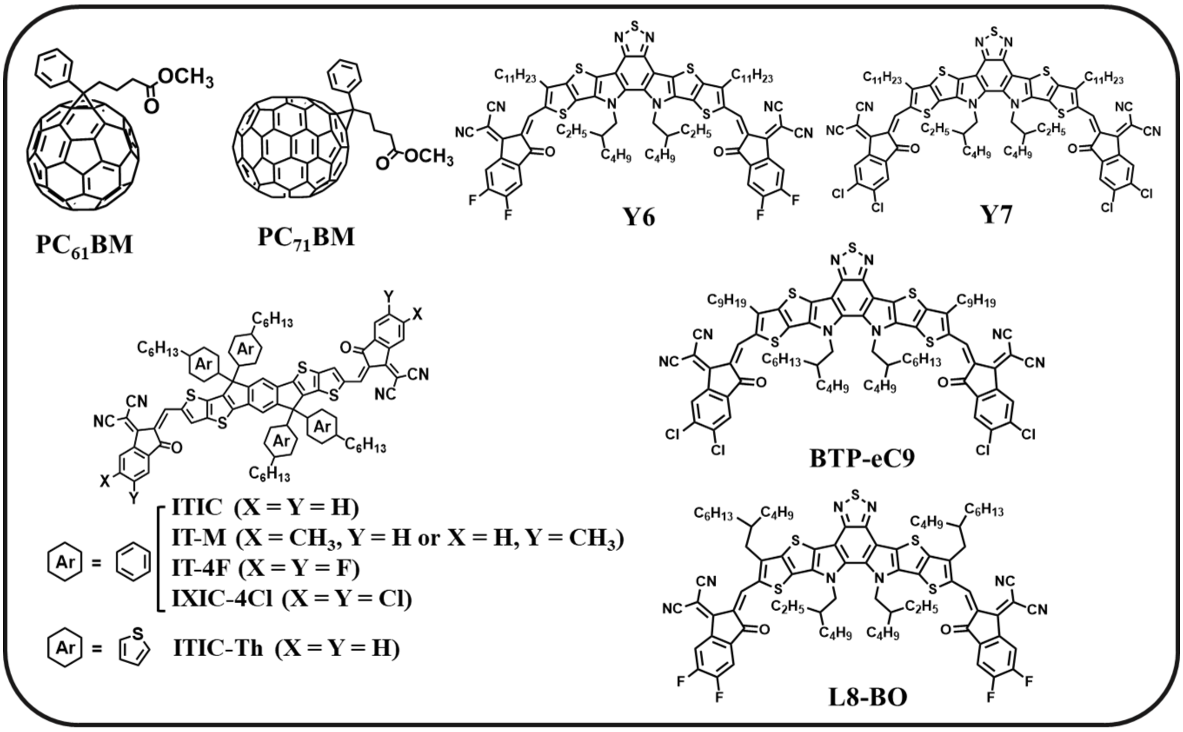

Figure 1.2.2. Representative acceptor for OSCs.

1.2.2 Additive

Active layer morphology has a crucial influence in the performance of OSC devices; hence, significant efforts have been made to develop morphology optimization approaches in order to maximize the potential of photoactive materials. Some research group develop the active layer materials by modification of backbone, side-chain, and substitution of the functional unit.[78-83] However, they have some limitations (complex synthesis process, unguaranteed performance). Alternatively, additives applied in the process of active layer fabrication have proven to be a common and straightforward approach to morphological control (**Figure 1.2.3**). Additives can classify two types; one is solvent and the other one is solid additives.

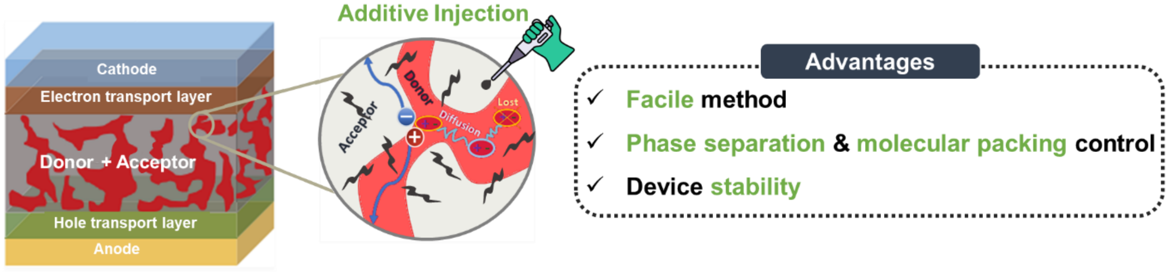

Figure 1.2.3. Advantages of additive in OSCs.

Solvent Additives

The solvent additive may solvate either the donor or the acceptor, which is a major benefit. It just has to be relatively miscible in the deposition solvent. The BHJ microstructure is altered by solvent additives, which change the molecular orientation and arrangement of pure donor/acceptor domains and the degree to which they are phase separated. Frequently, solvent additives increase the overall crystalline order, although the impact of any particular addition differs between D:A pairs. In 2006, the first effective solvent additive was reported. Peet et al. reported initially greater photocurrents from P3HT:PC61BM blend films when extra 1-octanedithiol (ODT) was utilized (**Figure 1.2.4**).[84, 85] The influence of six 1,8-di(R) octane compounds (where R is thio-, chloro-, bromo-, iodo-, cyano-, and acetate) fulfilling this condition on the morphology was investigated further.[86] Hoven group suggested 1-CN as a suitable solvent additive due to its high boiling point and better capacity to dissolve the polymer than the deposition solvent.[87] Based on this history, systematic computational approaches to discovering new additives have been proposed.[88-94]

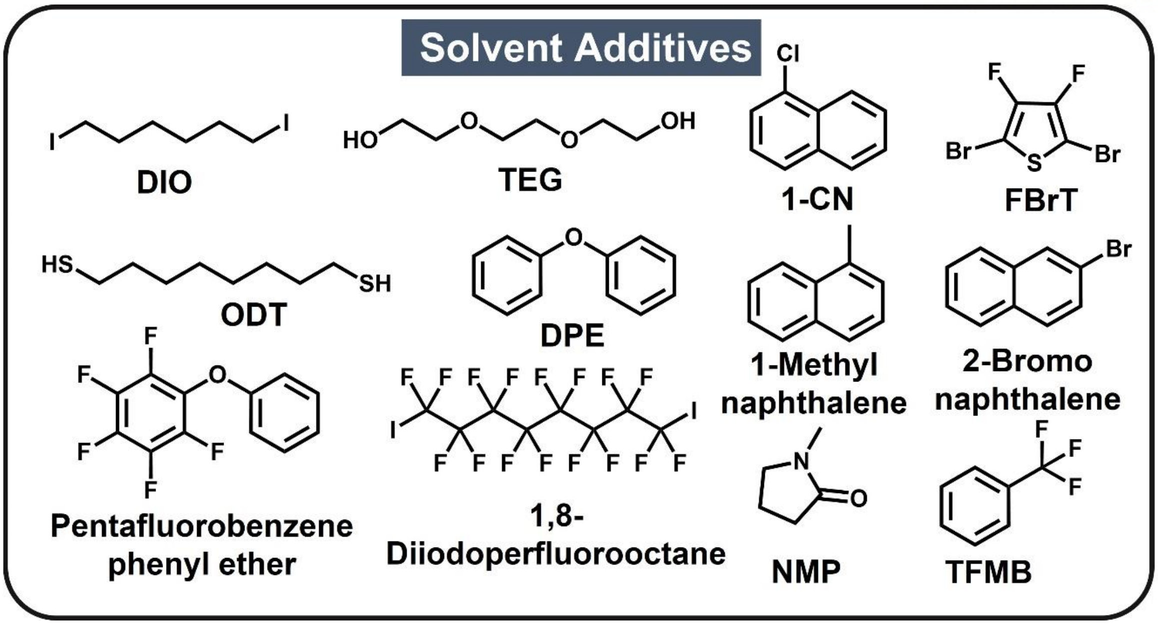

Figure 1.2.4. Representative solvent additives for OSCs.

Non-volatile Solid Additives

Due to their high boiling point, the solid additives in this category remained in the blend film after post-treatment. For doping blend films, nonvolatile solid additives with outstanding optical and electrical characteristics are ideally suited (**Figure 1.2.5**).

Wu et al. conceived the idea of solid additives. They added 2,3-dihydroxypyridine (DHP), a simple nonvolatile organic compound with a boiling point of 387 °C, to the fullerene-based organic solar cell. The proposed functioning mechanism is considerably distinct from liquid additives that are frequently employed. As a result, J_{SC} and FF increased dramatically, leading to a greater PCE than the device without solid additives. In 2016, the Cheng group used the term "molecular lock" to characterize the interaction of solid additive BPO and F-containing polymer donors.[95] The strong O–H···F bond facilitates the π–π stacking of polymer materials, but the "lock" might freeze the shape of blend films. Consequently, the BPO treatment increased the efficiency of all F-containing solar cells, although the PCEs of active layers without F atoms remained unaltered. In 2020, the Yang group researched a built-in electric field without poling processing by inserting developed PVDF-based ferroelectric additives into the active-layer matrices of OSCs. Due to the ferroelectric polarization induced by ferroelectric additives in a halogen-free processing system, remarkable efficiency are achieved.[96] Use of ferroelectric additives in halogen-free systems has promise in related organic-semiconductor domains for reasons that go beyond the improvement of production efficiency and environmental sustainability.

Adding both solvent and solid additives to boost the efficiency of a gadget may be an intriguing method. Du et al. added 1,10-decanediol (DDO), a halogen-free solid additive, to a fullerene-based active layer. They hypothesized that the solvent with a high boiling point, DIO, inhibits the aggregation of fullerenes, whereas DDO regulates the polymer donor and enhances crystallization, hence facilitating favorable charge transmission.In addition to these types of solid additives, various types of solid additives have been developed.[55, 97-100]

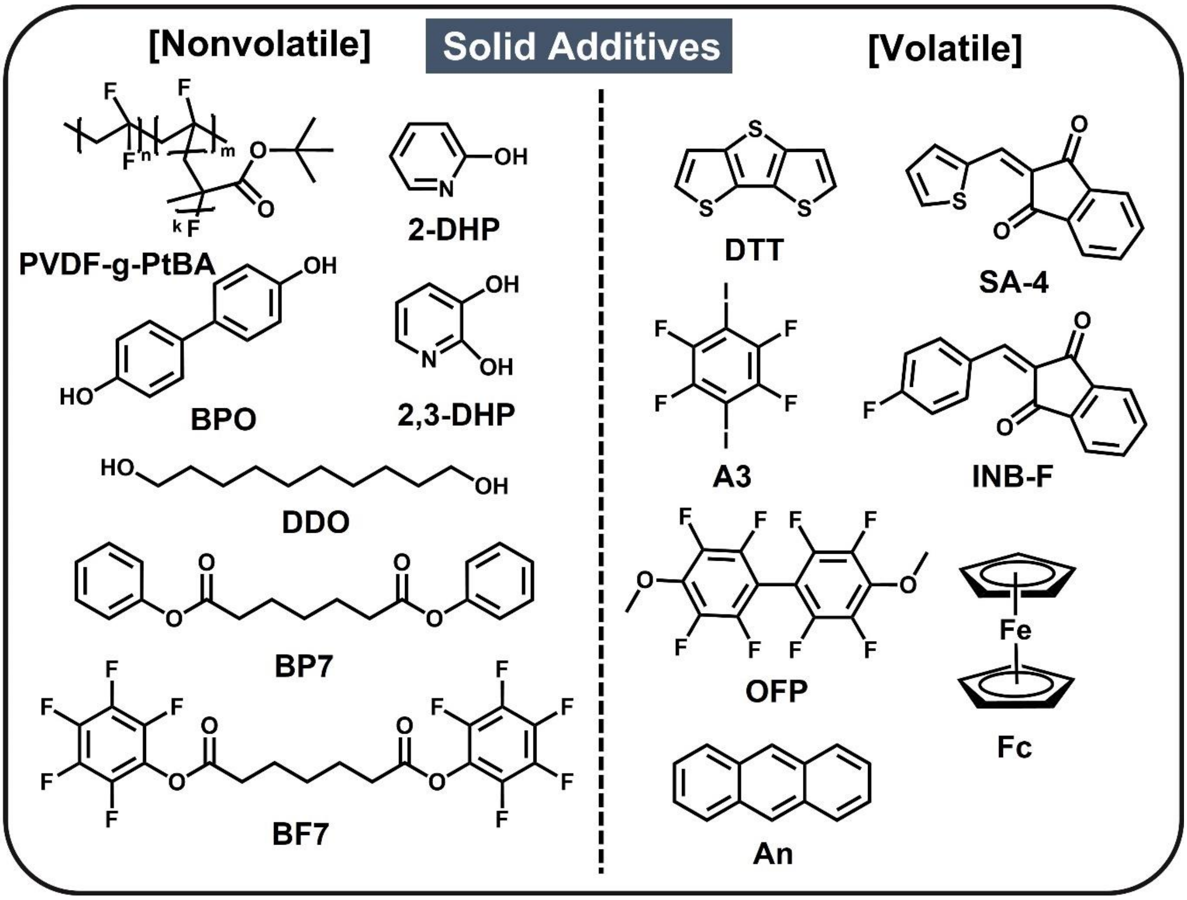

Figure 1.2.5. Representative solid additives for OSCs.

Volatile Solid Additives

As with non volatile additives, volatile solid additives may act as morphology-directing agents and can be removed after thermal annealing. Molecules having significant dipole moments or extremely crystalline structures are frequently the volatile solid additives that perform optimally in OSCs (**Figure 1.2.5**). Solid additives were designed for A–D–A-type photoactive materials because a similar structure is anticipated to enhance charge transfer in the active layers. For instance, the Yu group introduced a set of volatile solid additives designated SA1 to SA8.[101] The compounds displayed greater volatilization characteristics, leading in improved device performance. The author determined from the UV–Vis spectra that solid additives assisted to control the morphology of acceptors, but had no effect on the polymer donor. Meanwhile, the mechanisms of several interesting molecules were also investigated. Fu et al. introduced a “σ-hole”-containing volatile solid with an appropriate volatility named A3 (1,4-diiodotetrafluorobenzene) in organic solar cells. Simulations based on the DFT reveal that A3 has σ-holes that could create non-covalent interactions with lone electron pairs. A3 displayed a strong vibronic shoulder in the polymer blend film and a slight redshift in the acceptor film, indicating increased aggregation and orderly packing of the molecules when mixed with PM6 and Y6 individually. By inserting ferrocene into a BHJ as a highly volatile solid additive, Sun group reported a simple method for enhancing solar performance and photostability.[102] Ferrocene is a commercially available aromatic organic transition metal compound. Bao et al. found that dithieno[3,2b:2′,3′-d]thiophene (DTT), a volatile solid additive with high crystallinity, may inhibit the self-aggregation of acceptor molecules. In addition, the combination of CN and DTT might boost the JSC and FF of OSCs through synergistic effects.[103] Anthracene (An) can also affect the morphology and provide unprecedented opportunities for developing cutting-edge OSCs.[104] In this approach, solid additives have shown substantial promise for altering the active layer morphology and increasing the PCE of various OSCs, which considerably widens the photovoltaics research toolkit.[105-111] Based on this, I look at the role of additives in OSCs by applying newly synthesized donor materials using the commonly used solvent additive. Additionaly, I design the multipurpose solid additives for organic solar cells based on each characteristic by categorizing additives into three types (nonvolatile polymer additives, nonvolatile small molecule additives, and volatile small molecule additives).

1.3 References

1. A. Facchetti, *Chemistry of Materials*, 2011, **23**, 733-758.
2. S. Fratini, M. Nikolka, A. Salleo, G. Schweicher and H. Sirringhaus, *Nature Materials*, 2020, **19**, 491-502.
3. C. G. Granqvist, *Advanced Materials*, 2003, **15**, 1789-1803.
4. N. Kannan and D. Vakeesan, *Renewable and Sustainable Energy Reviews*, 2016, **62**, 1092-1105.
5. G. Yu, J. Gao, J. C. Hummelen, F. Wudl and A. J. Heeger, *Science*, 1995, **270**, 1789-1791.
6. A. E. Becquerel, *Annalen der Physick und Chemie*, 1841, **54**.
7. C. E. Fritts, *American Journal of Science*, 1883, **s3-26**, 465-472.
8. A. J. A. L. R. Pochettino, 1906, **15**, 355.
9. R. N. Marks, J. J. M. Halls, D. D. C. Bradley, R. H. Friend and A. B. Holmes, *Journal of Physics: Condensed Matter*, 1994, **6**, 1379.
10. W. Shockley and H. J. Queisser, *Journal of Applied Physics*, 1961, **32**, 510-519.
11. C. W. Tang, *Applied Physics Letters*, 1986, **48**, 183-185.
12. L. X. Chen, *ACS Energy Letters*, 2019, **4**, 2537-2539.
13. B. Kippelen and J.-L. Brédas, *Energy & Environmental Science*, 2009, **2**, 251-261.
14. F. Yang, Y. Huang, Y. Li and Y. Li, *npj Flexible Electronics*, 2021, **5**, 30.
15. M. Hiramoto, H. Fukusumi and M. Yokoyama, *Applied Physics Letters*, 1992, **61**, 2580-2582.
16. D. Wöhrle and D. Meissner, *Advanced Materials*, 1991, **3**, 129-138.
17. A. Facchetti, *Materials Today*, 2013, **16**, 123-132.
18. C.-Y. Liao, Y. Chen, C.-C. Lee, G. Wang, N.-W. Teng, C.-H. Lee, W.-L. Li, Y.-K. Chen, C.-H. Li, H.-L. Ho, P. H.-S. Tan, B. Wang, Y.-C. Huang, R. M. Young, M. R. Wasielewski, T. J. Marks, Y.-M. Chang and A. Facchetti, *Joule*, 2020, **4**, 189-206.
19. L.-K. Ma, Y. Chen, P. C. Y. Chow, G. Zhang, J. Huang, C. Ma, J. Zhang, H. Yin, A. M. Hong Cheung, K. S. Wong, S. K. So and H. Yan, *Joule*, 2020, **4**, 1486-1500.
20. M. Nam, M. Cha, H. H. Lee, K. Hur, K.-T. Lee, J. Yoo, I. K. Han, S. J. Kwon and D.-H. Ko, *Nature Communications*, 2017, **8**, 14068.
21. B. Ray and M. A. Alam, *Solar Energy Materials and Solar Cells*, 2012, **99**, 204-212.
22. C. J. Brabec, M. Heeney, I. McCulloch and J. Nelson, *Chemical Society Reviews*, 2011, **40**, 1185-1199.
23. D. H. Kim, J. Mei, A. L. Ayzner, K. Schmidt, G. Giri, A. L. Appleton, M. F. Toney and Z. Bao, *Energy & Environmental Science*, 2014, **7**, 1103-1109.
24. S. Li, C.-Z. Li, M. Shi and H. Chen, *ACS Energy Letters*, 2020, **5**, 1554-1567.
25. Y. Wang and X. Zhan, *Advanced Energy Materials*, 2016, **6**, 1600414.
26. J. Zhang, H. S. Tan, X. Guo, A. Facchetti and H. Yan, *Nature Energy*, 2018, **3**, 720-731.

27. M. D. M. Faure, C. Dindault, N. A. Rice and B. H. Lessard, *ACS Omega*, 2022, **7**, 7541-7549.
28. M. D. M. Faure and B. H. Lessard, *Journal of Materials Chemistry C*, 2021, **9**, 14-40.
29. R. Sun, Q. Wu, J. Guo, T. Wang, Y. Wu, B. Qiu, Z. Luo, W. Yang, Z. Hu, J. Guo, M. Shi, C. Yang, F. Huang, Y. Li and J. Min, *Joule*, 2020, **4**, 407-419.
30. K. Weng, L. Ye, L. Zhu, J. Xu, J. Zhou, X. Feng, G. Lu, S. Tan, F. Liu and Y. Sun, *Nature Communications*, 2020, **11**, 2855.
31. L. Zhan, S. Li, X. Xia, Y. Li, X. Lu, L. Zuo, M. Shi and H. Chen, *Advanced Materials*, 2021, **33**, 2007231.
32. Y. Cui, Y. Xu, H. Yao, P. Bi, L. Hong, J. Zhang, Y. Zu, T. Zhang, J. Qin, J. Ren, Z. Chen, C. He, X. Hao, Z. Wei and J. Hou, *Advanced Materials*, 2021, **33**, 2102420.
33. D. Li, N. Deng, Y. Fu, C. Guo, B. Zhou, L. Wang, J. Zhou, D. Liu, W. Li, K. Wang, Y. Sun and T. Wang, *Advanced Materials*, 2022, 2208211.
34. Y. Wei, Z. Chen, G. Lu, N. Yu, C. Li, J. Gao, X. Gu, X. Hao, G. Lu, Z. Tang, J. Zhang, Z. Wei, X. Zhang and H. Huang, *Advanced Materials*, 2022, **34**, 2204718.
35. P. Bi, S. Zhang, Z. Chen, Y. Xu, Y. Cui, T. Zhang, J. Ren, J. Qin, L. Hong, X. Hao and J. Hou, *Joule*, 2021, **5**, 2408-2419.
36. T. Fukuhara, Y. Tamai and H. Ohkita, *Sustainable Energy & Fuels*, 2020, **4**, 4321-4351.
37. A. J. Gillett, A. Privitera, R. Dilmurat, A. Karki, D. Qian, A. Pershin, G. Londi, W. K. Myers, J. Lee, J. Yuan, S.-J. Ko, M. K. Riede, F. Gao, G. C. Bazan, A. Rao, T.-Q. Nguyen, D. Beljonne and R. H. Friend, *Nature*, 2021, **597**, 666-671.
38. S. Liu, J. Yuan, W. Deng, M. Luo, Y. Xie, Q. Liang, Y. Zou, Z. He, H. Wu and Y. Cao, *Nature Photonics*, 2020, **14**, 300-305.
39. N. Schopp, H. M. Luong, B. R. Luginbuhl, P. Panoy, D. Choi, V. Promarak, V. V. Brus and T.-Q. Nguyen, *ACS Energy Letters*, 2022, **7**, 1626-1634.
40. H. Cha and J. Wu, *Joule*, 2021, **5**, 1322-1325.
41. A. Jungbluth, P. Kaienburg and M. Riede, *Journal of Physics: Materials*, 2022, **5**, 024002.
42. B. Qi and J. Wang, *Physical Chemistry Chemical Physics*, 2013, **15**, 8972-8982.
43. M. Riede, D. Spoltore and K. Leo, *Advanced Energy Materials*, 2021, **11**, 2002653.
44. M. C. Scharber and N. S. Sariciftci, *Progress in polymer science*, 2013, **38**, 1929-1940.
45. K. Vandewal, S. Himmelberger and A. Salleo, *Macromolecules*, 2013, **46**, 6379-6387.
46. A. N. M. Alahmadi, *Polymers*, 2022, **14**, 889.
47. F. L. Araújo, D. R. B. Amorim, B. B. M. Torres, D. J. Coutinho and R. M. Faria, *Solar Energy*, 2020, **208**, 583-590.
48. F. Bencheikh, D. Duché, C. M. Ruiz, J.-J. Simon and L. Escoubas, *The Journal of Physical Chemistry C*, 2015, **119**, 24643-24648.
49. C. Caddeo, A. Filippetti, A. Bosin, C. Videlot-Ackermann, J. Ackermann and A. Mattoni, *Nano*

Energy, 2021, **82**, 105708.

50. N. Chandrasekaran, A. Kumar, L. Thomsen, D. Kabra and C. R. McNeill, *Materials Advances*, 2021, **2**, 2045-2054.
51. W. Li, Z. Xiao, J. A. Smith, J. Cai, D. Li, R. C. Kilbride, E. L. K. Spooner, O. S. Game, X. Meng, D. Liu, R. A. L. Jones, D. G. Lidzey and L. J. A. P. R. Ding, *Applied Physics Letters*, 2019.
52. Y. Li, Y. Zhang, B. Wu, S. Pang, X. Yuan, C. Duan, F. Huang and Y. Cao, *Solar RRL*, 2022, **6**, 2200073.
53. Y. Tang, H. Sun, Z. Wu, Y. Zhang, G. Zhang, M. Su, X. Zhou, X. Wu, W. Sun, X. Zhang, B. Liu, W. Chen, Q. Liao, H. Y. Woo and X. Guo, *Advanced Science*, 2019, **6**, 1901773.
54. X. Xu, G. Zhang, L. Yu, R. Li and Q. Peng, *Advanced Materials*, 2019, **31**, 1906045.
55. Q. Zhang, C. Bao, S. Cui, P. Zhong, K. Zhang, W. Zhu and Y. Liu, *Journal of Materials Chemistry C*, 2020, **8**, 16551-16560.
56. J. Hofinger, C. Putz, F. Mayr, K. Gugujonovic, D. Wielend and M. C. Scharber, *Materials Advances*, 2021, **2**, 4291-4302.
57. Q. Liang, J. Han, C. Song, X. Yu, D.-M. Smilgies, K. Zhao, J. Liu and Y. Han, *Journal of Materials Chemistry A*, 2018, **6**, 15610-15620.
58. Z. Liu, *Organic Electronics*, 2021, **93**, 106153.
59. C. Sun, S. Qin, R. Wang, S. Chen, F. Pan, B. Qiu, Z. Shang, L. Meng, C. Zhang, M. Xiao, C. Yang and Y. Li, *Journal of the American Chemical Society*, 2020, **142**, 1465-1474.
60. R. Szymanski, R. Henry, S. Stuard, U. Vongsaysy, S. Courtel, L. Vellutini, M. Bertrand, H. Ade, S. Chambon and G. Wantz, *Solar RRL*, 2020, **4**, 2000538.
61. Y. Wang, C. Xu, C. Wang, Y. Yan, Q. Sun, X. Ma and F. Zhang, *Journal of Polymer Science*, 2022, **60**, 968-974.
62. J. Zhang, W. Liu, S. Chen, S. Xu, C. Yang and X. Zhu, *Journal of Materials Chemistry A*, 2018, **6**, 22519-22525.
63. W. Zhao, D. Qian, S. Zhang, S. Li, O. Inganäs, F. Gao and J. Hou, *Advanced Materials*, 2016, **28**, 4734-4739.
64. D. Chen, A. Nakahara, D. Wei, D. Nordlund and T. P. Russell, *Nano Letters*, 2011, **11**, 561-567.
65. S. H. Han, G. M. Kim and S. Y. Oh, *Journal of nanoscience and nanotechnology*, 2015, **15**, 5446-5449.
66. C. Kapnopoulos, E. D. Mekeridis, L. Tzounis, C. Polyzoidis, S. Tsimikli, C. Gravalidis, A. Zachariadis, A. Laskarakis and S. Logothetidis, *Materials Today: Proceedings*, 2016, **3**, 746-757.
67. M.-A. Pan, T.-K. Lau, Y. Tang, Y.-C. Wu, T. Liu, K. Li, M.-C. Chen, X. Lu, W. Ma and C. Zhan, *Journal of Materials Chemistry A*, 2019, **7**, 20713-20722.

68. J. Yang, N. Clark, M. Long, J. Xiong, D. J. Jones, B. Yang and C. Zhou, *Solar Energy*, 2015, **113**, 181-188.

69. Y. Lin, J. Wang, Z.-G. Zhang, H. Bai, Y. Li, D. Zhu and X. Zhan, *Advanced Materials*, 2015, **27**, 1170-1174.

70. Y. Cui, H. Yao, J. Zhang, K. Xian, T. Zhang, L. Hong, Y. Wang, Y. Xu, K. Ma, C. An, C. He, Z. Wei, F. Gao and J. Hou, *Advanced Materials*, 2020, **32**, 1908205.

71. Y.-Y. Yu, K.-Y. Shih, Y.-C. Peng, Y.-C. Chiu, C.-C. Kuo, C.-C. Yang and C.-P. Chen, *Materials Chemistry and Physics*, 2022, **282**, 125971.

72. J. Yuan, Y. Zhang, L. Zhou, G. Zhang, H.-L. Yip, T.-K. Lau, X. Lu, C. Zhu, H. Peng, P. A. Johnson, M. Leclerc, Y. Cao, J. Ulanski, Y. Li and Y. Zou, *Joule*, 2019, **3**, 1140-1151.

73. L. Zhan, S. Li, Y. Li, R. Sun, J. Min, Z. Bi, W. Ma, Z. Chen, G. Zhou, H. Zhu, M. Shi, L. Zuo and H. Chen, *Joule*, 2022, **6**, 662-675.

74. J. Cao, L. Yi, L. Zhang, Y. Zou and L. Ding, *Journal of Materials Chemistry A*, 2023.

75. S. Li, R. Zhang, M. Zhang, J. Yao, Z. Peng, Q. Chen, C. Zhang, B. Chang, Y. Bai, H. Fu, Y. Ouyang, C. Zhang, J. A. Steele, T. Alshahrani, M. B. J. Roeffaers, E. Solano, L. Meng, F. Gao, Y. Li and Z.-G. Zhang, *Advanced Materials*, 2022, 2206563.

76. Q. Ma, Z. Jia, L. Meng, H. Yang, J. Zhang, W. Lai, J. Guo, X. Jiang, C. Cui and Y. Li, *Advanced Functional Materials*, 2022, 2210733.

77. L. Xie, A. Lan, Q. Gu, S. Yang, W. Song, J. Ge, R. Zhou, Z. Chen, J. Zhang, X. Zhang, D. Yang, B. Tang, T. Wu and Z. Ge, *ACS Energy Letters*, 2022, 361-371.

78. D. Chen, S. Liu, B. Huang, J. Oh, F. Wu, J. Liu, C. Yang, L. Chen and Y. Chen, *Small*, 2022, **18**, 2200734.

79. X. Deng, Y. Fang, B. Huang, F. Liao, K. Liu, J. Zhang, S. Chen, S. Kim, C. Yang, D. Ye, J. Liu and L. Chen, *Chemical Communications*, 2022, **58**, 11823-11826.

80. B. Huang, X. Deng, H. Jin, K. Liu, S. Chen, Z. Ma, J. Oh, C. Yang, J. Liu and L. Chen, *Journal of Materials Chemistry A*, 2022, **10**, 18714-18722.

81. S. Lee, G. Park, M. Jeong, B. Lee, S. Jeong, J. Park, Y. Cho, S. M. Noh and C. Yang, *ACS Applied Materials & Interfaces*, 2022, **14**, 33614-33625.

82. J. Liu, J. Liu, J. Deng, B. Huang, J. Oh, L. Zhao, L. Liu, C. Yang, D. Chen, F. Wu and L. Chen, *Journal of Energy Chemistry*, 2022, **71**, 631-638.

83. L. Wang, T. Wang, J. Oh, Z. Yuan, C. Yang, Y. Hu, X. Zhao and Y. Chen, *Chemical Engineering Journal*, 2022, **442**, 136068.

84. J. Peet, C. Soci, R. C. Coffin, T. Q. Nguyen, A. Mikhailovsky, D. Moses and G. C. Bazan, *Applied Physics Letters*, 2006, **89**, 252105.

85. J. T. Rogers, K. Schmidt, M. F. Toney, E. J. Kramer and G. C. Bazan, *Advanced Materials*, 2011, **23**, 2284-2288.

86. J. K. Lee, W. L. Ma, C. J. Brabec, J. Yuen, J. S. Moon, J. Y. Kim, K. Lee, G. C. Bazan and A. J. Heeger, *Journal of the American Chemical Society*, 2008, **130**, 3619-3623.

87. C. V. Hoven, X.-D. Dang, R. C. Coffin, J. Peet, T.-Q. Nguyen and G. C. Bazan, *Advanced Materials*, 2010, **22**, E63-E66.

88. K. R. Graham, J. Mei, R. Stalder, J. W. Shim, H. Cheun, F. Steffy, F. So, B. Kippelen and J. R. Reynolds, *ACS Applied Materials & Interfaces*, 2011, **3**, 1210-1215.

89. H. I. Kim, M. Kim, C. W. Park, H. U. Kim, H.-K. Lee and T. Park, *Chemistry of Materials*, 2017, **29**, 6793-6798.

90. T. H. Lee, S. Y. Park, B. Walker, S.-J. Ko, J. Heo, H. Y. Woo, H. Choi and J. Y. Kim, *RSC Advances*, 2017, **7**, 7476-7482.

91. J. Y. Na, M. Kim and Y. D. Park, *The Journal of Physical Chemistry C*, 2017, **121**, 13930-13937.

92. A. Sharenko, D. Gehrig, F. Laquai and T.-Q. Nguyen, *Chemistry of Materials*, 2014, **26**, 4109-4118.

93. E.-P. Yao, C.-C. Chen, J. Gao, Y. Liu, Q. Chen, M. Cai, W.-C. Hsu, Z. Hong, G. Li and Y. Yang, *Solar Energy Materials and Solar Cells*, 2014, **130**, 20-26.

94. Z. Zheng, E. He, J. Wang, Z. Qin, T. Niu, F. Guo, S. Gao, Z. Ma, L. Zhao, X. Lu, Q. Xue, Y. Cao, G. T. Mola and Y. Zhang, *Journal of Materials Chemistry A*, 2021, **9**, 26105-26112.

95. P. Cheng, C. Yan, T.-K. Lau, J. Mai, X. Lu and X. Zhan, *Advanced Materials*, 2016, **28**, 5822-5829.

96. T. Kumari, S. Jung, Y. Cho, H.-P. Kim, J. W. Lee, J. Oh, J. Lee, S. M. Lee, M. Jeong, J. M. Baik, W. Jo and C. Yang, *Nano Energy*, 2020, **68**, 104327.

97. X. Du, X. Li, H. Lin, L. Zhou, C. Zheng and S. Tao, *Journal of Materials Chemistry A*, 2019, **7**, 7437-7450.

98. P. Fan, W. Sun, X. Zhang, Y. Wu, Q. Hu, Q. Zhang, J. Yu and T. P. Russell, *Advanced Functional Materials*, 2021, **31**, 2008699.

99. Q. Guo, Y. Liu, M. Liu, H. Zhang, X. Qian, J. Yang, J. Wang, W. Xue, Q. Zhao, X. Xu, W. Ma, Z. Tang, Y. Li and Z. Bo, *Advanced Materials*, 2020, **32**, e2003164.

100. B. Xu, G. Sai-Anand, G. E. Unni, H.-M. Jeong, J.-S. Kim, S.-W. Kim, J.-B. Kwon, J.-H. Bae and S.-W. Kang, *Applied Surface Science*, 2019, **484**, 825-834.

101. R. Yu, H. Yao, L. Hong, Y. Qin, J. Zhu, Y. Cui, S. Li and J. Hou, *Nature Communications*, 2018, **9**, 4645.

102. L. Ye, Y. Cai, C. Li, L. Zhu, J. Xu, K. Weng, K. Zhang, M. Huang, M. Zeng, T. Li, E. Zhou, S. Tan, X. Hao, Y. Yi, F. Liu, Z. Wang, X. Zhan and Y. Sun, *Energy & Environmental Science*, 2020, **13**, 5117-5125.

103. S. Bao, H. Yang, H. Fan, J. Zhang, Z. Wei, C. Cui and Y. Li, *Advanced Materials*, 2021, **33**, 2105301.

104. H. Fan, H. Yang, Y. Wu, O. Yildiz, X. Zhu, T. Marszalek, P. W. M. Blom, C. Cui and Y. Li, *Advanced Functional Materials*, 2021, **31**, 2103944.

105. J. Cai, H. Wang, X. Zhang, W. Li, D. Li, Y. Mao, B. Du, M. Chen, Y. Zhuang, D. Liu, H.-L. Qin, Y. Zhao, J. A. Smith, R. C. Kilbride, A. J. Parnell, R. A. L. Jones, D. G. Lidzey and T. Wang, *Journal of Materials Chemistry A*, 2020, **8**, 4230-4238.

106. S. Chen, J. Ye, Q. Yang, J. Oh, D. Hu, K. Yang, G. O. Odunmbaku, F. Li, Q. Yu, Z. Kan, Z. Xiao, C. Yang, S. Lu and K. Sun, *Journal of Materials Chemistry A*, 2021, **9**, 2857-2863.

107. J. Fu, H. Chen, P. Huang, Q. Yu, H. Tang, S. Chen, S. Jung, K. Sun, C. Yang, S. Lu, Z. Kan, Z. Xiao and G. Li, *Nano Energy*, 2021, **84**, 105862.

108. J. Fu, S. Chen, K. Yang, S. Jung, J. Lv, L. Lan, H. Chen, D. Hu, Q. Yang, T. Duan, Z. Kan, C. Yang, K. Sun, S. Lu, Z. Xiao and Y. Li, *iScience*, 2020, **23**.

109. Y. Yan, Y. Liu, J. Zhang, Q. Zhang and Y. Han, *Journal of Materials Chemistry C*, 2021, **9**, 3835-3845.

110. R. Yu, H. Yao, Z. Chen, J. Xin, L. Hong, Y. Xu, Y. Zu, W. Ma and J. Hou, *Advanced Materials*, 2019, **31**, 1900477.

111. X. Zhang, J. Cai, C. Guo, D. Li, B. Du, Y. Zhuang, S. Cheng, L. Wang, D. Liu and T. Wang, *Small*, 2021, **17**, 2102558.

CHAPTER 2 Solvent Additive

Solvent Additive in Random Copolymer-based Active Layers for Efficient OSCs

2.1.1 Motivation and Research Background

With the surging demand for prospective renewable energy resources for a sustainable future, rapid innovation of BHJ OSC with p-type donors and n-type acceptors has been made in the past decades that have focused on their cost-effectiveness, lightweight, flexibility, solution processibility, and large-area/semi-transparent device fabrication capability.[1-4] PCEs for single-junction cells that have been reported as a result of considerable study on both material evolution (especially, the development of nonfullerence acceptors, such as ITIC, Y6, N3, and their derivatives) and device engineering represent the reliable potential of OSCs.[5-17]

Benzo[1,2-c:4,5-c']dithiophene-4,8-dione (BDD) is one of the most extensively utilized electron-accepting building blocks for high-performance copolymers due to its planar and symmetrical fused-ring structure and self-assembly properties.[18-24] Thus, BDD-based copolymers have made extraordinary strides in enhancing the PCEs of BHJ OSCs.[25] Recently, the BDD isomer benzo[1,2-b:4,5-c′]dithiophene-4,8-dione (*i*BDD) was developed.[26] It displayed a stronger intermolecular connection, a higher absorption coefficient, a larger dipole moment, and a greater propensity to take electrons than BDD. Despite the fact that *i*BDD-based copolymers have been described, their development and device performance continue to considerably lag behind those of BDD-based copolymers.

Recent research has demonstrated the extensive influence of side chains beyond solubility on device construction, notably in terms of molecular ordering, charge transport, film morphology, and OSC characteristics. In addition to the modification of the backbone, the side chains of copolymers have garnered substantial study.[27-30] Few investigations have been reported on the side-chain engineering of the BDD unit, which includes 2-ethylhexyl (EH) solubilizing groups.[31-33]

In addition to the beneficial effect of alkylsilyl side chains induced by $\sigma^*(\mathrm{Si})$–$\pi^*(\mathrm{C})$ bond interaction on the performance of OSCs, our focus on the chemistry of *i*BDD has promoted the design and synthesis of triisopropylsilyl (TIPS)-substituted (*i*BDD-Si), as well as *i*BDD-Si-based copolymers (PM6, PM6-5Si, PM6-10Si, and PM6-15Si) with varying contents in the backbone.[34,35] The integration of *i*BDD-Si into the backbone has been seen to affect the optical property (particularly the absorption coefficients), energy levels, and molecular packing. To evaluate the photovoltaic performance of organic solar cells, copolymers were utilized as the donor and N3 as the acceptor.

Among these, the PM6-5Si:N3-based OSC demonstrated the highest PCE of 17.01 %, which was significantly more than that of the PM6 copolymer-based device without the *i*BDD-Si control unit. This finding is a consequence of the blend device's balanced charge transport, increased charge generation/dissociation kinetics, and minimized overall energy and recombination losses. Our findings suggest that *i*BDD-Si is a potential constituent of high-performance conjugated materials for OSCs.

2.1.2 Synthesis and Characterization

Starting with 2,5-dibromothiophene-3,4-dicarboxylic acid (**1**), BDDTh-Br_2 was synthesized using the reported procedure.[36] Its isomeric analog with TIPS side chains (*i*BDD-Si, compound **4**) was obtained using the Friedel–Crafts acylation cyclization of 2,5-dibromothiophene-3,4-dicarbonyl dichloride (**2**) and triisopropyl(thiophen-2-yl)silane (**3**) (**Figure 2.1.1a and b** and **Scheme 2.1.1**) in the presence of $AlCl_3$. In principle, 3,4,5-unsubstituted thiophene (**3**) has two possible intermolecular cyclization pathways (i.e., 3,4- and 4,5-cyclizations) for two consecutive Friedel–Crafts reactions of the formed acylium ions. Thus, using 2D NOESY and conventional NMR, we thoroughly examined the chemical structure of 4. NOE correlation signals may be generated by the coupling between the 3-proton in the thienyl unit and those in the TIPS substituent in the case of *i*BDD-Si formed by 4,5-cyclization, but they are absent in the case of 3,4-cyclization because the protons are too far apart (see **Figure 2.1.1c**). The NMR spectrum of compound **4** reveals three proton peaks: one thienyl proton (H_a), one methyl proton (H_b), and one methine proton (H_c) of TIPS, shown in yellow, blue, and green, respectively. As shown in **Figure 2.1.1d**, there are two distinct off-diagonal NOE signals (A at (7.78, 1.12) and B at (7.78, 1.39) ppm peaks corresponding to H_a–H_c and H_a–H_b couplings, respectively), which verifies the 4,5-cyclized *i*BDD-Si structure. ^{13}C NMR, high-resolution mass spectrometry, and EA were used to further confirm the purity and structure of *i*BDD-Si. The improved selectivity of 4,5-cyclization in **3** may be due to the more stable sigma complexes for the initial electrophilic 5-position assault of the acylium ion as the electrophile compared to the 3- or 4-position attacks (see the different numbers of the resonance forms in **Figure 2.1.1e**). Stille coupling of **4** and tributyl(thiophen-2-yl)stannane produced thiophene flanked *i*BDDTh-Si (**5**), which was then brominated with NBS to form *i*BDDTh-Si-Br_2. Theoretical simulations using DFT B3LYP on a 6–31G* basis found that the *i*BDDTh-Si moiety has somewhat deeper-lying energy levels than the BDDTh-EH moiety (**Figure 2.1.9**). In addition, the frontier energy levels of *i*BDDTh-Si and BDDTh-EH, as calculated by their CV measurements, are in agreement with the aforementioned simulation outcomes.

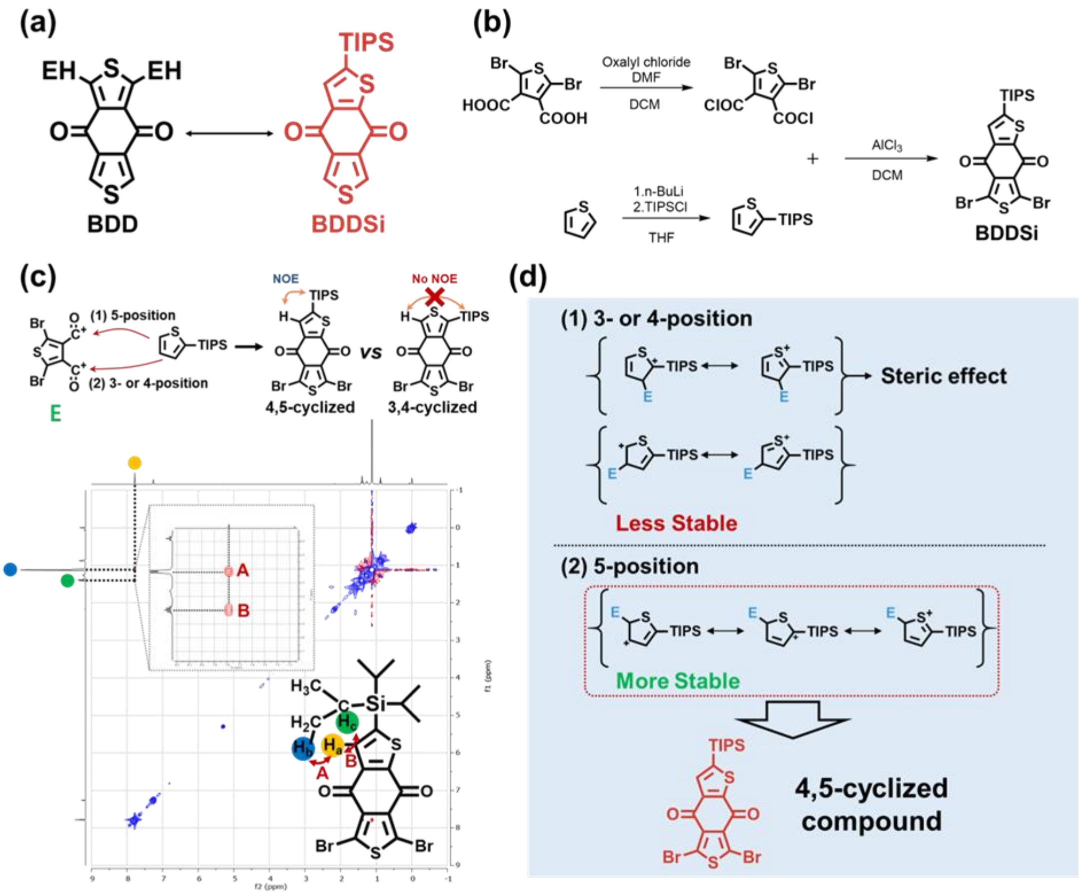

Figure 2.1.1. (a) Molecular structures of BDD and *i*BDD-Si. (b) Synthesis of the *i*BDD-Si core unit. (c) NOE availability of two possible isomeric structures. (d) Spectrum in 2D NOESY of the *i*BDD-Si. (e) Comparing the resonance structures and stabilities of intermediates at different substitution positions.

Compared to BDDTh-EH, the optical characteristic of *i*BDDTh-Si as a thin film exhibited a redshifted onset and was broader (**Figure 2.1.2**). The aforementioned outcomes are a result of the combined impact of the more stable quinoidal structure of *i*BDD compared to BDD and the σ*(Si)–π*(C) bond interaction caused by the Si-atom side chains.[26,34,35]

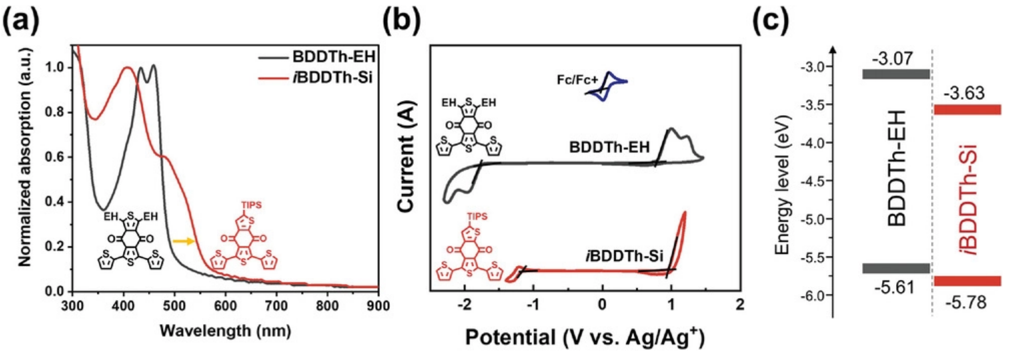

Figure 2.1.2. (a) UV–Vis spectra and (b) CV of BDDTh-EH and *i*BDDTh-Si units. (c) Energy level ofr BDDTh-EH and *i*BDDTh-Si.

Using palladium-catalyzed stille polymerization, we introduced various ratios of the iBDDTh-Si unit into the PM6 backbone matrix to form a series of iBDD-Si-based copolymers denoted as PM6-xSi (x = 5, 10, and 15), where x indicates the feeding ratios of iBDDTh-Si **(Figure 2.1.3a)**. The reference copolymer PM6 was also synthesized and analyzed to elucidate the influence of the iBDDTh-Si in the backbone. Due to their low solubility/processability at higher concentrations, we were only able to synthesis and study copolymers containing up to 15 % *i*BDDTh-Si (**see Figures 2.1.10 and 2.1.11, and Table 2.1.3**).

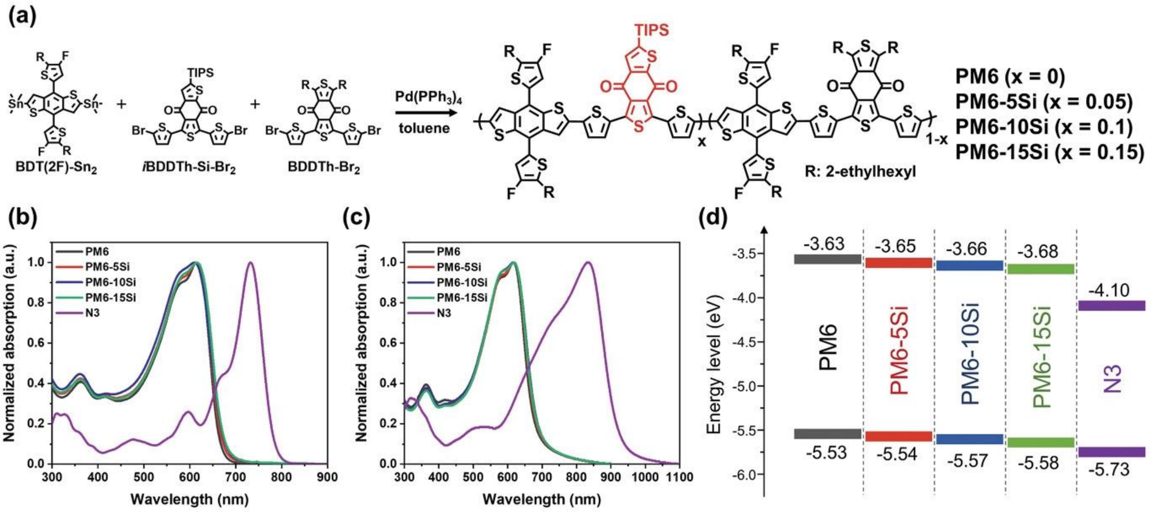

Figure 2.1.3. (a) Chemical structures and synthetic routes of donor copolymers. Normalized UV–Vis spectra of copolymers (b) in solution and (c) as thin films. (d) Diagrams depicting the energy levels of the four copolymers and N3.

The molecular weights of the copolymers were determined using high-temperature gel permeation chromatography with 1,2,4-trichlorobenzene as the eluent at 100 °C. M_n/PDI of PM6-15Si, PM6-10Si, PM6-5Si, and PM6 were 29.5 kDa/3.81, 30.9 kDa/2.52, 31.3 kDa/2.21, 32.7 kDa/2.93, respectively. As shown in FT-IR (**Figure 2.1.12**), *i*BDD-Si-containing copolymers showed Si–C bond stretching vibrational band at 880 cm^{-1} corresponding to TIPS group.[37] The strength of Si–C band relative to the C–O one at 1649 cm^{-1} is manifested in the order of PM6-5Si < PM6-10Si < PM6-15Si. In addition, a negligible variation (less than 0.3%) between the EA and expected values for the copolymers indicated that they were synthesized according to the feed ratios within the experimental error range. In the Supplementary Information, the precise synthesis conditions and characterisation are described. (**Figures 2.1.13–2.1.21**). **Figure 2.1.3b** and **c** depict the UV–Vis absorption spectra of the copolymers in dilute CF solution and thin films, respectively, and **Table 2.1** summarizes the pertinent data. All the copolymers displayed two unique absorption bands at 300–400 and 500–660 nm, which may be related to the π– π^* transition and ICT between the donor and acceptor units. In addition to similar UV–Vis spectra between the solution and matching copolymer films, no substantial chromic shift was seen when the iBDDTh-Si block was incorporated into the PM6 host backbone. Upon closer examination, however, we discovered that the absorption coefficients of the films rose somewhat with increasing *i*BDDTh-Si concentration in the backbone (**Figure 2.1.22**), which is suggestive of efficient photon use. In dilute solution, all copolymers displayed considerable temperature-dependent aggregation behavior (**Figures 2.1.23 and 2.1.24**).

Table 2.1.1. Optical and electrochemical properties of the copolymers and N3.

Samples	$\lambda_{\max}^{\mathrm{sol}}$ **(nm)**	$\lambda_{\max}^{\mathrm{film}}$ **(nm)**	λ_{onset} **(nm)**	E_g^{opt} **(eV)**	E_{HOMO} **(eV)**	E_{LUMO} **(eV)**	E_g^{CV} **(eV)**	***M*n (kDa)**	**PDI**
PM6	613	616	688	1.80	-5.53	-3.63	1.90	32.7	2.93
PM6-5Si	613	617	688	1.80	-5.54	-3.65	1.89	31.3	2.21
PM6-10Si	613	617	689	1.80	-5.57	-3.66	1.91	30.9	2.52
PM6-15Si	614	618	690	1.80	-5.58	-3.68	1.90	29.5	3.81
N3	732	833	923	1.34	-5.73	-4.10	1.63	-	-

CV measurements were used to determine the electrochemical characteristics of the copolymers, and **Figure 2.1.25** and **Figure 2.1.3d** depict the HOMO and LUMO energies. Despite the minor and steady decrease in energy levels found at greater *i*BDDTh-Si concentrations, no significant variation was observed in the HOMO/LUMO levels of any of the copolymers. Consequently, iBDD-Si-containing copolymers may be employed as donor materials in BHJ OSCs paired with narrow-bandgap nonfullerene acceptors, such as Y6 and N3.

DFT molecular simulations were also performed to examine the electron density distributions and optimal molecular conformations of the three dimer models as a function of the implanted iBDDTh content in the backbone. To simplify the BDD, the lengthy EH side chains were substituted with methyl groups. As shown in **Figure 2.1.4**, introduction of the *i*BDDTh unit can reduce the torsional angles in the conjugated backbone. Thus, resulting in the coplanarity of the dimer models in the order: (BDT(2F)–BDDTh)$_2$ < (BDT(2F)–BDDTh)–(BDD(2F)–*i*BDDTh-Si) < (BDT(2F)–*i*BDDTh-Si)$_2$. In addition, the *i*BDDTh-Si models exhibited greater net dipole moments than the (BDT(2F)–BDDT)$_2$ models. Notably, the LUMO electron concentrations were more localized on iBDD-Si than on BDD in the iBDDTh-Si-containing models, indicating that iBDD-Si is a more electron-deficient group than BDD, consistent with the monomers' CV results presented before. Based on the theoretical calculations, we anticipate that the iBDD-Si-containing copolymers will have an effective molecular packing structure and display the ICT effect.

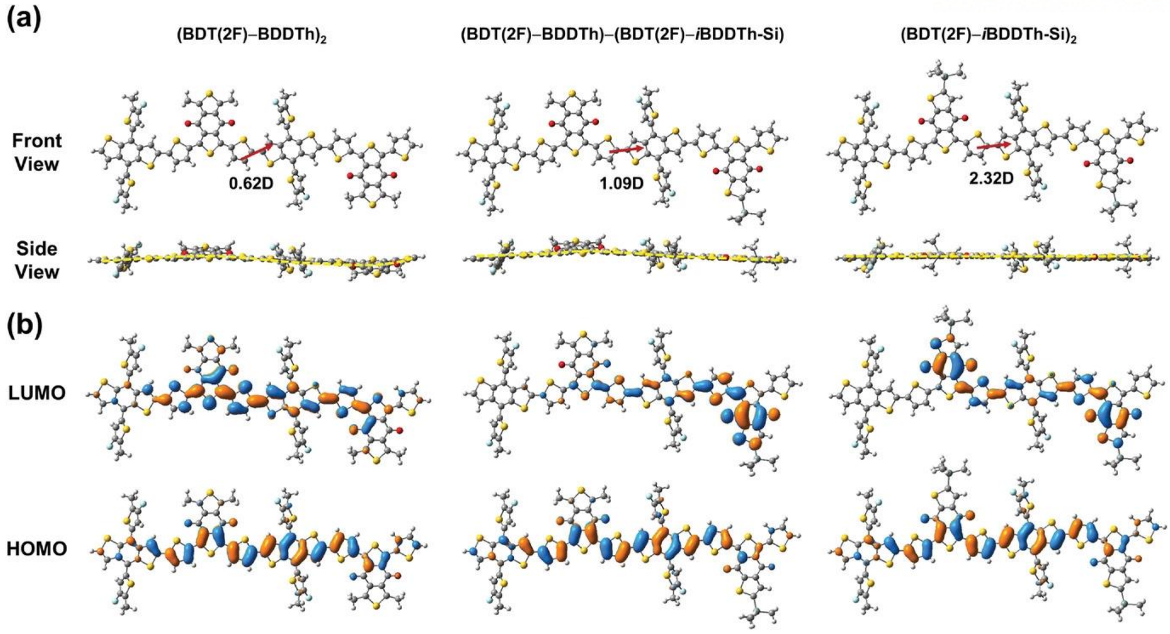

Figure 2.1.4. (a) optimized simulated geometries and (b) electron density distributions of various sequences of dimer models.

2.1.3 Photovoltaic Performance

OSCs with a single junction based on copolymer donors were manufactured with a conventional configuration. The nonfullerene acceptor N3 with a small bandgap was selected for the BHJ OSC study due to its superior electron transport capabilities, perfect complementary absorption, and adequate energy level alignment.[18-24] The *J*–*V* curves of the optimized devices are depicted in **Figure 2.1.5a**, and the relevant photovoltaic parameters are summarized in **Table 2.1.2**. The optimized OSC based on PM6:N3 exhibited a PCE of 15.15% with V_{OC} of 0.838 V, J_{SC} of 25.21 mA cm^{-2}, and FF of 71.72%, which are comparable with the previously reported PM6:N3 system.[38] The OSC based on PM6-5Si:N3 demonstrated the greatest performance among those evaluated, with a maximum PCE of 17.01 % and increased photovoltaic parameters—V_{OC} of 0.852 V, J_{SC} of 26.32 mA cm^{2}, and FF of 75.81 %. The acceptable PCE values for PM6-10Si:N3- and PM6-15Si:N3-based OSCs were 14.86 and 13.74 %, respectively. Since the PM6-10Si and PM6-15Si copolymer donors demonstrated somewhat decreased HOMO levels, it was predicted that their use would result in greater V_{OC} values. Several additional parameters (e.g., molecule orientation, electrical property, domain purity, etc.) besides the HOMO of the copolymer donor may be extrapolated to influence the V_{OC}.[39-42] **Figure 2.1.26** depicts the EQE spectra, which cover the wavelength range of 300–900 nm. The integrated J_{SC} values from the EQE measurement are within 5% agreement with those from the *J*–*V* curves.

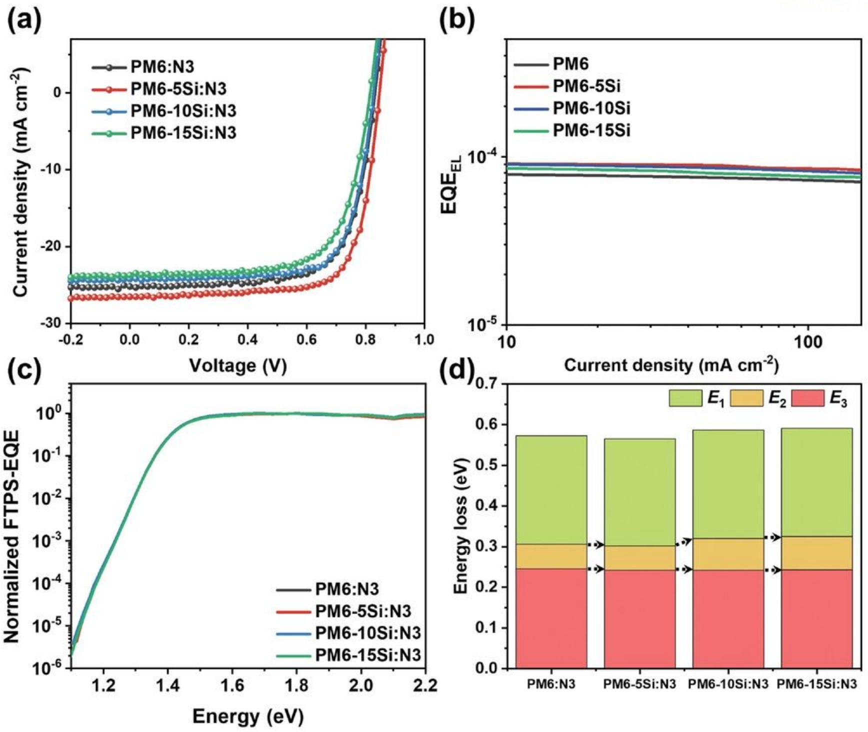

Figure 2.1.5. (a) *J*–*V* curves of the OSCs constructed from the copolymers:N3 blends. (b) EQE_{EL} spectra of OSCs at varying current densities. (c) The devices' normalized FTPS-EQE values. d) Diagrams of calculated energy loss.

Table 2.1.2. Photovoltaic parameters of the OSC devices.

Active Layer	V_{OC} [V]	J_{SC} [mA cm^{-2}]	FF [%]	PCE [%] [a)]	Integrated J_{SC} [mA cm^{-2}]
PM6:N3	0.838 (0.833)	25.21 (24.97)	71.72 (71.67)	15.15 (14.91)	24.61
PM6-5Si:N3	0.852 (0.850)	26.32 (26.12)	75.81 (75.25)	17.01 (16.71)	25.31
PM6-10Si:N3	0.833 (0.831)	24.48 (24.31)	72.87 (72.31)	14.86 (14.60)	23.57
PM6-15Si:N3	0.829 (0.819)	23.98 (23.73)	69.07 (69.15)	13.74 (13.48)	23.08

[a)] The average PCE values in parentheses were obtained from 16 devices.

To understand the reason for the unusual V_{OC} trend observed, we investigated in detail the energy losses in the optimized devices. The total E_{loss} can be expressed as follows:

$$E_{\text{loss}} = \Delta E_1 + \Delta E_2 + \Delta E_3$$

where ΔE_1 originates from inevitable radiative recombination owing to the Shockley–Queisser limit, ΔE_2 is an additional radiative recombination below the bandgap related to charge dynamics, and ΔE_3 arises from nonradiative recombination.[43] ΔE_3 is obtained from the formula $\Delta E_3 = -\mathrm{kT}\ \ln(\mathrm{EQE}_{EL})$, where k is the Boltzmann constant, T the temperature in K, and EQE_{EL} the EQE of EL when charge carriers are injected in dark conditions.[44] The associated EL, FTPS-EQE, and EQE_{EL} spectra of the OSCs are shown in **Figure 2.1.5b,c** and **Figure 2.1.27**, and the extracted values are shown in **Figure 2.1.5d** and **Table 2.1.4**.

Both ΔE_1 and ΔE_3 values differed very slightly amongst all devices, however PM6-5Si:N3, which demonstrated the highest performance, had significantly lower values. Besides, ΔE_2 for the PM6:N3- and PM6-5Si:N3-based devices was 0.06 eV, which is definitely lower than that of PM6-10Si:N3- and PM6-15Si:N3-based devices by 0.022 eV, showing that the dominant loss channel correlates with ΔE_2 as the key reason for the V_{OC} reduction. The calculated E_{loss} (0.573, 0.565, 0.574, and 0.591 eV for PM6:N3, PM6-5Si:N3, PM6-10Si:N3, and PM6-15Si:N3, respectively) are consistent with the VOCs of the corresponding OSCs. ΔE_2 is related to the charge dynamics, which is severely influenced by the charge-carrier behaviors and morphology.[39-42] It will be investigated using various techniques below.

First, single-carrier devices were fabricated to evaluate the μ_h and μ_e mobilities using the SCLC method in the hole-only and electron-only device structures (**Figure 2.1.28** and **Table 2.1.5**). Both μ_h and μ_e for the PM6:N3- and PM6-5Si:N3-based devices were 1.0×10^{-4} cm^2 V^{-1} s^{-1}, which is ≈2–3 times higher than those of the other devices. Comparatively, PM6-5Si:N3 had a more balanced μ_e/μ_h. These results reflect the elevated J_{SC} and FF values observed for the PM6-5Si:N3 system.

For each optimized device, the J_{ph} was shown as a function of the effective V_{eff} in order to comprehend the charge generation and dissociation rates (**Figure 2.1.6a**). The J_{sat} at $V_{eff} > 1.0$ V for all tested devices was in the order: PM6-15Si:N3 < PM6-10Si:N3 < PM6:N3 < PM6-5Si:N3. Under short-circuit conditions, the exciton dissociation and charge extraction probabilities were likewise approximated as J_0/J_{sat} and J_{ph}/J_{sat}, respectively (**Table 2.1.6**), and they followed the same order as the J_{sat}. This demonstrates the occurrence of effective exciton dissociation and charge extraction in the PM6-5Si:N3 material, which lowered ΔE_2, and explains its improved device performance.

To investigate the kinetics of charge recombination, the J_{SC} and V_{OC} were measured as functions of the light intensity (I).[45] As shown in **Figure 2.1.6b and c**, PM6-5Si:N3 exhibited the closest α to 1 (0.994) and the lowest n values compared to the other films, indicating a reduction in both the monomolecular and bimolecular recombination processes, which correlate with the E_{loss} results above.

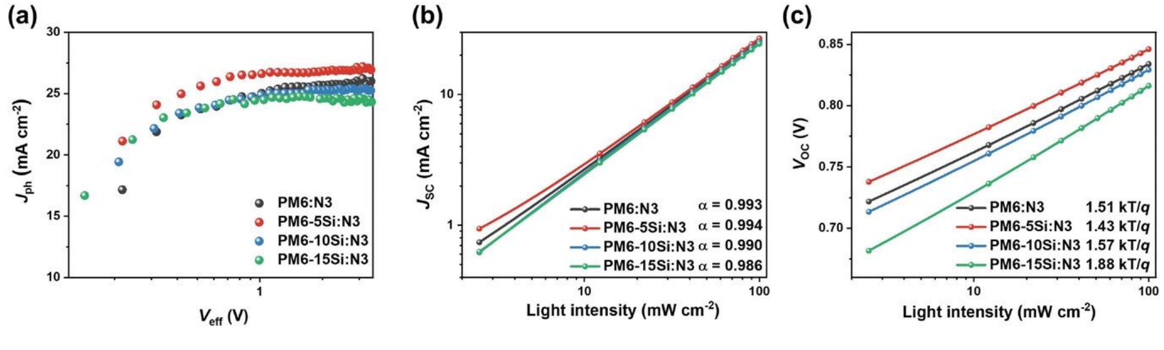

Figure 2.1.6. (a) J_{ph}–V_{eff} curves and measurements of (b) J_{SC} and (c) V_{OC} versus light intensity of the OSCs.

Next, in light of the fact that practical application is one of the most important concerns for future commercialization and mass production of OSCs, we fabricated large-area 0.92 cm^2 OSC devices and compared the photovoltaic performances.(**Figure 2.1.29** and **Table 2.1.7**) The PM6-5Si-based device achieved the highest PCE of 14.20 %. We see that the large devices exhibited the same PCE trend as the small-area devices, but with somewhat substantial PCE variances. This suggests that the photovoltaic properties with large areas are far more sensitive to the chemical structures and/or the solubility of the active layer materials.[46]

2.1.4 Film Morphology

Tapping-mode AFM and TEM were used to examine the surface and bulk morphologies, respectively, of the optimized blend films (**Figure 2.1.7** and **Figure 2.1.30**). Despite having a smooth and uniform surface, PM6-5Si:N3 exhibited a smaller RMS value and a more distinct fibrillar-like characteristic than the other blend films. The TEM pattern of PM6:N3 revealed uniform, featureless textures, but PM6-10Si:N3 and PM6-15Si:N3 exhibited significant aggregated clusters. Nonetheless, the PM6-5Si:N3 blend generated a nanoscale phase-separated structure with appropriate domain sizes, indicating strong domain connectivity. Then, we studied further the phase separation by surface tensions measured by contact angle measurements for droplets of DI water and ethylene glycol on the pristine films (**Figure 2.1.31**). As was seen in previous studies of Si-atom containing copolymers, the surface tensions of the copolymer films dropped as the number of *i*BDD-Si units in the copolymer backbone increased.[47,48] To measure the miscibility of the donor copolymers and N3, we also calculated the Flory–Huggins interaction parameters (χ) for the blend films. As seen from **Table 2.1.8** the χ values of the donor copolymers:N3 blends are in order of PM6-15Si:N3 (0.419K) > PM6-10Si:N3 (0.396K) > PM6-5Si:N3 (0.316K) > PM6:N3 (0.288K), indicating that the blend miscibility was gradually reduced with increasing *i*BDD-Si content. These results accord with the increasing domain size trend in the TEM images.

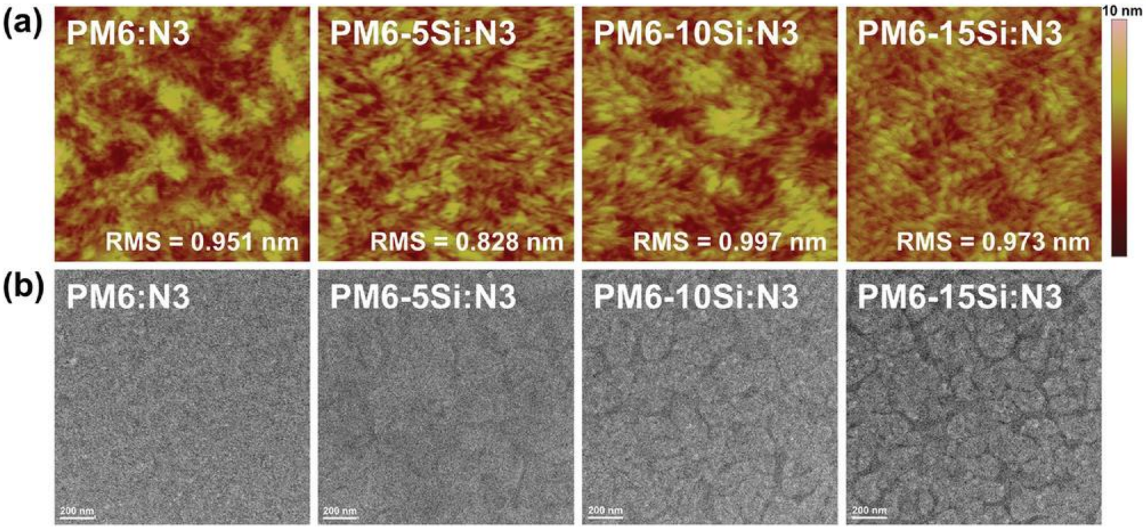

Figure 2.1.7. (a) AFM height images and (b) TEM images of the blend films.

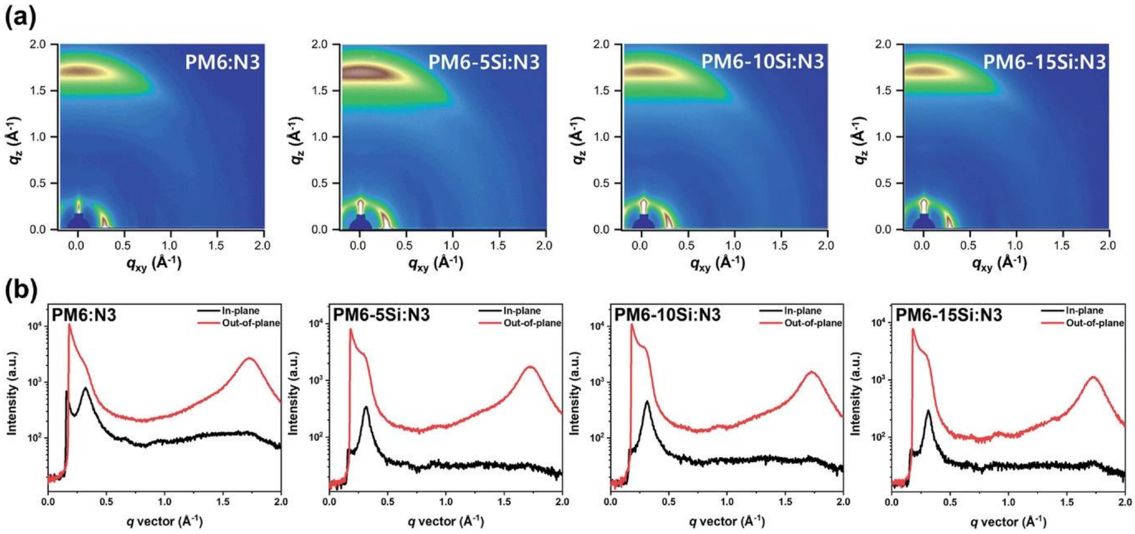

Figure 2.1.8. (a) 2D GIWAXS patterns and (b) corresponding line cut profiles of the blend films.

To further analyze the link between solid morphology and performance, we assessed the GIWAXS of pure and blended films. **Figures 2.1.8** and **2.1.32** depict the 2D GIWAXS images, and **Table 2.1.9** provides their crystallographic characteristics. As observed in the prior literatures, both pristine PM6 donor and N3 acceptor films displayed a strong (010) *π*–*π* stacking peak in the q_z direction and a broad (100) lamellar peak in both the q_z and q_{xy} directions, indicating a preferential face-on orientation. In addition to such diffraction patterns, (010) IP *π*–*π* stacking and multilamellar (*h*00) OP peaks were observed in the *i*BDD-Si-containing pristine copolymer films, indicating the formation of a long-range ordered 3D textured lamellar structure (coexistence of face-on and edge-on orientations) as the *i*BDDTh-Si unit was incorporated into the backbone. To quantify the crystalline orientation of the films, we plotted azimuthal pole figures for (100) lamellar peaks and (010) *π*–*π* stacking peaks (**Figure 2.1.33 and 2.1.34**) and summarized the calculated face-on/edge-on ratios in **Table 2.1.10**; Higher edge-on populations for both of lamellar and π–π stacking were observed in the neat copolymer films as the *i*BDD-Si contents increased, which further illustrated the aforementioned 3D texture of crystallites. In addition, PM6-5Si possessed greater lamellar and π–π stacking CCL than the other pristine donors. This shows that crystallinity can be improved by inserting a small, optimal amount of *i*BDDTh-Si into the backbone of PM6 despite its nonperiodic sequential structure.[49,50]

After blending with the N3 acceptor, all blend films were more likely to adopt a predominant face-on orientation, as shown by the significant OP π–π stacking peak.[51,52] In addition, in the pole figures of the blend films, the π–π stacking peaks not only confirmed the presence of exclusive face-on crystallites along the OP directions, but the lamellar peaks also revealed the presence of small populations of edge-on crystallites. These patterns are comparable to those reported in unmodified donor copolymer films. Considering the vertical charge transmission, it is important to note that the totally face-on features of the blend films are desired for photovoltaic applications.[53-55] Also, the CCL_{010} values for the blend films retained the trends reported in the pure copolymer donor films, indicating a more crystalline nature of the PM6-5Si:N3 blend, which can further improve the charge transfer and carrier dynamics in comparison to the other systems.[56,57]

2.1.5 Conclusion

In conclusion, a fused-ring tricyclic heterocycle with a TIPS side chain was designed as an isomer of the well-established BDD electron-accepting unit. Then, we produced a series of copolymers of variable composition (PM6, PM6-5Si, PM6-10Si, and PM6-15Si) and used them as donors in BHJ OSCs. Introducing varying quantities of the *i*BDD-Si unit into the copolymer backbone fine-tuned the optical property, energy levels, and molecular packing, hence improving the OSC performance. When blended with N3 as an acceptor, the PM6-5Si-based OSCs produced the best PCE of 17.01 % which is much higher than the PM6-based device used as the control (15.15 %). The exceptional performance of the PM6-5Si:N3 device has been attributed to its balanced charge transport, enhanced charge generation/dissociation kinetics, and reduced E_{loss} and recombination losses, as determined by a thorough characterization of its structural, electrical, and morphological properties. Our findings shed insight on the structure–property–performance correlations in *i*BDD-Si-containing copolymers and may result in enhanced design criteria for the modification of BDD derivatives for high-performance solar systems.

2.1.6 Supporting Information

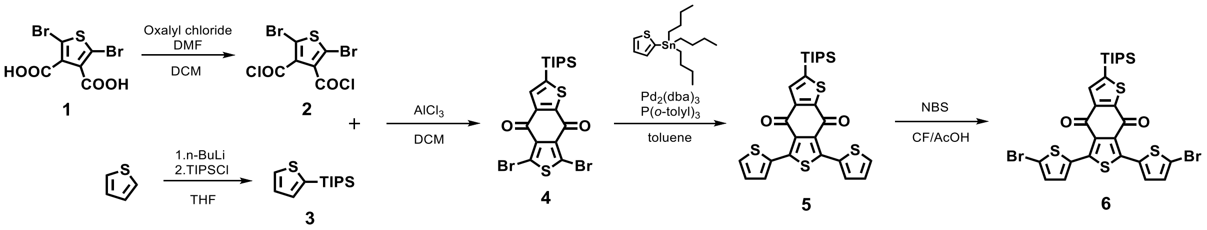

Scheme 2.1.1. Synthetic scheme of *i*BDDTh-Si-Br$_2$.

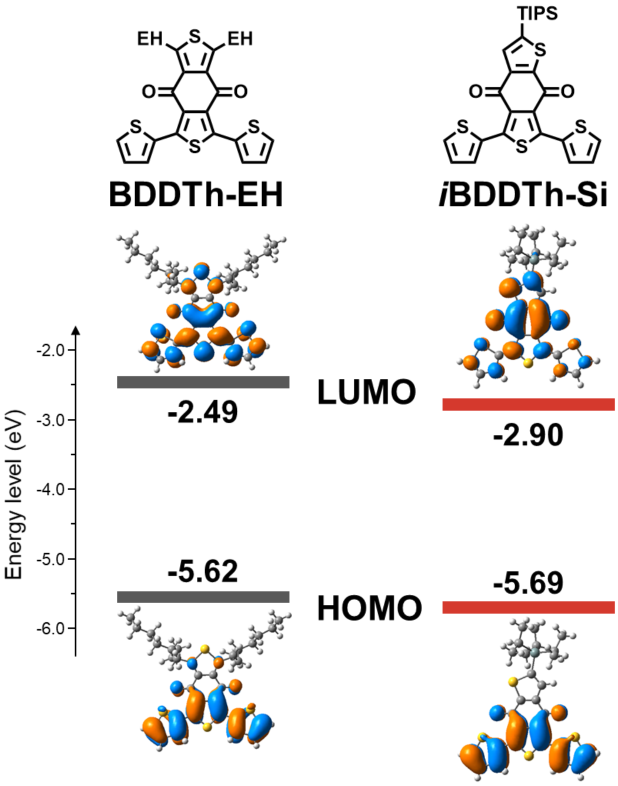

Figure 2.1.9. Derived HOMO and LUMO levels by DFT calculations of BDDTh-EH and *i*BDDTh-Si.

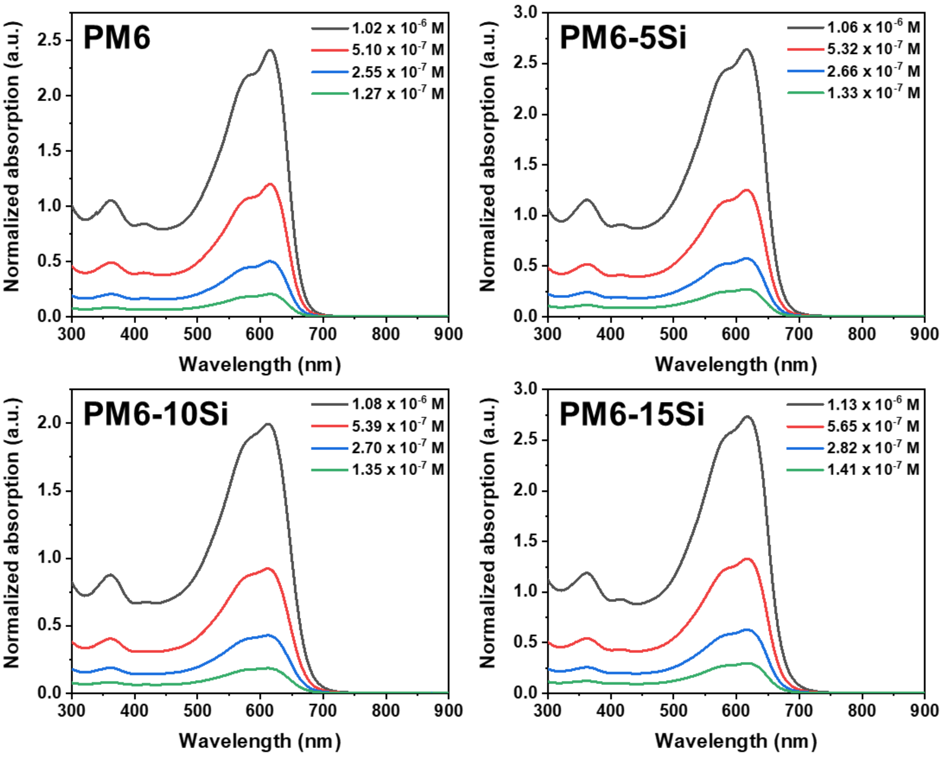

Figure 2.1.10. UV-Vis absorption spectra on different concentrations of the copolymers in CF solutions.

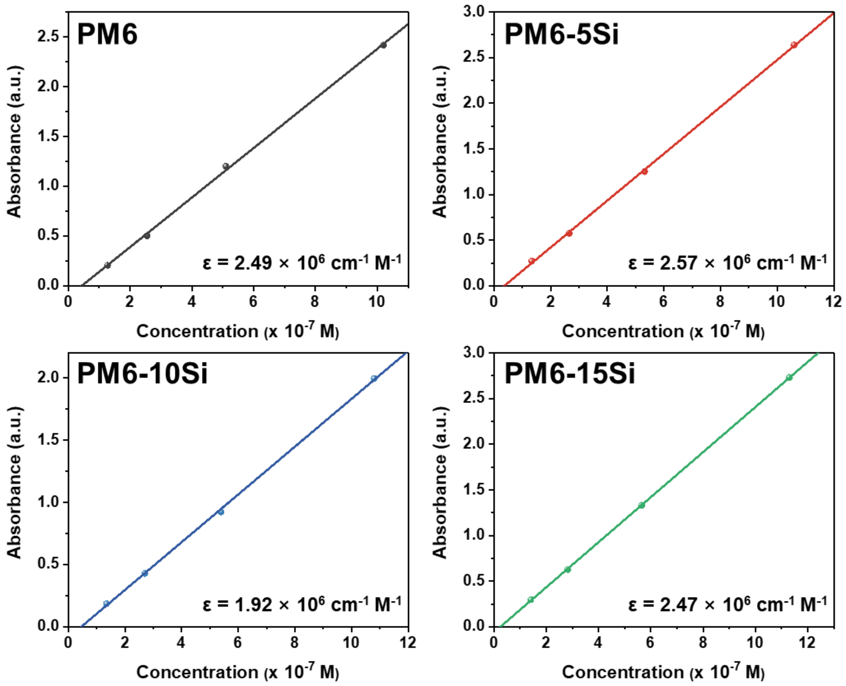

Figure 2.1.11. Calibration plots of the measured concentration dependent absorbance of the copolymers.

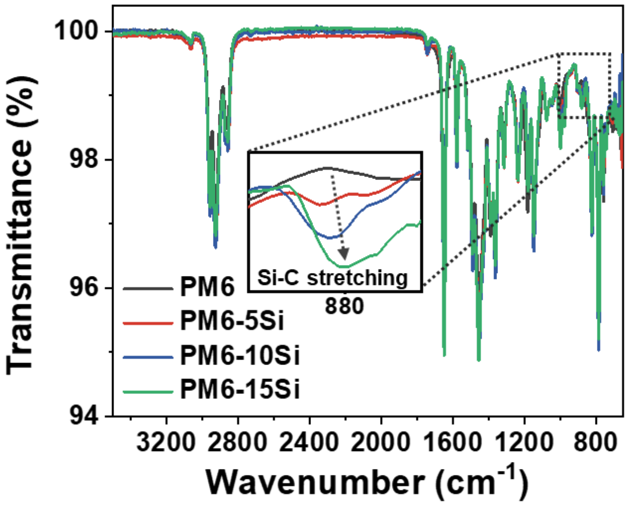

Figure 2.1.12. Fourier-transform infrared spectroscopy of the copolymers.

Table 2.1.3. Solubility of the copolymers in chloroform.

	PM6	PM6-5Si	PM6-10Si	PM6-15Si
Solubility in chloroform (mg mL^{-1})	23.71	18.99	16.96	10.79

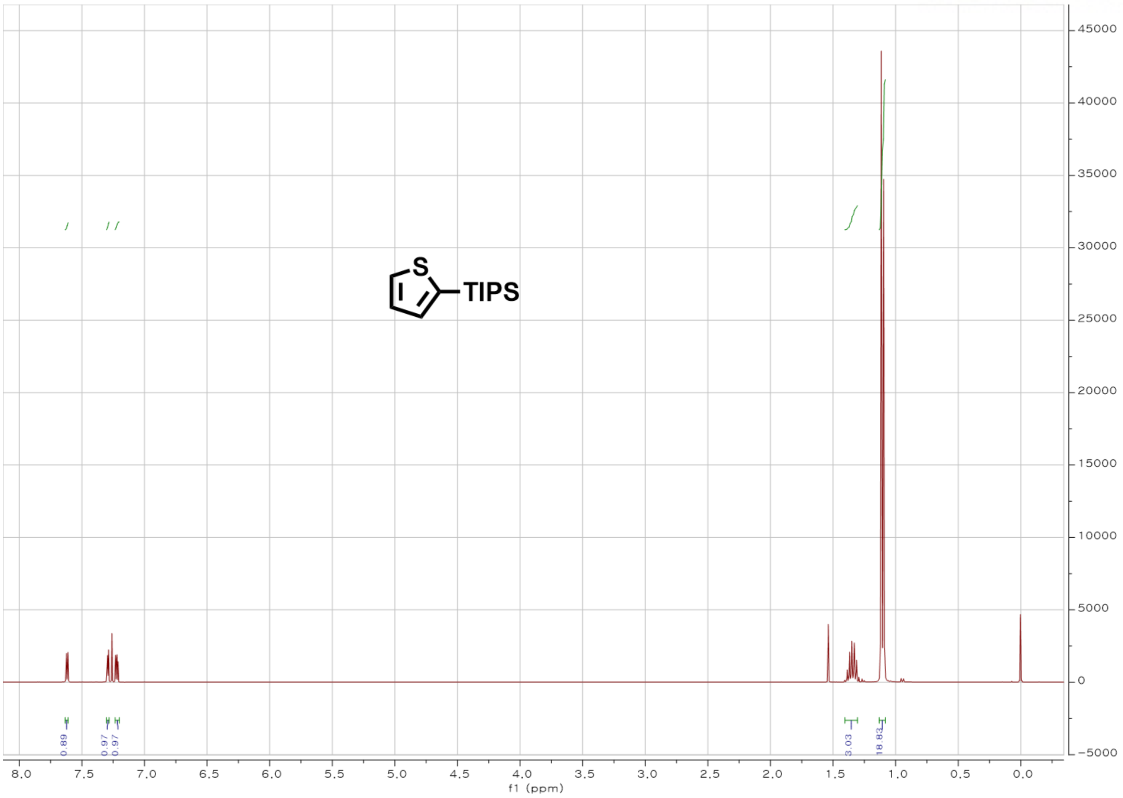

Figure 2.1.13. ^{1}H NMR spectrum of **3**.

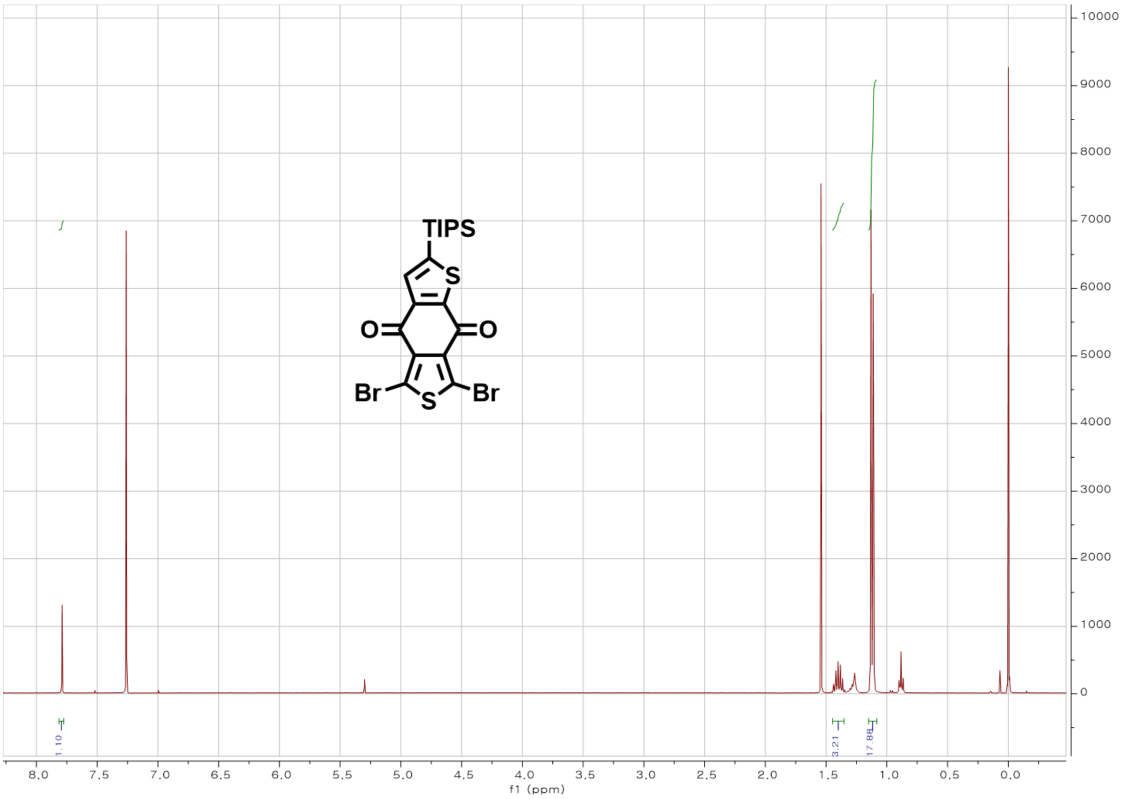

Figure 2.1.14. ^{1}H NMR spectrum of **4**.

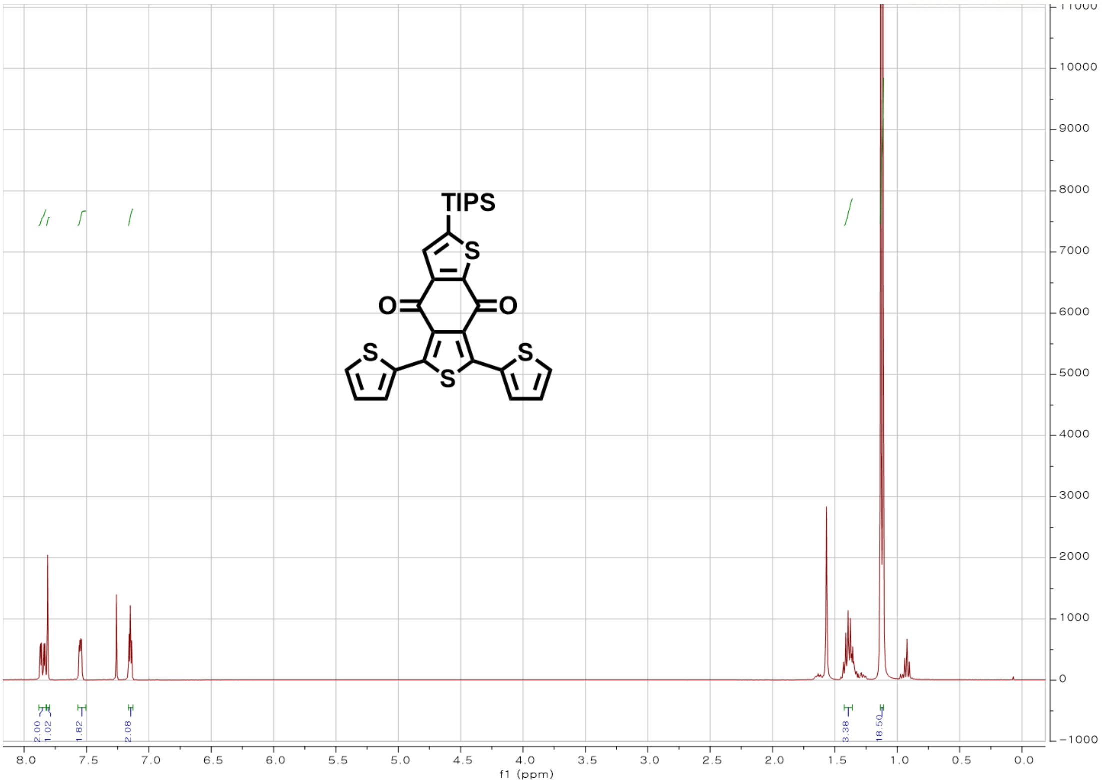

Figure 2.1.15. ^{1}H NMR spectrum of **5**.

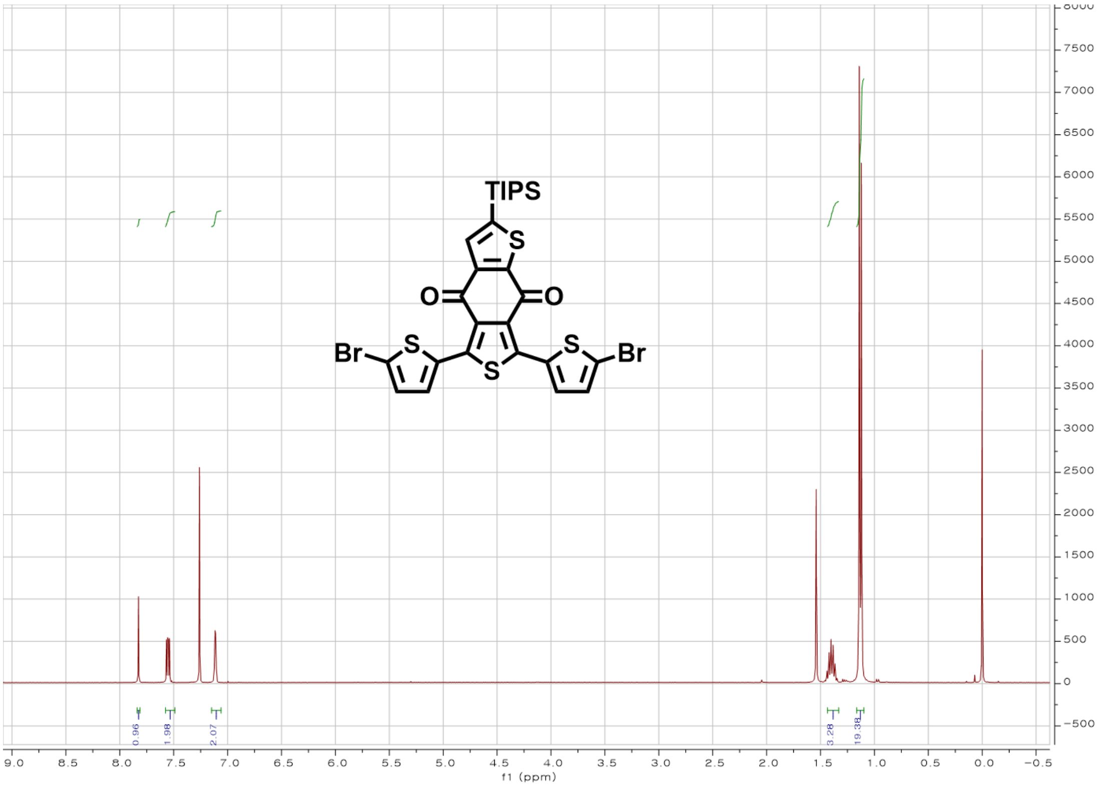

Figure 2.1.16. ^{1}H NMR spectrum of *i*BDDTh-Si-Br$_2$.

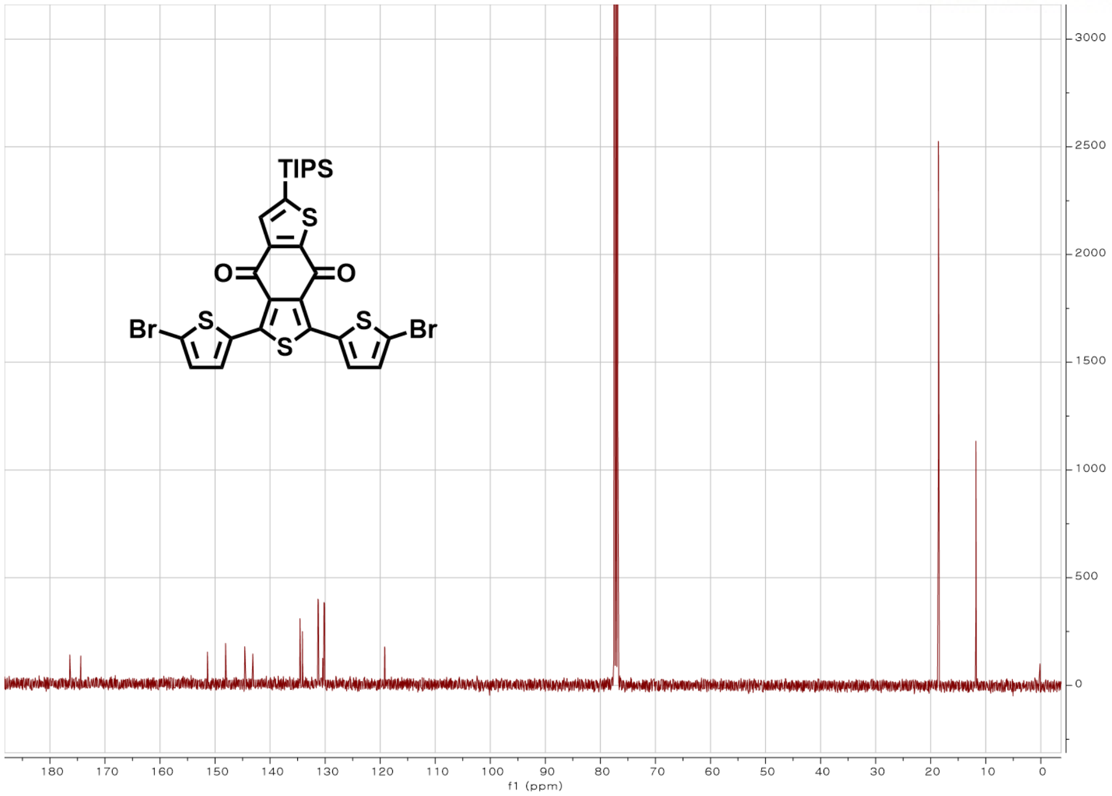

Figure 2.1.17. ^{13}C NMR spectrum of *i*BDDTh-Si-Br$_2$.

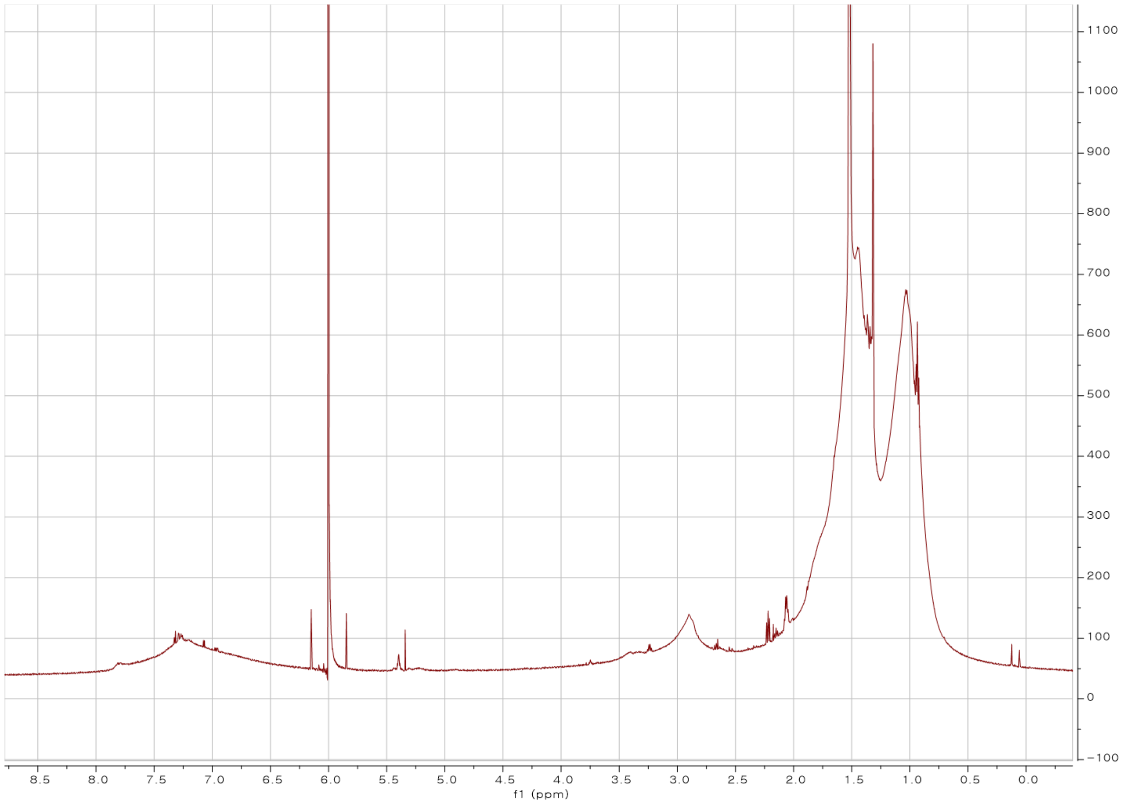

Figure 2.1.18. ^{1}H NMR spectrum of PM6.

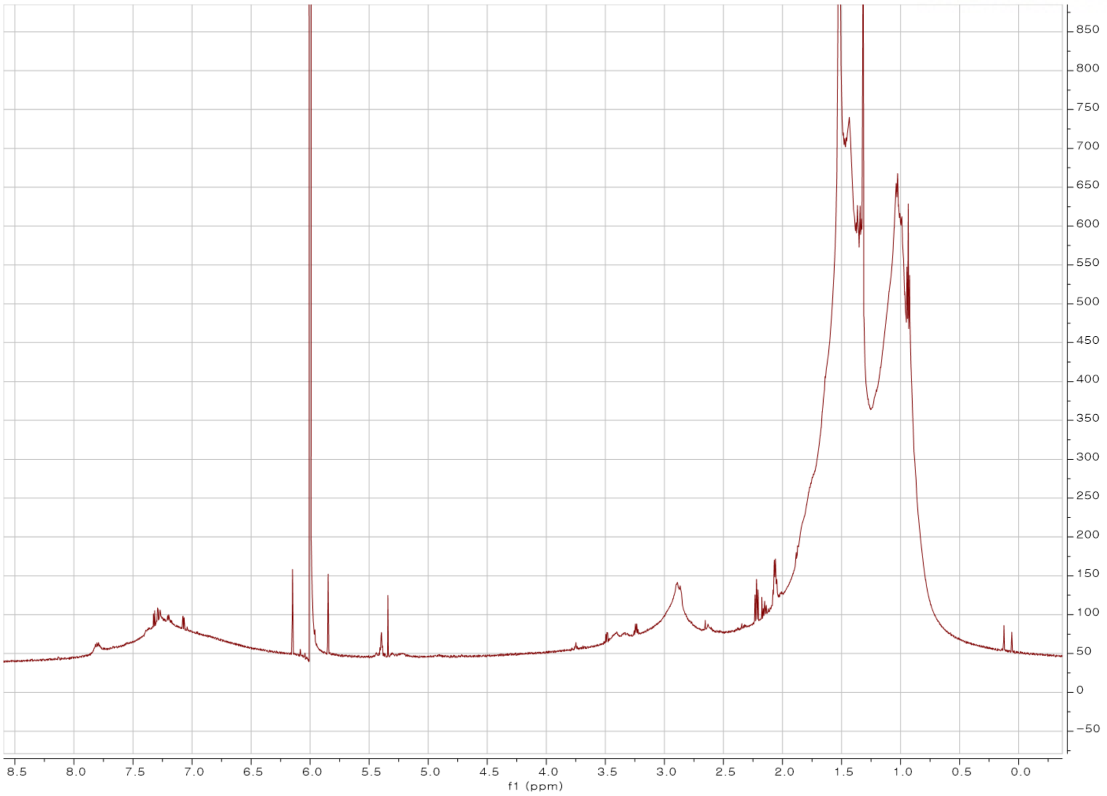

Figure 2.1.19. ^{1}H NMR spectrum of PM6-5Si.

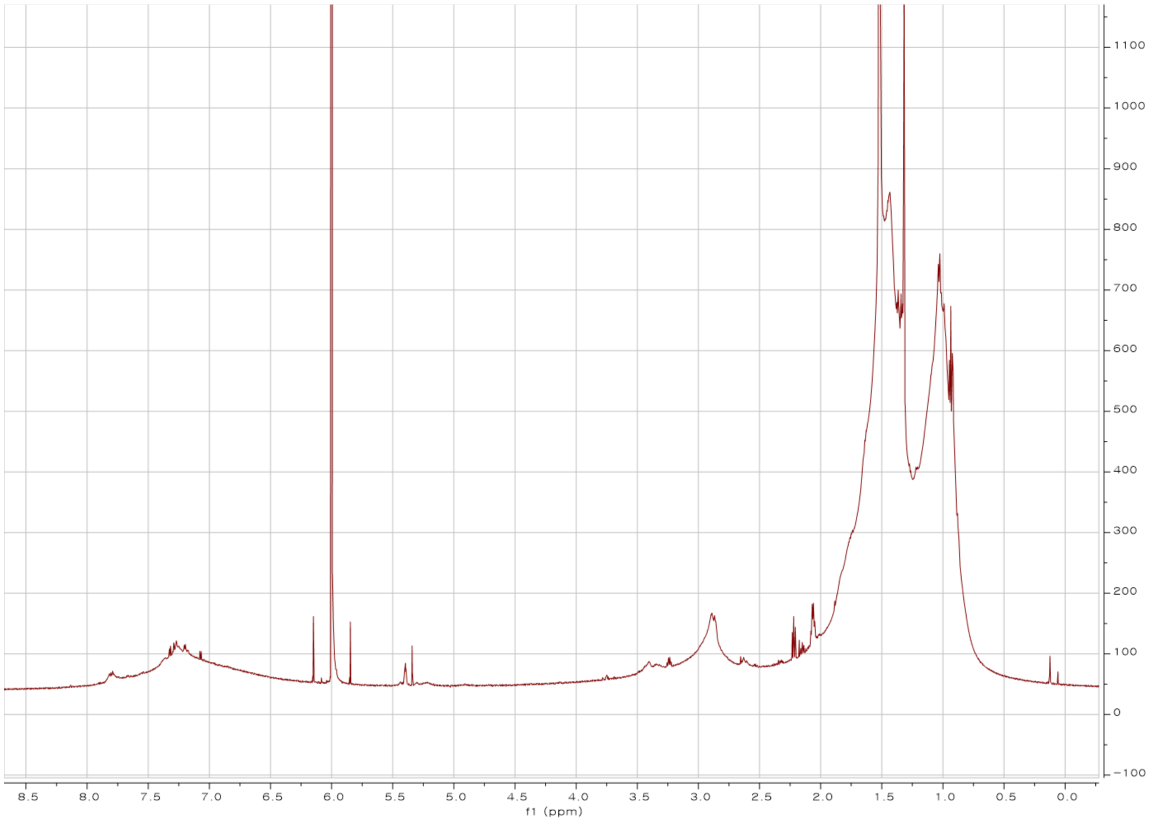

Figure 2.1.20. ^{1}H NMR spectrum of PM6-10Si.

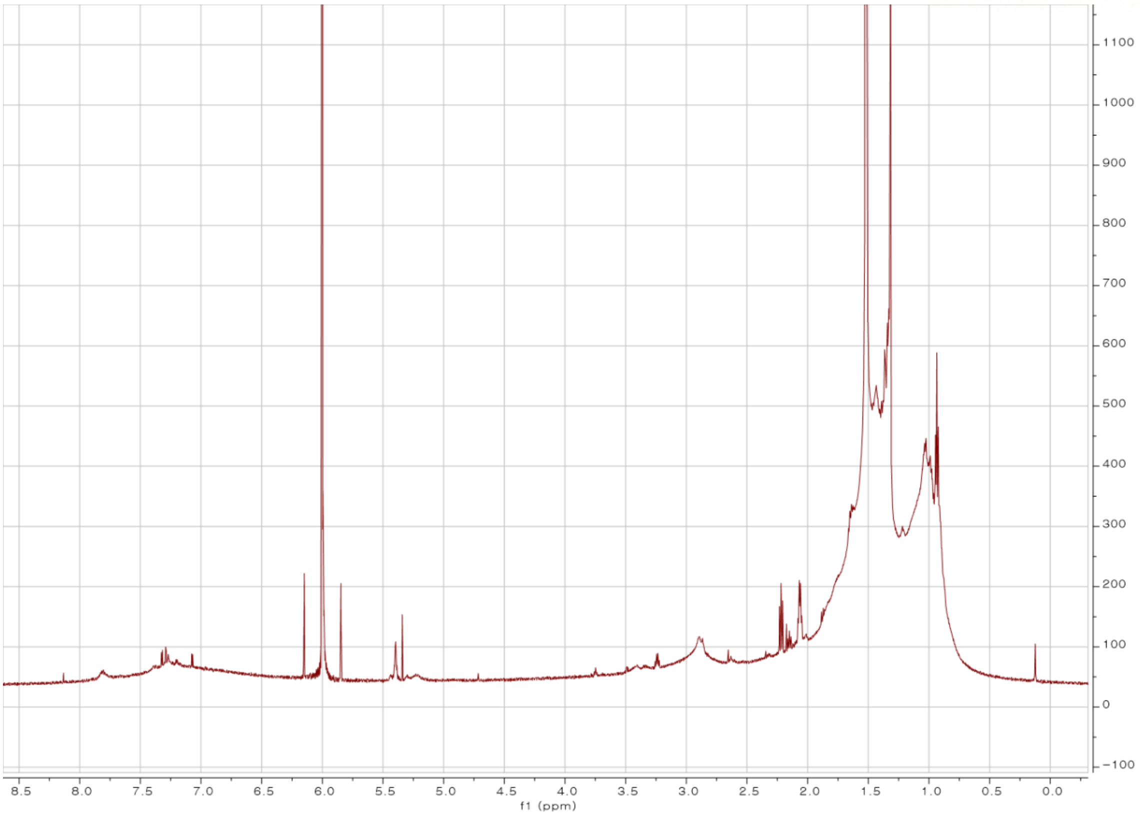

Figure 2.1.21. ^{1}H NMR spectrum of PM6-15Si.

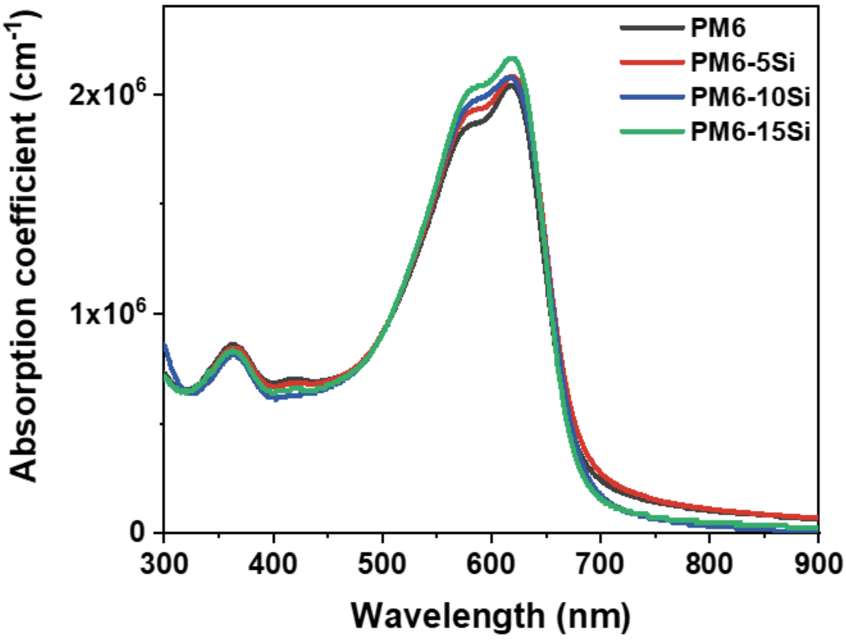

Figure 2.1.22. Absorption coefficient of the neat copolymer films.

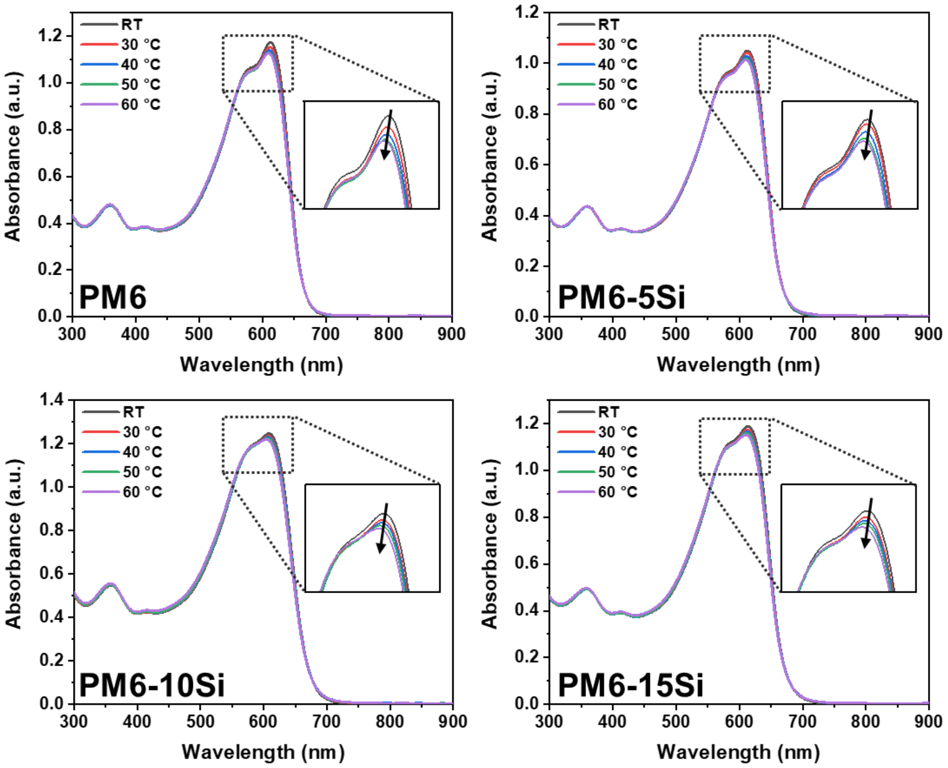

Figure 2.1.23. Temperature-dependent UV-Vis spectra of copolymers in dilute CF solution.

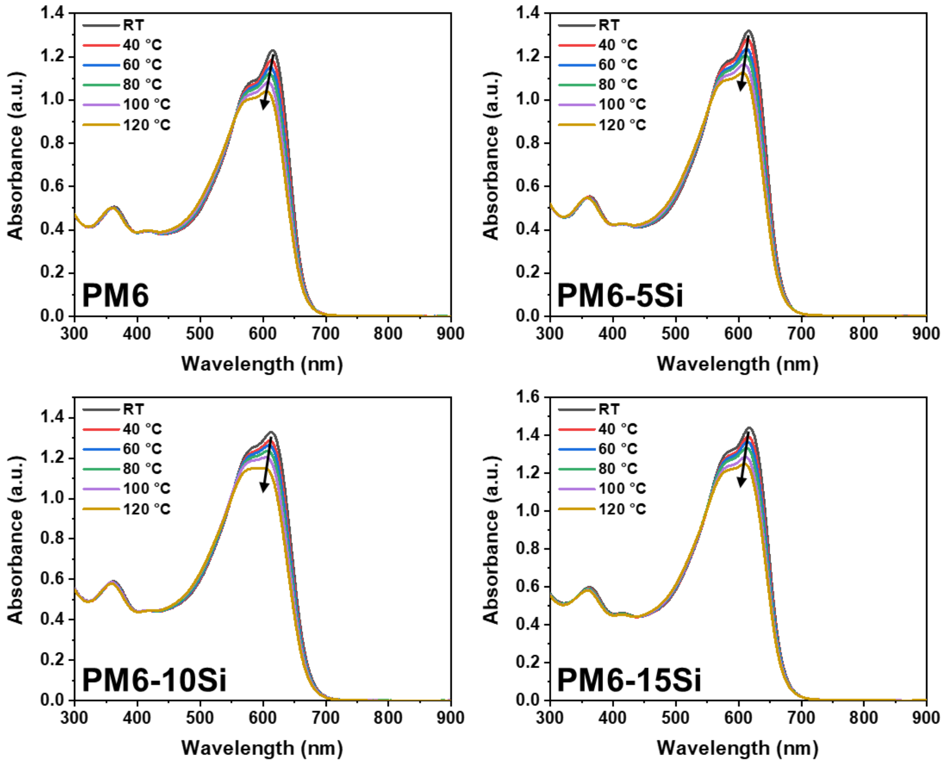

Figure 2.1.24. Temperature-dependent UV-Vis spectra of copolymers in dilute CB solution.

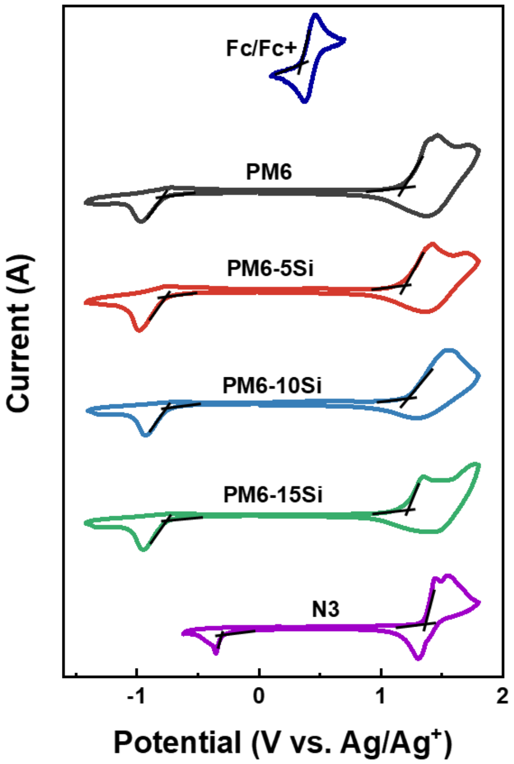

Figure 2.1.25. Cyclic voltammograms of the copolymers and N3 measured in 0.1 M tetra-*n*-butylammonium hexafluorophosphate (*n*-Bu_4NPF_6) solution in acetonitrile at a scan rate of 100 mV s^{-1}.

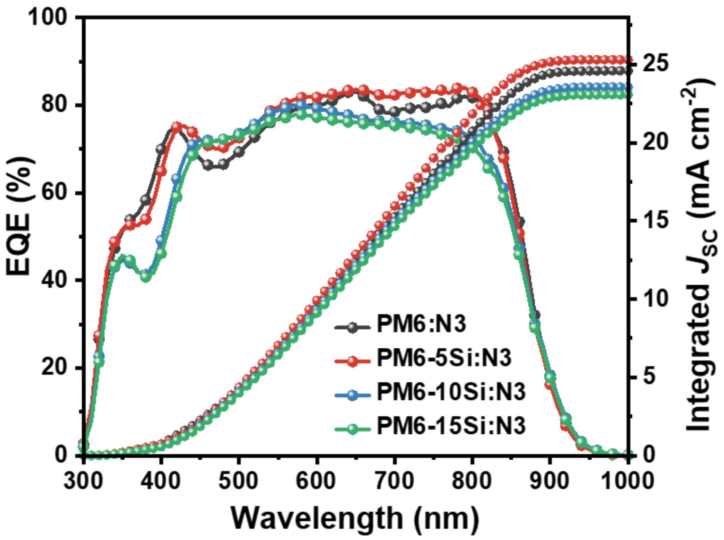

Figure 2.1.26. EQE spectra and integrated J_{SC} of the fabricated OSCs based on the copolymers:N3 blends.

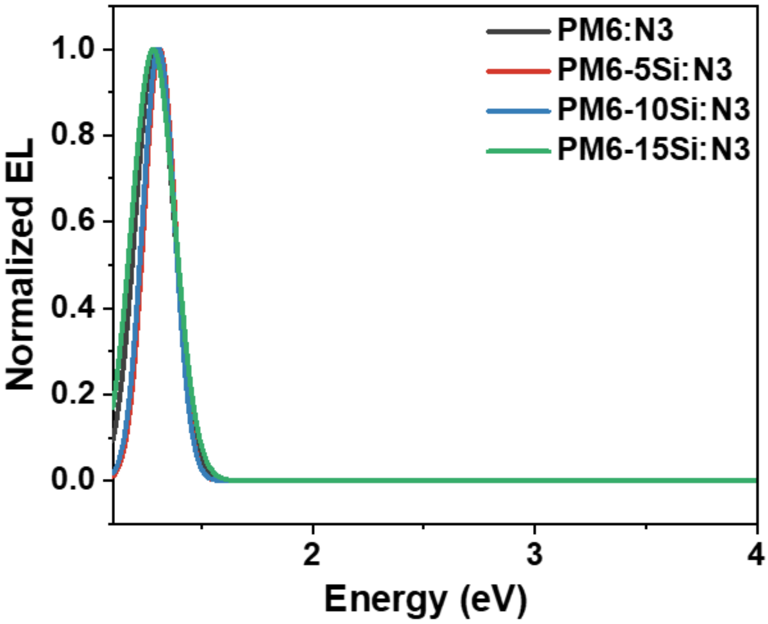

Figure 2.1.27. Electroluminescence spectra of the OSC devices.

Table 2.1.4. Calculated energy loss summary of the OSC devices.

Active Layer	E_g (eV)	qV_{OC} (eV)	E_{loss} (eV)	ΔE_1 (eV)	ΔE_2 (eV)	ΔE_3^{cal} (eV)	EQE_{EL}^{exp}	ΔE_3^{exp} (eV)
PM6:N3	1.411	0.838	0.573	0.267	0.060	0.246	6.859 x 10^{-5}	0.247
PM6-5Si:N3	1.418	0.853	0.565	0.263	0.060	0.242	8.564 x 10^{-5}	0.242
PM6-10Si:N3	1.420	0.833	0.574	0.267	0.078	0.242	8.159 x 10^{-5}	0.243
PM6-15Si:N3	1.421	0.830	0.591	0.266	0.082	0.243	7.722 x 10^{-5}	0.244

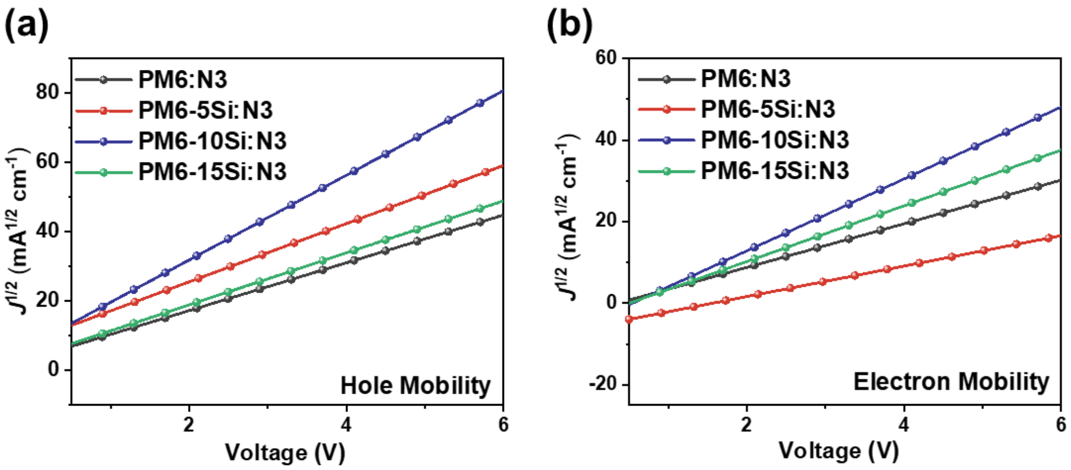

Figure 2.1.28. (a) Hole-only and (b) electron-only SCLC fitting of the blend films.

Table 2.1.5. Charge carrier mobilities of the devices.

Active layer	μ_h (cm^2 V^{-1} s^{-1})	μ_e (cm^2 V^{-1} s^{-1})	μ_e/μ_h
PM6:N3	1.01×10^{-4}	1.33×10^{-4}	1.32
PM6-5Si:N3	1.16×10^{-4}	1.13×10^{-4}	0.97
PM6-10Si:N3	7.40×10^{-5}	7.84×10^{-5}	1.05
PM6-15Si:N3	6.35×10^{-5}	4.33×10^{-5}	0.68

Table 2.1.6. Exciton dissociation and charge collection probabilities of the devices.

Active Layer	Exciton dissociation probability (%)	Charge collection probability (%)
PM6:N3	95.51	85.38
PM6-5Si:N3	96.59	87.18
PM6-10Si:N3	95.01	84.28
PM6-15Si:N3	94.54	85.05

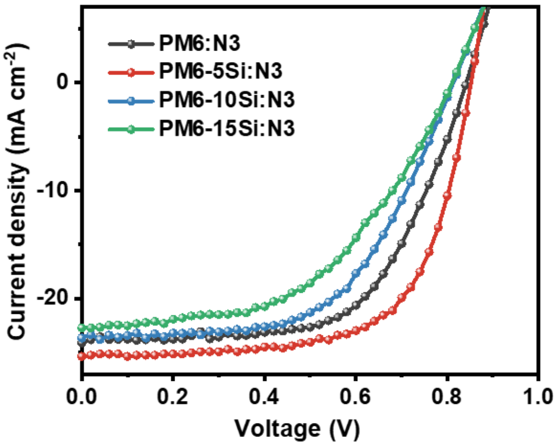

Figure 2.1.29. *J-V* curves of the fabricated OSCs based on the copolymers:N3 blends with device area of 0.92 cm^2.

Table 2.1.7. Photovoltaic parameters of the OSCs devices with area of 0.92 cm^2 under AM 1.5G (100 mW cm^{-2}).

Active Layer	Device Area (cm^2)	V_{OC} (V)	J_{SC} (mA cm^{-2})	FF (%)	PCE (%) [a]
PM6:N3	0.92	0.830 (0.827 ± 0.003)	23.62 (23.37 ± 0.35)	62.48 (62.13 ± 0.36)	12.24 (12.01 ± 0.22)
PM6-5Si:N3	0.92	0.849 (0.845 ± 0.004)	24.94 (24.55 ± 0.39)	66.81 (66.34 ± 0.45)	14.20 (13.87 ± 0.34)
PM6-10Si:N3	0.92	0.814 (0.810 ± 0.004)	23.51 (23.26 ± 0.47)	57.62 (57.11 ± 0.51)	11.12 (10.75 ± 0.37)
PM6-15Si:N3	0.92	0.802 (0.799 ± 0.005)	22.86 (22.32 ± 0.55)	52.64 (52.12 ± 0.54)	9.65 (9.30 ± 0.35)

[a] The average PCE values in parentheses were obtained from 10 devices.

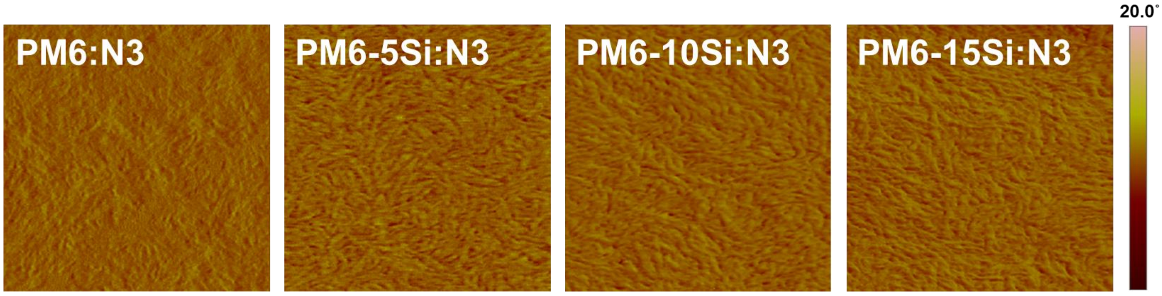

Figure 2.1.30. AFM phase images of the blend films.

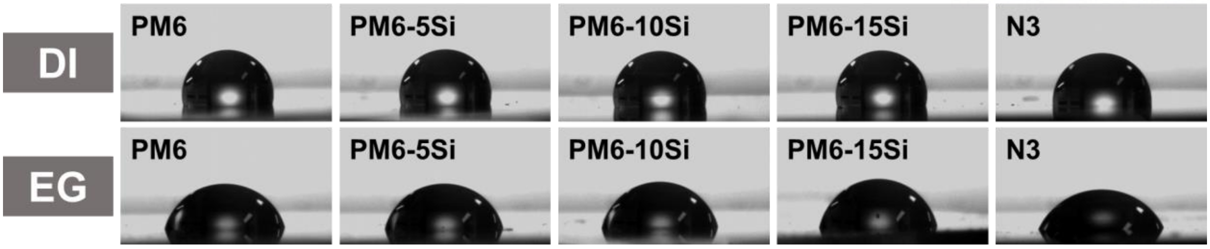

Figure 2.1.31. Contact angle measurement images of the neat films by using DI water and ethylene glycol.

Table 2.1.8. Contact angles and surface tensions of the neat films and derived Flory-Huggins parameters.

Film	Contact Angle		χ (mN m^{-1})	χ $^{a)}$
	θ_{DI} (°)	θ_{EG} (°)		
PM6	105.9	80.1	20.78	0.288*K*
PM6-5Si	106.2	80.6	20.55	0.316*K*
PM6-10Si	107.2	82.1	19.94	0.396*K*
PM6-15Si	108.9	83.5	19.78	0.419*K*
N3	100.8	70.2	25.96	-

[a)] χ values were derived from the donor copolymers:N3 blends.

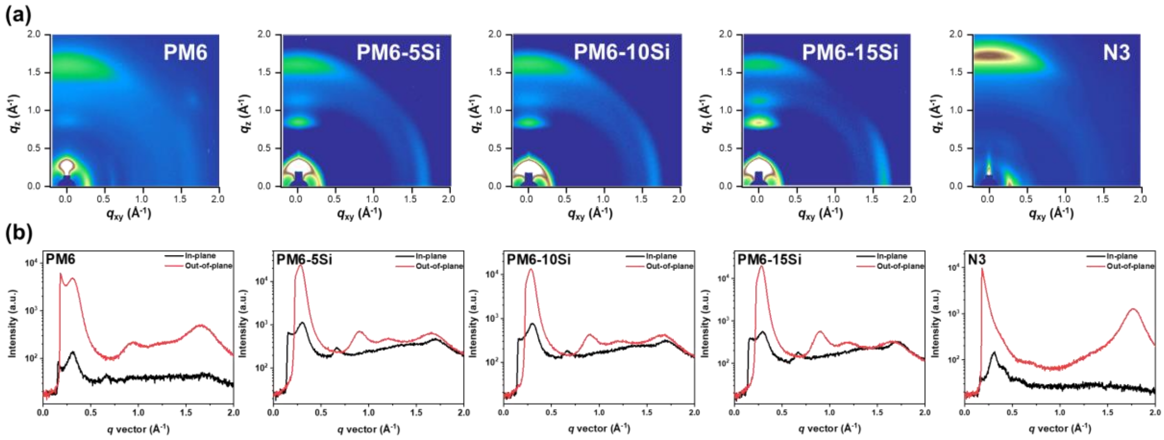

Figure 2.1.32. (a) 2D GIWAXS patterns and (b) linecut profiles of the neat copolymers and N3.

Table 2.1.9. Derived GIWAXS parameters of the blend films.

Samples	In-plane			Out-of-plane		
	lamellar stacking (100)			π-π stacking (010)		
	q (Å^{-1})	*d*-spacing (Å)	Coherence length (Å)	q (Å^{-1})	*d*-spacing (Å)	Coherence length (Å)
PM6	0.298	21.084	138.253	1.653	3.800	48.582
PM6-5Si	0.299	21.009	146.497	1.657	3.791	49.343
PM6-10Si	0.294	21.092	119.044	1.650	3.807	46.146
PM6-15Si	0.291	21.561	111.663	1.648	3.812	44.145
N3	0.304	20.641	198.199	1.769	3.552	83.894
PM6:N3	0.313	20.054	195.160	1.726	3.640	72.941
PM6-5Si:N3	0.316	19.914	203.636	1.727	3.639	75.979
PM6-10Si:N3	0.312	20.147	192.270	1.722	3.649	71.229
PM6-15Si:N3	0.312	20.166	188.979	1.719	3.655	70.416

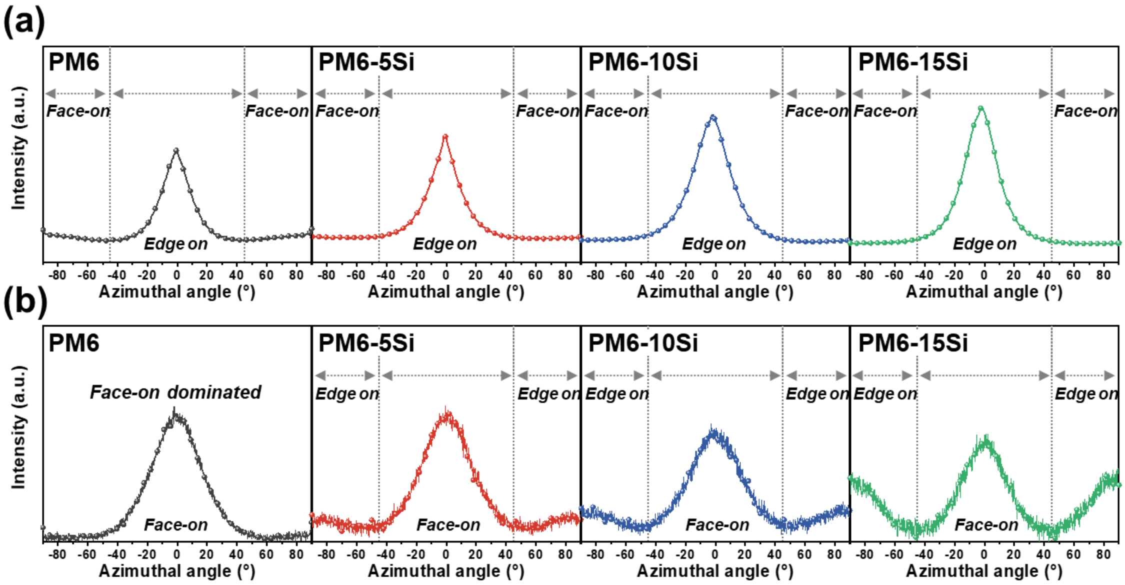

Figure 2.1.33. Azimuthal pole figures of the neat copolymers for (a) lamellar stacking and (b) π–π stacking crystallites.

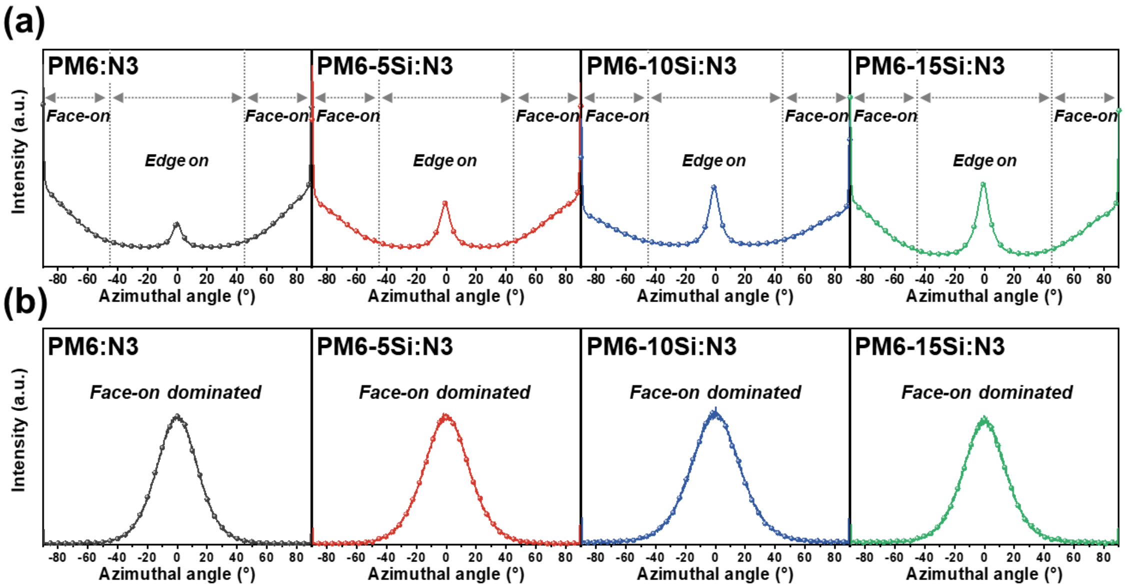

Figure 2.1.34. Azimuthal pole figures of the blend films for (a) lamellar stacking and (b) π–π stacking crystallites.

Table 2.1.10. Face-on/Edge-on ratio of neat copolymers and blend films for lamellar stacking and π–π stacking crystallites.

Samples	Face-on/Edge-on ratio	
	(100) Lamellar stacking	(010) π-π stacking
PM6	0.54	Face-on only
PM6-5Si	0.49	9.09
PM6-10Si	0.34	3.85
PM6-15Si	0.31	1.37
PM6:N3	4.35	Face-on only
PM6-5Si:N3	3.70	Face-on only
PM6-10Si:N3	3.03	Face-on only
PM6-15Si:N3	2.78	Face-on only

2.1.7 Reference

1. Y. Cho, T. Kumari, S. Jeong, S. M. Lee, M. Jeong, B. Lee, J. Oh, Y. Zhang, B. Huang, L. Chen, C. Yang, *Nano Energy*, 2020, **75**, 104896
2. Q. Fan, W. Su, S. Chen, T. Liu, W. Zhuang, R. Ma, X. Wen, Z. Yin, Z. Luo, X. Guo, L. Hou, K. Moth-Poulsen, Y. Li, Z. Zhang, C. Yang, D. Yu, H. Yan, M. Zhang, E. Wang, *Angewandte Chemie International Edition*, 2020, **59**, 19835
3. D. He, F. Zhao, J. Xin, J. J. Rech, Z. Wei, W. Ma, W. You, B. Li, L. Jiang, Y. Li, C. Wang, *Advanced Energy Materials*, 2018, **8**, 1802050
4. D. Koo, S. Jung, J. Seo, G. Jeong, Y. Choi, J. Lee, S. M. Lee, Y. Cho, M. Jeong, J. Lee, J. Oh, C. Yang, H. Park, *Joule*, 2020, **4**, 1021
5. B. Lee, S. Jeong, Y. Cho, M. Jeong, S. M. Lee, J. Oh, C. Yang, *Advanced functional Materials,* 2020, **30**, 2005037
6. S. H. Park, A. Roy, S. Beaupré, S. Cho, N. Coates, J. S. Moon, D. Moses, M. Leclerc, K. Lee, A. J. Heeger, *Nature Photonics*, 2009, **3**, 297
7. G. Yu, J. Gao, J. C. Hummelen, F. Wudl, A. J. Heeger, *Science*, 1995, **270**, 1789.
8. Y. Cui, H. Yao, J. Zhang, T. Zhang, Y. Wang, L. Hong, K. Xian, B. Xu, S. Zhang, J. Peng, Z. Wei, F. Gao, J. Hou, *Nature Communications*, 2019, **10**, 2515
9. K. Jiang, Q. Wei, J. Y. L. Lai, Z. Peng, H. K. Kim, J. Yuan, L. Ye, H. Ade, Y. Zou, H. Yan, *Joule*, 2019, **3**, 3020
10. Z. Peng, K. Jiang, Y. Qin, M. Li, N. Balar, B. T. O'Connor, H. Ade, L. Ye, Y. Geng, *Advanced Energy Materials*, 2021, **11**, 2003506
11. J. Yuan, Y. Zhang, L. Zhou, G. Zhang, H.-L. Yip, T.-K. Lau, X. Lu, C. Zhu, H. Peng, P. A. Johnson, M. Leclerc, Y. Cao, J. Ulanski, Y. Li, Y. Zou, *Joule*, 2019, **3**, 1140
12. W. Zhao, D. Qian, S. Zhang, S. Li, O. Inganäs, F. Gao, J. Hou, *Advanced Materials*, 2016, **28**, 4734
13. Z. Zhou, W. Liu, G. Zhou, M. Zhang, D. Qian, J. Zhang, S. Chen, S. Xu, C. Yang, F. Gao, H. Zhu, F. Liu, X. Zhu, *Advanced Materials,* 2020, **32**, 1906324.
14. H. Bin, L. Gao, Z.-G. Zhang, Y. Yang, Y. Zhang, C. Zhang, S. Chen, L. Xue, C. Yang, M. Xiao, Y. Li, *Nature Communications*, 2016, **7**, 13651
15. Y. Cho, T. H. Lee, S. Jeong, S. Y. Park, B. Lee, J. Y. Kim, C. Yang, ACS *Applied Energy Materials*, 2020, **3**, 7689
16. D. Qian, Z. Zheng, H. Yao, W. Tress, T. R. Hopper, S. Chen, S. Li, J. Liu, S. Chen, J. Zhang, X.-K. Liu, B. Gao, L. Ouyang, Y. Jin, G. Pozina, I. A. Buyanova, W. M. Chen, O. Inganäs, V. Coropceanu, J.-L. Bredas, H. Yan, J. Hou, F. Zhang, A. A. Bakulin, F. Gao, *Nature Materials*, 2018, **17**, 703

17. K. D. Rosenthal, M. P. Hughes, B. R. Luginbuhl, N. A. Ran, A. Karki, S.-J. Ko, H. Hu, M. Wang, H. Ade, T.-Q. Nguyen, *Advanced Energy Materials*, 2019, **9**, 1901077.

18. H. Sun, T. Liu, J. Yu, T.-K. Lau, G. Zhang, Y. Zhang, M. Su, Y. Tang, R. Ma, B. Liu, J. Liang, K. Feng, X. Lu, X. Guo, F. Gao, H. Yan, *Energy & Environmental Science*, 2019, **12**, 3328

19. J. Wu, G. Li, J. Fang, X. Guo, L. Zhu, B. Guo, Y. Wang, G. Zhang, L. Arunagiri, F. Liu, H. Yan, M. Zhang, Y. Li, *Nature Communications*, 2020, **11**, 4612

20. S. Zhang, Y. Qin, J. Zhu, J. Hou, *Advanced Materials*, 2018, **30**, 1800868

20. B. Zheng, L. Huo, Y. Li, *NPG Asia Materials*, 2020, **12**, 3

24. Z. Zheng, H. Yao, L. Ye, Y. Xu, S. Zhang, J. Hou, *Materials Today*, 2020, **35**, 115.

25. M. Zhang, X. Guo, W. Ma, H. Ade, J. Hou, *Advanced Materials*, 2015, **27**, 4655.

26. P. Chao, H. Chen, Y. Zhu, H. Lai, D. Mo, N. Zheng, X. Chang, H. Meng, F. He, *Advanced Materials*, 2020, **32**, 1907059.

27. C. Cui, W.-Y. Wong, Y. Li, *Energy & Environmental Science*, 2014, **7**, 2276

28. B. Fan, L. Ying, P. Zhu, F. Pan, F. Liu, J. Chen, F. Huang, Y. Cao, *Advanced Materials*, 2017, **29**, 1703906;

29. T. Kurosawa, X. Gu, K. L. Gu, Y. Zhou, H. Yan, C. Wang, G.-J. N. W, *Advanced Energy Materials*, 2018, **8**, 1701552

30. C. R. McNeill, *Energy & Environmental Science*, 2012, **5**, 5653.

31. T. Liu, X. Pan, X. Meng, Y. Liu, D. Wei, W. Ma, L. Huo, X. Sun, T. H. Lee, M. Huang, H. Choi, J. Y. Kim, W. C. H. Choy, Y. Sun, *Advanced Materials*, 2017, **29**, 1604251

32. X. Pan, W. Xiong, T. Liu, X. Sun, L. Huo, D. Wei, M. Yu, M. Han, Y. Sun, *Journal of Materials Chemistry C*, 2017, **5**, 4471

33. L. Ye, W. Li, X. Guo, M. Zhang, H. Ade, *Chemistry of Materials*, 2019, **31**, 6568.

34. Z. Genene, A. Negash, B. A. Abdulahi, R. T. Eachambadi, Z. Liu, N. Van den Brande, J. D'Haen, E. Wang, K. Vandewal, W. Maes, J. Manca, W. Mammo, S. Admassie, *Organic Electronics,* 2020, **77**, 105572

35. G. Xu, L. Chen, H. Lei, Z. Liao, N. Yi, J. Liu, Y. Chen, *Journal of Materials Chemistry A*, 2019, **7**, 4145.

36. D. Qian, L. Ye, M. Zhang, Y. Liang, L. Li, Y. Huang, X. Guo, S. Zhang, Z. A. Tan, J. Hou, *Macromolecules*, 2012, **45**, 9611

37. W. Xu, C. Ma, J. Ma, T. Gan, G. Zhang, *ACS Applied Materials & Interfaces*, 2014, **6**, 4017

38. L. Arunagiri, Z. Peng, X. Zou, H. Yu, G. Zhang, Z. Wang, J. Y. Lin Lai, J. Zhang, Y. Zheng, C. Cui, F. Huang, Y. Zou, K. S. Wong, P. C. Y. Chow, H. Ade, H. Yan, *Joule*, 2020, **4**, 1790.

39. G. Han, Y. Yi, *Advanced Theory and Simulations*, 2019, **2**, 1900067

40. S. M. Menke, N. A. Ran, G. C. Bazan, R. H. Friend, *Joule,* 2018, **2**, 25

41. N. A. Ran, S. Roland, J. A. Love, V. Savikhin, C. J. Takacs, Y.-T. Fu, H. Li, V. Coropceanu, X.

Liu, J.-L. Brédas, G. C. Bazan, M. F. Toney, D. Neher, T.-Q. Nguyen, *Nature Communications*, 2017, **8**, 79.

42. A. Rao, P. C. Y. Chow, S. Gélinas, C. W. Schlenker, C.-Z. Li, H.-L. Yip, A. K. Y. Jen, D. S. Ginger, R. H. Friend, *Nature*, 2013, **500**, 435.
43. Z. Zhou, S. Xu, J. Song, Y. Jin, Q. Yue, Y. Qian, F. Liu, F. Zhang, X. Zhu, *Nature Energy*, 2018, **3**, 952.
44. J. Yao, T. Kirchartz, M. S. Vezie, M. A. Faist, W. Gong, Z. He, H. Wu, J. Troughton, T. Watson, D. Bryant, J. Nelson, *Physical Review Applied*, 2015, **4**, 014020.
45. A. K. K. Kyaw, D. H. Wang, V. Gupta, W. L. Leong, L. Ke, G. C. Bazan, A. J. Heeger, *ACS Nano*, 2013, **7**, 4569.
46. Y. Cui, H. Yao, L. Hong, T. Zhang, Y. Tang, B. Lin, K. Xian, B. Gao, C. An, P. Bi, W. Ma, J. Hou, *National Science Review*, 2020, **7**, 1239.
47. Q. Wang, Z. Hu, Z. Wu, Y. Lin, L. Zhang, L. Liu, Y. Ma, Y. Cao, J. Chen, *ACS Applied Materials & Interfaces*, 2020, **12**, 4659.
48. Q. Wang, M. Li, Z. Peng, N. Kirby, Y. Deng, L. Ye, Y. Geng, *Science China Chemistry*, 2021, **64**, 478.
49. H. Lei, B. Huang, L. Chen, S. Chen, G. Xu, S. Huang, Y. Tan, C. Yang, Y. Chen, *Solar RRL*, 2019, **3**, 1900122.
50. T. Zhang, C. An, Q. Lv, J. Qin, Y. Cui, Z. Zheng, B. Xu, S. Zhang, J. Zhang, C. He, J. Hou, *Journal of Energy Chemistry*, 2021, **59**, 30.
51. M. Li, Y. Zhou, L. Yang, S. Shen, Y. Liu, Y. Chen, J. Song, Z. Bo, *Journal of Materials Chemistry A*, 2020, **8**, 22416.
52. H. Fan, T. Vergote, S. Xu, S. Chen, C. Yang, X. Zhu, *Materials Chemistry Frontiers*, 2018, **2**, 760.
53. W. Ma, J. R. Tumbleston, M. Wang, E. Gann, F. Huang, H. Ade, *Advanced Energy Materials*, 2013, **3**, 864.
54. B. P. Rand, D. Cheyns, K. Vasseur, N. C. Giebink, S. Mothy, Y. Yi, V. Coropceanu, D. Beljonne, J. Cornil, J.-L. Brédas, J. Genoe, *Advanced Functional Materials*, 2012, **22**, 2987.
55. A. Ojala, A. Petersen, A. Fuchs, R. Lovrincic, C. Pölking, J. Trollmann, J. Hwang, C. Lennartz, H. Reichelt, H. W. Höffken, A. Pucci, P. Erk, T. Kirchartz, F. Würthner, *Advanced Functional Materials*, 2012, **22**, 86.
56. Z. Li, L. Ying, P. Zhu, W. Zhong, N. Li, F. Liu, F. Huang, Y. Cao, *Energy & Environmental Science*, 2019, **12**, 157
57. Y. Qin, H. Chen, J. Yao, Y. Zhou, Y. Cho, Y. Zhu, B. Qiu, C.-W. Ju, Z.-G. Zhang, F. He, C. Yang, Y. Li, D. Zhao, *Nature Communications*, 2020, **11**, 58

CHAPTER 3 Solid Additives

Nonvolatile Polymer Additives with a High Dielectric Constant for Efficient and Stable OSCs

3.1.1 Motivation and Research Background

The field of BHJ OSCs has been a thriving research ground due to the possibility of combining affordable technology, mechanical flexibility, and the prospect of integration by using conformable materials. This is a result of the increasing need for renewable and sustainable energy sources. The nanoscale phase-separated morphology of the electron-accepting and electron-donating phases is crucial for the efficient functioning of BHJ OSCs. To create such a morphology, a variety of techniques, including solvent and thermal annealing and the use of solvent processing additives, have been investigated.[1-8] Among them, the usage of solvent additives is the most intriguing due to its simplicity of application and efficiency in boosting PCEs. On many different OSC platforms, considerable PCE improvements have been seen despite the fact that various solvent processing additives (such as DIO, DClO, and CN) function via different mechanisms.[9-19] Typically, after finalizing the manufacture of devices, a small volume portion of the solvent additives remains in the active layer due to their high boiling temperatures.[20-23] In actuality, the solvent additive-derived peak performance BHJ shape simply denotes a metastable condition.[24, 25] As a consequence, residual solvent additives may result in additional morphological development of the optimized BHJ film, hence often lowering OSC performance with poor repeatability. Even if it is extremely sensitive to the drying kinetics, eliminating the remaining solvent additives is necessary as an extra step to remove this negative impact (e.g., high vacuum and/or thermal annealing).[26]

Therefore, nonvolatile solid additives that preserve the blend film have been anticipated to properly regulate the morphology using a one-step production technique.[27] According to Reynolds et al., the first nonvolatile polymer additive improved PCE by around 70% when compared to the non-addition control device when PDMS was used as a polymer additive. [28] Additionally, Bazan et al. showed that a modest quantity of PS added to an active layer enhances the macroscopic film homogeneity and decreases needless dewetting from the substrate.[29, 30] Consequently, our group thoroughly compared the effects of three polymer additives (PMMA, PDMS, and PS) vs the commonly used solvent DIO on the photovoltaic property of a BHJ system.[31] The development of innovative polymer additives that are more successful at boosting performance and can be effectively applied to a variety of active layers and incorporated in ink formulations that can be processed using roll-to-roll compatible equipment should also be a priority. PS-*b*-PPFS diblock copolymer and PPFS, which are fluorinated analogues of PS with variable fluorine concentration in the backbone, were synthesized in this study. To shed light on the optimal choice of polymer additives for molecular BHJ OSCs, we further compared the effects of PPFS in other OSC systems. It's worth noting that NF-OSCs have gained more attention from researchers because of their potential advantages over traditional fullerene-based OSCs.[11, 32-39]

3.1.2 Materials and Characterization

In the first step, PS was synthesized in p-xylene solution at 110 ºC using 1-bromoethyl benzene as a macroinitiator in the isothermal ATRP. The PS NMR clearly demonstrates signals at 4.34-4.60 ppm attributed to protons positioned on the carbon near to bromine at the developing polymer chain end, as well as protons from large aromatic and aliphatic areas of PS repeating units (**Figures 3.1.8−3.1.10**). PS-*b*-PPFS was synthesized utilizing ATRP and PS as the macroinitiator to form a diblock copolymer. Furthermore, the PPFS homopolymer was synthesized using a conventional radical polymerization method. In the experimental part, each polymer's detailed synthesis and characterization, as well as its average molecular weight and polydispersity as measured by the GPC, are described. The resultant polymer additives were spin-cast onto a glass/Al substrate in order to calculate the ε_r using C–V measurements. At room temperature, the measurements were taken in the frequency range of 100-105 Hz. By using the capacitance equation, it was possible to determine the relative dielectric constants of PPFS, PS-*b*-PPFS, and PS as a function of frequency (**Figure 3.1.1**). The calculated dielectric constants increased monotonically as the degree of fluorine in the polymer repeat unit increased, ranging from PS (ε_r = 2.121) to PS-*b*-PPFS (ε_r = 4.032) to PPFS (ε_r = 5.174) in that order.

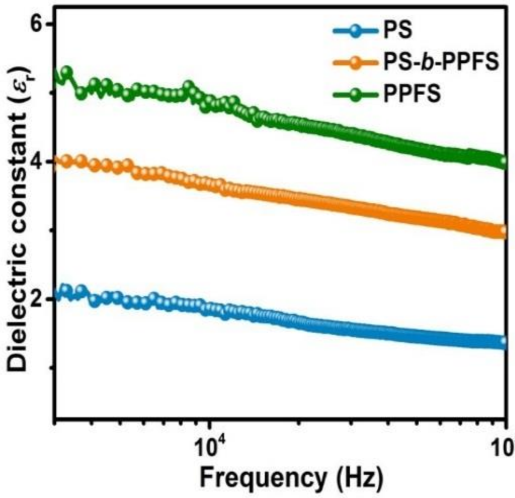

Figure 3.1.1. Dielectric constants of capacitance-based frequency dependence using PPFS, PS-*b*-PPFS, and PS.

3.1.3 Photovoltaic Properties

Nest, we investigated how three polymer additions impact the photovoltaic performance of OSCs utilizing the produced polymer additives. To minimize the work function of Al in a standard ITO/PEDOT:PSS device, PDINO was employed as the cathode interlayer: ITO/PEDOT:PSS/PBDB-TT5:ITIC/PDINO/Al (**Figure 3.1.2b**). Both the active layer and polymer additive molecular structures and energy diagrams used in OSCs are shown in **Figures 3.1.2a** and **3.1.2c**, respectively. In accordance with our research, the weight ratio of PBDB-TT5:ITIC was 1:1 and the total blend's chlorobenzene concentration was 20 mg mL^{-1}.[40] In **Figure 3.1.3a**, the devices' representative *J-V* characteristics under the illumination of simulated AM 1.5G are depicted, and **Table 3.1.1** summarizes the pertinent data. **Figure 3.1.11** and **Table 3.1.2** ontain a summary of every additional device-related data.

First, the devices without additives had an optimal PCE of 7.90%, a V_{OC} of 0.86 V, J_{SC} of 14.30 mA cm^{-2}, and an FF of 65.3%. We then measured how the additives effected the OSC's performance. The effect of various DIO additive amounts was then partially tested. In accordance with the results, the best device created utilizing the 0.5% DIO additive achieves a PCE of 8.63%, with V_{OC} = 0.87 V, J_{SC} = 14.36 mA cm^{-2}, and FF = 68.8%. By incorporating up to 5.0% (w/w) of polymer additives into the active layer, the ideal quantity was reduced to 2.0% (w/w) for all polymer additives. Polymer additives used on the PBDB-TT5:ITIC film improved the total PCEs, similar to what was seen when DIO was used. In the DIO-processed system, the PCE improvement may be attributed in large part to the noticeable rise in FF accompanied by just a little shift in J_{SC}. However, when polymer additives were applied, the J_{SC} and V_{OC} values rose properly, along with a minor improvement in FF. Because of the large increase in both J_{SC} and V_{OC}, the optimal amount of PPFS addition produced the greatest results, increasing PCEs by as much as 9.29 %. The higher V_{OC} values of PS- and PPFS-processed devices relative to non-additive devices may be attributable to the synergistic features of the adjustable dielectric property and morphology upon their incorporation, which will be investigated in detail in the sections that follow. As demonstrated in **Figure 3.1.3b**, the complementary absorptions of PBDB-TT5 and ITIC are responsible for the excellent photovoltaic responses observed in all of the EQE curves for the optimized devices. When additives, namely PPFS, were added, the EQE values clearly increased, which matched the trend of the J_{SC} values determined from *J-V* measurements.

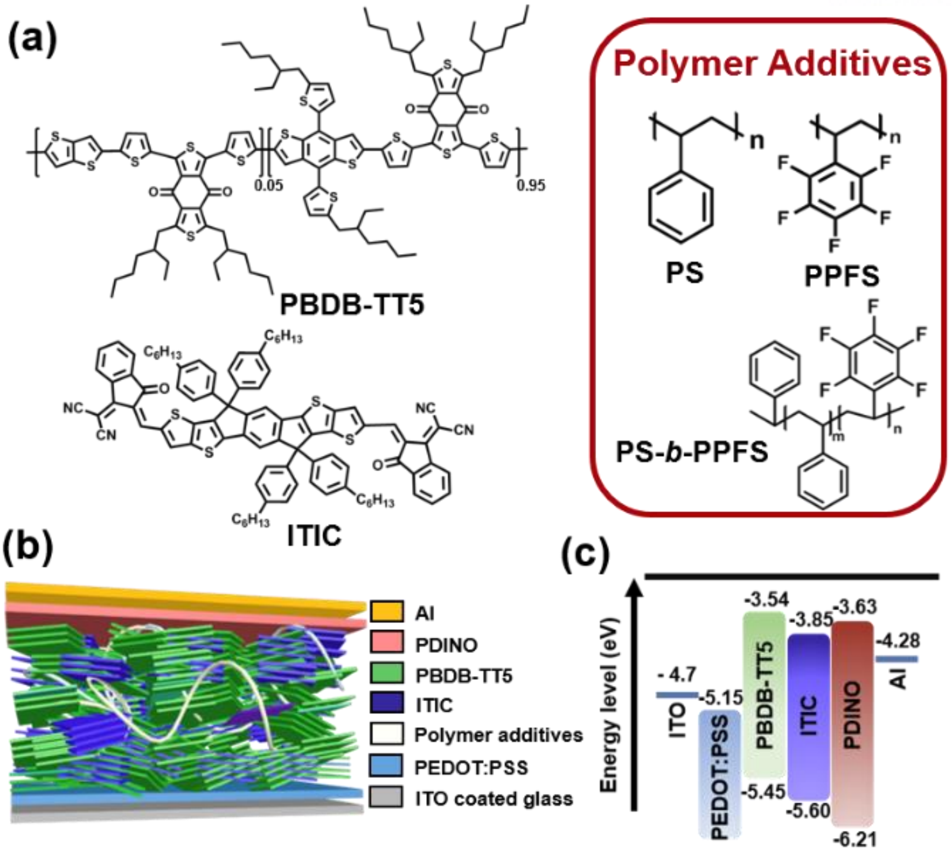

Figure 3.1.2. (a) Structures of the active layers and additives. (b) Conventional device architecture. c) Diagram illustrating the materials' energies.

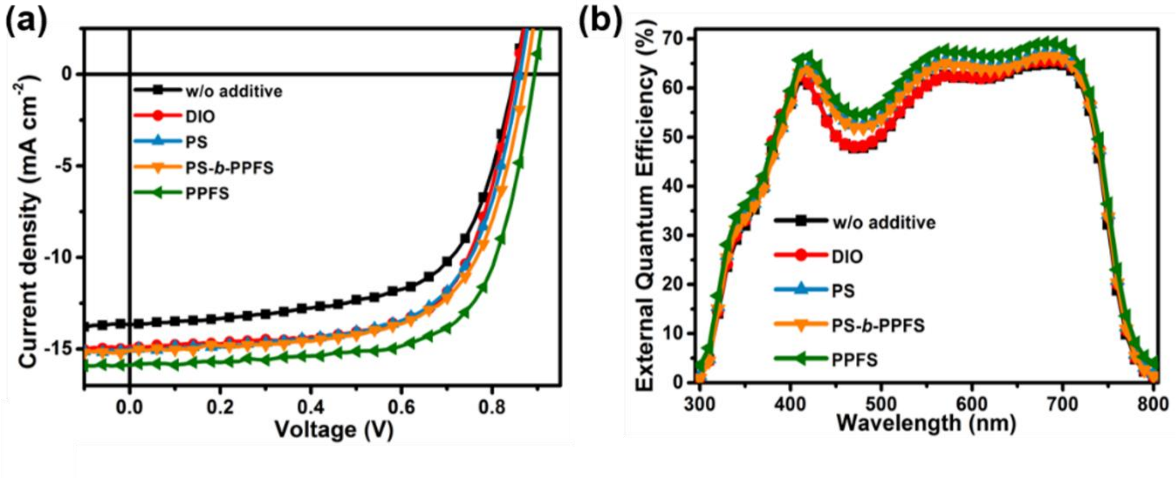

Figure 3.1.3. (a) The *J-V* curves with appropriate additive concentrations. (b) the EQE spectra for PBDB-TT5:ITIC films.

Table 3.1.1. Photovoltaic characteristics of NF-OSCs.

Additive (w/w) or (v/v)	**V_{OC} [V]**	**J_{SC} [mA cm^{-2}]**	**FF [%]**	**PCE [a] [%]**	**μ_e [cm^2 V s^{-1}]**	**μ_h [cm^2 V s^{-1}]**	**μ_e/μ_h**	**Thickness [nm]**
None	0.861(0.866)	14.30 (13.99)	65.30 (65.22)	7.90 (7.63)	3.37×10^{-4}	1.40×10^{-4}	2.36	97.3
0.5% DIO	0.873 (0.873)	14.36 (14.29)	68.85 (68.88)	8.63 (8.47)	4.46×10^{-4}	2.16×10^{-4}	2.06	101.2
2% PS	0.894 (0.887)	14.92 (14.71)	65.77 (65.51)	8.56 (8.51)	1.47×10^{-4}	4.22×10^{-4}	0.35	120.7
2% PS-*b*-PPFS	0.870 (0.863)	15.20 (15.40)	66.20 (66.43)	8.75 (8.62)	3.40×10^{-4}	5.33×10^{-4}	0.64	123.3
2% PPFS	0.889 (0.886)	15.92 (15.73)	66.02 (66.30)	9.29 (9.18)	2.66×10^{-4}	2.98×10^{-4}	0.89	122.7

[a] The numbers within the parentheses represent the average values from over 16 devices.

As described in the Experimental Information section, the charge carrier mobilities of the optimized films with and without various additives were determined using the SCLC method with a thickness of 100 to 150 nm. **Figure 3.1.12** depicts the plots of the current density against voltage of the devices for the mobility measurements, and **Table 3.1.1** summarizes the results. The μ_h and μ_e mobilities for the blend film without additive were 1.40×10^{-4} and 3.37×10^{-4} cm^2/Vs, respectively. It has been discovered that the inclusion of DIO enhances both μ_h and μ_e values. The addition of polymer additives, on the other hand, increases the μ_h values as in the DIO case, but the change in μ_es appears to be type dependent; for example, the addition of PS-*b*-PPFS results in a very similar μ_e to the blend film processed without additive, whereas the e values for the films containing PS or PPFS drop obviously to $1.47 \times 10^{-4} – 2.66 \times 10^{-4}$ cm^2/Vs. As a result, films treated with additives have more balanced μ_h and μ_e values than non-additive produced films. The buildup of charges (μ_h and μ_e) is deleterious to the device's FF, which is one of the reasons for the OSC's relatively low FF without additive.

We also investigated at the additive-free and additive-containing devices from the perspective of the light intensity dependence of the *J*–*V* characteristics. Quantitatively, J_{SC} follows a power-law dependency on light intensity (*I*) ($J_{SC} \propto I$), where denotes the amount of bimolecular recombination.[41,42]

When compared to the additive-free blend film (α = 0.962), the substantially greater slopes (0.972 – 0.964) in the *J*–*I* plots are evident for all additive cases (**Figure 3.1.4a**), suggesting a lesser degree of bimolecular recombination. In most cases, a low bimolecular recombination corresponds with a high FF obtained in the devices. Note that the significantly lower FF values reported for devices employing polymer additives compared to those containing DIO are most likely owing to the slightly thicker active layers produced by their viscosity. As shown in **Figure 3.1.4b**, on the other hand, the slops (*kT/q*) are 1.46, 1.49, 1.64, 1.75, and 1.78 for the PPFS, PS-*b*-PPFS, PS, DIO, and additive free cases, respectively, indicating that there is relatively weak trap-assisted recombination process in the PS-*b*-PPFS and PPFS-containing devices.

As illustrated in **Figure 3.1.4c**, we assessed the J_{ph} on the V_{eff} to get a deeper understanding of the additives' effect on the charge dynamics of the NF-OSC platform. Despite the lower change in *P(E,T)* values at the maximum power output voltage for all instances, the PPFS-processed device exhibits the greatest *P(E,T)* retention rate of 82.2%, indicating easier charge dissociation and extraction (**Figure 3.1.4d** and **Table 3.1.3**). By combining the above findings regarding the dependence of J_{SC} and V_{OC} on light intensity and the voltage dependence of J_{ph}, we find that the additives-containing OSCs, and in particular the PPFS-based one, have the lowest recombination loss and the highest charge extraction and collection efficiency, respectively.

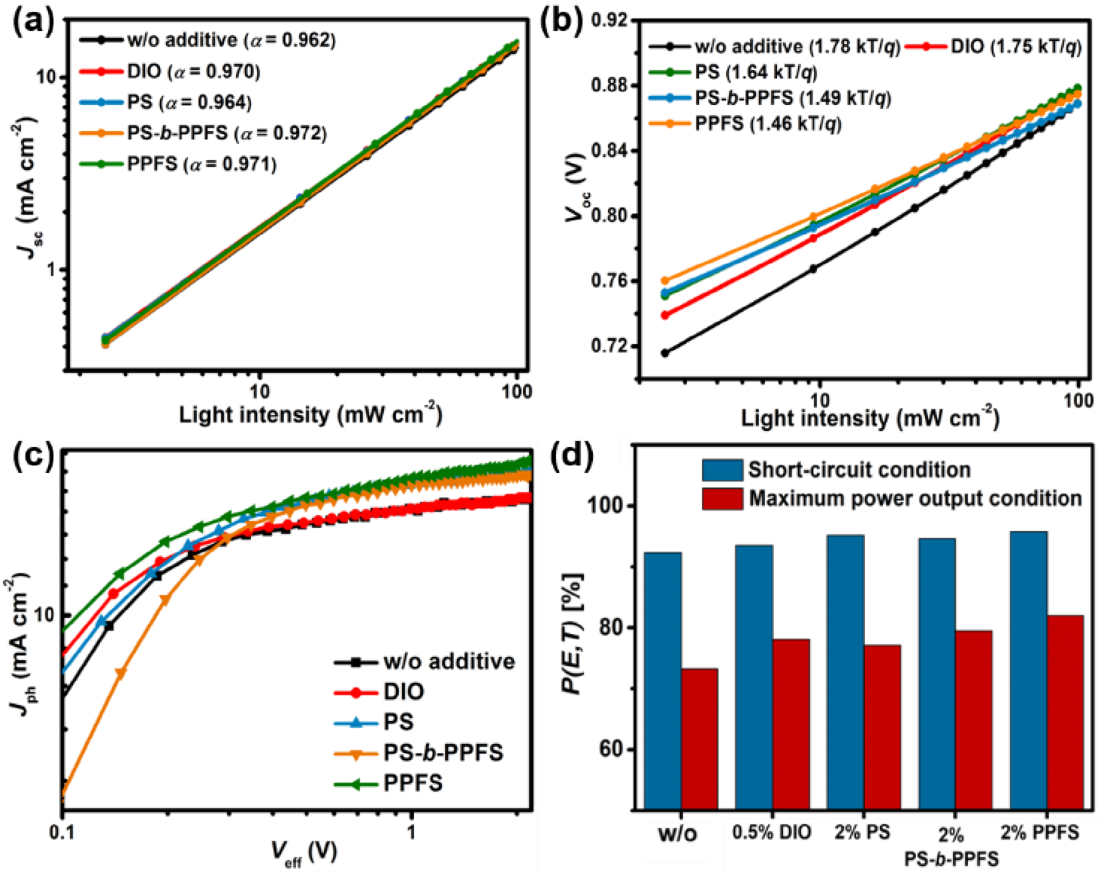

Figure 3.1.4. Light intensity dependence of (a) J_{SC} and (b) V_{OC} for optimal devices. (c) J_{ph} vs V_{eff} plots and (d) *P(E,T)* values histogram for maximum power outage and short circuit situations.

3.1.4 Morphological Properties

Following that, we used GIWAXS, AFM, and TEM to examine the shape and molecular packing features of the mix films as a function of the additions. **Figure 3.1.5** shows that all of the blend films had a lamellar packing diffuse ring at q ≈ 0.292 Å^{-1} and a strong π-π stacking reflection peak at q ≈1.685 Å^{-1} in the IP direction, indicating a preferential face-on molecular packing orientation with respect to the substrate. In fact, similar positions of both (100) and (010) peaks are found in all cases, showing that the lamellar and π-πstacking distances stay almost unaltered when the additives are added. The CCL_{010} calculated using the Scherrer equation, on the other hand, clearly demonstrated additive type-dependent behavior (**Table 3.1.4**). CCL_{010} values, for example, marginally rise with the addition of PS-*b*-PPFS, PS, or DIO, but drop with the PPFS additive, culminating in the least value of 19.88 Å in the PPFS-containing film. A possible explanation for this finding is that the PPFS additive make to improve the inter-miscibility of PBDB-TT5 and ITIC components, which is essential to maximize the PCE of the device.[6,31,43-45] The least RMS roughness value recorded from the PPFS-containing film might further demonstrate the most intermixed feature, as shown in the AFM images in **Figure 3.1.13**. All of the blend films with additives exhibit somewhat better phase separation than the non-additive one (**Figure 3.1.13**), which may be useful for excitons separation and charge transportation, despite the difficulties in clearly identifying the differences between each blend film in the TEM images.

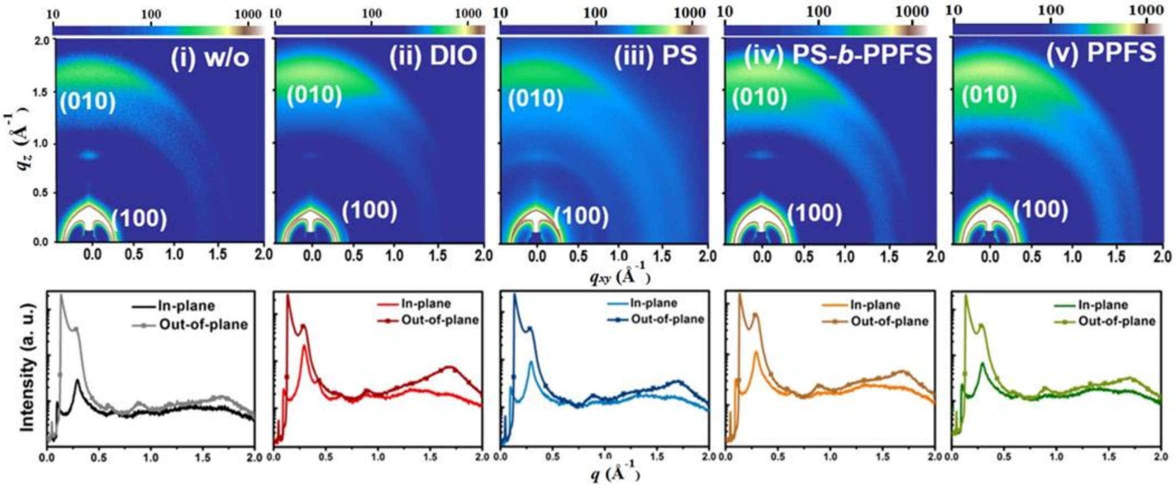

Figure 3.1.5. Blend films with and without additives (top) and line-cut profiles (bottom) of GIWAX.

3.1.5 Device Stability

The stability of OSC devices, in addition to PCE values, has been recognized as a critical field of research in both the academic and commercial industries. Concerning this problem, we investigated the stability of five optimized devices. At first, the devices were tested for 10 min at temperatures between 150 ºC and 250 ºC to see how they would hold up to the heat (**Figure 3.1.6** and **Figure 3.1.14**). Despite the fact that thermal treatment at extremely high temperatures (200 °C) decreases the values of all photovoltaic parameters in all the devices, the performance loss of the PPFS-containing device compared to the other devices was mitigated to some degree. In addition, the PPFS-containing device displayed greater long-term thermal stability at 150 °C, the highest temperature attained during OSCs' actual operation. In contrast to the dramatic PCE decreases reported in the other devices after 8 h of annealing at 150 °C, the PPFS-containing device maintained a PCE of 7.59 % after annealing. In addition, we conducted a 20-day evaluation of the devices' long-term durability without encapsulation in an inert environment at ambient temperature. In all cases, V_{OC}s become somewhat stable after 20 days. Nonetheless, a dramatic fall in both J_{SC} and FF is noted, leading to a decline in PCE. Therefore, the adoption of PPFS is likely to enhance the devices' long-term stability, resulting in the maximum degree of PCE retention (>7.82%). Notably, the stability of the polymer additive added devices is much superior than that of the DIO-processed device, which instantly declined throughout the device stability testing, performing even worse than the non-additive scenario.

As mentioned previously, the introduction of polymer additives into the active layer led to the formation of thicker films, demonstrating the unique interactions between the existing blend components and polymer additives. Thus, we infer that the enhanced stability of the devices is due, in part, to the morphological stabilization provided by the viscous polymer additives. Similar outcomes attributable to polymer additives have been documented in other recent investigations.[46-48] In spite of having the lowest molecular weight and, presumably, the lowest viscosity compared to the other polymer additives employed in this research, the usage of PPFS proved to be the most effective method for simultaneously improving and stabilizing the performance. The inclusion of PPFS additives with a high dielectric constant may hold the key to this question since it leads to an increase in the active layer's dielectric properties. To test this hypothesis, we used impedance spectroscopy to estimate the dielectric constant of the optimal blend films with each polymer component. As a frequency function, **Figure 3.1.15** depicts the relative dielectric constants of the optimal blend films with PPFS, PS-b-PPFS, and PS. The trends of the capacitance-derived dielectric constants of the neat films are consistent with the sequence of PPFS- > PS-*b*-PPFS- > PS-containing films for the values of the dielectric constants.[49,50] In addition, the augmentation of dielectric constant values of blend films including

DIO is a consequence of the smaller domain size of the blend film when compared to the blend film by itself. This result verifies that the PPFS additive may correctly improve the dielectric property of the active layer, which closely corresponds to the observed extraordinary performance and stability in comparison to other polymer additive situations. Increasing the dielectric constant on an OSC application might be advantageous for generating high PCEs with the intended effects.[50-54]

We further explored the adaptability of the PPFS additive by including it into OSCs with PTB7-Th:PNDI-T10, J71:ITIC, and PTB7-Th:PC71BM systems (Their chemical structures in **Figure 3.1.16**). **Figure 3.1.17** depicts the *J*–*V* characteristics of the devices, and **Table 3.1.5** summarizes the relevant photovoltaic performances. In the Experimental information section, each device's optimization is described in depth. **Figure 3.1.7** provides a summary of the PCE values of various BHJ PSC types with and without PPFS. As seen in each instance, PPFS-containing devices produced PCE values that were considerably higher than the equivalent control device without PPFS. Specifically, the addition of PPFS has consistently increased PCEs, but the addition of DIO has a detrimental impact on J71:ITIC and PTB7-Th:PNDI-T10. This finding indicates that the PPFS additive is a flexible experimental control approach for enhancing OSC performance.

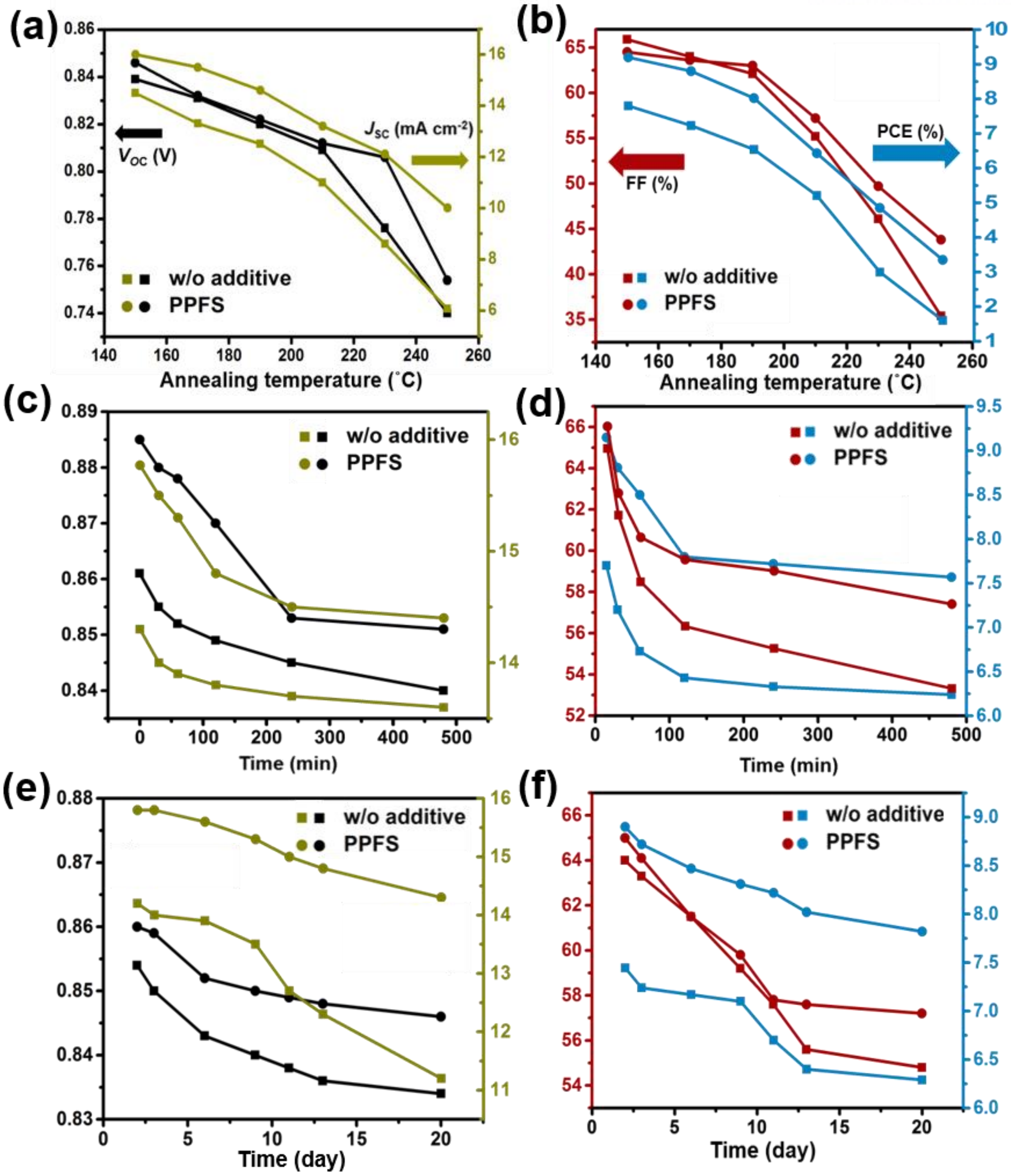

Figure 3.1.6. Device stability of the w/o additive and PPFS additive contained films under different conditions: (a), (b) annealing-temperature stability in the N_2-filled glovebox; (c), (d) thermal-time stability at 150 ˚C; (e), (f) in the N_2-filled glovebox.

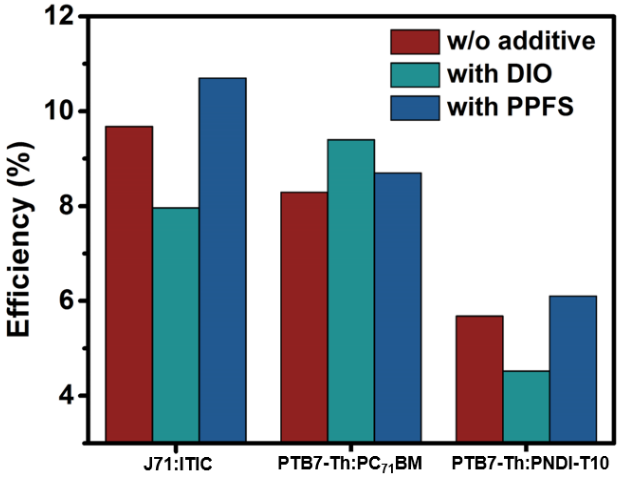

Figure 3.1.7. PCE values in various OSCs active systems with and without additives.

3.1.6 Conclusion

In conclusion, using the PBDB-TT5:ITIC test-bed system, we compared the morphology and photovoltaic performance of the volatile solvent processing DIO and nonvolatile solid polymer additives. Higher dielectric constant values were reported for polymer additives with higher fluorine concentrations (PPFS > PS-*b*-PPFS > PS). We discovered that all of the additives increased device performance, with PPFS providing the greatest benefit (from PCE of 7.90 % to 9.29 %). Furthermore, the PPFS-containing device outperformed the others in terms of device stability (e.g., thermal and long-term stabilities). The outstanding PCE and stability achievements were a result of the combined effects of the PPFS's unique interactions and the improved dielectric property, as seen by the change in the morphology and dielectric constant of the active layer. We also used the PPFS additive in various blend systems; in all instances, the inclusion of PPFS improved the performance, particularly for J71:ITIC, resulting in a PCE as high as 10.70%. Our findings indicate that PPFS has broad potential as an additive for use in achieving high-performance and robust OSCs.

3.1.7 Supporting Information

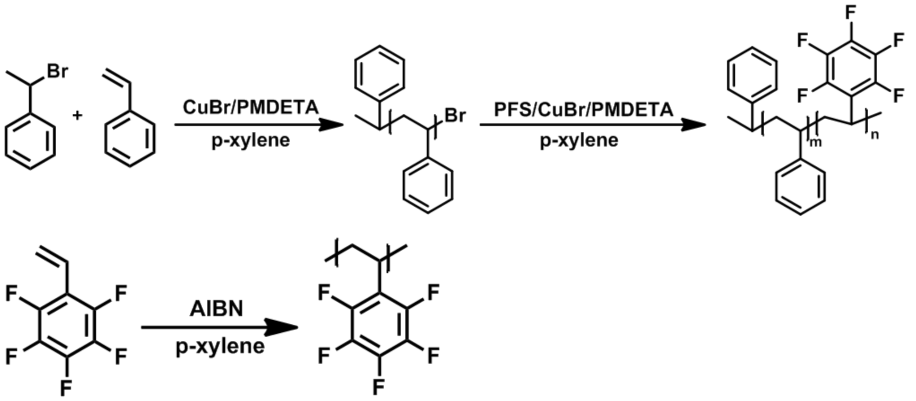

Scheme 3.1.1. Synthetic routes of PS, PS-*b*-PPFS and PPFS polymer additives**.**

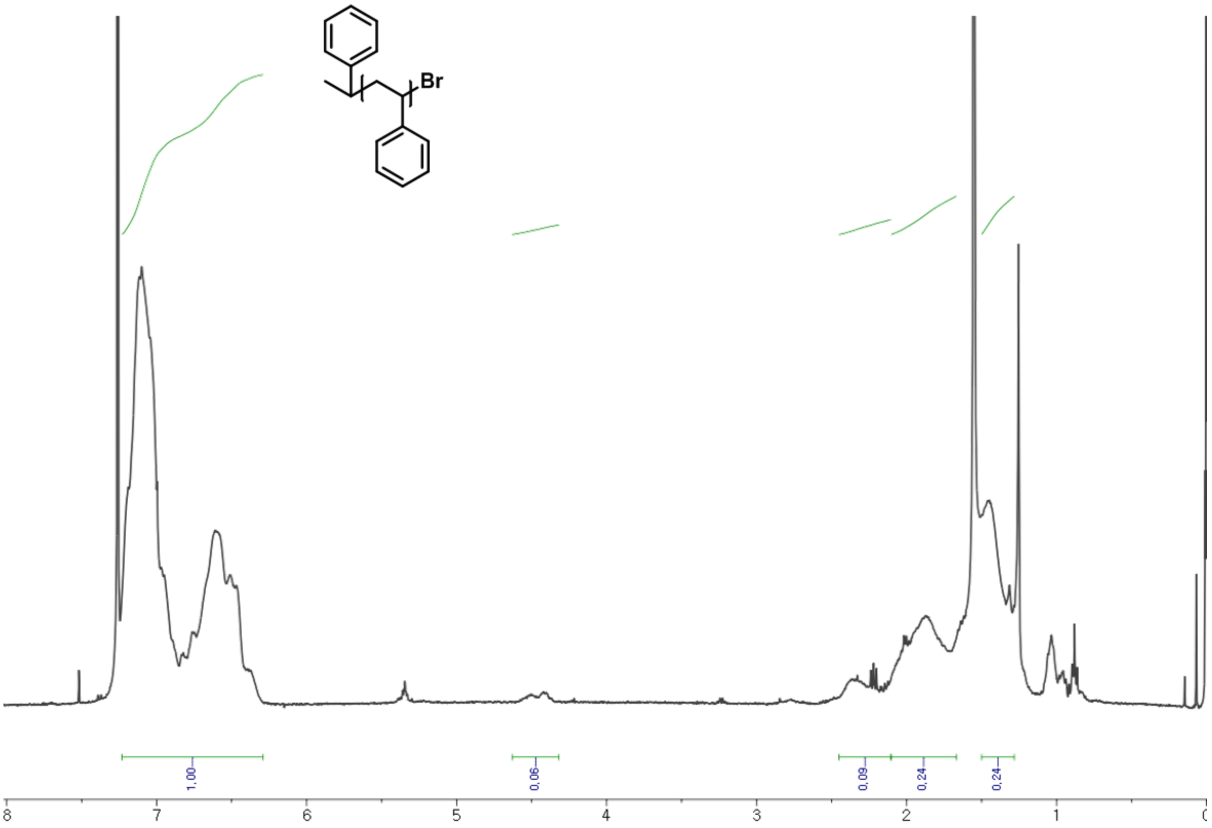

Figure 3.1.8. ^{1}H NMR data of PS-Br.

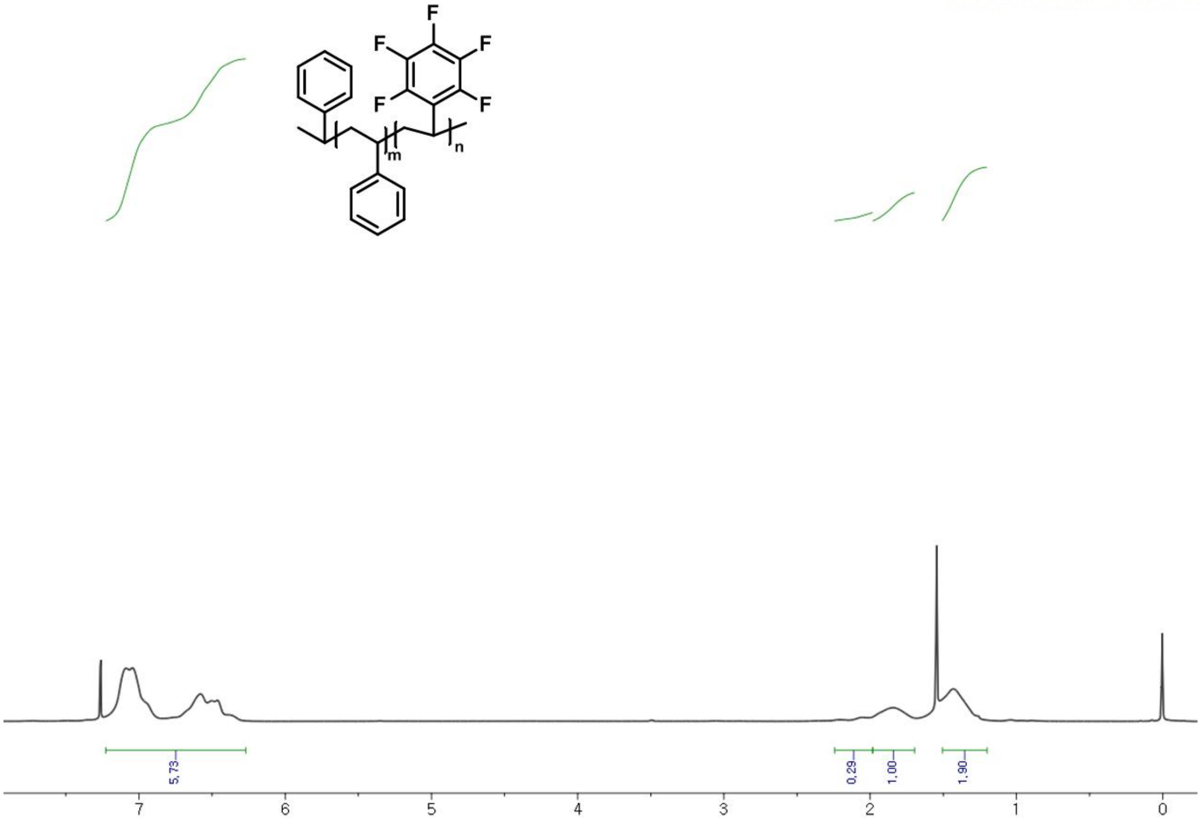

Figure 3.1.9. ^{1}H NMR data of PS-*b*-PPFS.

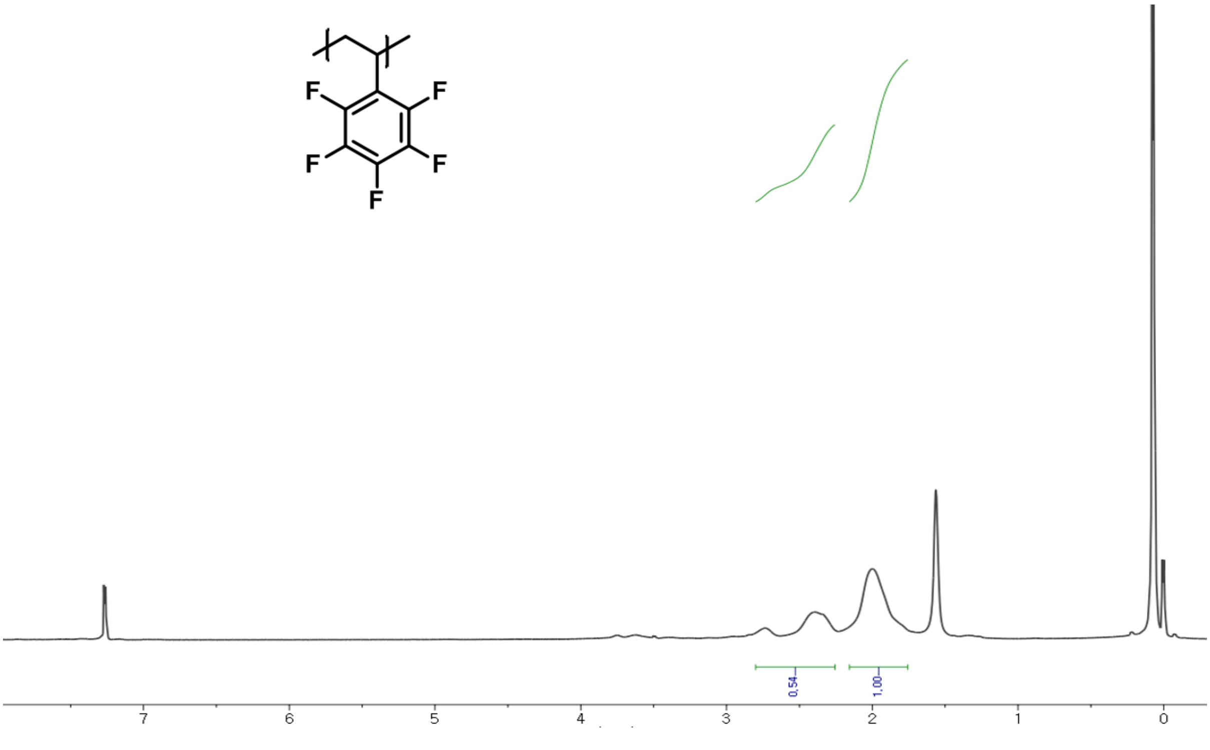

Figure 3.1.10. ^{1}H NMR data of PPFS.

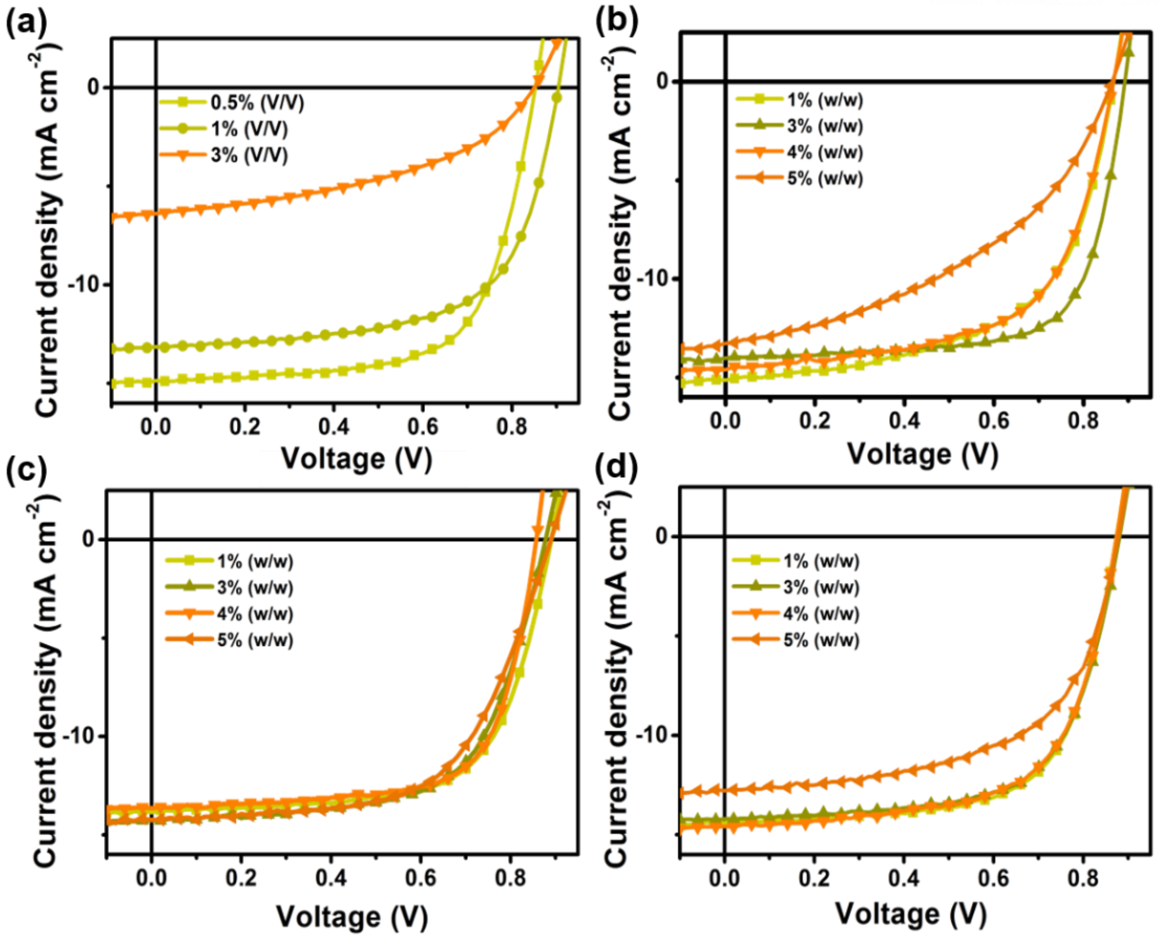

Figure 3.1.11. The *J*–*V* curves for PBDB-TT5:ITIC films with varying additive concentrations: (a) DIO, (b) PS, (c) PS-*b*-PPFS, and (d) PPFS.

Table 3.1.2. Photovoltaic parameters of NF-OSCs with different concentration of each additive.

Additive (v/v)	**V_{OC} [V]**	**J_{SC} [mA cm^{-2}]**	**FF**	**PCE [a] [%]**
1% DIO	0.904 (0.906)	13.15 (13.09)	63.55 (62.78)	7.58 (7.50)
2% DIO	0.889 (0.887)	9.16 (8.98)	59.69 (59.42)	4.86 (4.61)
3% DIO	0.849 (0.850)	6.39 (6.16)	44.09 (44.45)	2.39 (2.35)
1% PS	0.881 (0.882)	15.02 (14.99)	63.84 (63.46)	8.45 (8.36)
3% PS	0.894 (0.886)	14.87 (14.81)	64.01 (64.46)	8.51 (8.48)
4% PS	0.872 (0.876)	14.60 (14.83)	61.51 (60.94)	8.19 (8.07)
5% PS	0.886 (0.885)	13.37 (13.18)	50.01 (49.63)	5.92 (5.87)
1% PS-*b*-PPFS	0.887 (0.884)	14.46 (14.21)	67.92 (67.71)	8.51 (8.45)
3% PS-*b*-PPFS	0.882 (0.877)	15.00 (14.85)	64.90 (64.43)	8.42 (8.39)
4% PS-*b*-PPFS	0.901 (0.879)	13.62 (13.40)	69.01 (68.82)	8.10 (8.09)
5% PS-*b*-PPFS	0.884 (0.881)	14.77 (14.62)	63.90 (63.74)	8.22 (8.07)
1% PPFS	0.882 (0.876)	15.37 (14.88)	67.20 (66.87)	8.53 (8.43)
3% PPFS	0.894 (0.889)	15.19 (15.02)	65.75 (64.88)	8.87 (8.66)
4% PPFS	0.897 (0.886)	15.10 (14.74)	68.69 (67.42)	8.70 (8.53)
5% PPFS	0.889 (0.886)	15.92 (15.73)	66.02 (66.02)	8.51 (8.38)

[a] The values within the parentheses represent the average values from over 16 devices.

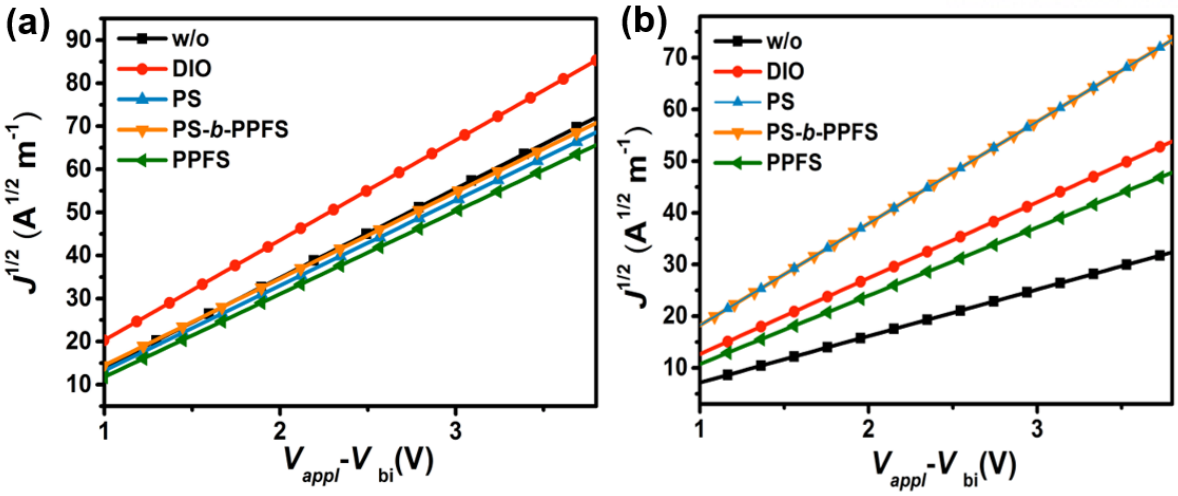

Figure 3.1.12. PBDB-TT5:ITIC blend film-based (a) electron-only and (b) hole-only devices with dark $J^{1/2}$–V graphs.

Table 3.1.3. *P(E. T)* values under short-circuit and maximum power output conditions.

Devices	***P*(*E*,*T*) [%]**	
	At short-circuit condition	**At maximum power output condition**
w/o additive	92.3	73.2
0.5% DIO	93.5	78.1
2% PS	95.2	77.1
2% PS-*b*-PPFS	94.6	79.5
2% PPFS	95.8	82.0

Table 3.1.4. The GIWAX out-of-plane and in-plane parameters.

Additive (*w/w*) or (*v/v*)	**Out-of-Plane**				**In-Plane**			
	π-π stacking cell axis (*010*)				**Unit cell long axis (*100*)**			
	q (Å^{-1})	*d*-spacing (Å)	FWHM (Å^{-1})	Coherence length (Å)	*q* (Å^{-1})	*d*-spacing (Å)	FWHM (Å^{-1})	Coherence length (Å)
w/o additive	1.685	3.723	0.272	21.055	0.292	21.530	0.0442	128.067
0.5% DIO	1.692	3.713	0.245	23.380	0.295	21.332	0.0456	126.106
2% PS	1.695	3.707	0.267	21.387	0.293	21.453	0.0481	117.677
2% PS-*b*-PPFS	1.692	3.714	0.266	21.485	0.292	21.518	0.0437	129.504
2% PPFS	1.696	3.704	0.287	19.883	0.295	21.315	0.0459	123.295

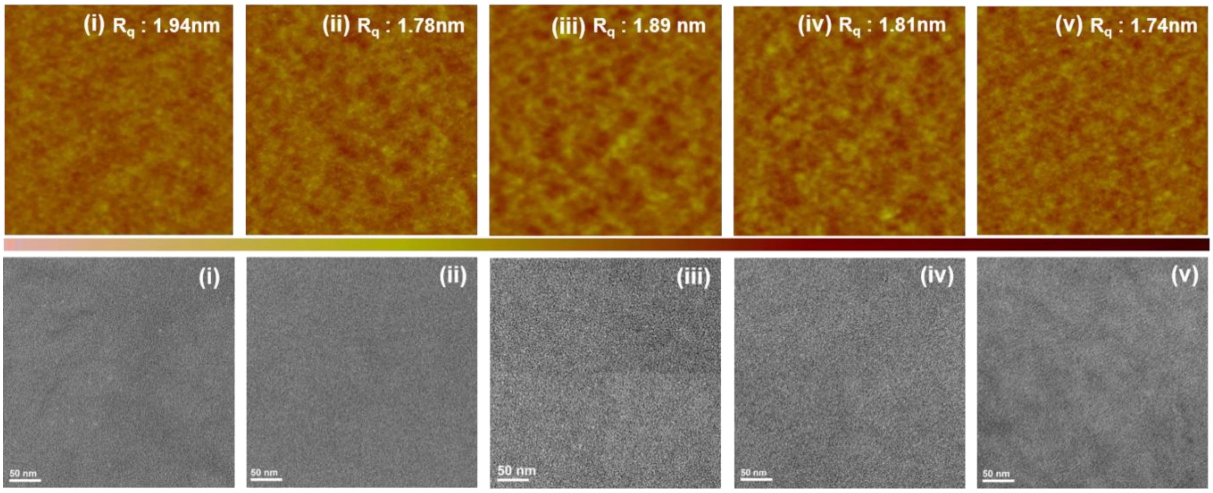

Figure 3.1.13. The AFM height images (top) and TEM images of the blend film (bottom): (i) w/o additive, (ii) DIO, (iii) PS, (iv) PS-*b*-PPFS, and (v) PPFS.

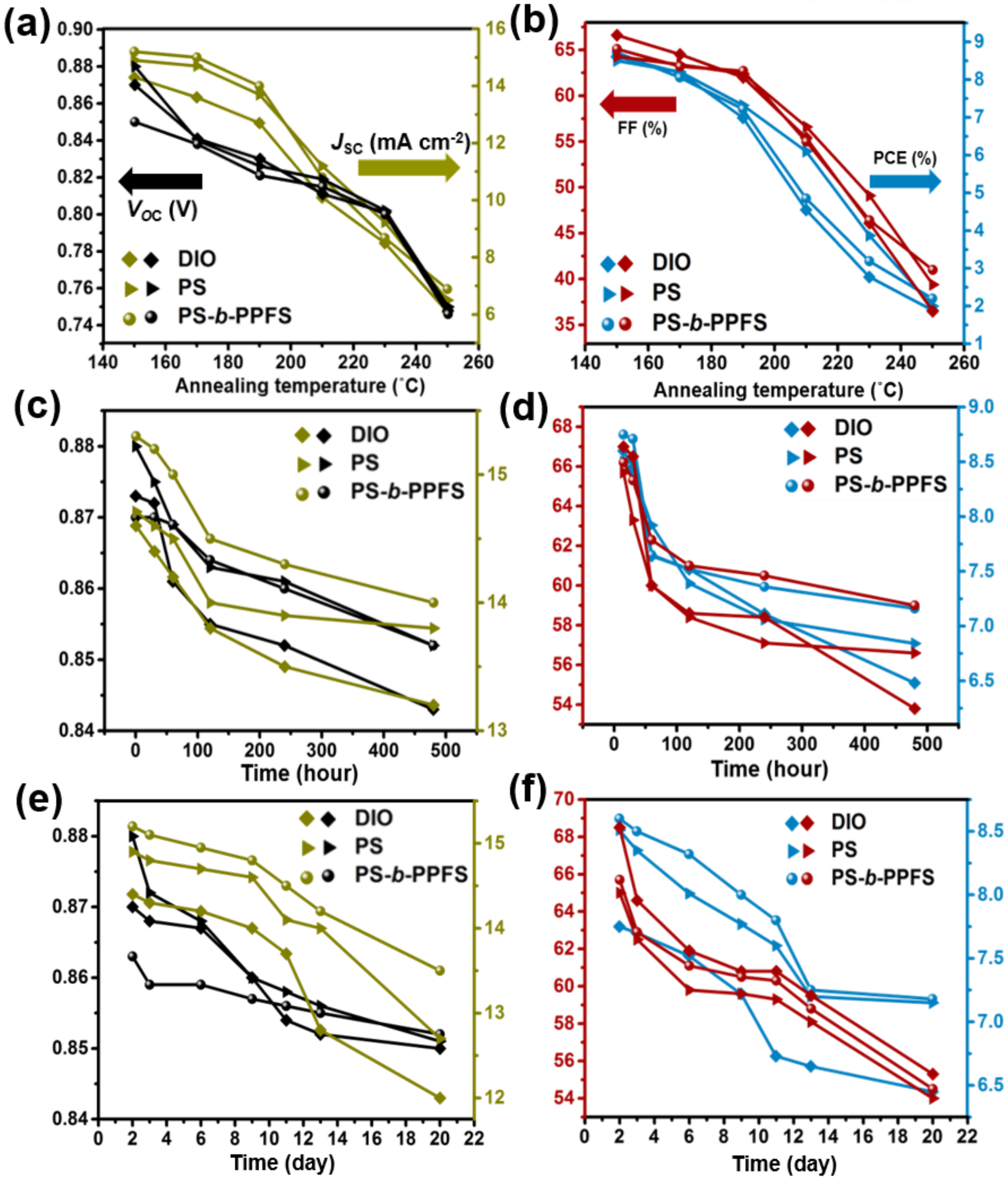

Figure 3.1.14. Under different conditions, the device stability of the various processing additive contained films: (a), (b) annealing-temperature stability in the N_2-filled glovebox; (c),(d) thermal-time stability at 150 ˚C; (e), (f) in the N_2-filled glovebox without capsulation of the long-term stability.

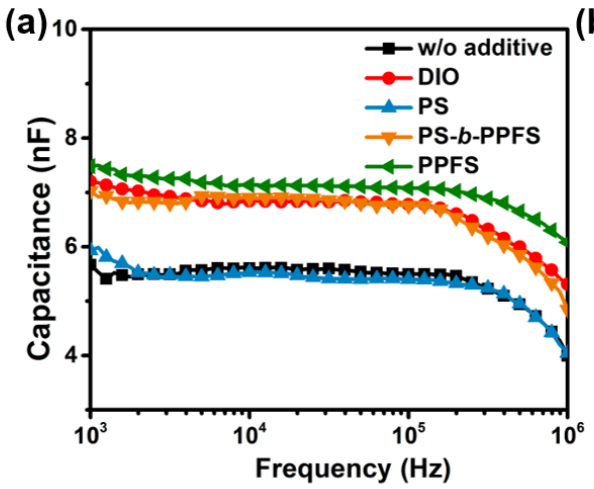

Figure 3.1.15. The frequency dependence of the (a) capacitance and (b) dielectric constant in the blend system.

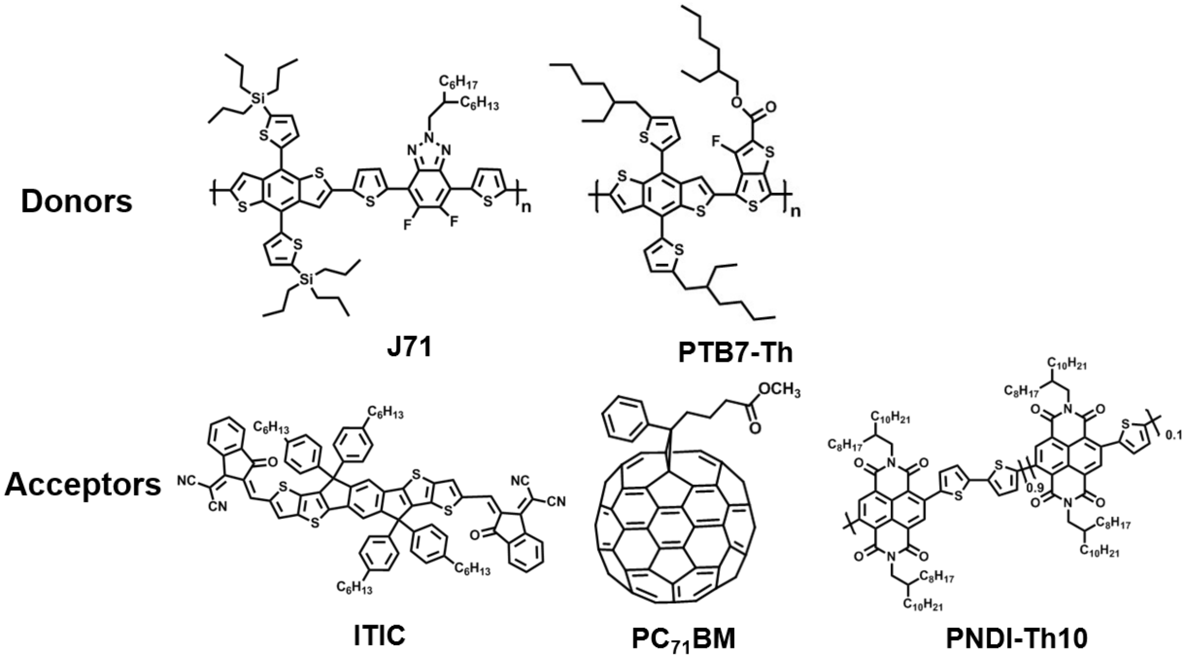

Figure 3.1.16. Donor and acceptor chemical structures employed in different host systems.

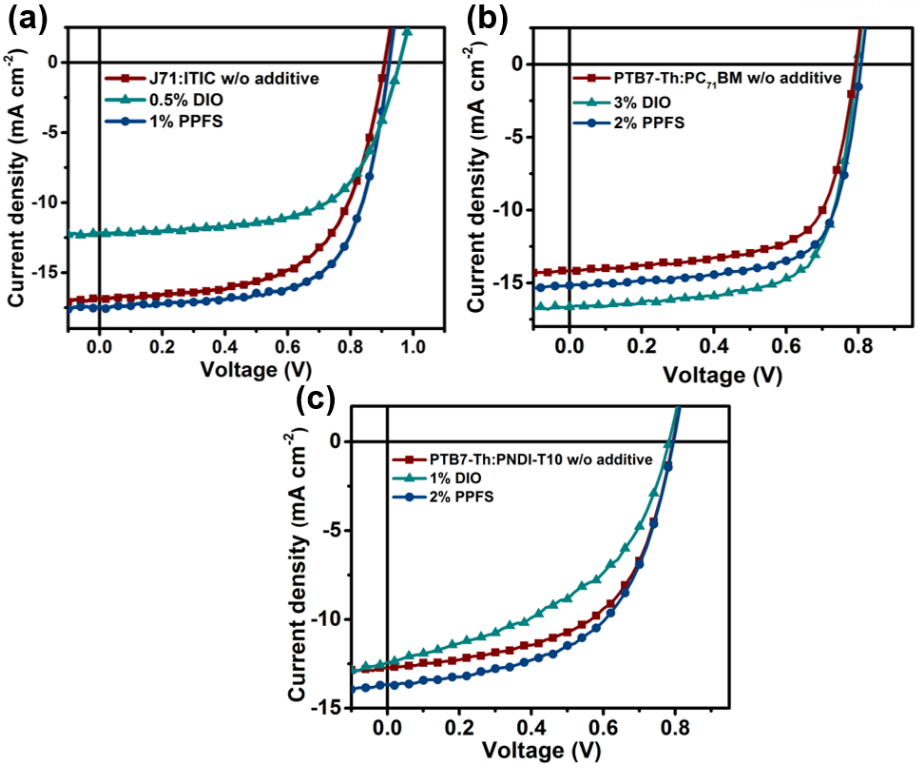

Figure 3.1.17. The *J-V* curves with optimal concentration additive (a) J71:ITIC, (b) PTB7-Th:PC$_{71}$BM, and (c) PTB7-Th:PNDI-T10.

Table 3.1.5. Photovoltaic parameters using various kinds of active layers, with and without additives.

Devices	Additive	V_{OC} [V]	J_{SC} [mA/cm^2]	FF [%]	PCE [a] [%]
J71:ITIC	**X**	0.919 (0.913)	17.15 (17.04)	61.30 (61.08)	6.68 (6.52)
J71:ITIC	**0.5% DIO**	0.922 (0.917)	15.38 (15.30)	56.01 (55.07)	7.96 (7.79)
J71:ITIC	**1% PPFS**	0.924 (0.927)	17.38 (17.08)	66.20 (65.77)	10.70 (10.43)
PTB7-Th:PC$_{71}$BM	**X**	0.785 (0.792)	15.60 (15.28)	67.64 (66.64)	8.29 (8.04)
PTB7-Th:PC$_{71}$BM	**3% DIO**	0.792 (0.793)	17.69 (17.45)	69.21 (68.87)	9.40 (9.20)
PTB7-Th:PC$_{71}$BM	**2% PPFS**	0.805 (0.804)	15.49 (15.76)	69.67 (68.75)	8.70 (8.56)
PTB7-Th:PNDI-T10	**X**	0.793 (0.804)	12.74 (12.44)	56.21 (55.96)	5.68 (5.64)
PTB7-Th:PNDI-T10	**1% DIO**	0.782 (0.786)	12.44 (12.08)	46.51 (44.96)	4.52 (4.10)
PTB7-Th:PNDI-T10	**2% PPFS**	0.795 (0.799)	13.69 (13.52)	56.10 (55.64)	6.10 (6.02)

[a] The values in parentheses are the averages of more than 16 devices.

3.1.8 References

1. O. K. Kwon, M. A. Uddin, J.-H. Park, S. K. Park, T. L. Nguyen, H. Y. Woo and S. Y. Park, *Advanced Materials*, 2016, **28**, 910-916.
2. Z. Li, X. Xu, W. Zhang, X. Meng, W. Ma, A. Yartsev, O. Inganäs, M. R. Andersson, R. A. J. Janssen and E. Wang, *Journal of the American Chemical Society*, 2016, **138**, 10935-10944.
3. J. H. Park, J.-I. Park, D. H. Kim, J.-H. Kim, J. S. Kim, J. H. Lee, M. Sim, S. Y. Lee and K. Cho, *Journal of Materials Chemistry*, 2010, **20**, 5860-5865.
4. H. Bin, L. Gao, Z.-G. Zhang, Y. Yang, Y. Zhang, C. Zhang, S. Chen, L. Xue, C. Yang, M. Xiao and Y. Li, *Nature Communications*, 2016, **7**, 13651.
5. S. Chen, S. Jung, H. J. Cho, N.-H. Kim, S. Jung, J. Xu, J. Oh, Y. Cho, H. Kim, B. Lee, Y. An, C. Zhang, M. Xiao, H. Ki, Z.-G. Zhang, J.-Y. Kim, Y. Li, H. Park and C. Yang, *Angewandte Chemie International Edition*, 2018, **57**, 13277-13282.
6. H. C. Liao, C. C. Ho, C. Y. Chang, M. H. Jao, S. B. Darling and W. F. Su, *Materials Today*, 2013, **16**, 326-336.
7. T. H. Lee, S. Y. Park, B. Walker, S.-J. Ko, J. Heo, H. Y. Woo, H. Choi and J. Y. Kim, *RSC Advances*, 2017, **7**, 7476-7482.
8. S. Y. Park, S. Song, Y. J. Yoon, T. H. Lee, N. G. An, B. Walker and J. Y. Kim, *RSC Advances*, 2018, **8**, 39777-39783.
9. W. Zhao, D. Qian, S. Zhang, S. Li, O. Inganäs, F. Gao and J. Hou, *Advanced Materials*, 2016, **28**, 4734-4739.
10. N. Zhou, X. Guo, R. P. Ortiz, S. Li, S. Zhang, R. P. H. Chang, A. Facchetti and T. J. Marks, *Advanced Materials*, 2012, **24**, 2242-2248.
11. S. Chen, S. M. Lee, J. Xu, J. Lee, K. C. Lee, T. Hou, Y. Yang, M. Jeong, B. Lee, Y. Cho, S. Jung, J. Oh, Z.-G. Zhang, C. Zhang, M. Xiao, Y. Li and C. Yang, *Energy & Environmental Science,* 2018, **11**, 2569-2580.
12. J. K. Lee, W. L. Ma, C. J. Brabec, J. Yuen, J. S. Moon, J. Y. Kim, K. Lee, G. C. Bazan and A. J. Heeger, *Journal of the American Chemical Society*, 2008, **130**, 3619-3623.
13. W. Chen, T. Xu, F. He, W. Wang, C. Wang, J. Strzalka, Y. Liu, J. Wen, D. J. Miller, J. Chen, K. Hong, L. Yu and S. B. Darling, *Nano Letters*, 2011, **11**, 3707-3713.
14. Y. An, J. Oh, S. Chen, B. Lee, S. M. Lee, D. Han and C. Yang, *Polymer Chemistry*, 2018, **9**, 593-602.
15. J. Yuan, Y. Xu, G. Shi, X. Ling, L. Ying, F. Huang, T. H. Lee, H. Y. Woo, J. Y. Kim, Y. Cao and W. Ma, *Journal of Materials Chemistry A*, 2018, **6**, 10421-10432.
16. Y. Zhou, K. L. Gu, X. Gu, T. Kurosawa, H. Yan, Y. Guo, G. I. Koleilat, D. Zhao, M. F. Toney and Z. Bao, *Chemistry of Materials*, 2016, **28**, 5037-5042.

17. X. Guo, C. Cui, M. Zhang, L. Huo, Y. Huang, J. Hou and Y. Li, *Energy & Environmental Science*, 2012, **5**, 7943-7949.

18. Y. Kim, H. R. Yeom, J. Y. Kim and C. Yang, *Energy & Environmental Science*, 2013, **6**, 1909-1916.

19. X. Hu, M. Wang, F. Huang, X. Gong and Y. Cao, *Synthetic Metals*, 2013, **164**, 1-5.

20. P. Cheng, J. Wang, Q. Zhang, W. Huang, J. Zhu, R. Wang, S.-Y. Chang, P. Sun, L. Meng, H. Zhao, H.-W. Cheng, T. Huang, Y. Liu, C. Wang, C. Zhu, W. You, X. Zhan and Y. Yang, *Advanced Materials*, 2018, **30**, 1801501.

21. P. Cheng, M. Zhang, T.-K. Lau, Y. Wu, B. Jia, J. Wang, C. Yan, M. Qin, X. Lu and X. Zhan, *Advanced Materials*, 2017, **29**, 1605216.

22. P. Cheng, C. Yan, T.-K. Lau, J. Mai, X. Lu and X. Zhan, *Advanced Materials*, 2016, **28**, 5822-5829.

23. P. Cheng, Y. Liu, S.-Y. Chang, T. Li, P. Sun, R. Wang, H.-W. Cheng, T. Huang, L. Meng, S. Nuryyeva, C. Zhu, K.-H. Wei, B. Sun, X. Zhan and Y. Yang, *Joule*, 2019, **3**, 432-442.

24. K. R. Graham, P. M. Wieruszewski, R. Stalder, M. J. Hartel, J. Mei, F. So and J. R. Reynolds, *Advanced Functional Materials*, 2012, **22**, 4801-4813.

25. K. Yao, Y.-X. Xu, X. Wang, F. Li and J. Yuan, *RSC Advances*, 2015, **5**, 93689-93696.

26. B. J. Tremolet de Villers, K. A. O'Hara, D. P. Ostrowski, P. H. Biddle, S. E. Shaheen, M. L. Chabinyc, D. C. Olson and N. Kopidakis, *Chemistry of Materials*, 2016, **28**, 876-884.

27. R. Yu, H. Yao, L. Hong, Y. Qin, J. Zhu, Y. Cui, S. Li and J. Hou, *Nature Communications*, 2018, **9**, 4645.

28. K. R. Graham, J. Mei, R. Stalder, J. W. Shim, H. Cheun, F. Steffy, F. So, B. Kippelen and J. R. Reynolds, *ACS Applied Materials & Interfaces*, 2011, **3**, 1210-1215.

29. C. McDowell, M. Abdelsamie, K. Zhao, D.-M. Smilgies, G. C. Bazan and A. Amassian, *Advanced Energy Materials*, 2015, **5**, 1501121.

30. Y. Huang, W. Wen, S. Mukherjee, H. Ade, E. J. Kramer and G. C. Bazan, *Advanced Materials*, 2014, **26**, 4168-4172.

31. T. Kumari, M. Moon, S.-H. Kang and C. Yang, *Nano Energy*, 2016, **24**, 56-62.

32. H. Zhang, H. Yao, J. Hou, J. Zhu, J. Zhang, W. Li, R. Yu, B. Gao, S. Zhang and J. Hou, *Advanced Materials*, 2018, **30**, 1800613.

33. J. Zhang, H. S. Tan, X. Guo, A. Facchetti and H. Yan, *Nature Energy*, 2018, **3**, 720-731.

34. Z. Zheng, Q. Hu, S. Zhang, D. Zhang, J. Wang, S. Xie, R. Wang, Y. Qin, W. Li, L. Hong, N. Liang, F. Liu, Y. Zhang, Z. Wei, Z. Tang, T. P. Russell, J. Hou and H. Zhou, *Advanced Materials*, 2018, **30**, 1801801.

35. Y. Lin, J. Wang, Z.-G. Zhang, H. Bai, Y. Li, D. Zhu and X. Zhan, *Advanced Materials*, 2015, **27**, 1170-1174.

36. S. Holliday, R. S. Ashraf, C. B. Nielsen, M. Kirkus, J. A. Röhr, C.-H. Tan, E. Collado-Fregoso, A.-C. Knall, J. R. Durrant, J. Nelson and I. McCulloch, *Journal of the American Chemical Society*, 2015, **137**, 898-904.

37. D. Xia, D. Gehrig, X. Guo, M. Baumgarten, F. Laquai and K. Müllen, *Journal of Materials Chemistry A*, 2015, **3**, 11086-11092.

38. C. Yan, S. Barlow, Z. Wang, H. Yan, A. K. Y. Jen, S. R. Marder and X. Zhan, *Nature Reviews Materials*, 2018, **3**, 18003.

39. P. Cheng, G. Li, X. Zhan and Y. Yang, *Nature Photonics*, 2018, **12**, 131-142.

40. M. Jeong, S. Chen, S. M. Lee, Z. Wang, Y. Yang, Z.-G. Zhang, C. Zhang, M. Xiao, Y. Li and C. Yang, *Advanced Energy Materials*, 2018, **8**, 1702166.

41. A. K. K. Kyaw, D. H. Wang, V. Gupta, W. L. Leong, L. Ke, G. C. Bazan and A. J. Heeger, *ACS Nano*, 2013, **7**, 4569-4577.

42. P. Schilinsky, C. Waldauf and C. J. Brabec, *Applied Physics Letters*, 2002, **81**, 3885-3887.

43. L. Gao, Z.-G. Zhang, H. Bin, L. Xue, Y. Yang, C. Wang, F. Liu, T. P. Russell and Y. Li, *Advanced Materials*, 2016, **28**, 8288-8295.

44. J. Rivnay, S. C. B. Mannsfeld, C. E. Miller, A. Salleo and M. F. Toney, *Chemical Reviews*, 2012, **112**, 5488-5519.

45. H. Hu, K. Jiang, G. Yang, J. Liu, Z. Li, H. Lin, Y. Liu, J. Zhao, J. Zhang, F. Huang, Y. Qu, W. Ma and H. Yan, *Journal of the American Chemical Society*, 2015, **137**, 14149-14157.

46. K. H. Park, Y. An, S. Jung, H. Park and C. Yang, *ACS Nano*, 2017, **11**, 7409-7415.

47. K. H. Park, Y. An, S. Jung, H. Park and C. Yang, *Energy & Environmental Science*, 2016, **9**, 3464-3471.

48. H.-S. Lee, H. Ahn, J. W. Jo, B. Kim and H. J. Son, *Journal of Materials Chemistry A*, 2016, **4**, 18383-18391.

49. B. Gautam, E. Klump, X. Yi, I. Constantinou, N. Shewmon, A. Salehi, C. K. Lo, Z. Zheng, J.-L. Brédas, K. Gundogdu, J. R. Reynolds and F. So, *Advanced Materials*, 2018, **30**, 1801392.

50. I. Constantinou, X. Yi, N. T. Shewmon, E. D. Klump, C. Peng, S. Garakyaraghi, C. K. Lo, J. R. Reynolds, F. N. Castellano and F. So, *Advanced Energy Materials*, 2017, **7**, 1601947.

51. L. J. A. Koster, S. E. Shaheen and J. C. Hummelen, *Advanced Energy Materials*, 2012, **2**, 1246-1253.

52. K. S. Nalwa, J. A. Carr, R. C. Mahadevapuram, H. K. Kodali, S. Bose, Y. Chen, J. W. Petrich, B. Ganapathysubramanian and S. Chaudhary, *Energy & Environmental Science*, 2012, **5**, 7042-7049.

53. J. Brebels, J. V. Manca, L. Lutsen, D. Vanderzande and W. Maes, *Journal of Materials Chemistry A*, 2017, **5**, 24037-24050.

54. X. Liu, K. S. Jeong, B. P. Williams, K. Vakhshouri, C. Guo, K. Han, E. D. Gomez, Q. Wang

and J. B. Asbury, *The Journal of Physical Chemistry B*, 2013, **117**, 15866-15874.

CHAPTER 3 Solid Additives

Nonvolatile Antioxidant Additives for High Photo-Oxidative Stabilization OSCs

3.2.1 Motivation and Research Background

Recent research efforts have focused on developing cutting-edge active materials, device topologies, and processing methods resulting in laboratory-scale heterojunction OSCs with PCEs above 17%.[1-8] These excellent PCEs can be reached primarily in OSCs manufactured in an inert condition, and their PCEs decline dramatically when exposed to air and light containing H_2O and O_2.[9-11] Despite the likelihood of buffer interlayer and metal electrode degradation in OSCs, the observed PCE loss is mostly due to photo-induced oxidation of active layer components. Because of the irreversible radical oxidation process, organic materials are extremely sensitive to deterioration under the effect of combined stressors (oxygen, water, and light).[12-14] Organic semiconductors' principal photodegradation processes are triplet-mediated singlet oxygen synthesis or anion-mediated superoxide radical anion formation. Organic semiconductor radicals react quickly with the ground state of oxygen, resulting in the forming of hydroperoxide. Furthermore, singlet oxygen may target the reactive sites of photoactive compounds.

In addition to the need for transparent, high-protecting packaging materials, encapsulation quality must be desired. Another approach is to develop organic semiconductors that are intrinsically more stable against the above stressors, resulting in increased device stability but falling short of the PCE.[15,16] Along with high PCE, stability is the most demanding condition for OSCs to meet and represents the single largest barrier to their widespread commercialization. Through the use of commercial antioxidant additives as radical scavengers into the active layers, Turkovic et al. devised a unique technique for photo-oxidative stabilization of OSCs; Min et al. have recently undertaken more study on this issue.[17,18] Meanwhile, many studies have suggested boosting the active-layer matrix's dielectric constant to increase OSC performance by modifying different variables linked to Coulombic interactions in the films.[19-21] Recent research has shown that the inclusion of nonvolatile solid additives (e.g., polymer additives with high dielectric constant and ferroelectric characteristics) can provide some favorable qualities and, as a result, increase PCE values.[22,23]

The purpose of this research was to synthesize antioxidant compounds based on BHT by modifying their dielectric characteristics using PF and CN chains. The photovoltaic properties of the model

PM6:IT4F system, comprising BHT–CN and BHT–PF, were compared to those of commercial octadecyl-BHT and DIO reference standards. In addition to having a higher initial PCE (12.79 %) than the optimized control with DIO, the BHT-PF-processed OSC without encapsulation demonstrated improved long-term stability, with 33 % PCE loss after 1 hr of exposure to light, H_2O, and O_2 (compared to 83 % PCE loss for the DIO-processed control devices). We also found that the BHT–PF additive boosted the long-term stability of other host systems, including PM6:Y6 and J71:ITIC, while keeping initial PCE values equivalent to those obtained from optimized OSCs.

3.2.2 Synthesis and Simulation

The BHT-based additives were produced from 3-(3,5-*di-tert*-butyl-4-hydroxyphenyl)propionic acid and associated alcohols by a Steglich-type ester coupling with DCC and DMAP, whereas, in the case of BHT–CN, Kolbe nitrile synthesis was also used to convert the primary bromide (1) with sodium cyanide into the CN functionality. **Scheme 3.2.1** and the Experimental Section contain detailed synthetic routes and characterization. **Figure 3.2.1a** illustrates their molecular structures together with the net dipole moments and electrostatic potential map determined by DFT and the BHT–ref data**.** Because of their high electron-withdrawing ability, the ester and CN regions of BHT-based compounds have negative electrostatic potentials.[24,25] Fully extended alkyl chains were found to be almost parallel to the BHT unit, while PF alkyl chains were aligned at an angle to its plane. Furthermore, the net dipole moments of BHT–CN and BHT–PF were greater than those of BHT–ref.[26,27]

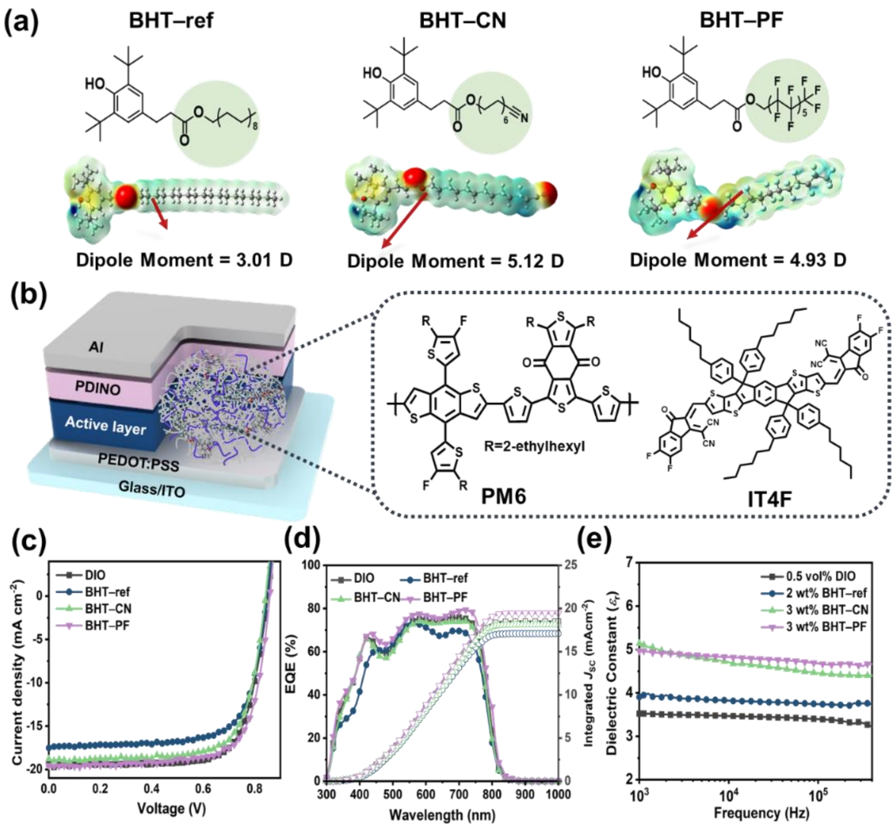

Figure 3.2.1. (a) Antioxidant additive molecular structures. (b) PM6 and IT4F molecular structures and device structures. (c) PM6:IT4F device *J-V* curves with additives. (d) The optimized devices' EQE spectra and calculated J_{SC}. (e) The dielectric constant of the composite film with additives was determined using capacitance measurements.

3.2.3 Device Properties

We fabricated PM6:IT4F devices with a standard structure to explore the effect of BHT-based additives on photovoltaic cell performance. (see **Figure 3.2.1b)** DIO is universally acknowledged as the most effective solvent additive for increasing the PCE of the PM6:IT4F system. Using the previously published optimal conditions, we thoroughly optimized the PM6:IT4F OSC as a reference device.[28] The optimal PCE for the device processed with DIO was 12.11%, with a V_{OC} of 0.855 V, J_{SC} of 19.23 mA cm^{-2}, and FF of 73.71%. Then we started looking at the effects of different weight percentages of BHT-based additives on the performance of OSC while maintaining the ideal PM6:IT4F ratio and annealing process. **Figure 3.2.1c** depicts the representative *J-V* characteristics of the devices and **Table 3.2.1** summarizes the relevant parameters. **Table 3.2.4** shows all of thstudiesdy examined the photovoltaic characteristics as a function of BHT-based antioxidant additive concentrations. In comparison to the control device treated with DIO, the addition of BHT–ref and BHT–CN to the active layer lowered performance, but the inclusion of the optimum BHT–PF enhanced PCE (up to 12.79%) due mostly to an increase in J_{SC}. Notably, the optimal PCEs were achieved with 3.0% (w/w) BHT–PF and BHT–CN additions and with 2.0% (w/w) BHT–ref additive. **Figure 3.2.1d** shows the EQE spectra of PM6:IT4F devices with additives, which show a reasonable margin of error with the J_{SC} from the *J-V* curve.

Table 3.2.1. Photovoltaic performance of PM6:IT4F systems with appropriate antioxidant concentrations as the additive under AM 1.5G light.

Additive	***Voc*** **[V]**	***Jsc*** **[mA cm^{-2}]**	**FF** **[%]**	**PCE** $^{a)}$ **[%]**
0.5 vol% DIO	0.854 (0.851 ± 0.002)	19.22 (18.97 ± 0.45)	73.72 (73.19±0.28)	12.12 (11.81 ± 0.31)
2 wt% BHT–ref	0.835 (0.835 ± 0.003)	17.54 (17.31 ± 0.40)	71.20 (69.88 ± 0.31)	10.43 (10.38 ± 0.32)
3 wt% BHT–CN	0.854 (0.852 ± 0.002)	18.60 (18.24 ± 0.38)	73.23 (72.65 ± 0.27)	11.63 (11.29 ± 0.47)
3 wt% BHT–PF	0.858 (0.856 ± 0.004)	20.27 (20.02 ± 0.31)	73.47 (72.73± 0.22)	12.78 (12.44 ± 0.30)

a) The numbers in parentheses are the averages of more than 16 devices.

To get a better understanding of the processes behind the influence of BHT-based additives on photovoltaic performance, we first used an impedance analyzer to determine the ε_r of the films with each of the optimal additive concentrations (**Figure 3.2.1e**). The measurement was carried out in the dark at low frequencies of 103–106 Hz, with the active layer completely depleted.[29] In the low-frequency regime, the ε_r values are in the order BHT-PF (~4.8) ≥ BHT–CN (~4.7) > BHT–ref (~3.8) > DIO (~3.5) suggesting that the polar PF and CN alkyl chains contribute to relatively improved dielectric characteristics inside the active layer. This may result in enhanced dipolar polarization of the excited state at the donor/acceptor interface, as well as delocalization of charge transfer states in the active layer; hence, BHT–PF and BHT–CN-processed devices should exhibit enhanced charge transport and recombination dynamics.[30]

Then, using the SCLC method, we determined the μ_h and μ_e in the devices, as seen in **Figure 3.2.2a and b**, with the findings reported in **Table 3.2.2.**[31] The μ_h/μ_e ratio of the blended film with DIO was 0.81. The μ_e and μ_h values were 5.70×10^{-4} and 4.60×10^{-4} cm^2 V^{-1} s^{-1}, respectively. Both μ_e and μ_h values reduced by roughly an order of magnitude for the BHT-processed film (3.69×10^{-5} and 6.99×10^{-5} cm^2 V^{-1} s^{-1}), although the BHT–PF- and BHT–CN-processed films exhibited a modest decrease ($\mu_e = 1.80 \times 10^{-4} - 1.34 \times 10^{-5}$ cm^2 V^{-1} s^{-1} and $\mu_h = 2.22 \times 10^{-4}$–$2.18 \times 10^{-5}$ cm^2 V^{-1} s^{-1} The extent to which the μ_h/μ_e ratio are balanced is consistent with the FF trend in the OSCs.

Table 3.2.2. Hole and electron mobility of PM6:IT4F systems with appropriate antioxidant concentrations.

Additive	Hole mobility [μ_h] ($cm^2\ V^{-1}\ s^{-1}$)	Electron mobility [μ_e] ($cm^2\ V^{-1}\ s^{-1}$)	μ_h/μ_e
0.5 vol% DIO	4.61 x 10^{-4}	5.70 x 10^{-4}	0.81
2 wt% BHT–ref	6.98 x 10^{-5}	3.68 x 10^{-5}	1.89
3 wt% BHT–CN	2.17 x 10^{-4}	1.35 x 10^{-4}	1.63
3 wt% BHT–PF	2.23 x 10^{-4}	1.80 x 10^{-4}	1.23

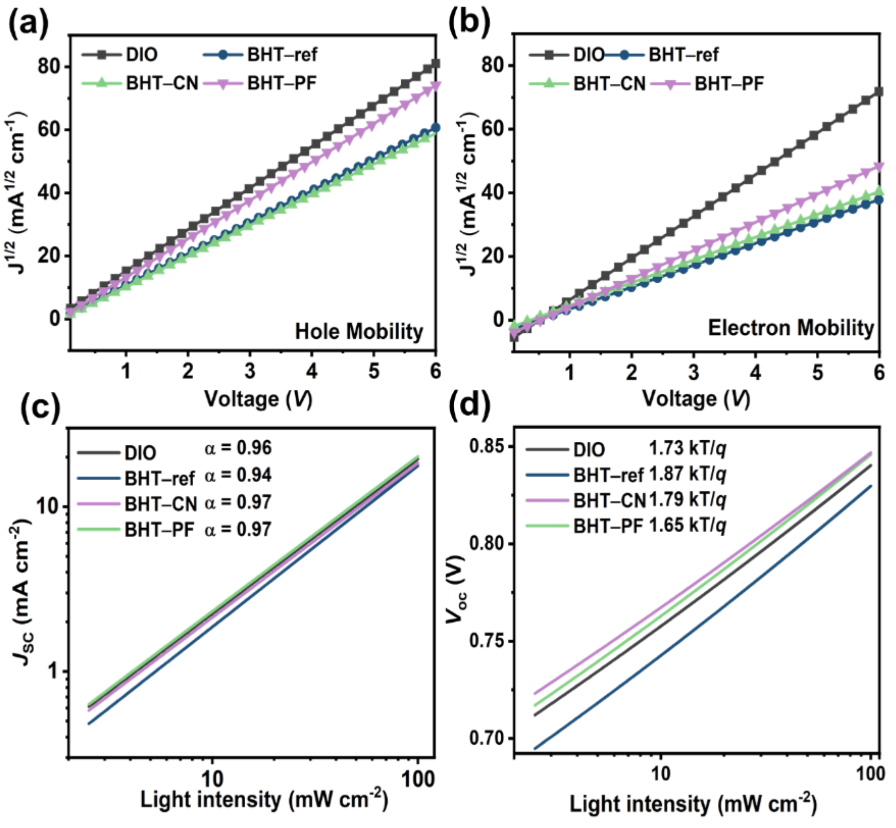

Figure 3.2.2. PM6:IT4F blend film mobility with different additives, (a) hole-only mobility and (b) electron-only mobility. The optimized devices' light intensity dependence on (c) J_{SC} and (d) V_{OC}.

Figures 3.2.2c and **d** show the results of describing the dependence of the *J-V* characteristics on the light intensity, which was used to investigate the recombination behavior of the devices. The BHT-processed blend film shows a lesser slope ($\alpha = 0.94$) than DIO-processed blend film ($\alpha = 0.96$), showing an increase in bimolecular recombination loss.[32-34] In contrast, there was a minor increase in slope (α = 0.97), which is significantly connected with the high dielectric property generated by the presence of BHT–PF and BHT–CN, as predicted above. **Figure 3.2.2d** depicts that the slopes of V_{OC} vs the logarithm of I are 1.65, 1.79, 1.87, and 1.73 kT/q for BHT–PF, BHT–CN, BHT–ref, and DIO, respectively. These results indicate that the BHT–PF-processed device has the smallest trap-assisted recombination loss, coinciding with its observed minimal V_{OC} fluctuation.

To further comprehend the impact the charge dynamics of the OSC system, the J_{ph} on the V_{eff} was also measured.[32-34] Under short-circuit conditions, the J_{ph}/J_{sat} values (**Figure 3.2.7** and **Table 3.2.5**) - that are largely exciton dissociation efficacy - were manifested in the sequence of BHT–ref < DIO < BHT–CN < BHT–PF films, implying that the effective charge extraction and dissociation occur in the BHT–PF-processed device. The factors stated above explain why the BHT-PF-processed device has superior photovoltaic performance.

3.2.4 Morphological Properties

In this investigation, GIWAXS, AFM, and TEM were utilized to examine the molecular packing characteristics and morphology of blend films as a function of the solvent or solid additives. As seen in **Figure 3.2.8** by a lamellar packing (100) and a strong π–π stacking (010) reflection peak in the out-of-plane direction, all blend films have a preferred face-on molecular packing orientation. The BHT-PF-processed film, on the other hand, showed not only shorter lamellar d-spacing (CCL_{100}) and π–π stacking distances (CCL_{010}), but also moderate decrease in crystallite coherence lengths. (See **Table 3.2.6**). This research illustrates that employing BHT–PF in active layer materials increases dense packing and smaller crystallites.[35]

Figure 3.2.3 shows AFM images of a blend film, which not only reveal similar, fine phase separated networks throughout the film, but also reveal that the roughness of the BHT-PF treated film predicts the development of smaller crystallite sizes. In addition, the TEM pictures confirmed the relatively uniform bulk characteristics in each blend case (**Figure 3.2.9**). The smoother and smaller domain sizes obtained by the inclusion of BHT–PF likely account for much of the increase in J_{SC} of the device with BHT–PF, as this allowed for more effective dissociation of excitons into free carriers over a larger interfacial area between the donor and acceptor.

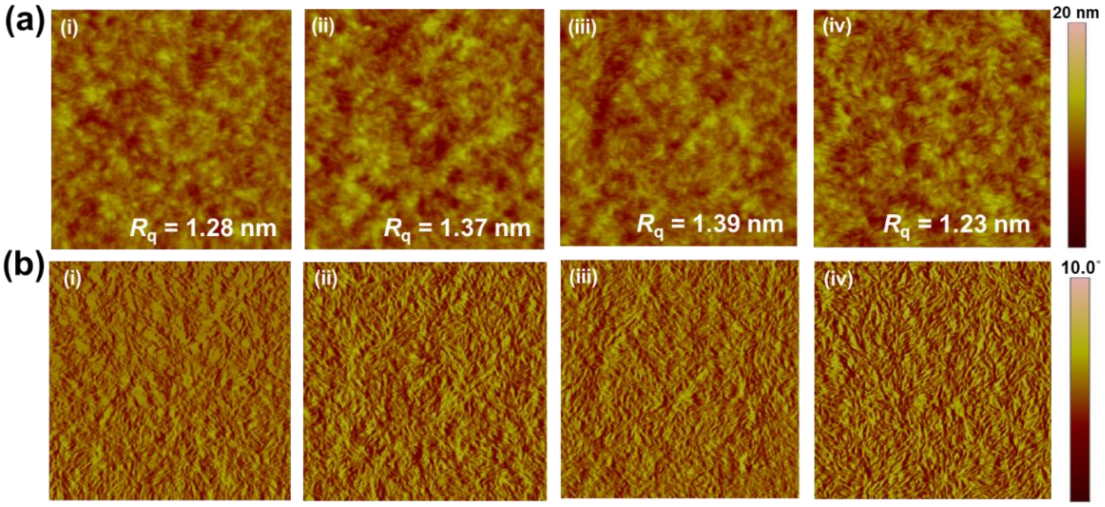

Figure 3.2.3. The AFM pictures for (a) height and (b) phase along with the corresponding *R*q of the blend films containing the following additives: (i) DIO, (ii) BHT–ref, (iii) BHT–CN, and (iv) BHT–PF.

3.2.5 Photo-Oxidation Stability

Following a thorough investigation of the additives' effects on morphology and photovoltaic characteristics, we began investigating the role of antioxidant polymer additives vs DIO in the stability of the PM6:IT4F model, which was the prime priority of our study. Optimized OSCs were aged for 200 hours in a dry, inert atmosphere at room temperature under the continuous illumination of a LED 1sun simulator. **Figure 3.2.10** depicts the *J*–*V* curves as a function of the stressing time, and **Tables 3.2.7–3.2.10** summarize the pertinent parameters. The PCE of the DIO-processed control device had deteriorated by more than 52% of its original value after 200 hours, whereas the PCE of the devices containing BHT-based antioxidant additives was substantially more stable, particularly for the BHT–PF-processed device, which had just 34% PCE degradation.

We expanded the test of unencapsulated OSCs' long-term stability in ambient conditions to include H_2O and O_2. As demonstrated in **Figure 3.2.4**, when exposed to light and ambient conditions, all unencapsulated devices degraded much quicker than those in a dry N_2 environment. **Figure 3.2.11–3.2.14** and **Table 3.2.11** describe the information and statistics. This suggests that atmospheric H_2O and O_2 are primarily accountable for the photo-oxidative destruction of OSCs. To get a better understanding of the additive's effect, we also evaluated the device's stability without the additive, which indicated a 63% decrease in PCE (from 10.41% to 3.89%). (see **Figure 3.2.15** and **Table 3.2.12** for photovoltaic parameters in detail) It is possible that the formation of iodine radicals and residual problems account for the observed more severe reduction in PCE in the DIO-processed device (83% PCE degradation under the same conditions).[36-38] After 60 minutes of exposure to ambient conditions with light, however, great stability was detected in the presence of BHT-based antioxidant additives; specifically, the usage of BHT–PF significantly stabilized the device (33 % PCE loss over the 60 min). Furthermore, we constructed OSCs with an inverted structure to better understand the influence of the BHT–PF additive on device stability. **Figure 3.2.16** and **Table 3.2.13–3.7.14** demonstrate that the inverted OSC with BHT–PF additive exhibited lower PCE loss (17%) than the DIO-contained inverted OSC (61% PCE loss) after 60 min at room temperature. As a consequence, the BHT unit is expected to serve a significant role in inhibiting the radical breakdown pathway of active materials, hence retaining performance. Notably, the PCE degradation of the devices is mostly caused by a significant decrease in the J_{SC}; the changing trend in the PCE and J_{SC} values can be clearly seen by comparing the results of the BHT–PF- and DIO-processed devices (see **Figure 3.2.5a and b**).

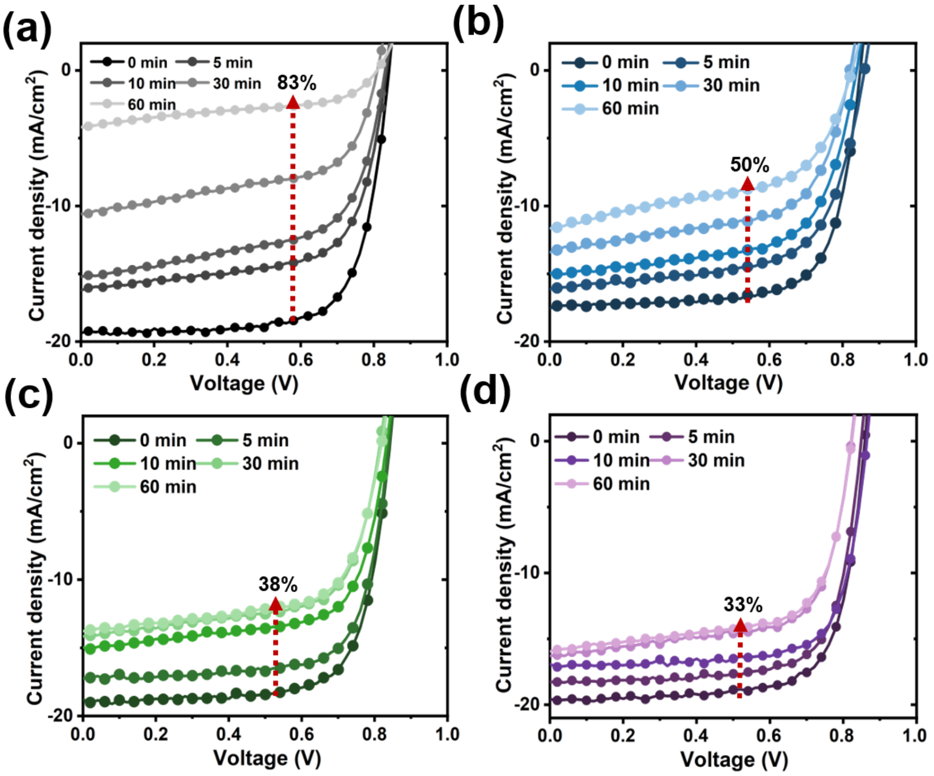

Figure 3.2.4. *J-V* curves exposed to light and ambient conditions within various time intervals for the (a) DIO, (b) BHT–ref, (c) BHT–CN, and b) BHT–PF systems.

As demonstrated in **Figure 3.2.5c**, the DIO-processed blend film exhibits severe photobleaching when exposed to ambient conditions, but films containing BHT-based additives photo-oxidize significantly less. We investigated the development of the absorption intensity of active materials-only blend films using UV-Vis absorption spectra as evidence of photobleaching suppression in blend films using BHT-based additives (**Figure 3.2.17**). Furthermore, the FT-IR analysis of the films (**Figure 3.2.18–3.2.19**) demonstrates that after 1 hour of irradiation, the peak intensity of the signals in pure IT4F films (-CH_2 at 2855 cm^{-1} and 2917 cm^{-1}, -CN at 2219 cm^{-1}, and -C=C at 1538 cm^{-1}) not only begins to decrease, but a broad band in the range between 3400 cm^{-1} and 3100 cm^{-1} corresponding to -OH groups. This suggests that the IT4F π-conjugated system has been destroyed (**Figure 3.1.18**). Furthermore, after one hour of irradiation, the intensity in pure PM6 films (-C=C in the aromatic ring at 1430~1530 cm^{-1} and -CH_2 at 2926 and 2854 cm^{-1}) reduced considerably (**Figure 3.1.19**). In contrast, after being exposed to the same radiation, films that have been optimized with BHT-PF in both IT4F and PM6 show almost unmodified FT-IR spectra. This conclusion implies that the reduced J_{SC} throughout the stability test is mostly the result of degradation of the active materials rather than the PDINO interlayer or/and the Al metal electrode. Notably, the BHT-PF film decreased band intensity loss in the region of 550-650 nm, which corresponds to PM6 donor polymer absorption, suggesting a significant photo-oxidative stabilizing influence on the donor species within the blend system. In addition, after 60 min of exposure to light and ambient conditions, the blend film with BHT-based additives revealed the same uniform, smooth morphology as the initial case, whereas the TEM images of the DIO-processed film exhibited aggressive, coarse textures (**Figure 3.2.5d**). This suggests that the introduction of BHT-based additives may also assist in maintaining the mix morphology under ambient and light conditions, hence improving the stability of the devices.

After finding that the BHT-PF additive had the most effective stabilizing additive effect in the previous section, we widened our long-term stability test to include additional systems, including J71:ITIC and PM6:Y6, under light and ambient conditions. First, the J71:ITIC (with 0.5 vol% DIO) and PM6:Y6 (with 0.5 vol% 1-CN) control devices were yielded appropriate PCE values of 10.40% and 15.52 %, respectively. On the other hand, the optimized OSCs with BHT–PF (3.0% (w/w)) yielded PCE values of 10.70% for J71:ITIC and 14.59% for PM6:Y6 that were comparable to the PCE values obtained in the optimized OSCs with each of the acceptable solvent additives. In contrast to the PCE losses reported for both unencapsulated devices treated with 1-CN and DIO, the comparable BHT–PF-processed devices exhibited extraordinary long-term stability (from the initial PCEs of 7.70% for J71:ITIC and 10.74% for PM6:Y6; 30.8%–24.9% PCE degradation). **Figure 3.2.6** and **Table 3.2.3** depict the variations in *J*–*V* curves and photovoltaic parameters as a function of exposure time. These findings show that by adding BHT–PF to different OSC platforms, photo-oxidation stability may be increased even in severe conditions, and that initial PCEs can be achieved that are competitive with the best values obtained using OSCs without the solvent additive.

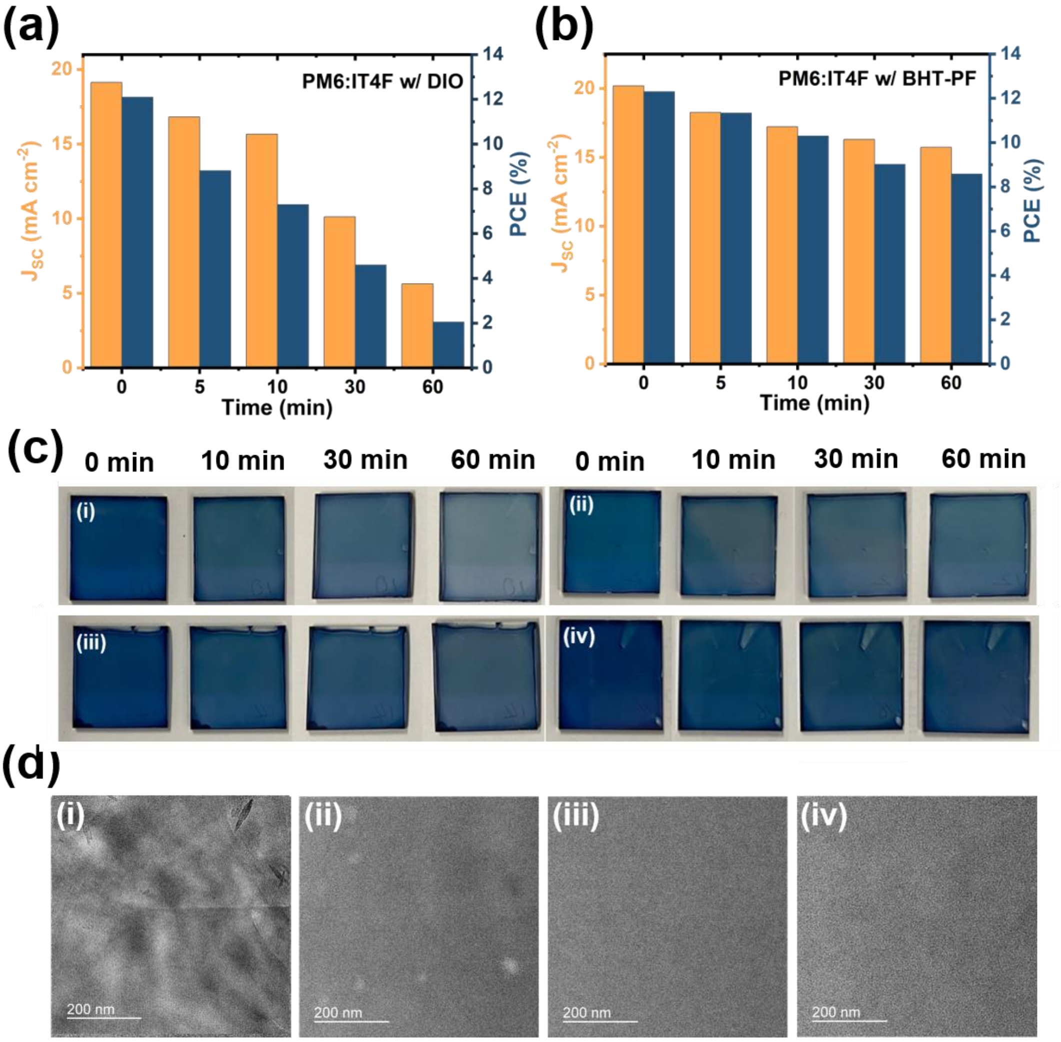

Figure 3.2.5. Histograms of PCE and J_{SC} parameters for (a) DIO and (b) BHT–PF as a function of time. (c) Photographs of PM6:IT4F blend films at various periods and d) TEM images after photoirradiation with the following additives: (i) DIO, (ii) BHT–ref, (iii) BHT–CN, and (iv) BHT–PF.

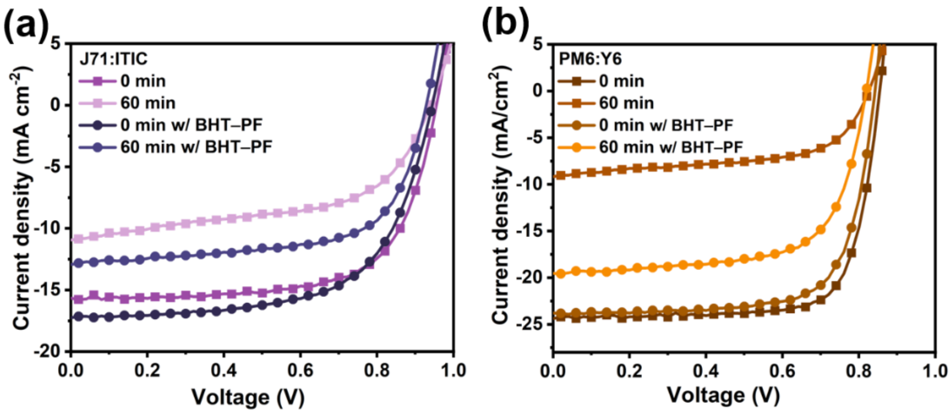

Figure 3.2.6. *J-V* curves of various OPV systems for (a) J71:ITIC and (b) PM6:Y6 at 0 min and 60 min under O_2 and ambient conditions.

Table 3.2.3. Photovoltaic characteristics of the J71:ITIC and PM6:Y6 systems using BHT–PF as an additive.

	Time [min]	**BHT–PF**	***V*oc [V]**	***J*sc [mA cm^{-2}]**	**FF [%]**	**PCE [a] [%]**
J71:ITIC	0 min	X	0.945 (0.949 ± 0.003)	16.37 (15.84 ± 0.31)	67.08 (67.20 ± 0.13)	10.40 (10.10 ± 0.17)
	60 min	X	0.940 (0.943 ± 0.004)	10.94 (10.09 ± 0.51)	54.36 (52.92 ± 0.27)	5.59 (5.04 ± 0.33)
	0 min	O	0.936 (0.934 ± 0.003)	16.86 (16.79 ± 0.18)	67.81 (65.67 ±0.32)	10.70 (10.30 ± 0.24)
	60 min	O	0.929 (0.929 ± 0.004)	12.93 (12.87 ± 0.12)	64.10 (64.38 ± 0.29)	7.70 (7.56 ± 0.25)
PM6:Y6	0 min	X	0.854 (0.852 ± 0.004)	24.11 (23.93 ± 0.26)	75.48 (75.07 ± 0.36)	15.52 (15.30 ± 0.21)
	60 min	X	0.826 (0.825 ± 0.001)	9.16 (8.67 ± 0.45)	58.47 (57.73 ± 0.26)	4.43 (4.14 ± 0.23)
	0 min	O	0.841 (0.839 ± 0.005)	23.80 (23.60 ± 0.61)	72.73 (72.31 ± 0.14)	14.59 (14.26 ± 0.33)
	60 min	O	0.820 (0.817 ± 0.004)	19.53 (19.67 ± 0.29)	67.11 (65.43 ± 0.32)	10.74 (10.51 ± 0.22)

[a] The numbers in parentheses are the averages of more than 12 devices.

3.2.6 Conclusion

Finally, we investigated the impact that antioxidant additives had on the photovoltaic properties and photo-oxidation stability of a PM6:IT4F-based host system. We observed that employing the optimal concentration of BHT–CN and BHT–PF additives leads in device performance that is comparable to, if not better than, the optimum control OSC with the DIO solvent addition. Notably, the BHT-PF-processed OSC showed superior long-term photo-oxidation stability; specifically, in the unencapsulated device stability test under the combined stressors, the BHT-PF-processed OSC retained 67% of the original PCE, as opposed to the DIO-processed control, which retained 33%. (83% PCE deterioration after 60 min). These improved device performances in terms of PCE and stability are principally due to the improved dielectric and radical scavenging capabilities of the BHT–PF-embedded active layer. Furthermore, we show that the addition of BHT–PF significantly enhances the long-term photo-oxidation stability of the other OSC platforms (PM6:Y6 and J71:ITIC). According to our findings, adding BHT-PF to OSCs allows for photo-oxidation stability to be implemented throughout a variety of different OSCs without significantly affecting the original optimal PCE values obtained from OSCs modified with suitable solvent additives.

3.2.7 Supporting Information

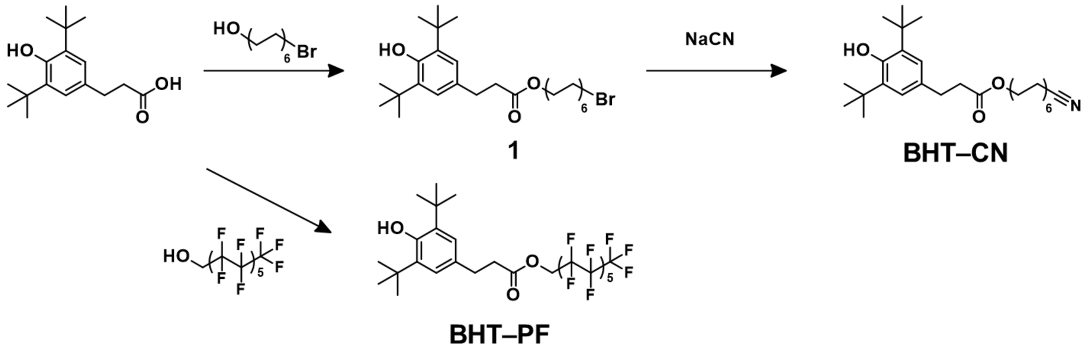

Scheme 3.2.1. Routes of synthesis for BHT–CN and BHT–PF.

Table 3.2.4. Summary of device parameters for PM6:IT4F binary devices comprising varying weight percentages of BHT-based additives under 1.5G AM irradiation at 100 mW cm^{-2}.

Additives	V_{OC} **[V]**	J_{SC} **[mA cm^{-2}]**	**FF [%]**	**PCE $^{a)}$ [%]**
1 wt% BHT	0.852 (0.845 ± 0.003)	18.32 (17.69 ± 0.35)	66.0 (66.6 ± 0.15)	10.30 (9.96 ± 0.33)
2 wt% BHT	0.836 (0.836 ± 0.003)	17.53 (17.32 ± 0.40)	71.21 (69.89 ± 0.31)	10.43 (10.39 ± 0.32)
3 wt% BHT	0.845 (0.848 ± 0.008)	17.42 (17.12 ± 0.40)	70.40 (69.8 ± 0.13)	10.40 (10.31 ± 0.32)
4 wt% BHT	0.840 (0.838 ± 0.005)	17.34 (16.98 ± 0.31)	68.12 (66.5 ± 0.12)	9.92 (9.76 ± 0.35)
5 wt% BHT	0.839 (0.833 ± 0.006)	17.01 (16.54 ± 0.19)	67.06 (64.2 ± 0.37)	9.56 (9.27 ± 0.15)
1 wt% BHT–CN	0.853 (0.853 ± 0. 005)	17.61 (17.50 ±0.38)	67.90 (66.70 ±0.68)	10.52 (9.91 ± 0.25)
2 wt% BHT–CN	0.844 (0.838 ± 0.008)	18.22 (18.10 ±0.28)	71.80 (71.50 ±0.11)	11.14 (10.70 ± 0.43)
3 wt% BHT-CN	0.855 (0.853 ± 0.002)	18.60 (18.25 ± 0.38)	73.24 (72.65 ± 0.27)	11.64 (11.30 ± 0.47)
4 wt% BHT–CN	0.844 (0.844 ± 0.001)	17.70 (17.60 ± 0.45)	71.70 (71.00 ± 0.37)	10.70 (10.57 ± 0.21)
5 wt% BHT–CN	0.845 (0.836 ±0.006)	17.30 (17.11 ±0.52)	66.90 (67.50 ±0.46)	9.81 (9.63 ± 0.48)
1 wt% BHT–PF	0.851 (0.850 ± 0.002)	18.57 (18.23 ± 0.34)	70.23 (68.78 ± 0.33)	11.10 (10.66 ± 0.28)
2 wt% BHT–PF	0.854 (0.850 ± 0.002)	19.40 (19.27 ± 0.45)	74.40 (74.20 ± 0.12)	12.30 (12.17 ± 0.41)
3 wt% BHT-PF	0.859 (0.857 ± 0.004)	20.27 (20.01 ± 0.31)	73.48 (72.74± 0.22)	12.79 (12.45 ± 0.30)
4 wt% BHT–PF	0.848 (0.846 ± 0.003)	19.01 (18.65 ± 0.23)	72.12 (70.31 ± 0.29)	11.62 (11.10 ± 0.33)
5 wt% BHT–PF	0.844 (0.840 ± 0.005)	18.63 (18.13 ± 0.22)	70.76 (71.12 ± 0.41)	11.12 (10.83 ± 0.17)

$^{a)}$ The values in the parentheses are the average values obtained from over 12 devices.

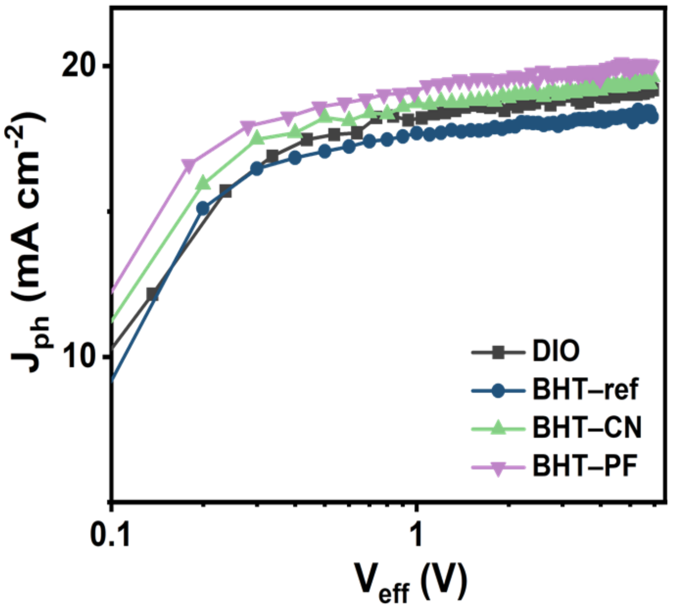

Figure 3.2.7. Plots of J_{ph} versus V_{eff} for PM6:IT4F with additives.

Table 3.2.5. Probabilities of charge extraction from PM6:IT4F devices with additives.

Additive	**Exciton dissociation probability (%)**
0.5 vol% DIO	96.10
2 wt% BHT–ref	94.40
3 wt% BHT–CN	96.19
3 wt% BHT–PF	96.28

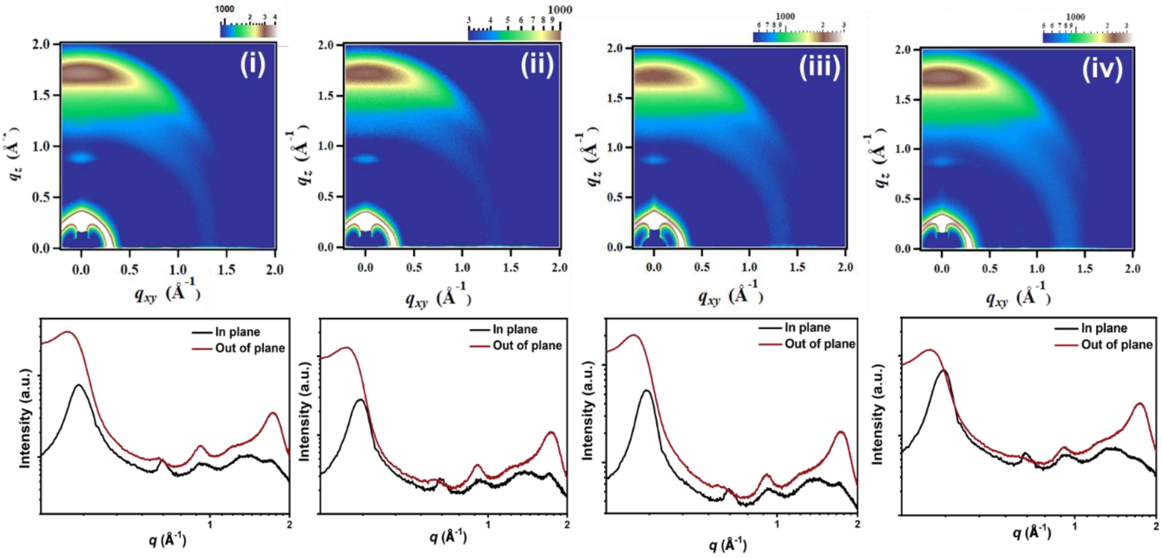

Figure 3.2.8. The GIWAXS pattern on blend film with additives (top) and the corresponding line-cut profiles (bottom) (i) DIO, (ii) BHT–ref, (iii) BHT–CN, (iv) BHT–PF.

Table 3.2.6. Out-of-plane and in-plane lattice parameters for binary blend films active layer films with and without BHT-based additives.

Additive	**Out-of-Plane** **π-π stacking cell axis *(010)***				**In-Plane** **Unit cell long axis *(100)***			
	q (Å^{-1})	***d*-spacing (Å)**	**FWHM (Å^{-1})**	**Coherence length (Å)**	**q (Å^{-1})**	***d*-spacing (Å)**	**FWHM (Å^{-1})**	**Coherence length (Å)**
0.5vol% DIO	1.738	3.615	0.247	23.17	0.320	19.61	0.0575	98.38
2wt% BHT–ref	1.751	3.589	0.238	24.05	0.325	19.34	0.0560	101.02
3wt% BHT–CN	1.741	3.609	0.246	23.26	0.325	19.41	0.0570	99.25
3wt% BHT–PF	1.744	3.602	0.257	22.27	0.327	19.24	0.0627	90.23

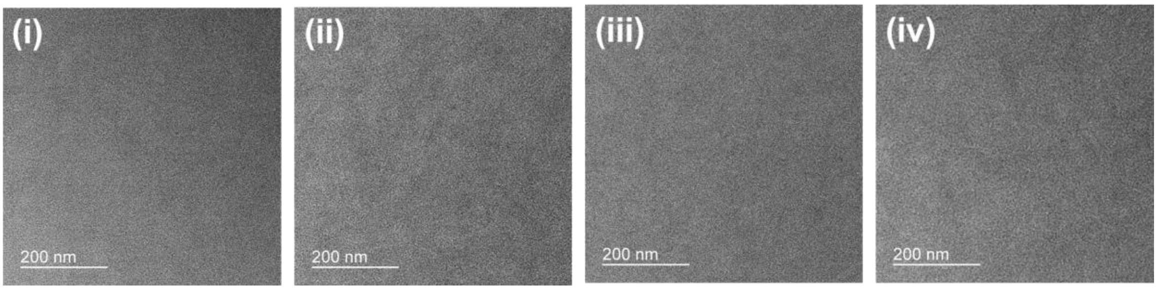

Figure 3.2.9. TEM images of PM6:IT4F blend films containing various additives. (i) DIO, (ii) BHT–ref, (iii) BHT–CN, and (iv) BHT–PF.

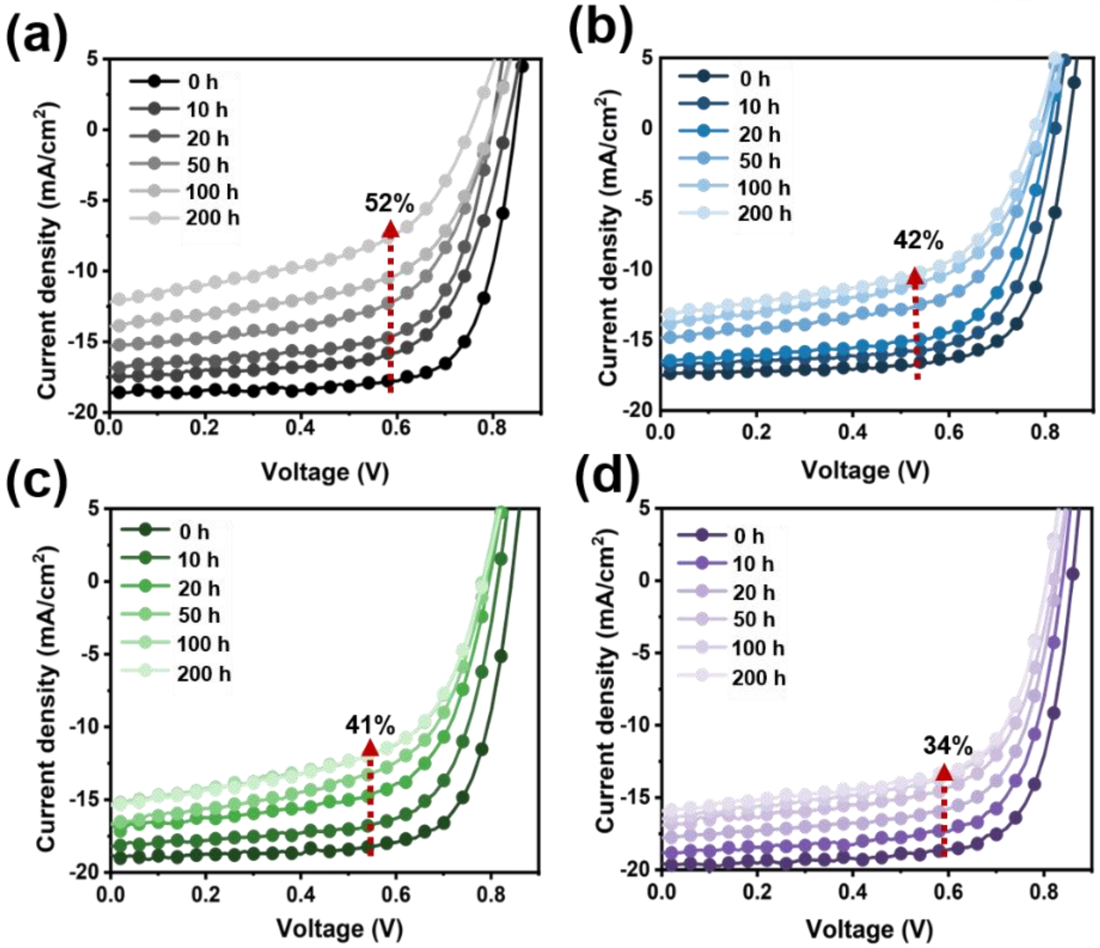

Figure 3.2.10. *J-V* curves exposed to light and N_2 environment over various time period of (a) DIO, (b) BHT–ref, (c) BHT–CN, and (d) BHT–PF systems.

Table 3.2.7. Device properties of PM6:IT4F devices with DIO additive under light and N_2 conditions with different degradation times are summarized.

Time [h]	V_{OC} [V]	J_{SC} [mA cm^{-2}]	FF [%]	PCE [a] [%]
10	0.825 (0.820 ± 0.005)	17.70 (17.28 ± 0.42)	69.10 (68.55 ± 0.55)	10.09 (9.77 ± 0.32)
20	0.807 (0.788 ± 0.003)	16.50 (16.80 ± 0.31)	66.10 (65.99 ± 0.11)	8.80 (8.71 ± 0.11)
50	0.792 (0.777 ± 0.006)	15.50 (15.42 ± 0.10)	60.41 (59.78 ± 0.63)	7.42 (7.27 ± 0.15)
100	0.783 (0.773 ± 0.005)	14.27 (13.95 ± 0.32)	55.90 (55.36 ± 0.54)	6.24 (5.96 ± 0.28)
200	0.767 (0.767 ± 0.003)	13.72 (13.26 ± 0.45)	54.81 (54.47 ± 0.34)	5.76 (5.34 ± 0.42)

[a] The values in the parentheses are the average values obtained from over 12 devices.

Table 3.2.8. Device properties of PM6:IT4F devices with BHT–ref additive under light and N_2 conditions with different degradation times are summarized.

Time **[h]**	V_{OC} **[V]**	J_{SC} **[mA cm^{-2}]**	**FF** **[%]**	**PCE** [a] **[%]**
10	0.823 (0.820 ± 0.003)	17.59 (17.44 ± 0.14)	64.52 (63.96 ± 0.22)	9.36 (9.15 ± 0.21)
20	0.819 (0.816 ± 0.003)	16.53 (16.11 ± 0.42)	61.33 (59.87 ± 0.41)	8.31 (7.87 ± 0.19)
50	0.810 (0.803 ± 0.005)	15.23 (14.86 ± 0.37)	58.48 (59.10 ± 0.62)	7.21 (7.04 ± 0.17)
100	0.804 (0.787 ± 0.004)	14.82 (14.50 ± 0.32)	57.83 (56.24 ± 0.36)	6.91 (6.41 ± 0.43)
200	0.782 (0.783 ± 0.002)	14.14 (13.95 ± 0.19)	54.73 (55.36 ± 0.63)	6.05 (6.01 ± 0.14)

[a] The values in the parentheses are the average values obtained from over 12 devices.

Table 3.2.9. Device properties of PM6:IT4F devices with BHT–CN additive under light and N_2 conditions with different degradation times are summarized.

Time **[h]**	V_{OC} **[V]**	J_{SC} **[mA cm^{-2}]**	**FF** **[%]**	**PCE** [a] **[%]**
10	0.833 (0.831 ± 0.002)	18.21 (18.01 ± 0.20)	70.88 (68.70 ± 0.22)	10.75 (10.28 ± 0.47)
20	0.810 (0.810 ± 0.003)	17.92 (17.94 ± 0.12)	68.44 (68.35 ± 0.10)	10.12 (9.93 ± 0.19)
50	0.809 (0.805 ± 0.004)	17.61 (17.45 ± 0.16)	65.27 (64.61 ± 0.65)	9.30 (9.08 ± 0.22)
100	0.791 (0.792 ± 0.001)	16.94 (16.86 ± 0.10)	63.61 (63.60 ± 0.11)	8.56 (8.49 ± 0.09)
200	0.780 (0.780 ± 0.002)	15.51 (15.51 ± 0.22)	56.24 (55.50 ± 0.44)	6.85 (6.71 ± 0.14)

[a] The values in the parentheses are the average values obtained from over 12 devices.

Table 3.2.10. Device properties of PM6:IT4F devices with BHT–PF additive under light and N_2 conditions with different degradation times are summarized.

Time **[h]**	***V***V_{OC} **[V]**	J_{SC} **[mA cm^{-2}]**	**FF** **[%]**	**PCE** $^{a)}$ **[%]**
10	0.852 (0.850 ± 0.002)	19.56 (19.37 ± 0.20)	73.32 (72.77 ± 0.55)	12.21 (11.98 ± 0.23)
20	0.836 (0.835 ± 0.001)	18.78 (18.44 ± 0.34)	71.24 (69.74 ± 0.35)	11.10 (10.74 ± 0.36)
50	0.826 (0.824 ± 0.002)	17.78 (17.41 ± 0.36)	67.24 (66.32 ± 0.62)	9.88 (9.51 ± 0.37)
100	0.816 (0.816 ± 0.001)	16.81 (16.50 ± 0.31)	64.22 (63.87 ± 0.36)	8.82 (8.60 ± 0.22)
200	0.813 (0.810 ± 0.003)	16.43 (16.22 ± 0.21)	63.54 (63.23 ± 0.31)	8.47 (8.30 ± 0.17)

[a)] The values in the parentheses are the average values obtained from over 12 devices.

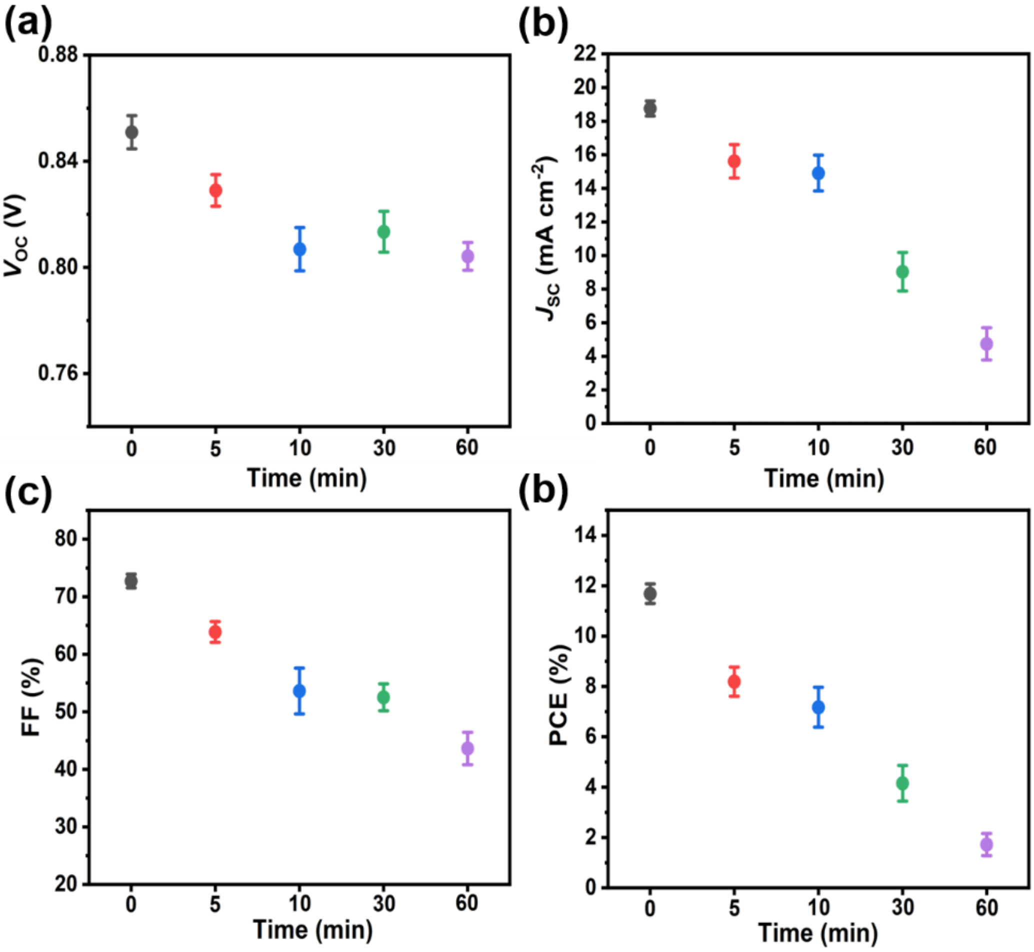

Figure 3.2.11. The following changes occurred in the PM6:IT4F with 0.5 vol% DIO devices: (a) V_{OC}, (b) J_{SC}, (c) FF, and (d) PCE. The error bars reflect one standard deviation over a set of 12 devices.

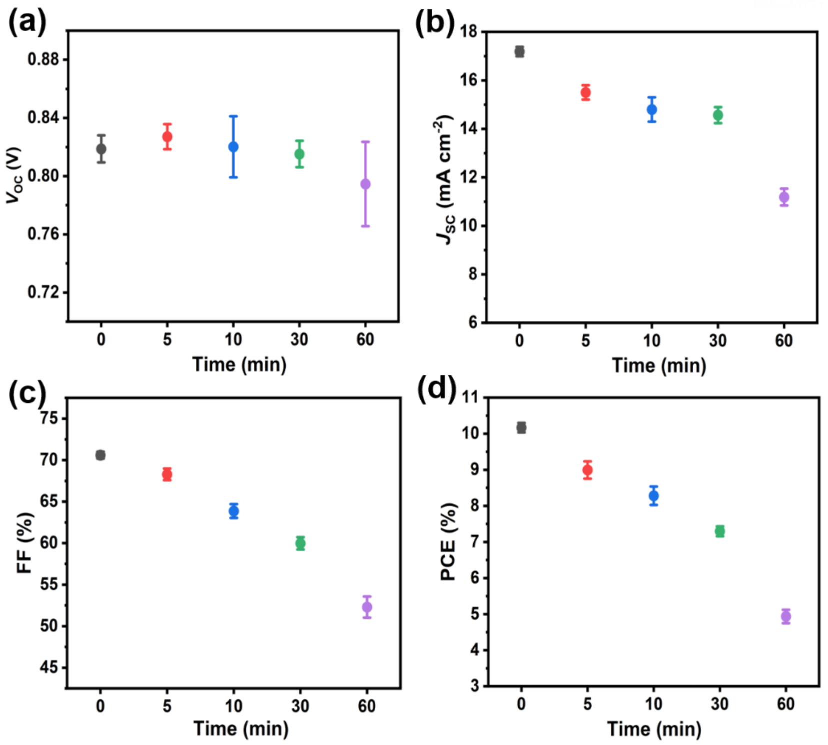

Figure 3.2.12. The following changes occurred in the PM6:IT4F with 2 wt% BHT–ref devices: (a) V_{OC}, (b) J_{SC}, (c) FF, and (d) PCE. The error bars reflect one standard deviation over a set of 12 devices.

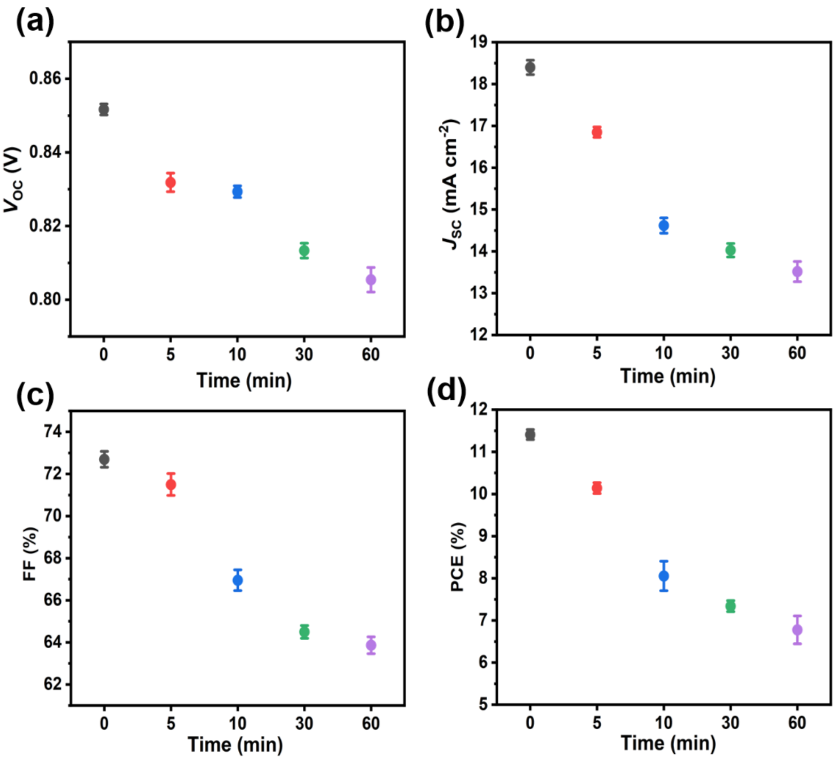

Figure 3.2.13. The following changes occurred in the PM6:IT4F with 3 wt% BHT–CN devices: (a) V_{OC}, (b) J_{SC}, (c) FF, and (d) PCE. The error bars reflect one standard deviation over a set of 12 devices.

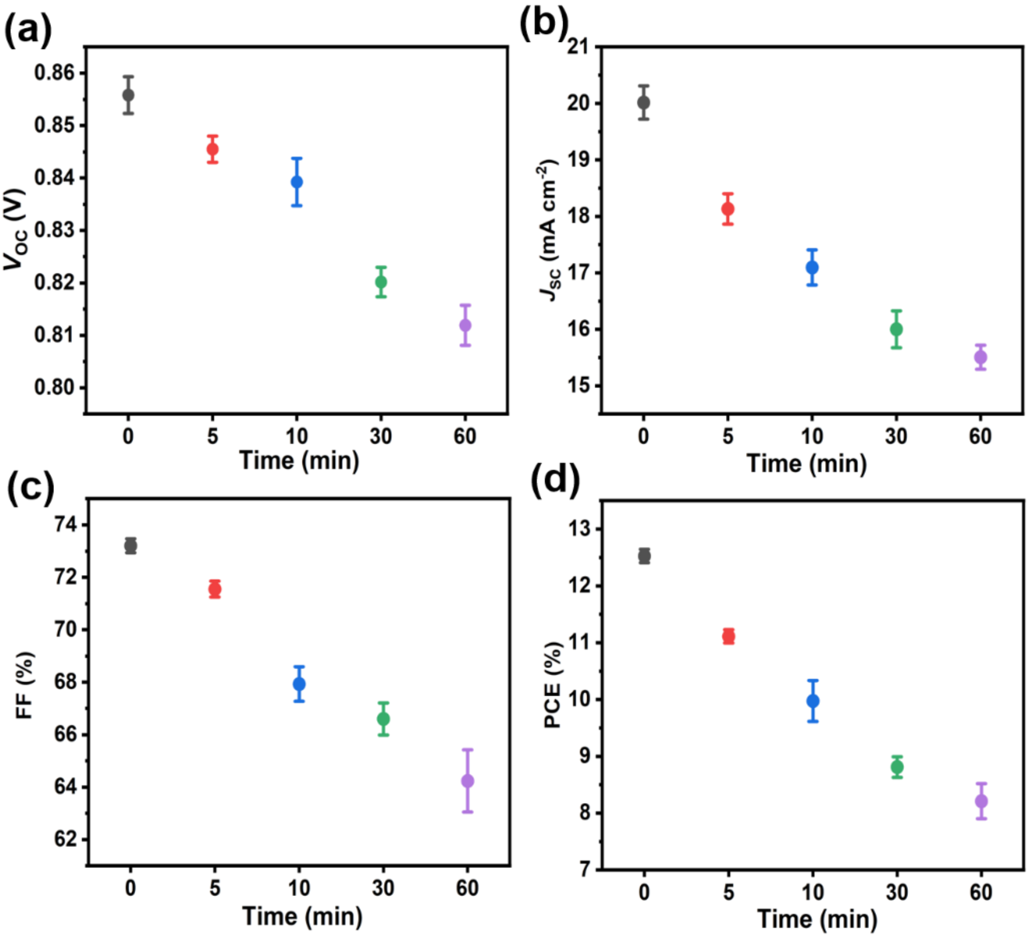

Figure 3.2.14. The following changes occurred in the PM6:IT4F with 3 wt% BHT–PF devices: (a) V_{OC}, (b) J_{SC}, (c) FF, and (d) PCE. The error bars reflect one standard deviation over a set of 12 devices.

Table 3.2.11. Summary of device parameters of PM6:IT4F devices with additives under light and ambient conditions with varying degradation times.

Time [min]	Additives	V_{OC} [V]	J_{SC} [mA cm^{-2}]	FF [%]	PCE a) [%]
5	0.5 vol% DIO	0.834 (0.832 ± 0.004)	16.42 (16.20 ± 0.20)	64.78 (64.40 ± 0.21)	8.81 (8.75 ± 0.19)
10	0.5 vol% DIO	0.817 (0.803 ± 0.005)	15.66 (15.68 ± 0.45)	58.80 (54.10 ± 0.41)	7.52 (6.82 ± 0.35)
30	0.5 vol% DIO	0.812 (0.809 ± 0.005)	10.12 (10.14 ± 0.46)	55.93 (54.30 ± 0.24)	4.60 (4.26 ± 0.26)
60	0.5 vol% DIO	0.806 (0.804 ± 0.002)	5.63 (5.48 ± 0.33)	45.62 (45.28 ± 0.35)	2.07 (1.57 ± 0.32)
5	2 wt% BHT–ref	0.835 (0.833 ± 0.002)	16.14 (15.79 ± 0.42)	69.20 (66.16 ± 0.23)	9.32 (9.27 ± 0.23)
10	2 wt% BHT–ref	0.833 (0.838 ± 0.003)	15.80 (15.48 ± 0.56)	64.77 (64.30 ± 0.26)	8.52 (8.47 ± 0.24)
30	2 wt% BHT–ref	0.828 (0.830 ± 0.002)	14.94 (14.95 ± 0.40)	60.65 (58.80 ± 0.21)	7.50 (7.34 ± 0.15)
60	2 wt% BHT–ref	0.812 (0.812 ± 0.005)	11.84 (11.01 ± 0.34)	53.74 (50.24 ± 0.30)	5.18 (5.01 ± 0.22)
5	3 wt% BHT–CN	0.838 (0.832 ± 0.003)	17.01 (16.78 ± 0.18)	72.82 (70.62 ± 0.39)	10.39 (10.18 ± 0.13)
10	3 wt% BHT–CN	0.833 (0.828 ± 0.002)	14.97 (14.83 ± 0.22)	67.40 (65.60 ± 0.45)	8.41 (8.35 ± 0.25)
30	3 wt% BHT–CN	0.815 (0.816 ± 0.002)	14.26 (14.04 ± 0.22)	64.80 (64.20 ± 0.22)	7.57 (7.43 ± 0.11)
60	3 wt% BHT–CN	0.810 (0.807 ± 0.004)	13.91 (13.51 ± 0.37)	64.72 (62.78 ± 0.37)	7.31 (7.05 ± 0.31)
5	3 wt% BHT–PF	0.848 (0.848 ± 0.002)	18.43 (17.90 ± 0.27)	72.45 (71.48 ± 0.22)	11.34 (11.10 ± 0.20)
10	3 wt% BHT–PF	0.843 (0.842 ± 0.005)	17.44 (17.06 ± 0.34)	70.17 (67.02 ± 0.28)	10.31 (10.02 ± 0.31)
30	3 wt% BHT–PF	0.823 (0.822 ± 0.004)	16.30 (16.00 ± 0.21)	67.40 (66.10 ± 0.32)	9.04 (8.87 ± 0.27)
60	3 wt% BHT–PF	0.817 (0.812 ± 0.005)	15.85 (15.40 ± 0.33)	66.20 (63.00 ± 0.23)	8.58 (8.34 ± 0.28)

a) The values in the parentheses are the average values obtained from over 12 devices.

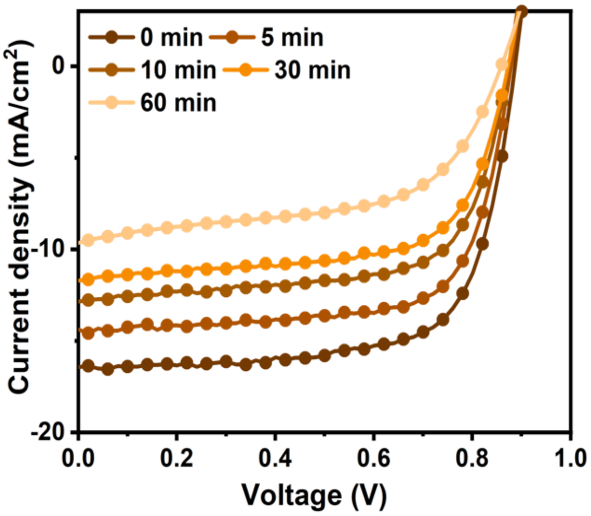

Figure 3.2.15. *J-V* curves exposed to light and ambient conditions over time in w/o additive.

Table 3.2.12. Device properties of PM6:IT4F devices without additives under light and ambient conditions with varying degradation times are summarized.

Time [min]	V_{OC} [V]	J_{SC} [mA cm^{-2}]	FF [%]	PCE $^{a)}$ [%]
0	0.887 (0.886 ± 0.001)	16.44 (16.01 ± 0.43)	71.52 (71.20 ± 0.23)	10.42 (10.10 ± 0.13)
5	0.879 (0.880 ± 0.001)	14.37 (14.22 ± 0.15)	70.98 (70.31 ± 0.24)	8.96 (8.79 ± 0.24)
10	0.873 (0.869 ± 0.004)	12.85 (12.29 ± 0.56)	66.88 (66.41 ± 0.47)	7.51 (7.09 ± 0.42)
30	0.868 (0.868 ± 0.001)	10.65 (10.31 ± 0.34)	62.36 (61.79 ± 0.57)	5.78 (5.53 ± 0.25)
60	0.855 (0.852 ± 0.003)	8.82 (8.50 ± 0.32)	51.41 (51.17 ± 0.24)	3.88 (3.71 ± 0.18)

[a)] The values in the parentheses are the average values obtained from over 12 devices.

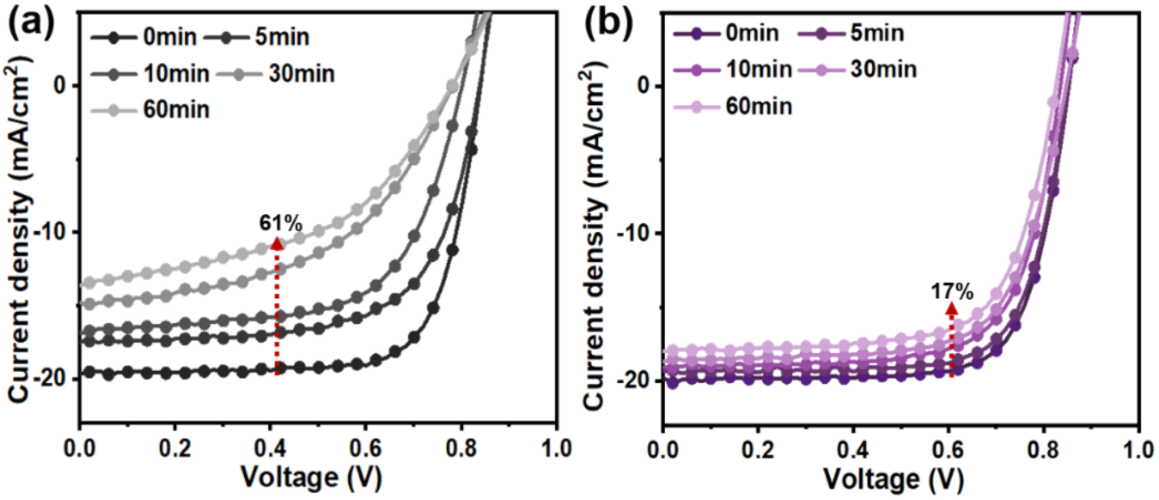

Figure 3.2.16. *J–V* curves exposed to light and ambient conditions over time in inverted devices with (a) 0.5 vol% DIO and (b) 3 wt% BHT–PF.

Table 3.2.13. Summary of inverted devices with 0.5 vol% DIO under light and ambient conditions with different degradation times.

Time [min]	V_{OC} **[V]**	J_{SC} **[mA cm^{-2}]**	**FF [%]**	**PCE $^{a)}$ [%]**
0	0.839 (0.836 ± 0.003)	20.21 (19.96 ± 0.25)	70.96 (70.54 ± 0.42)	12.04 (11.77 ± 0.27)
5	0.834 (0.833 ± 0.001)	16.47 (16.15 ± 0.32)	71.07 (70.67 ± 0.40)	9.76 (9.51 ± 0.25)
10	0.826 (0.828 ± 0.002)	15.97 (15.67 ± 0.30)	67.78 (67.51 ± 0.27)	8.95 (8.76 ± 0.19)
30	0.823 (0.820 ± 0.003)	13.67 (13.21 ± 0.46)	60.03 (59.79 ± 0.25)	6.75 (6.48 ± 0.27)
60	0.819 (0.818 ± 0.001)	11.88 (11.34 ± 0.54)	51.76 (51.24 ± 0.52)	5.09 (4.66 ± 0.43)

$^{a)}$ The values in the parentheses are the average values obtained from over 12 devices.

Table 3.2.14. Summary of ITO/ZnO/PM6:IT4F/MoO_3/Ag devices with 3 wt% BHT–PF under light and ambient conditions with different degradation times.

Time [min]	V_{OC} [V]	J_{SC} [mA cm^{-2}]	FF [%]	PCE [a] [%]
0	0.843 (0.842 ± 0.003)	20.91 (20.53 ± 0.37)	70.10 (69.85 ± 0.25)	12.37 (11.97 ± 0.40)
5	0.840 (0.839 ± 0.002)	20.35 (20.10 ± 0.25)	68.95 (68.47 ± 0.48)	11.78 (11.54 ± 0.24)
10	0.839 (0.837 ± 0.003)	19.90 (19.44 ± 0.46)	67.53 (67.12 ± 0.41)	11.27 (10.92 ± 0.35)
30	0.835 (0.833 ± 0.004)	19.37 (19.08 ± 0.38)	66.34 (65.96 ± 0.40)	10.73 (10.48 ± 0.33)
60	0.828 (0.826 ± 0.004)	18.90 (18.67 ± 0.23)	65.18 (64.80 ± 0.38)	10.20 (10.00 ± 0.20)

[a] The values in the parentheses are the average values obtained from over 12 devices.

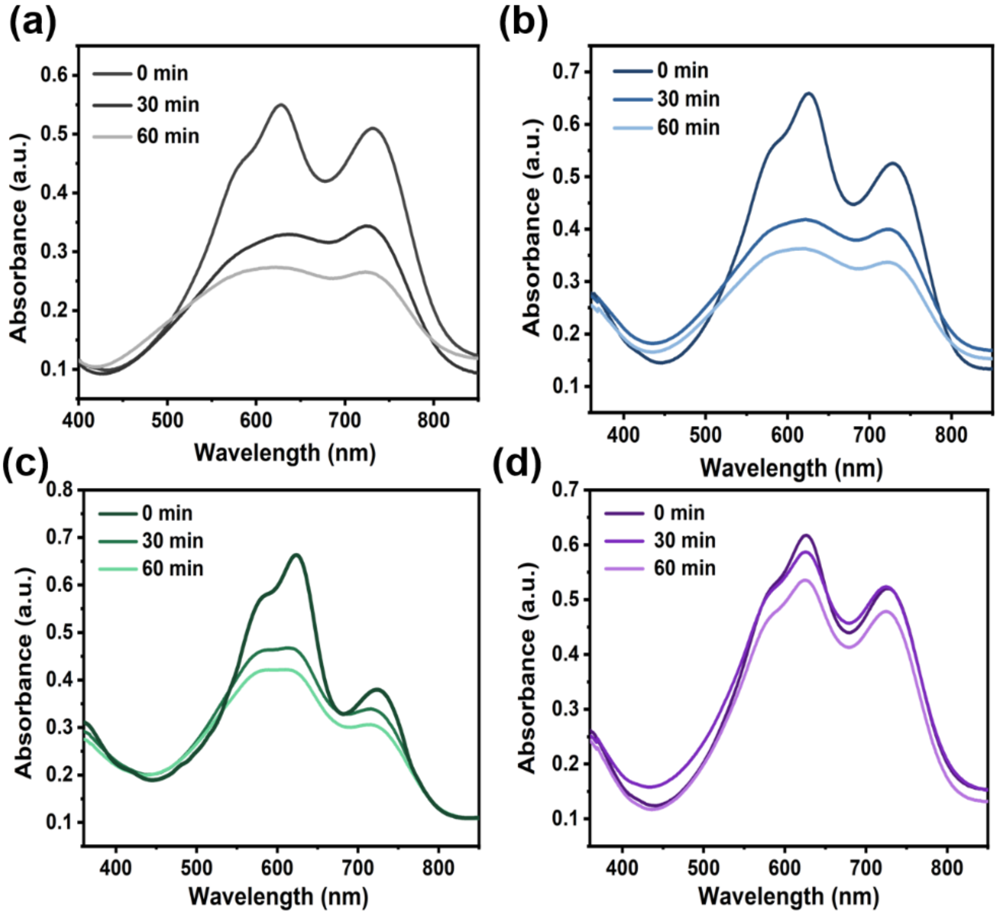

Figure 3.2.17. UV absorption spectra of PM6:IT4F films with various additives in light and ambient conditions; (a) DIO, (b) BHT–ref, (c) BHT–CN, and (d) BHT–PF.

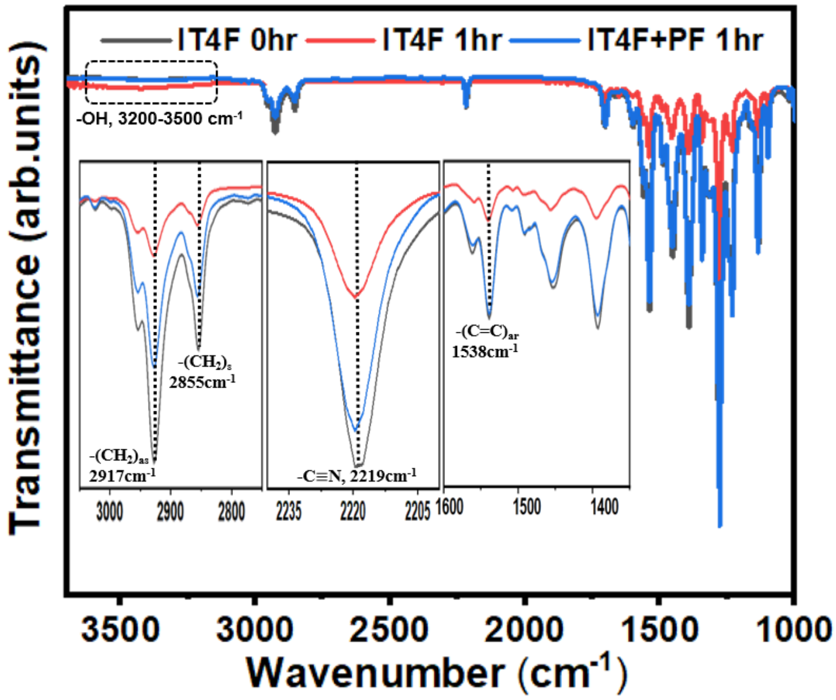

Figure 3.2.18. IT4F and IT4F+PF film FT-IR spectra under light and ambient conditions.

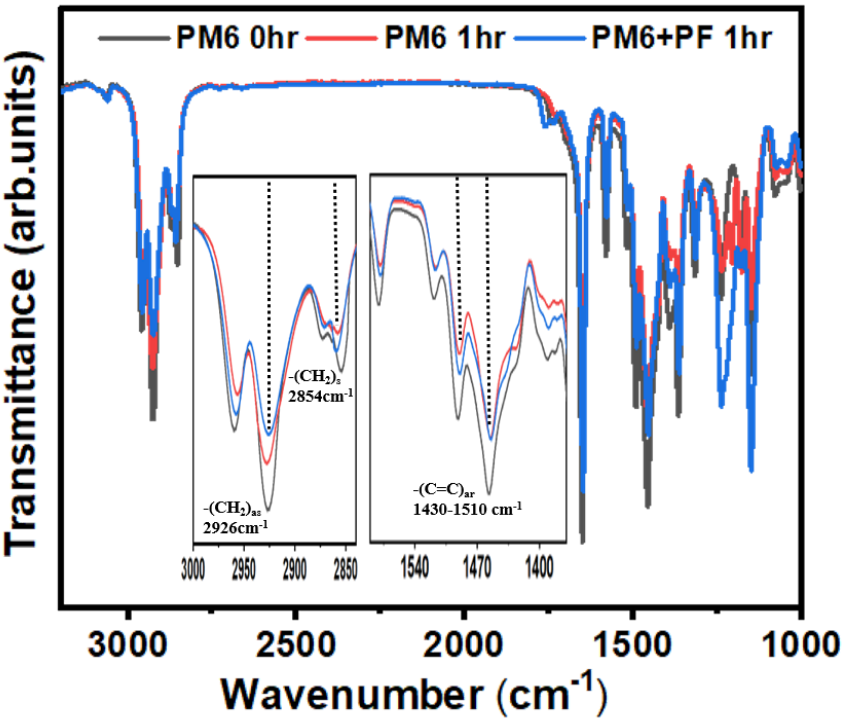

Figure 3.2.19. PM6 and PM6+PF film FT-IR spectra under light and ambient conditions.

3.2.8 References

1. M. Kaltenbrunner, M. S. White, E. D. Głowacki, T. Sekitani, T. Someya, N. S. Sariciftci, S. Bauer, *Nature Communications,* 2012, **3**, 770
2. Y. Liu, N. Qi, T. Song, M. Jia, Z. Xia, Z. Yuan, W. Yuan, K.-Q. Zhang, B. Sun, *ACS Applied Materials & Interfaces,* 2014, **6**, 20670
3. S. Chen, S. Jung, H. J. Cho, N.-H. Kim, S. Jung, J. Xu, J. Oh, Y. Cho, H. Kim, B. Lee, Y. An, C. Zhang, M. Xiao, H. Ki, Z.-G. Zhang, J.-Y. Kim, Y. Li, H. Park, C. Yang, *Angewandte Chemie International Edition,* 2018, **57**, 13277
4. D. Koo, S. Jung, J. Seo, G. Jeong, Y. Choi, J. Lee, S. M. Lee, Y. Cho, M. Jeong, J. Lee, J. Oh, C. Yang, H. Park, *Joule,* 2020, **4**, 1021.
5. C. Zhu, J. Yuan, F. Cai, L. Meng, H. Zhang, H. Chen, J. Li, B. Qiu, H. Peng, S. Chen, Y. Hu, C. Yang, F. Gao, Y. Zou, Y. Li, *Energy & Environmental Science,* 2020, **13**, 2459
6. L. Zhan, S. Li, T.-K. Lau, Y. Cui, X. Lu, M. Shi, C.-Z. Li, H. Li, J. Hou, H. Chen, *Energy & Environmental Science,* 2020, **13**, 635
7. Q. Liu, Y. Jiang, K. Jin, J. Qin, J. Xu, W. Li, J. Xiong, J. Liu, Z. Xiao, K. Sun, S. Yang, X. Zhang, L. Ding, *Science Bulletin,* 2020, **65**, 272
8. Y. Lin, B. Adilbekova, Y. Firdaus, E. Yengel, H. Faber, M. Sajjad, X. Zheng, E. Yarali, A. Seitkhan, O. M. Bakr, A. El-Labban, U. Schwingenschlögl, V. Tung, I. McCulloch, F. Laquai, T. D. Anthopoulos, *Advanced Materials,* 2019, **31**, 1902965.
9. T. Uchiyama, T. Sano, Y. Okada-Shudo, V. Vohra, *Journal of Materials Chemistry C,* 2020, **8**, 7162
10. M. O. Reese, A. M. Nardes, B. L. Rupert, R. E. Larsen, D. C. Olson, M. T. Lloyd, S. E. Shaheen, D. S. Ginley, G. Rumbles, N. Kopidakis, *Advanced Functional Materials,* 2010, **20**, 3476
11. H. K. H. Lee, A. M. Telford, J. A. Rohr, M. F. Wyatt, B. Rice, J. Y. Wu, A. D. Maciel, S. M. Tuladhar, E. Speller, J. McGettrick, J. R. Searle, S. Pont, T. Watson, T. Kirchartz, J. R. Durrant, W. C. Tsoi, J. Nelson, Z. Li, *Energy & Environmental Science,* 2018, **11**, 417.
12. E. M. Speller, A. J. Clarke, N. Aristidou, M. F. Wyatt, L. Francàs, G. Fish, H. Cha, H. K. H. Lee, J. Luke, A. Wadsworth, A. D. Evans, I. McCulloch, J.-S. Kim, S. A. Haque, J. R. Durrant, S. D. Dimitrov, W. C. Tsoi, Z. Li, *ACS Energy Letters.* 2019, **4**, 846
13. A. Rivaton, A. Tournebize, J. Gaume, P.-O. Bussière, J.-L. Gardette, S. Therias, *Polymer International,* 2014, **63**, 1335
14. S. Alem, S. Wakim, J. Lu, G. Robertson, J. Ding, Y. Tao, *ACS Applied Materials & Interfaces,* 2012, **4**, 2993.
15. S. Li, L. Zhan, F. Liu, J. Ren, M. Shi, C.-Z. Li, T. P. Russell, H. Chen, *Advanced Materials,* 2018, **30**, 1705208

16. N. Y. Doumon, F. V. Houard, J. Dong, P. Christodoulis, M. V. Dryzhov, G. Portale, L. J. A. Koster, *Journal of Materials Chemistry C,* 2019, **7**, 5104.
17. J. Guo, Y. Wu, R. Sun, W. Wang, J. Guo, Q. Wu, X. Tang, C. Sun, Z. Luo, K. Chang, Z. Zhang, J. Yuan, T. Li, W. Tang, E. Zhou, Z. Xiao, L. Ding, Y. Zou, X. Zhan, C. Yang, Z. Li, C. J. Brabec, Y. Li, J. Min, *Journal of Materials Chemistry A,* 2019, **7**, 25088
18. V. Turkovic, S. Engmann, N. Tsierkezos, H. Hoppe, U. Ritter, G. Gobsch, *ACS Applied Materials & Interfaces,* 2014, **6**, 18525.
19. K.-N. Zhang, M.-S. Niu, Z.-N. Jiang, Z.-H. Chen, T. Wang, M.-M. Wei, C.-C. Qin, L. Feng, W. Qin, S.-K. So, X.-T. Hao, *Solar RRL,* 2020, **4**, 1900552
20. J. Brebels, J. V. Manca, L. Lutsen, D. Vanderzande, W. Maes, *J. Mater. Chem. A* **2017**, *5*, 24037
21. M. P. Hughes, K. D. Rosenthal, N. A. Ran, M. Seifrid, G. C. Bazan, T.-Q. Nguyen, *Advanced Functional Materials,* 2018, **28**, 1801542.
22. J. Oh, S. Jung, M. Jeong, B. Lee, J. Lee, Y. Cho, S. M. Lee, S. Chen, Z.-G. Zhang, Y. Li, C. Yang, *Journal of Materials Chemistry C,* 2019, **7**, 4716
23. T. Kumari, S. Jung, Y. Cho, H.-P. Kim, J. W. Lee, J. Oh, J. Lee, S. M. Lee, M. Jeong, J. M. Baik, W. Jo, C. Yang, *Nano Energy,* 2020, **68**, 104327.
24. M. H. Yang, H. C. Jin, J. H. Kim, D. W. Chang, *Polymers,* 2019, **11**, 746
25. Q. He, M. Shahid, X. Jiao, E. Gann, F. D. Eisner, T. Wu, Z. Fei, T. D. Anthopoulos, C. R. McNeill, M. Heeney, *ACS Applied Materials & Interfaces,* 2020, **12**, 9555.
26. J. Wudarczyk, G. Papamokos, V. Margaritis, D. Schollmeyer, F. Hinkel, M. Baumgarten, G. Floudas, K. Müllen, *Angewandte Chemie International Edition,* 2016, **55**, 3220
27. A. Casey, J. P. Green, P. Shakya Tuladhar, M. Kirkus, Y. Han, T. D. Anthopoulos, M. Heeney, *Journal of Materials Chemistry A,* 2017, **5**, 6465.
28. W. Zhao, S. Li, H. Yao, S. Zhang, Y. Zhang, B. Yang, J. Hou, *Journal of the American Chemical Society,* 2017, **139**, 7148.
29. M. P. Hughes, K. D. Rosenthal, N. A. Ran, M. Seifrid, G. C. Bazan, T.-Q. Nguyen, *Advanced Functional Materials*, 2018, **28**, 1801542.
30. A. Armin, D. M. Stoltzfus, J. E. Donaghey, A. J. Clulow, R. C. R. Nagiri, P. L. Burn, I. R. Gentle, P. Meredith, *Journal of Materials Chemistry C,* 2017, **5**, 3736.
31. A. Armin, G. Juska, M. Ullah, M. Velusamy, P. L. Burn, P. Meredith, A. Pivrikas, *Advanced Energy Materials,* 2014, **4**, 1300954.
32. P. Schilinsky, C. Waldauf, C. J. Brabec, *Applied Physics Letters,* 2002, **81**, 3885
33. A. K. K. Kyaw, D. H. Wang, V. Gupta, W. L. Leong, L. Ke, G. C. Bazan, A. J. Heeger, *ACS Nano,* 2013, **7**, 4569
34. I. Riedel, J. Parisi, V. Dyakonov, L. Lutsen, D. Vanderzande, J. C. Hummelen, *Advanced Functional Materials,* **b**, **14**, 38.

35. X. Du, J. Zhao, H. Zhang, X. Lu, L. Zhou, Z. Chen, H. Lin, C. Zheng, S. Tao, *Journal of Materials Chemistry A,* 2019, **7**, 20139.

36. J. Yuan, Y. Zhang, L. Zhou, G. Zhang, H.-L. Yip, T.-K. Lau, X. Lu, C. Zhu, H. Peng, P. A. Johnson, M. Leclerc, Y. Cao, J. Ulanski, Y. Li, Y. Zou, *Joule,* 2019, **3**, 1140

37. M. Zhang, X. Guo, W. Ma, H. Ade, J. Hou, *Advanced Materials,* 2015, **27**, 4655

38. H. Bin, L. Gao, Z.-G. Zhang, Y. Yang, Y. Zhang, C. Zhang, S. Chen, L. Xue, C. Yang, M. Xiao, Y. Li, *Nature Communications,* 2016, **7**, 13651.

CHAPTER 3 Solid Additives

Benzothiadiazole-Based Volatile Additives for Favorable Interfacial Component Distribution in Layer-by-Layer OSCs

3.3.1 Motivation and Research Background

OSCs have received extensive attention owing to their potential advantages such as light-weight, low cost, processibility on flexible substrates, and low production cost via solution processing technology.[1-3] The BHJ have been applied into the construction of the active layer. The BHJ structure which is a one-step method using mixture of the donor and acceptor in the solution can provide bi-continuous interpenetrating formation of blend films, leading to sufficient interfaces and effective charge transport channels.[4–6] The PCE of BHJ OSCs has recently topped 18% in laboratory-scale single-junction OSCs, thanks to significant achievements in material development and device engineering.[7-11] However, the BHJ active layer has some severe disadvantages, which is originated from blend system; (i) high morphological sensitivity to the time of the blend solution, (ii) an extremely complicated process with numerous parameters (e.g., domain size and mixed-phase), (iii) constrained vertical component distribution construction, and (iv) difficulties constantly regulating the appropriate morphology.[12-16] Before BHJ OSCs were developed, stacked device formation was fabricated (LBL process method), which involves the sequential deposition of donor and acceptor layers.[17-19] Disappointingly, the LBL PCEs were less than 2%, far lower than the BHJ device results.[20,21] This is because the active layer has restricted donor/acceptor interfaces, which is a disadvantage for this strategy.[22] As a result of its significant ability to bypass the infamous flaws associated with the BHJ approach, the LBL technique is regaining favor as a promising alternative.[13,23–28] In addition, research has shown that LBL OSCs may be more suited for large-scale OSC industrial applications because to their greater stability and ecologically favorable manufacturing compared to BHJ OSCs.[24,25,29–31] Despite the recent publication of several high-performance OSCs using the LBL technique, these studies still lag far behind those of BHJ OSCs; they lack a clear and quantifiable morphological image and the underlying mechanism driving the formation of the LBL film.

Solid additives have lately gained a significant deal of interest in the OSC community due to their numerous advantageous properties, such as their excellent morphology-directing capabilities, easy post-treatments, and better device stability; As a result, they are increasingly indispensable for high-performance devices.[11,32–35] Rarely are effective solid additives in LBL systems recorded, despite their prevalence.[36,37]

To further our knowledge of LBL OSCs and to shed light on the functional role played by solid additives, we investigate the effects of additives, such as benzothiadiazole and its fluorinated analogs, on the film morphology and device performance of the PM6/Y6-based LBL platform. In optoelectronic applications, BT derivatives are the most desired building blocks for producing high-performance conjugated materials.[5,38–41] As a result, we hypothesized that the compatibility of their backbone topologies with high-performance active layer materials may promote intermolecular interactions between BTs and active layer materials, therefore modifying the morphology of the active layer. When the optimal amount of FBT was added to the PM6 donor layer of the PM6/Y6-based LBL OSCs in this investigation, the morphology was improved, and the PCE was 16.63%, which was higher than the PCE of the references without and with CN. More enticingly, by applying the FBT treatment in the expanded LBL platform toolboxes, we were able to achieve a PCE of up to 17.71% with minimal device-to-device variability caused by the polymers' varying molecular weights. In addition, large-scale devices were manufactured, achieving PCEs of 16.10% (0.92 cm^2) and 10.93% (2.50 cm^2) with highly homogeneous performance.

3.3.2 Characterization of Solid additives

Before delving into the analysis, we emphasize the peculiar and fascinating qualities of BT derivatives (BT, FBT, and 2FBT), such as their ease of synthesis or commercial availability, strong stability and electro-optical capabilities, and ability to adopt a quinoid structure (**Figure 3.3.1**).[42,43] TGA indicated that between 50 and 70 degrees Celsius, all BT derivatives started to lose weight (**Figure 3.3.8**), confirming their high volatility for use as solid additives in OSCs. Using density functional theory at the B3LYP/6-31G level, we also computed the ESP distribution of the BT derivatives (**Figure 3.3.1a**). The asymmetric FBT has a more localized charge distribution than the symmetric structures (BT and 2FBT), providing a potential for enhanced intermolecular electrostatic interactions with photoactive materials in a polarized molecular environment.[44] We anticipate that using BT solid additives in the fabrication of donor & acceptor layers would result in substantially different intermolecular dynamics, resulting in drastically different crystallinity/morphology and, as a consequence, significantly different device performance.

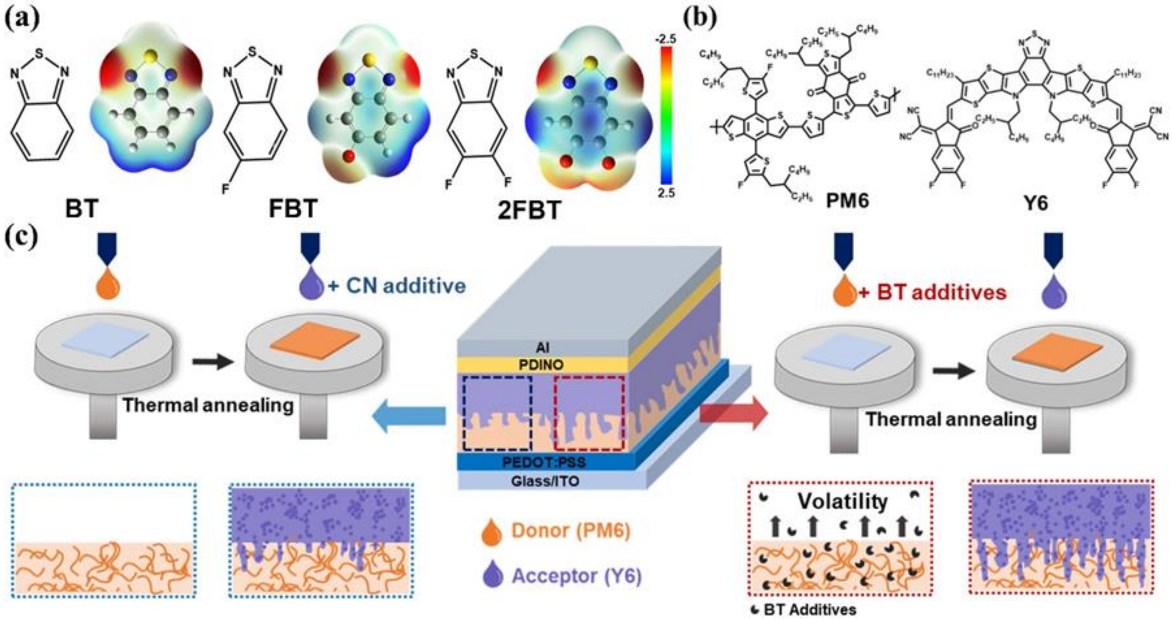

Figure 3.3.1. (a) The electrostatic charge distribution in additive structures of BT, FBT, and 2FBT. (b) The molecular structures of PM6 and Y6. (c) Schematic depiction of the active layer development based on additive types.

GIWAX was then used to examine the effect of BT-based additives on the crystalline and orientation characteristics of each Y6 acceptor and PM6 donor film. The GIWAX data (**Figures 3.3.2** and **3.3.9** and **Tables 3.3.5** and **3.3.6**) shows that the microstructures of the Y6 acceptor films were remarkably consistent independent of the BT solid additives used, with a prominent π–π diffraction peak in the OOP direction and a lamellar peak in the IP direction. In contrast, the addition of solid additives to the PM6 significantly enhanced the microstructural ordering and led to the formation of larger crystallites; this is evidenced by more distinct (010) π–π diffraction peaks and long-range ordered (*h*00) lamellar diffraction peaks along with OOP as well as the increased crystallite coherence lengths (CCL_{h00} = 47.96–39.29 Å and CCL_{010} = 28.68–20.67 Å). The preferential intermolecular interactions between the BT solid additives and the PM6 polymer may be responsible for the observed well-controlled morphology. We noticed that when we compared the TEM and AFM images of PM6 donor films without and with BT solid additives (**Figures 3.3.10** and **3.3.11** the additive treated PM6 donor films had higher R_q values and more linked crystalline structures. These findings may give further evidence of the enhanced crystalline nature caused by the use of BT-based additives

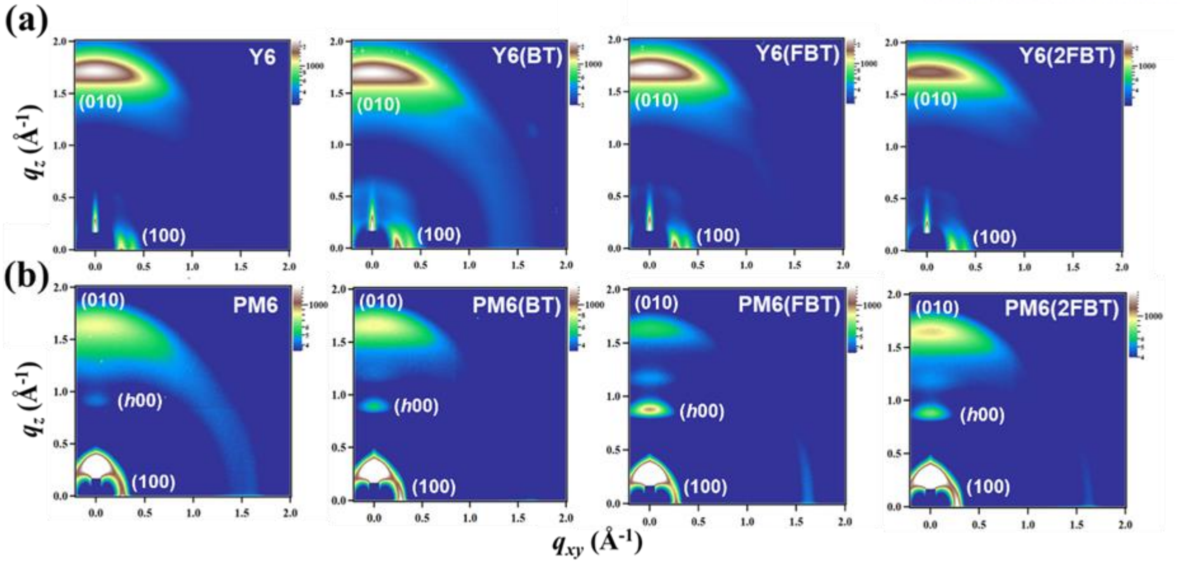

Figure 3.3.2. Images of (a) Y6 films and (b) PM6 films with and without BT-based additives in GIWAX.

3.3.3 Photovoltaic Properties

LBL devices with and without conventional structures were fabricated to study the effect of BT-based additivess on photovoltaic properties (**Figure 3.3.3b** demonstrates the molecular structures of PM6 and Y6). Based on the LBL layer, the optimal fabrication for PM6/Y6 used CF solvent with a 0.5% CN solvent additive and thermal annealngi at 100 ºC for 5 min in the donor and acceptor layers.[36,45] All of the devices investigated in this work were fabricated under the same conditions (the schematic illustration for the fabrication of LBL systems is shown in **Figure 3.3.1c**).

Despite TGA data demonstrating the volatility of the BT-based additives at low temperature, further testing demonstrated their full removal in the optimal devices: after annealing for 5 minutes at 100 °C, (i) the removal of their residues on the surface film of the Si substrate (**Figure 3.3.12a**), (ii) utilizing sublimation experiment to acquire BT solid additives in bulk state (**Figure 3.3.12b**) and (iii) The loss of their distinctive peak at 821 cm^{-1} as determined by FT-IR in films mixed with PM6 and solid additives (**Figure 3.3.13**).[46] In order to show that BT solid additives volatilize appropriately in fabricated LBL devices, we examined PM6 + BT solid additives (weight ratio of 1:1) using TGA (**Figure 3.3.14**). In the TGA profile, a weight loss of 50% is observed while keeping the temperature at 100 °C for 5 min, suggesting that our solid additives volatilize perfectly in the fabricated devices under optimal conditions. As a consequence, we can rule out the likelihood of solid additives remaining in OSC devices after fabrication.

We initially examined the performances of the PM6/Y6 reference LBL systme without and with a 0.5% CN additive, attaining PCEs of 14.75% (without additive), 14.80% (CN addition into the PM6 donor layer, called PM6(CN)/Y6), and 15.74% (CN addition into the Y6 acceptor layer, named PM6/Y6(CN)) (see **Figure 3.3.3a** and **Table 3.3.1**). The improvement in PCEs for CN-processed LBL systems is mostly due to the improvement in FFs. The performance of PM6/Y6 devices with BT-based additives was adjusted by varying their loading concentrations (10–40% (w/w) addition into the donor or acceptor layers, respectively). **Figure 3.3.3b** depicts the optimal *J–V* characteristics, and **Table 3.3.1** summarizes the photovoltaic parameters. **Figures 3.3.15–3.3.17** and **Tables 3.3.7–3.3.9** contain the additional data for this investigation.

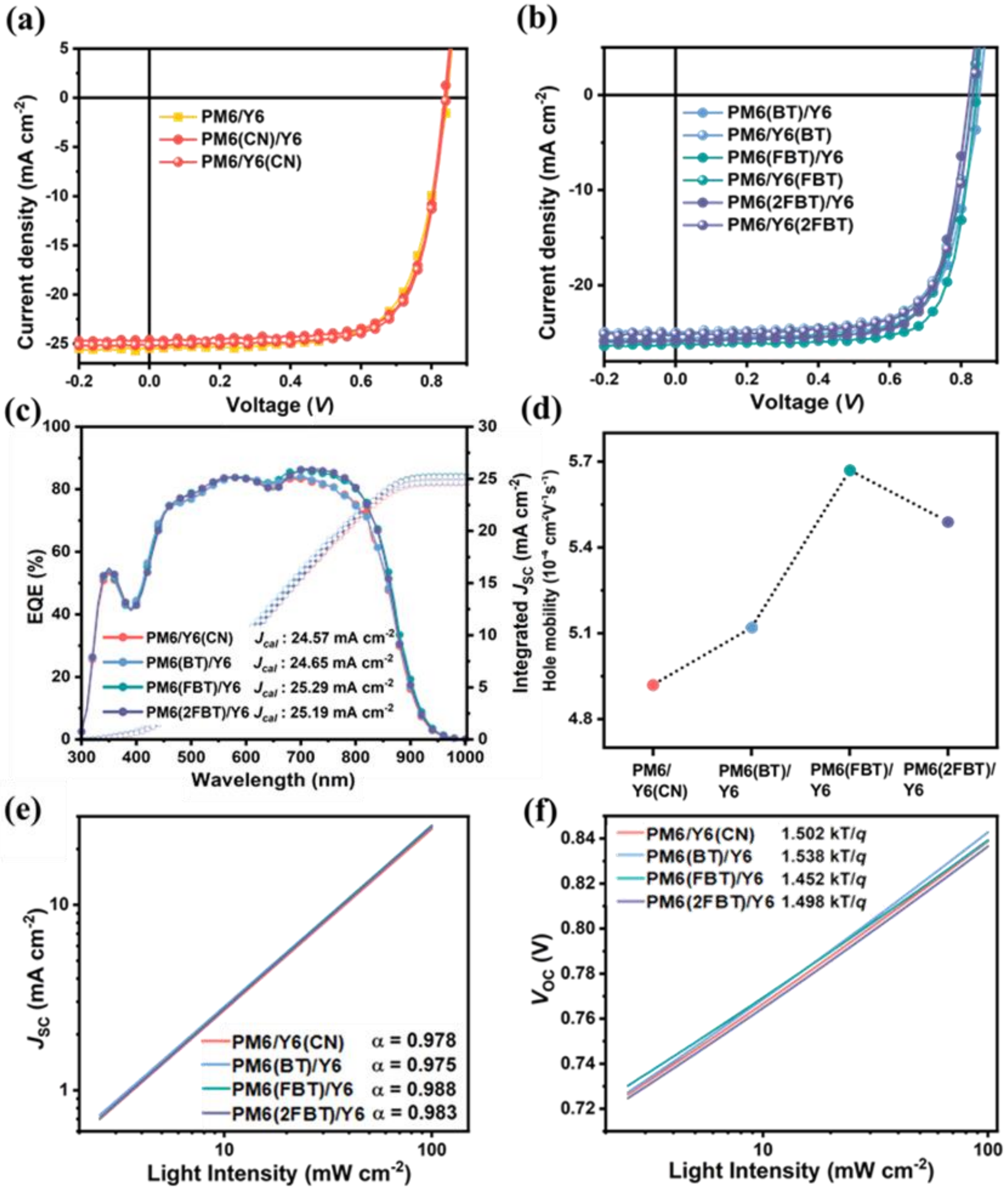

Figure 3.3.3. (a) PM6/Y6 LBL *J-V* curves w/o and w/ CN additive. (b) PM6/Y6 LBL *J-V* curves with BT-based additives. (c) EQE curves and (d) SCLC hole mobility of PM6/Y6-based devices with various additives. Plots of (e) J_{SC} and (f) V_{OC} versus light intensity.

Table 3.3.1 A summary of the device parameters for PM6/Y6 devices with various additive types under AM 1.5G illumination.

System	**V_{OC} [V]**	**J_{SC} [mA cm^{-2}]**	**FF [%]**	**PCE [a] [%]**
PM6/Y6	0.852 (0.852)	25.45 (25.05)	68.02 (67.89)	14.75 (14.48)
PM6(CN)/Y6	0.841 (0.839)	24.61 (24.25)	71.40 (70.95)	14.80 (14.42)
PM6/Y6(CN)	0.844 (0.842)	25.13 (24.71)	74.21 (73.62)	15.74 (15.28)
PM6(BT)/Y6	0.849 (0.845)	25.70 (25.16)	71.03 (70.45)	15.49 (15.21)
PM6/Y6(BT)	0.835 (0.834)	25.13 (24.86)	70.77 (70.61)	14.85 (14.63)
PM6(FBT)/Y6	0.842 (0.841)	26.14 (25.83)	75.57 (75.24)	16.63 (16.31)
PM6/Y6(FBT)	0.831 (0.829)	25.48 (25.15)	72.37 (71.87)	15.40 (15.03)
PM6(2FBT)/Y6	0.839 (0.836)	25.83 (25.41)	72.88 (72.31)	15.79 (15.33)
PM6/Y6(2FBT)	0.830 (0.830)	25.31 (25.19)	70.98 (70.74)	14.91 (14.77)

[a] the parentheses are obtained from 16 devices for the average.

Contrary to the LBL systems with CN additive, as shown in **Table 3.3.1**, the device performance of BT solid additives trends showed the opposite tendency. The LBL devices fabricated by applying BT-based additives to the PM6 donor layer (designated as PM6/Y6 (solid additive)) displayed greater PCEs and enhanced photovoltaic characteristics compared to the OSCs fabricated by applying BT-based solid additives to the Y6 acceptor layer. This discrepancy may be owing to differing mechanisms between the two types of additives; specifically, the high-boiling-point CN solvent additive facilitates diffusion and crystallization.[31,47] Whereas the volatile BT solid additives provided enough room for interdiffusion and self-assembly of the two components, resulting in the required vertical component distribution with appropriate acceptor/donor interfaces.[48]

In addition, the addition of additives led to an increase in J_{SC}s and a slightly decrease in V_{OC}. In order to achieve high performance, 30% (w/w) of PM6 was added to the FBT and 2FBT processed files, whereas in the BT case, 20% (w/w) of PM6 was added. The greatest PCE was achieved by the FBT/Y6-processed device (16.63%), with increases in the J_{SC} and FF values that were much greater than those of the completely optimized device with CN, proving the efficacy of FBT as a solid additive in LBL systems. In this study, we compared the characteristics of the optimized PM6/Y6(CN) reference device to those of the PM6 (solid additive)/Y6 device.

The EQE curves of the LBL devices with different additives are shown in **Figure 3.3.3c**. The use of fluorinated BT solid additives (FBT and 2FBT) in LBL systems may assist in the organization of the optimal morphology, as shown by the fact that devices treated with FBT and 2FBT show an increase in EQE between 400 and 900 nm. Importantly, we found that the EQE was significantly increased by the FBT and 2FBT additive systems from 650 to 900 nm, which suggests that the desired form of the PM6/Y6 treated with FBT or 2FBT may activate the photon-to-electron reaction from the Y6 phase (the detailed explanation is mentioned in the morphology section). The EQE values are also quite close to the J_{SC} values calculated from the J–V characteristics, falling within a margin of error of 5%.

We analyzed the charge-carrier dynamics to understand about the functional significance of the solid volatile additives within the PM6 donor layer in the LBL devices. First, μ_h values were obtained by fitting the J–V curves in the SCLC (**Figure 3.3.18**), as reported in **Figure 3.3.3d** and **Table 3.3.10**.[49,50] The order of the μ_h values was PM6(FBT)/Y6 > PM6(2FBT)/Y6 > PM6(BT)/Y6 > PM6/Y6(CN). To understand more about the charge carrier mobilities of LBL systems that have been treated with CN and BT additives, photo-CELIV measurement was used. **Figure 3.3.19** shows that the FBT-treated device has the highest mobility compared to the other devices, confirming the interpretation of the SCLC data. The impact of the additives on the charge recombination of the devices was subsequently assessed by examining the light intensity (I) dependent J–V characteristics, as shown in **Figure 3.3.3e and f**. Shockley–Read–Hall and bimolecular recombination losses were found to be considerably low in PM6(FBT)/Y6, as shown by its greater $\alpha = 0.988$ and lower slope of 1.452 kT/q compared to the other devices.[51,52] We plotted the J_{ph} with the V_{eff} for the devices (**Figure 3.3.20**) and then estimated J_{ph}/J_{sat} under the short-circuit situation and at the highest power output (**Table 3.3.11**), where J_{sat} is the saturated J_{ph} at a suitably high V_{eff}. The J_{ph}/J_{sat} values of the PM6(FBT)/Y6 device were higher than those of the other devices (J_{ph}/J_{sat} = 97.4–98.8% under the short-circuit condition and J_{ph}/J_{sat} = 75.1–77.35% at the maximum power output), indicating more efficient exciton dissociation and charge collection in the PM6(FBT)/Y6 device. The higher J_{SC} and FF values observed in the PM6(FBT)/Y6 device may be attributed to the combination of improved μ_h, recombination behavior, and charge dissociation/extraction efficiency.

3.3.4 Morphological Properties

In this work, we used GIWAXS, AFM, and TEM to investigate the morphology and molecular ordering/packing properties of LBL films with different additives. According to GIWAX data displayed in **Figure 3.3.4**, all LBL films showed an IP (100) peak and a significant OOP (010) peak, suggesting face-on organization on the substrate. All LBL films treated with BT solid additives have higher lamellar d–spacing and π–πstacking distance values than the CN LBL reference film (**Table 3.3.12**). CCL_{100} and CCL_{010} values rose relative to the other films treated with FBT and 2FBT, corresponding with the trends reported for PM6 neat films. The GIWAXS results indicate that the charge carrier transport properties are improved by the use of FBT or 2FBT solid additives, since these compounds tend to enhance the crystallite size of the PM6/Y6 layers while maintaining their molecular orientation.[25] This finding corroborates the view in the preceding EQE section.

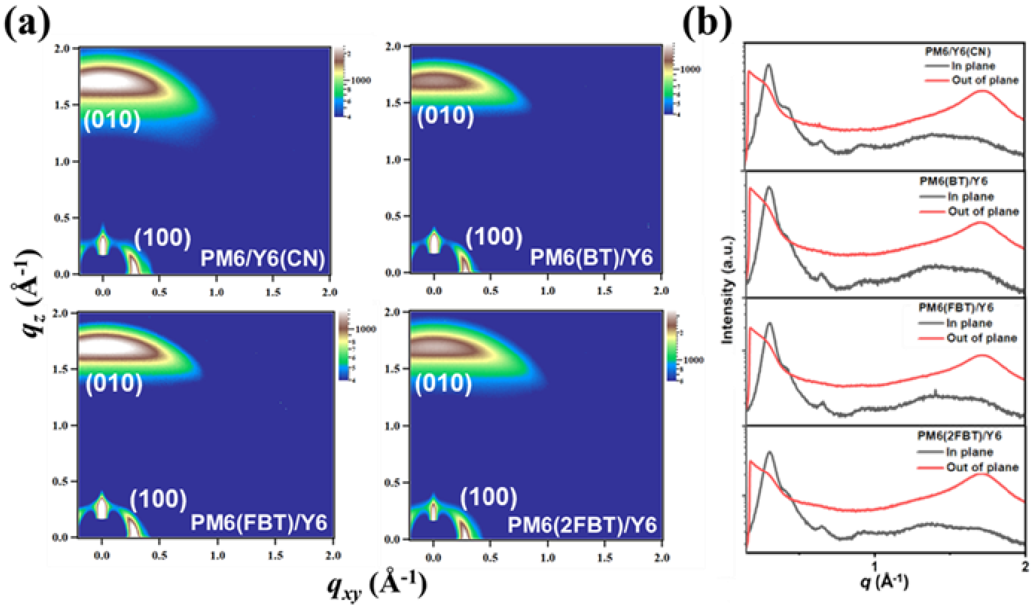

Figure 3.3.4. (a) GIWAX images and (b) line cut profiles matching the PM6/Y6 LBL films with additives.

As demonstrated in **Figure 3.3.21**, the AFM images of all the films show no discernible distinction in the phase separation surfaces, with modest R_qs on the top layer (Y6). In AFM, the PM6(2FBT or FBT)/Y6 film exhibits finer phase separation and increased roughness as compared to the PM6/Y6 film containing the CN additive. The enhancement in EQE between 650 and 900 nm is interpreted as a result of the formation of favorable morphology with the 2FBT or FBT additive, which enhances the donor/acceptor domain interfacial regions and therefore effectively boosts exciton dissociation probability. In contrast, their TEM data reveal evidently distinct bulk morphological characteristics; for instance, compared to the reference film with CN and BT, uniformly produced larger domains were found in the 2FBT and FBT solid additive-processed LBL films (**Figure 3.3.22**). In particular, the LBL film with FBT could construct interpenetrating networks with a larger domain size than the other cases, which accounted for the decreased recombination loss and increased charge transport/generation efficiency.[53]

3.3.5 Broad Applications

It is commonly understood that a polymer's molecular weight has a major influence on macromolecular organization, microstructure, optoelectronic and charge transport characteristics.[25,54,55] Hence, it is a crucial determinant of OSC performance. In addition to the optimal-molecular-weight PM6 batch (M_n

= 41 kDa) used in the aforementioned study, we synthesized lower- and higher-M_n PM6 batches (designated as *L*-PM6 (M_n = 30 kDa) and *H*-PM6 (M_n = 49 kDa), respectively) by varying the reaction time (see the Experimental section for the detailed information). To compare the effects of CN and FBT additives on the OSC performance of the *H*-PM6 and *L*-PM6/Y6 LBL platforms, we used these two batches under optimal conditons. **Figure 3.3.5a** depicts the *J–V* curves of the four LBL devices (*L*-PM6(FBT)/Y6, *H*-PM6(FBT)/Y6, *L*-PM6/Y6(CN), and *H*-PM6/Y6(CN)), and **Table 3.3.2** provides a summary of the photovoltaic parameters. As predicted, the PCEs of devices made with *L*-PM6 and *H*-PM6 were lower than those made with PM6 with the ideal molecular weight. In a prior study, the reason behind this phenomenon was addressed in depth.[56] In any case, the FBT-processed devices clearly outperform the CN-processed devices (higher PCE of *L*-PM6(FBT)/Y6 than *L*-PM6/Y6(CN) and higher PCE of *H*-PM6(FBT)/Y6 than *H*-PM6(CN)). We also used TEM to examine the morphology of *H*-PM6 and PM6 with and without FBT. As demonstrated in **Figure 3.3.23**, both the untreated *H*-PM6 and PM6 films exhibit excessive aggregation, whereas the FBT-treated films exhibit potentially more optimum aggregates with acceptable domain sizes.

Table 3.3.2. Summary of PM6/Y6 device properties under AM 1.5G illumination with different molecular weights of PM6.

System	V_{OC} [V]	J_{SC} [mA cm^{-2}]	FF [%]	PCE a) [%]
***L*-PM6/Y6(CN)**	0.839 (0.838)	24.70 (24.32)	72.03 (70.49)	14.93 (14.37)
***H*-PM6/Y6(CN)**	0.818 (0.819)	23.90 (23.40)	62.66 (61.58)	12.25 (11.80)
***L*-PM6(FBT)/Y6**	0.839 (0.837)	25.27 (24.98)	74.87 (74.26)	15.87 (15.34)
***H*-PM6(FBT)/Y6**	0.816 (0.813)	24.25 (23.78)	73.65 (73.01)	14.57 (14.12)

a) the parentheses are obtained from 16 devices for the average.

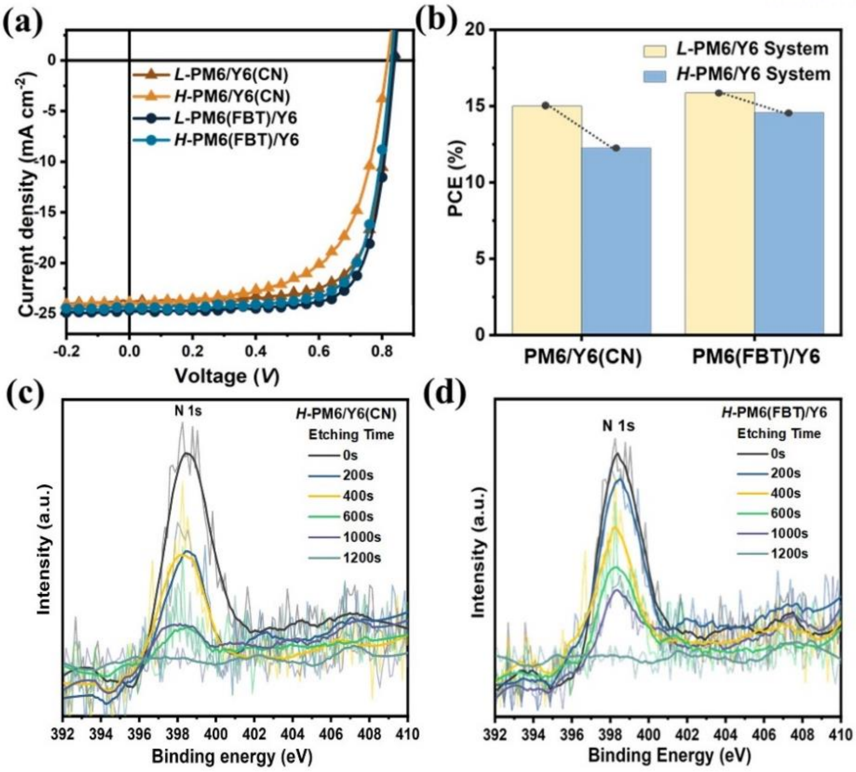

Figure 3.3.5. (a) *J-V* curves and (b) histograms of PM6/Y6-based devices with varying PM6 molecular weights without and with FBT additive. (c) and (d) XPS spectra of the *H*-PM6/Y6 device with CN and FBT additive.

Notably, the PCEs of CN-processed devices are extremely sensitive to the M_ns of PM6, whereas the PCEs of FBT-processed devices are much less sensitive to their change (**Figure 3.3.5b**). Such positive results demonstrate the feasibility of utilizing the FBT solid additive to resolve a notable problem with OSCs.

XPS measurements were used to further understand the vertical component distribution of the optimum *H*-PM6(FBT)/Y6 and *H*-PM6/Y6(CN) LBL films. The depth profiles of the blend film with a nitrogen N 1s peak (398 eV) are depicted in **Figures 3.3.5c and d.** Because the N element was present solely in the Y6 acceptor and not in the PM6 donor, the N signal was detected as a quantitative feature at various depths. Unetched films exhibited strong N 1s signals, indicating an excellent distribution of Y6 in the upper area of LBL systems. As the etching period time increased, the N 1s signal steadily diminished. At different etching depths, the N 1s signals in the FBT-processed film were consistently stronger than in the CN-processed film, indicating the possible occurrence of downward interdiffused development of the Y6 acceptor into the PM6 donor layer phase (so-called pseudo-bilayer morphology); as a result, charge separation and transport may be improved. **Figure 3.3.23** exhibits morphology-related data, such as AFM and TEM images, that is consistent with the results obtained in the aforementioned comparison investigations with the optimal-M_n PM6 batch.

To evaluate the FBT's broad applicability, we selected two best LBL systems from the most up-to-date LBL OSCs: PTQ10/Y6 and PM6/BTP-eC9 (the chemical structures of PTQ10 and BTP-eC9 are illustrated in **Figure 3.3.24)**. The previously described optimized approach was used to fabricate the reference devices (the most recently reported LBL OSCs are listed in **Table 3.3.13**).[23] In summary, the addition of the solvent additive (0.25% (v/v) for Y6 and 0.5% (v/v) for BTP-eC9) to the acceptor layer, total thermal annealing at 100 °C for 10 min, and the addition of 30% (w/w) FBT to the PM6 donor layer resulted in excellent performance for the FBT-processed LBL systems. **Figure 3.3.6** depicts the *J*–*V* curves of the four LBL devices, and **Table 3.3.3** lists the device parameters. The PTQ10(FBT)/Y6 and PM6(FBT)/BTP-eC9 devices produced comparable V_{OC}s, but larger J_{SC}s and higher FFs than their respective DIO-processed counterparts, as demonstrated in the aforementioned PM6/Y6 LBL systems. Consequently, PTQ10(FBT)/Y6 and PM6(FBT)/BTP-eC9 devices could reach PCEs of 16.01% and 17.71%, respectively, when compared to PM6/BTP-eC9(DIO) and PTQ10/Y6(DIO) devices (**Table 3.3.14**).

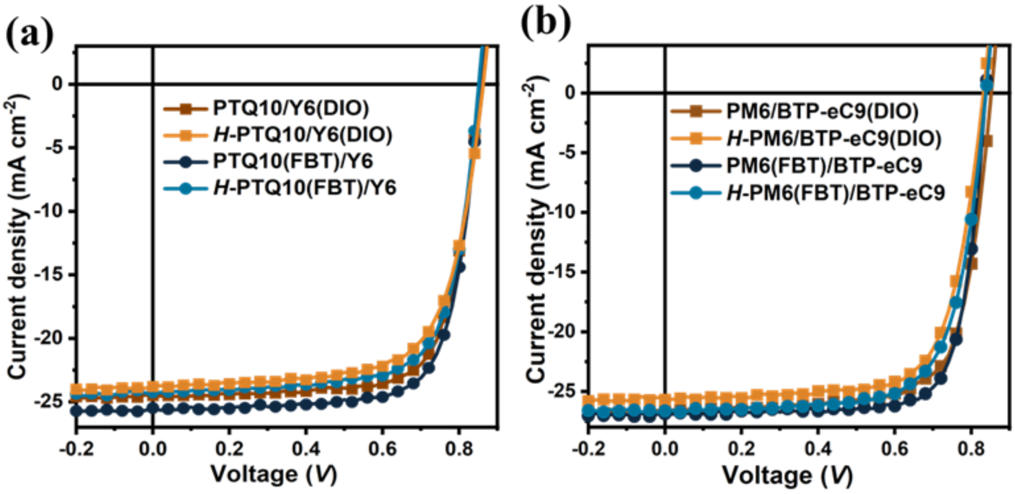

Figure 3.3.6. *J*-*V* curves of a) the PTQ10/Y6 system and b) the PM6/BTP-eC9 system with varied donor molecular weights without and with FBT additive.

In this work, we examined the performance of LBL devices with higher concentrations of the M_ns-based donor polymers *H*-PTQ10 and *H*-PM6(for information on the M_n values of PTQ10, see the supporting information section). The device performances of the *H*-PTQ10 and *H*-PM6-based devices were somewhat lower than the equivalent values above. The FBT-processed PTQ10/Y6 and PM6/BTP-eC9 systems exhibit reduced PCE fluctuation while altering the M_ns of the polymers compared to the DIO-processed systems. (see **Table 3.3.15**). The aforementioned findings suggest that the PCEs of polymer-based OSCs may be increased by adding the FBT solid additive, while device-to-device variation is kept to a minimum.

Table 3.3.3. PTQ10/Y6 and PM6/BTP-eC9 systems with various donor molecular weights without and with FBT additive.

System	V_{OC} **[V]**	J_{SC} **[mA cm^{-2}]**	**FF [%]**	**PCE [a] [%]**
PTQ10/Y6 (DIO)	0.853 (0.854)	24.37 (23.83)	74.01 (73.51)	15.42 (14.96)
***H*-PTQ10/Y6 (DIO)**	0.853 (0.851)	23.90 (23.62)	68.94 (68.61)	14.10 (13.79)
PTQ10 (FBT)/Y6	0.851 (0.851)	25.12 (24.66)	74.85 (74.35)	16.01 (15.61)
***H*-PTQ10 (FBT)/Y6**	0.845 (0.847)	24.25 (23.89)	72.59 (72.17)	14.87 (14.60)
PM6/BTP-eC9 (DIO)	0.837 (0.837)	26.13 (25.82)	78.83 (78.67)	17.24 (16.99)
***H*-PM6/BTP-eC9 (DIO)**	0.830 (0.830)	25.60 (25.44)	72.38 (72.04)	15.38 (15.21)
PM6 (FBT)/BTP-eC9	0.835 (0.833)	26.68 (26.50)	79.52 (79.21)	17.71 (17.48)
***H*-PM6 (FBT)/BTP-eC9**	0.829 (0.828)	26.48 (26.27)	73.76 (73.44)	16.19 (15.97)

[a] the parentheses are obtained from 12 devices for the average.

Furthermore, printing large-area OSCs is considered a necessary step in their use in industrial applications. As a result, we attempted to create LBL devices with large areas of 0.92 cm^2 (near to 1 cm^2), which is the usual area for large-area devices. **Figure 3.3.25a** shows the *J-V* curves of the large area devices, and **Table 3.3.4** describes the photovoltaic parameters. To begin, the J_{SC} was lower and the FF was higher in the DIO-containing control reference OSCs. Lower J_{SC} and FF values are possible in large-area single cells due to increased recombination processes and sheet resistance in contrast to small-area control devices. In contrast, the large-area FBT-processed PM6/BTP-eC9 OSCs yield superior PCEs of 16.10% with higher J_{SC} and FF values. Moreover, in order to confirm the maximal effect of FBT treatment on large-area devices, we manufactured 2.50 cm^2 LBL OSC devices. Large-area devices treated with FBT obtain a PCE of 10.93%, which indicates well for the application of the FBT solid additive in achieving efficient large-scale fabrication of OSCs, as compared to the control reference devices, which reach a PCE of 9.63% (**Figure 3.3.25b** and **Table 3.3.4**). Intriguingly, the large-area FBT-processed PM6/BTP-eC9 OSCs demonstrate superior reproducibility in terms of device performance, with more than 15 devices within trivial error ranges of 6.71/19.00% (DIO-contained devices) and 3.85/9.33% (FBT-contained devices) for device areas of 0.92 cm^2 and 2.50 cm^2, respectively (**Figure 3.3.7**).

Table 3.3.4. Summary of PM6/BTP-eC9 LBL device characteristics at 0.92 cm^2 and 2.50 cm^2 under AM 1.5G illumination.

System	Device area (cm^2)	V_{OC} [V]	J_{SC} [mA cm^{-2}]	FF [%]	PCE $^{a)}$ [%]
PM6/ BTP-eC9(DIO)	0.92	0.830 (0.828)	25.73 (25.27)	72.56 (71.62)	15.49 (14.96)
PM6(FBT)/ BTP-eC9		0.825 (0.821)	26.29 (26.01)	74.22 (73.81)	16.10 (15.75)
PM6/ BTP-eC9(DIO)	2.50	0.830 (0.825)	18.67 (17.78)	62.13 (61.35)	9.63 (8.98)
PM6(FBT)/ BTP-eC9		0.823 (0.819)	20.63 (19.98)	64.38 (63.54)	10.93 (10.40)

a) the parentheses are obtained from 15 devices for the average.

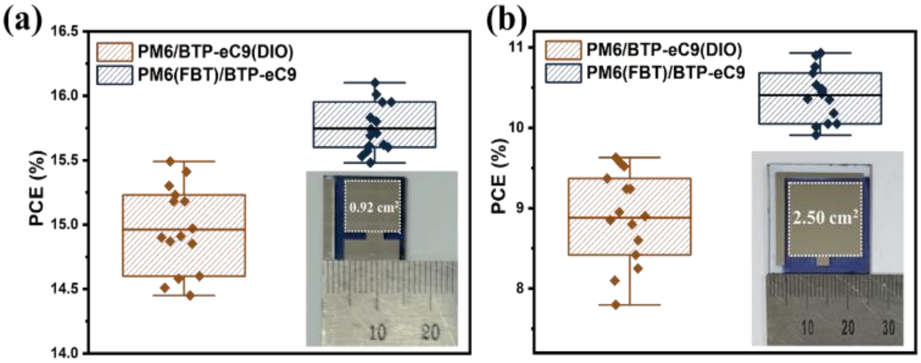

Figure 3.3.7. PCE variants of PM6/BTP-eC9 LBL devices measuring 0.92 cm^2 and 2.50 cm^2. The solid transverse lines within the boxes represent the average values for each of 15 LBL-based devices.

3.3.6 Conclusion

In conclusion, we introduced BT derivatives into a PM6/Y6-based platform to assess if they are beneficial solid additives for improving morphology and solar performance. The optimal addition of FBT to the PM6 donor layer enhanced charge transport/generation properties and suppressed recombination loss by causing structural and morphological variations, such as appropriate interpenetrating networks with optimal domain size and pseudo-bilayer structures. Therefore, the PM6(FBT)/Y6-processed device was able to obtain a remarkable PCE of 16.63%, which is much higher than the fully optimized references. When the experiment was extended to the other LBL systems

(PTQ10/Y6 and PM6/BTP-eC9), adopting FBT resulted in the best PCE of up to 17.71% with a significant decrease in device-to-device variations due to various M_ns-polymer batches. In addition, efficient large-area OSCs (PCEs = 16.10% (0.92 cm^2) and 10.93% (2.50 cm^2)) with robust device reproducibility were fabricated by leveraging the unique benefits of FBT-processed LBL systems. These findings show that FBT is a potential method for improving the device performance of LBL OSCs while reducing performance variability among device sizes.

3.3.7 Supporting Information

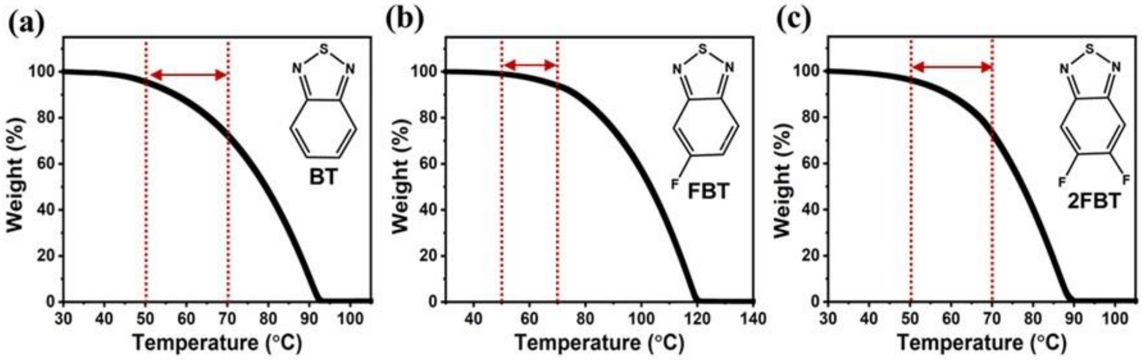

Figure 3.3.8. TGA plots of (a) BT, (b) FBT and (c) 2FBT material at a scan rate of 10 °C min^{-1}.

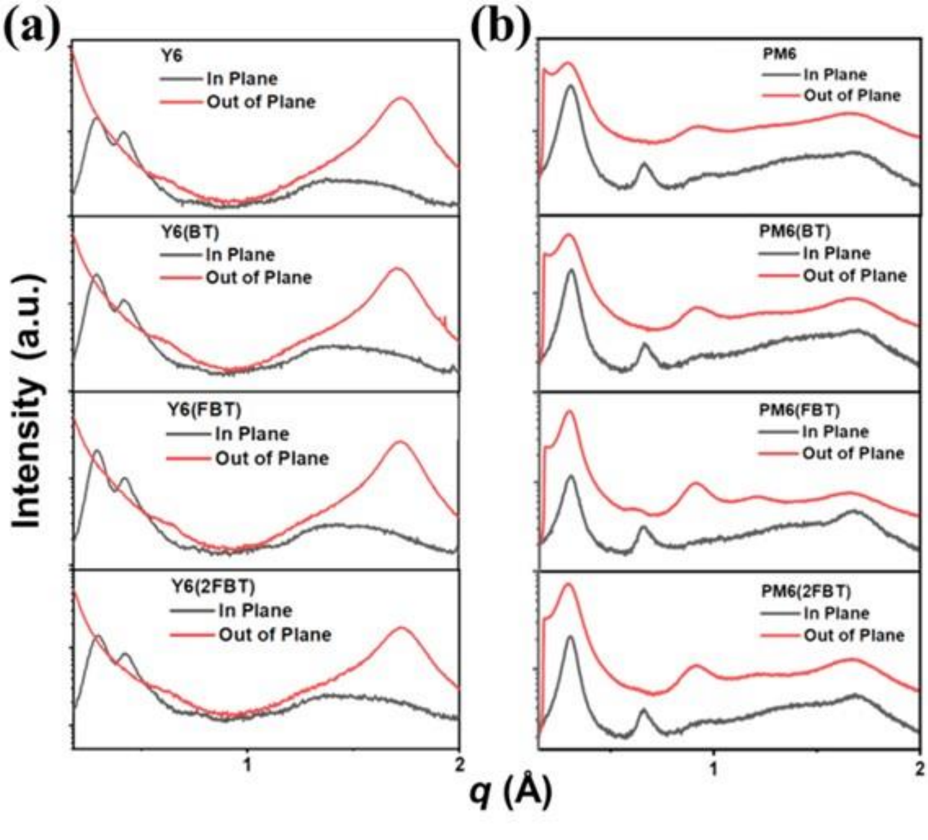

Figure 3.3.9. line cut profiles of the (a) Y6 films and (b) PM6 without and with BT solid additives.

Table 3.3.5. Lattice parameters for Y6 neat films without and with BT solid additives.

System	Out-of-Plane				In-Plane			
	π-π stacking (010)				Lamellar packing (100)			
	q (Å^{-1})	d-spacing (Å)	FWHM (Å^{-1})	Coherence length (Å)	q (Å^{-1})	d-spacing (Å)	FWHM (Å^{-1})	Coherence length (Å)
Y6	1.721	3.650	0.191	29.873	0.297	21.160	0.084	67.429
Y6(BT)	1.710	3.672	0.197	28.955	0.291	21.611	0.082	68.982
Y6(FBT)	1.725	3.643	0.205	27.906	0.293	21.471	0.074	68.731
Y6(2FBT)	1.727	3.638	0.207	27.638	0.295	21.303	0.083	68.607

Table 3.3.6. Lattice parameters for PM6 neat films without and with BT solid additives.

System	Out-of-Plane							
	π-π stacking (010)				Lamellar packing (h00)			
	q (Å^{-1})	d-spacing (Å)	FWHM (Å^{-1})	Coherence length (Å)	q (Å^{-1})	d-spacing (Å)	FWHM (Å^{-1})	Coherence length (Å)
PM6	1.636	3.840	0.370	15.427	0.918	6.842	0.157	36.195
PM6(BT)	1.662	3.775	0.212	26.979	0.919	6.840	0.144	39.295
PM6(FBT)	1.650	3.809	0.276	20.672	0.912	6.890	0.118	47.966
PM6(2FBT)	1.655	3.797	0.199	28.684	0.911	6.900	0.138	41.223

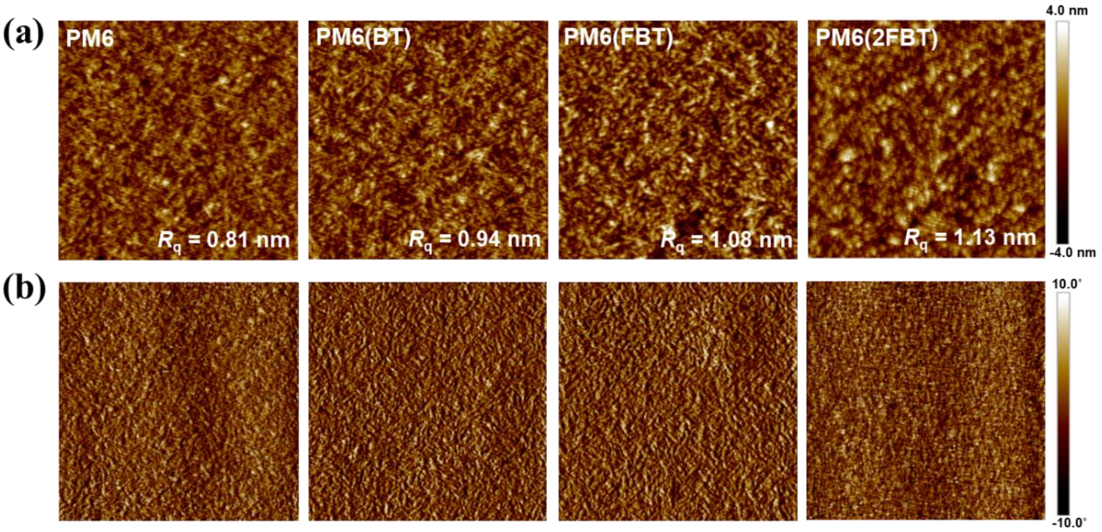

Figure 3.3.10. (a) Height and (b) phase AFM images (scan size 2 x 2 μm) of PM6 neat films without and with BT solid additives.

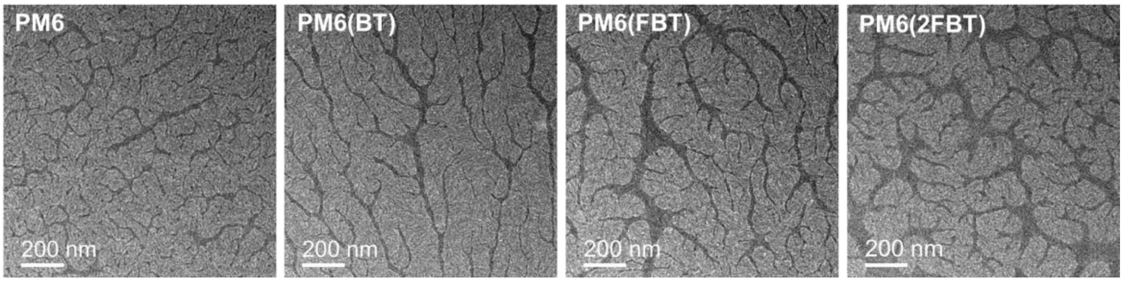

Figure 3.3.11. TEM images of PM6 neat films without and with BT solid additives.

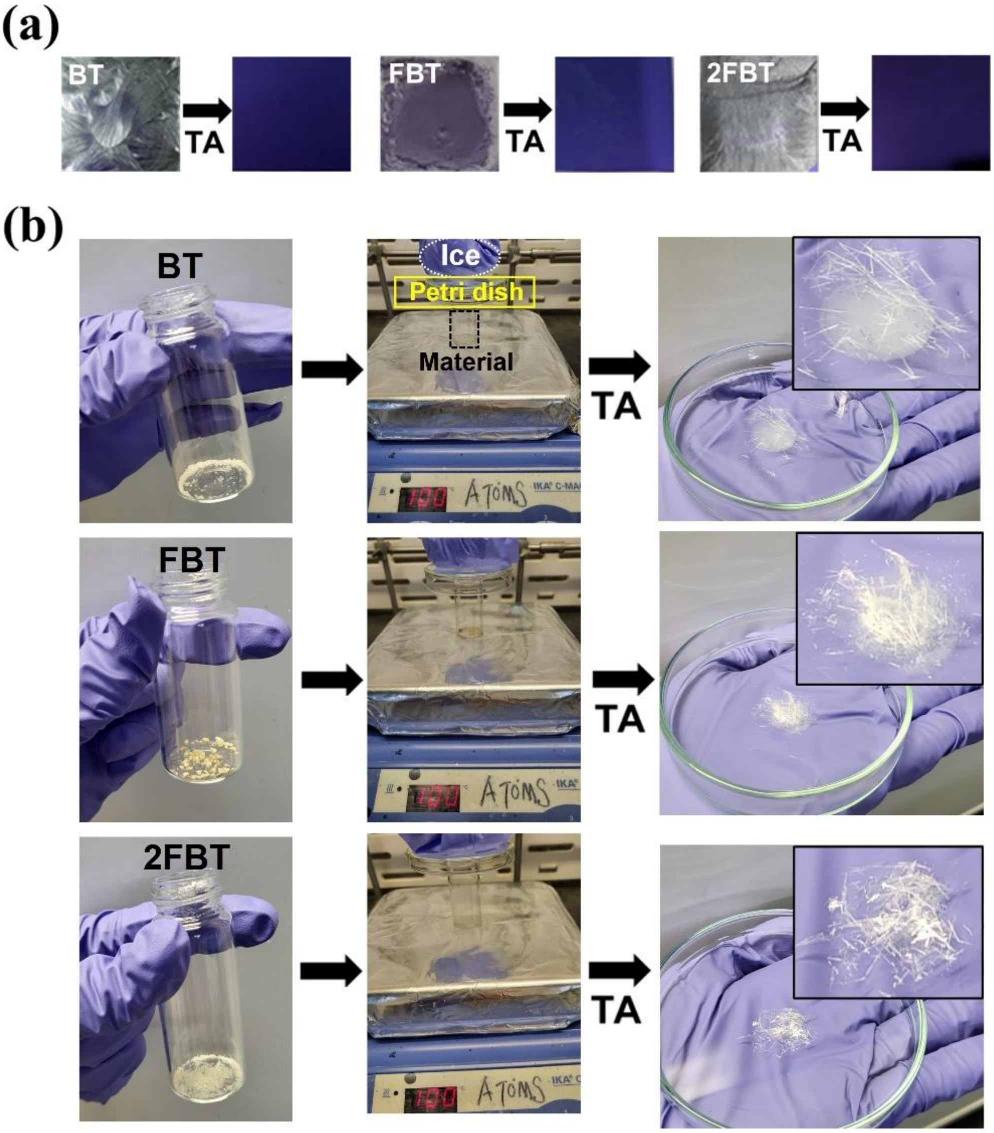

Figure 3.3.12. Photographs of BT solid additives (a) film on the Si substrate and (b) bulk in the vial followed by thermal annealing at 100 °C for 5 min.

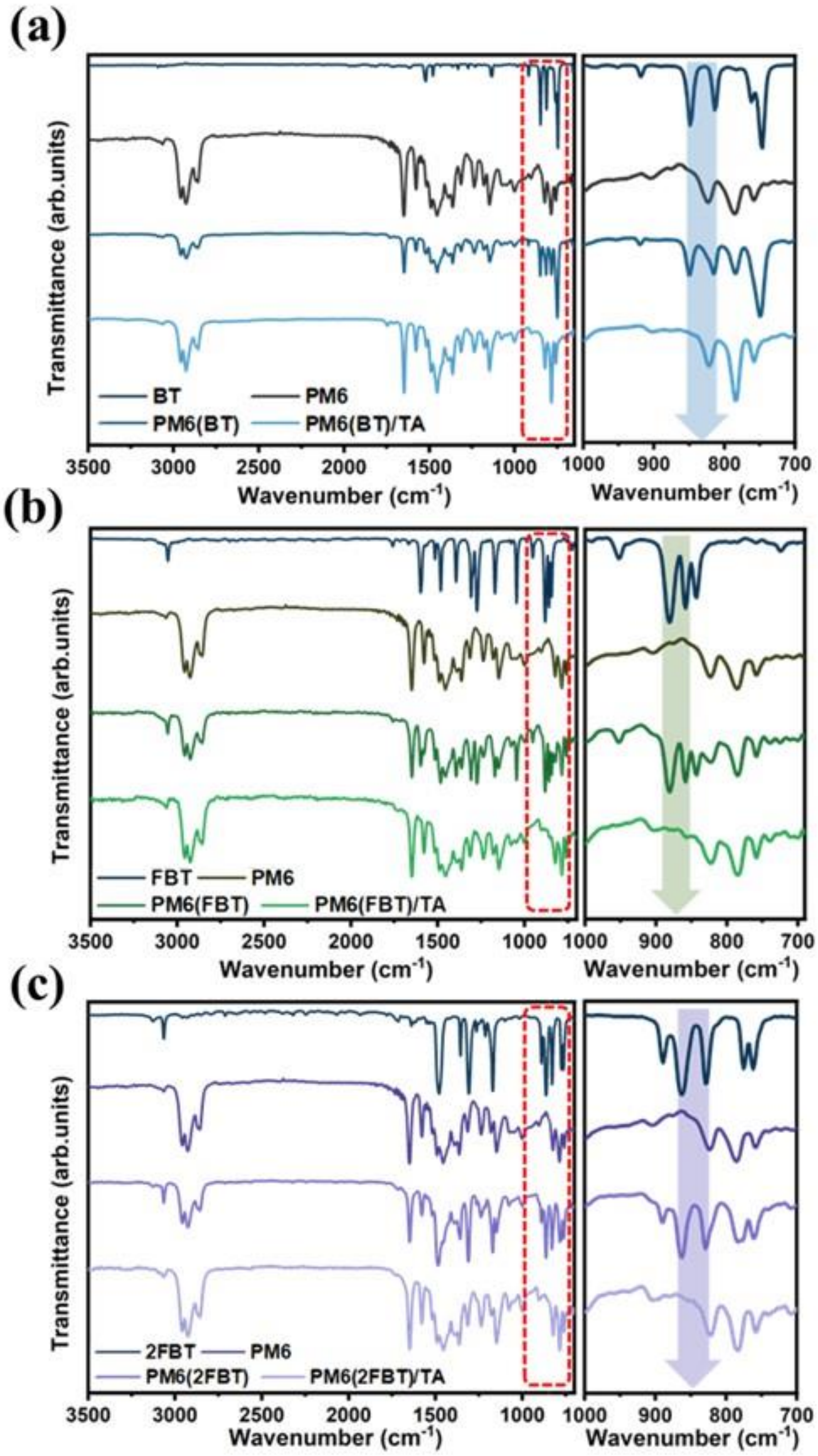

Figure 3.3.13. FT-IR spectra of PM6 films with (a) BT, (b) FBT, and (c) 2FBT under TA at 80 °C for 5 min.

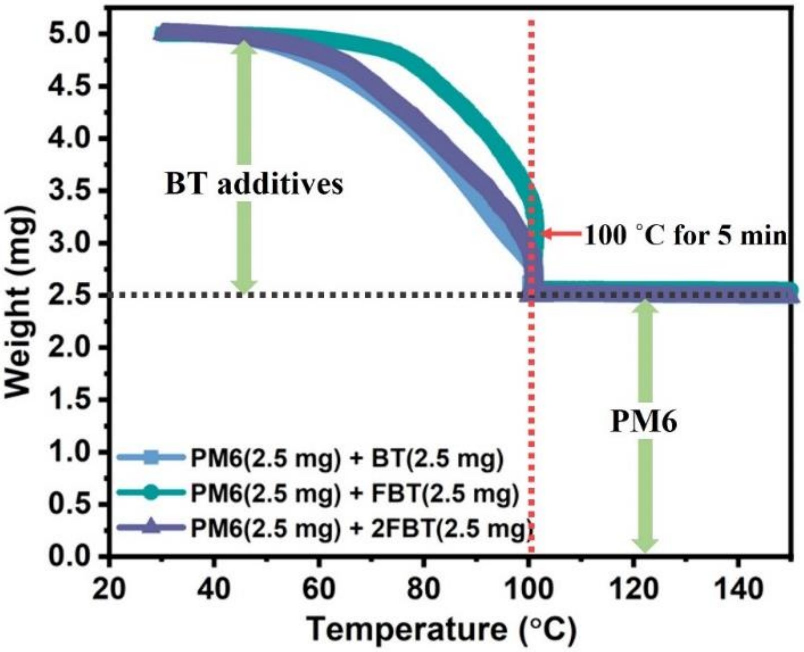

Figure 3.3.14. TGA plot of PM6:BT-solid additives (weight ratio of 1:1) at a scan rate of 10.0 °C min^{-1} and in the heating process, the temperature was held for 5 min at 100 °C.

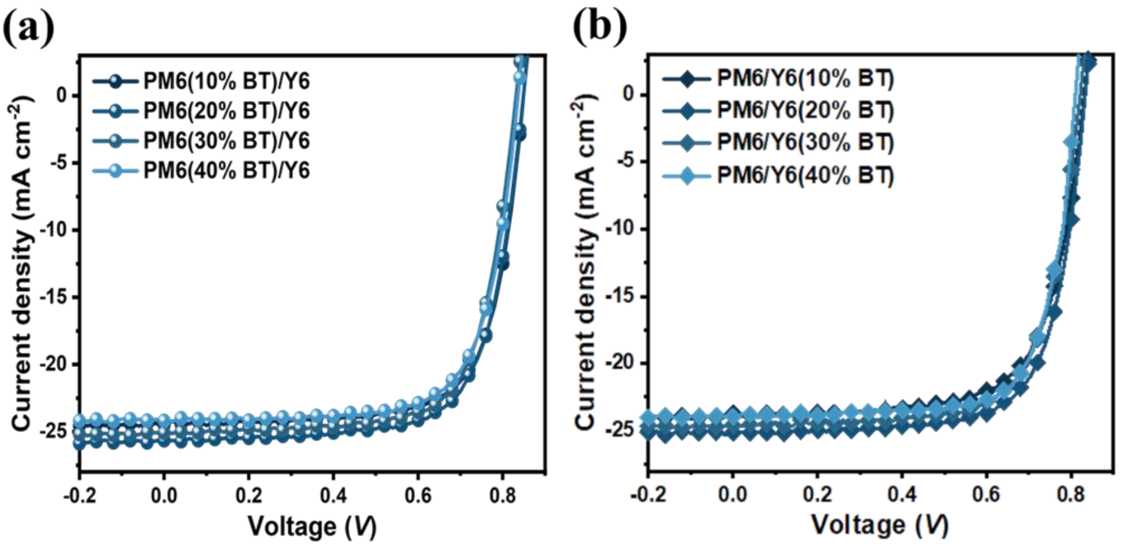

Figure 3.3.15. *J-V* curves of the PM6/Y6 LBL system with a different weight ratio of BT additive on (a) donor and (b) acceptor layer.

Table 3.3.7. Summary of device parameters of PM6/Y6 devices with different weight ratios of BT additive on donor or acceptor layer under illumination of AM 1.5G (100 mW cm^{-2}).

System	V_{OC} [V]	J_{SC} [mA cm^{-2}]	FF [%]	PCE [a] [%]
PM6(10% BT)/Y6	0.849 (0.843)	24.58 (24.20)	71.52 (71.23)	14.930. (14.51)
PM6(20% BT)/Y6	0.849 (0.842)	25.70 (25.17)	71.02 (70.45)	15.49 (15.21)
PM6(30% BT)/Y6	0.843 (0.840)	25.05 (24.88)	70.87 (70.68)	14.97 (14.76)
PM6(40% BT)/Y6	0.840 (0.832)	24.17 (23.85)	70.60 (70.35)	14.33 (13.93)
PM6/Y6(10% BT)	0.836 (0.836)	24.48 (24.39)	70.24 (70.03)	14.37 (14.28)
PM6/Y6(20% BT)	0.835 (0.833)	25.13 (24.87)	70.78 (70.61)	14.85 (14.63)
PM6/Y6(30% BT)	0.832 (0.831)	24.60 (24.43)	70.55 (70.37)	14.44 (14.29)
PM6/Y6(40% BT)	0.822 (0.819)	24.06 (23.65)	70.26 (69.57)	13.89 (13.38)

[a] the statistical values in parentheses are obtained from 16 cells.

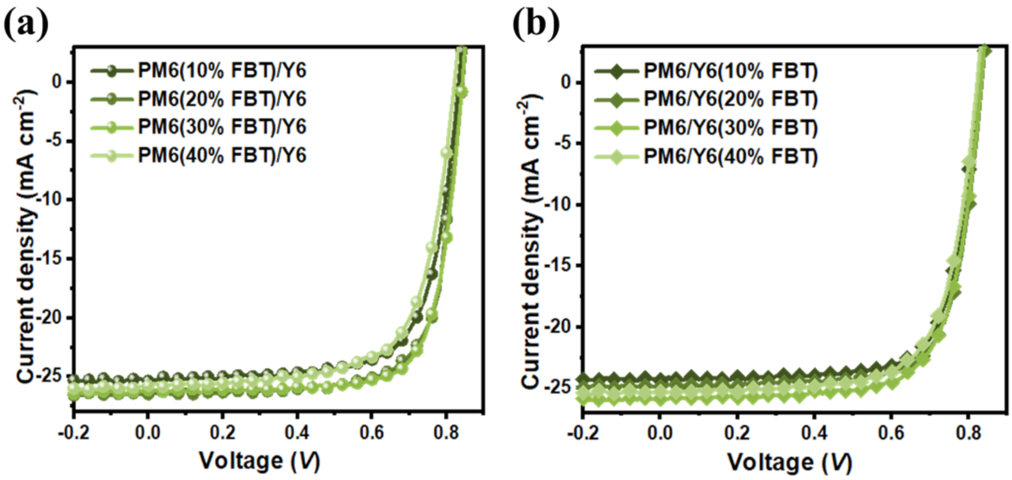

Figure 3.3.16. *J-V* curves of the PM6/Y6 LBL system with a different weight ratio of FBT additive on (a) donor and (b) acceptor layer.

Table 3.3.8. Summary of device parameters of PM6/Y6 devices with different weight ratios of FBT additive on donor or acceptor layer under illumination of AM 1.5G (100 mW cm^{-2}).

System	V_{OC} **[V]**	J_{SC} **[mA cm^{-2}]**	**FF [%]**	**PCE$^{a)}$ [%]**
PM6(10% FBT)/Y6	0.845 (0.840)	25.19 (24.93)	74.90 (73.67)	15.94 (15.43)
PM6(20% FBT)/Y6	0.843 (0.841)	25.73 (25.36)	75.72 (75.48)	16.42 (16.09)
PM6(30% FBT)/Y6	0.842 (0.840)	26.14 (25.83)	75.31 (75.19)	16.63 (16.31)
PM6(40% FBT)/Y6	0.838 (0.835)	25.44 (25.20)	73.22 (72.81)	15.61 (15.32)
PM6/Y6(10% FBT)	0.833 (0.832)	24.74 (24.35)	71.27 (71.06)	14.69 (14.39)
PM6/Y6(20% FBT)	0.833 (0.833)	25.02 (24.88)	71.52 (71.32)	14.91 (14.78)
PM6/Y6(30% FBT)	0.831 (0.828)	25.48 (25.15)	71.68 (71.27)	15.40 (15.03)
PM6/Y6(40% FBT)	0.825 (0.825)	25.28 (25.08)	70.84 (70.55)	14.77 (14.60)

$^{a)}$ the statistical values in parentheses are obtained from 16 cells.

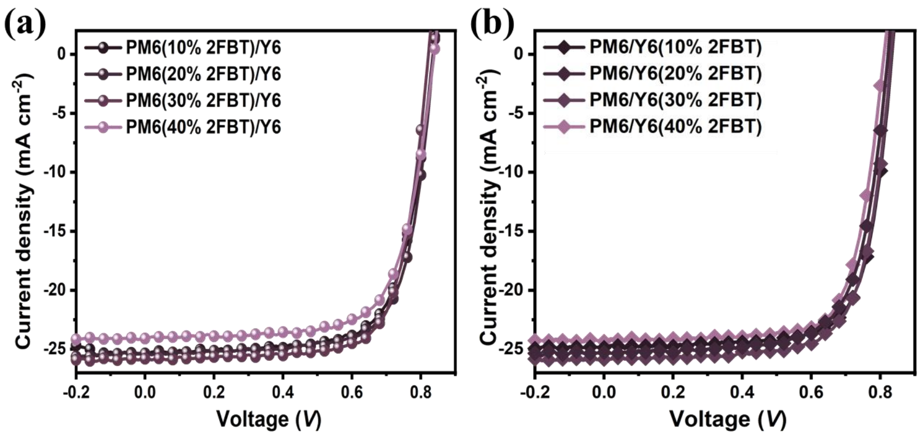

Figure 3.3.17. *J-V* curves of the PM6/Y6 LBL system with a different weight ratio of 2FBT additive on (a) donor and (b) acceptor layer.

Table 3.3.9. Summary of device parameters of PM6/Y6 devices with different weight ratios of 2FBT additive on donor or acceptor layer under illumination of AM 1.5G (100 mW cm^{-2}).

System	V_{OC} [V]	J_{SC} [mA cm^{-2}]	FF [%]	PCE [a] [%]
PM6(10% 2FBT)/Y6	0.842 (0.840)	25.43 (24.81)	70.02 (69.83)	14.99 (14.54)
PM6(20% 2FBT)/Y6	0.840 (0.842)	25.71 (25.41)	71.32 (70.90)	15.40 (15.17)
PM6(30% 2FBT)/Y6	0.839 (0.834)	25.83 (25.41)	72.88 (72.30)	15.79 (15.32)
PM6(40% 2FBT)/Y6	0.835 (0.833)	24.52 (23.95)	71.47 (71.14)	14.63 (14.20)
PM6/Y6(10% 2FBT)	0.835 (0.835)	24.67 (24.37)	70.03 (69.88)	14.43 (14.22)
PM6/Y6(20% 2FBT)	0.834 (0.833)	24.93 (24.81)	70.42 (70.27)	14.64 (14.52)
PM6/Y6(30% 2FBT)	0.830 (0.830)	25.31 (25.18)	70.98 (70.75)	14.91 (14.78)
PM6/Y6(40% 2FBT)	0.828 (0.826)	24.22 (24.00)	70.56 (70.36)	14.15 (13.95)

[a] the statistical values in parentheses are obtained from 16 cells.

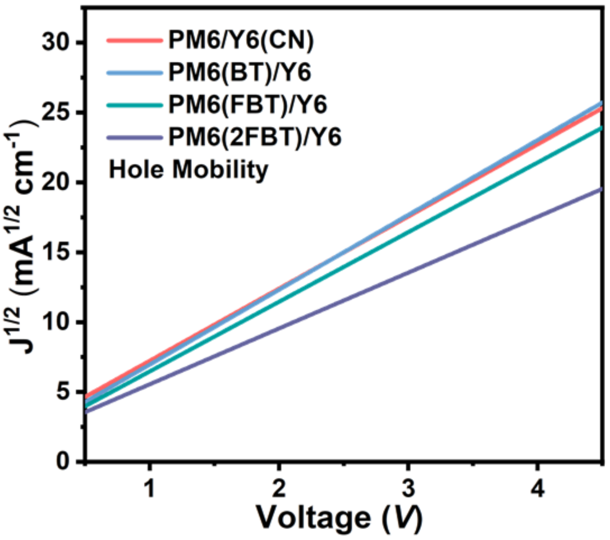

Figure 3.3.18. SCLC plots of hole only devices with PM6/Y6 LBL system with optimized additives.

Table 3.3.10. Hole mobility parameters of the PM6/Y6 devices with optimized additives**.**

System	μ_h [$cm^2V^{-1}s^{-1}$]
PM6/Y6(CN)	4.92×10^{-4}
PM6(BT)/Y6	5.12×10^{-4}
PM6(FBT)/Y6	5.67×10^{-4}
PM6(2FBT)/Y6	5.49×10^{-4}

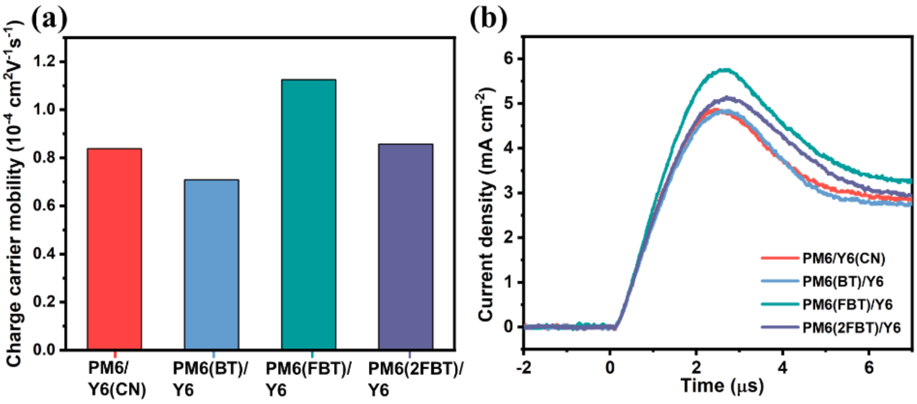

Figure 3.3.19. (a) Charge carrier mobility of LBL-based devices calculated from photo-CELIV. (b) Photo-CELIV measurement on the optimized devices.

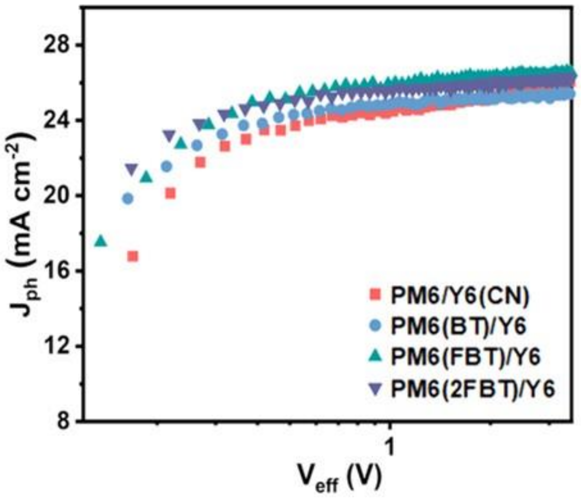

Figure 3.3.20. J_{ph} versus V_{eff} plots of the PM6/Y6 OSCs with optimized additives.

Table 3.3.11. Exciton dissociation probabilities and charge extraction probabilities of the devices.

System	Exciton dissociation probability (%)	Charge extraction probability (%)
PM6/Y6(CN)	97.71	76.21
PM6(BT)/Y6	97.42	75.06
PM6(FBT)/Y6	99.13	78.88
PM6(2FBT)/Y6	98.81	77.35

Table 3.3.12. Lattice parameters in out-of-plane and in-plane direction for LBL active layer films with optimized additives.

System	Out-of-Plane				In-Plane			
	π-π stacking (010)				Lamellar packing (100)			
	q (Å^{-1})	d-spacing (Å)	FWHM (Å^{-1})	Coherence length (Å)	q (Å^{-1})	d-spacing (Å)	FWHM (Å^{-1})	Coherence length (Å)
PM6/Y6(CN)	1.721	3.650	0.219	26.168	0.309	20.334	0.079	71.605
PM6(BT)/Y6	1.708	3.678	0.223	25.614	0.303	20.712	0.078	72.522
PM6(FBT)/Y6	1.709	3.672	0.215	26.646	0.305	20.579	0.074	76.308
PM6(2FBT)/Y6	1.713	3.667	0.211	27.090	0.304	20.654	0.074	76.754

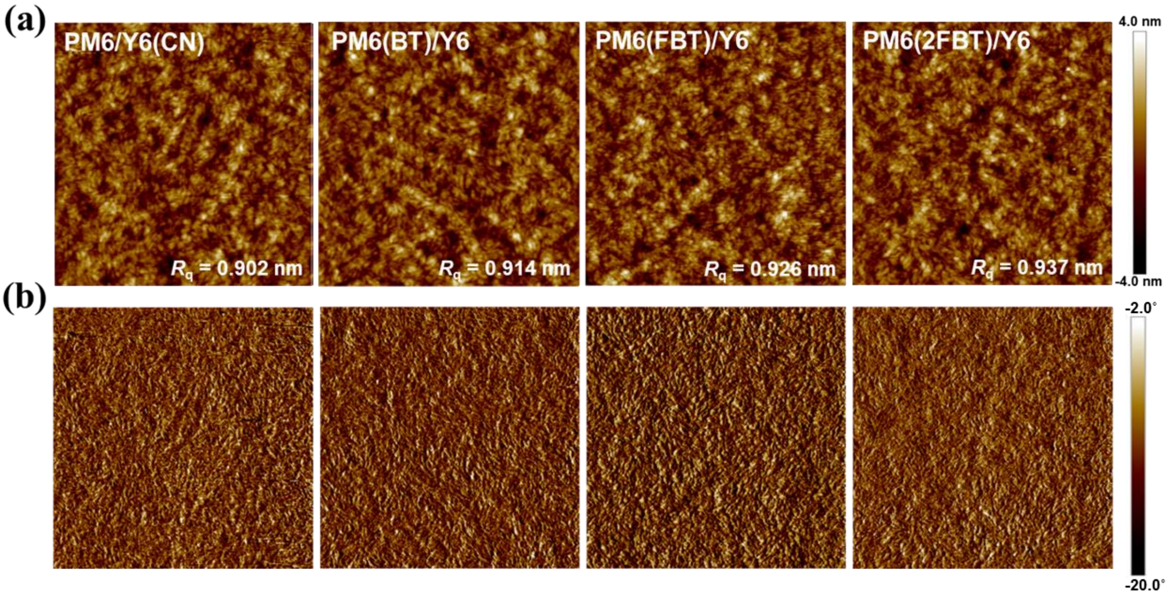

Figure 3.3.21. (a) Height and (b) phase AFM images (scan size 2 x 2 μm) of PM6/Y6 LBL system with optimized additives.

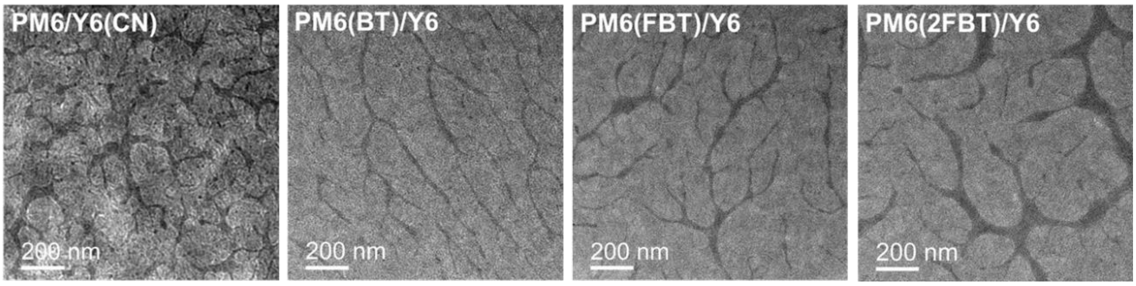

Figure 3.3.22. TEM images of PM6/Y6 LBL system with optimized additives.

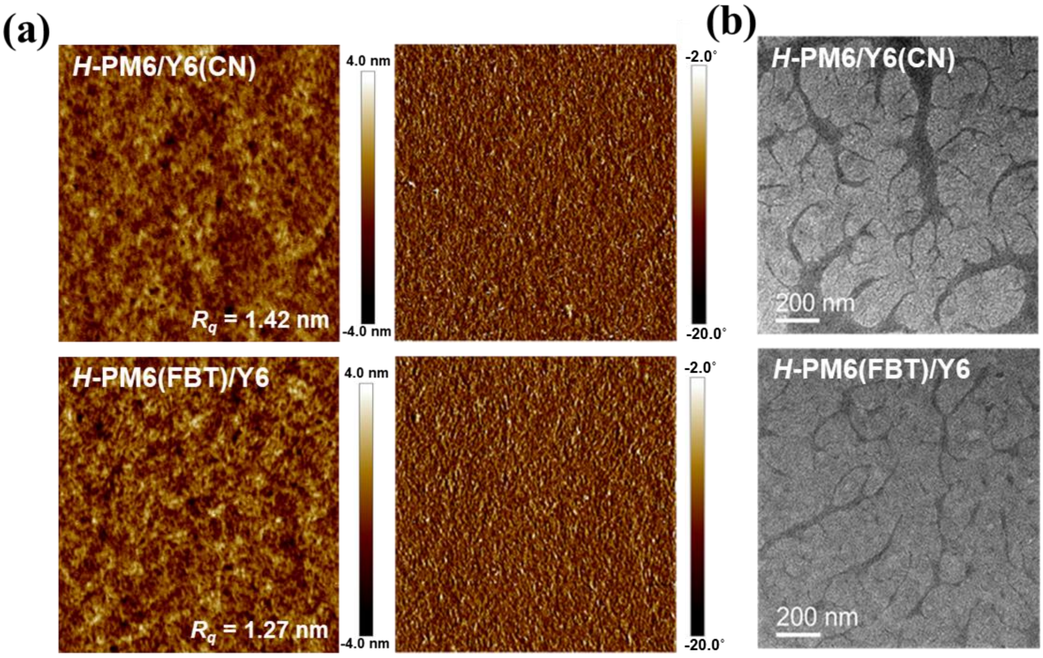

Figure 3.3.23. (a) AFM (scan size 2 x 2 μm) and (b) TEM images of *H*-PM6/Y6 LBL system with optimized additives.

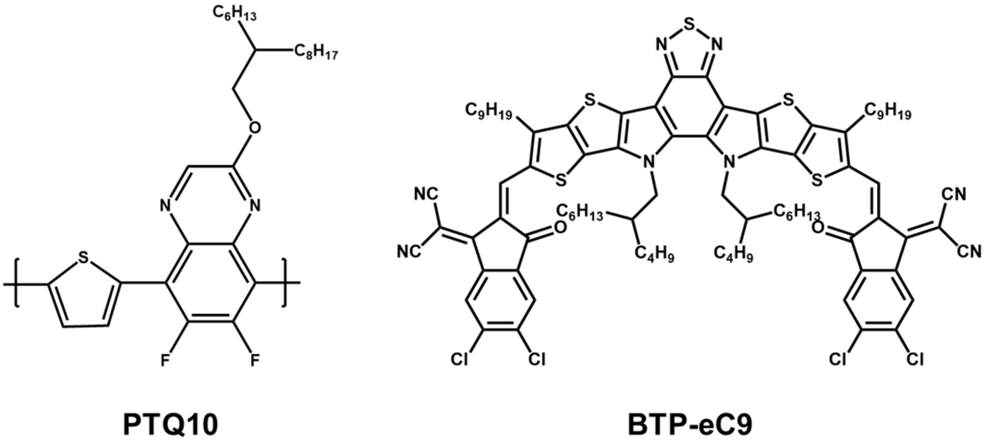

Figure 3.3.24. Chemical structures of PTQ10 and BTP-eC9.

Table 3.3.13. Summary of recently reported LBL OSCs.

Year	**Active layer**	**Processing Solvent**	**V_{OC} [V]**	**J_{SC} [mA cm^{-2}]**	**FF [%]**	**PCE [%]**	**Reference**
2019	PTQ10/IDIC	CF/CF	0.943	18.75	69.66	12.32	57
2020	PTQ10/Y6	CF/CF	0.849	24.49	72.63	15.10	58
2020	PM6/Y6-2Cl	CF/CF	0.849	25.88	72.30	15.89	58
2020	PM6/Y6-C2	CF/CF	0.834	25.82	73.99	15.93	58
2020	PM6/Y6	CF/CF	0.840	25.22	72.49	16.35	58
2020	PT2/Y6	CB/CF	0.83	26.7	74.4	16.5	59
2021	PM6/Y6	CB/CF	0.800	24.5	73.5	14.42	60
2021	PM6/N3:PC71BM	CF/CF	0.841	26.49	78.2	17.42	61
2021	PM6/BTP-eC9	*o*-xylene/*o*-xylene	0.840	26.65	78.1	17.48	62
2021	PM6/BTP-eC9	CF/CF	0.839	26.91	77.7	17.54	62
2021	PM6/BO-4Cl:BTP-S2	CF/CF	0.861	27.14	78.04	18.16	63
2022	PM6/Y6	CF/CF	0.861	25.76	73.67	16.35	64
2022	PM6/Y6:TIT-2Cl	CF/CF	0.876	26.63	77.93	18.18	64

Table 3.3.14. Summary of recently reported PM6-based OSCs treated with volatile solid additives.

Year	**System**	**Active layer**	**Additive**	**V_{OC} [V]**	**J_{SC} [mA cm^{-2}]**	**FF [%]**	**PCE [%]**	**Reference**
2020	BHJ	PM6:Y6	Ferrocene	0.838	26.71	76.0	17.40	65
2020	BHJ	PBDB-T-2F:BTP-4F	INB-5F	0.81	27.7	74.3	16.4	66
2020	BHJ	PM6:TPT10	BDT-1	0.899	24.80	73.00	16.26	67
2021	BHJ	PBDB-TF:BO4Cl	DTBF	0.846	26.2	77.0	17.1	68
2021	BHJ	PM6:Y6	Anthracene	0.844	25.91	77.8	17.02	69
2021	BHJ	PM6:Y6	A3	0.82	26.50	76.05	16.5	70
2021	LBL	PM6/Y6	DDO	0.85	25.51	77.45	16.93	71
2021	LBL	PBDB-TF/Y6	DTBF	0.823	26.0	76.6	16.4	72
2022	**LBL**	**PM6/BTP-eC9**	**FBT**	**0.835**	**26.68**	**79.52**	**17.71**	**Our Work**

Table 3.3.15. PCE variations according to molecular weights of donor polymer on different systems.

System	**ΔPCE [a)]**
PTQ10/Y6(DIO) *H*-PTQ10/Y6(DIO)	1.32
PTQ10(FBT)/Y6 *H*-PTQ10(FBT)/Y6	1.14
PM6/BTP-eC9(DIO) *H*-PM6/BTP-eC9(DIO)	1.86
PM6(FBT)/BTP-eC9 *H*-PM6(FBT)/BTP-EC9	1.52

[a)] the values follow this equation ($\mathrm{PCE}_{\mathrm{donor/acceptor}}$-$\mathrm{PCE}_{H\text{-}\mathrm{donor/acceptor}}$).

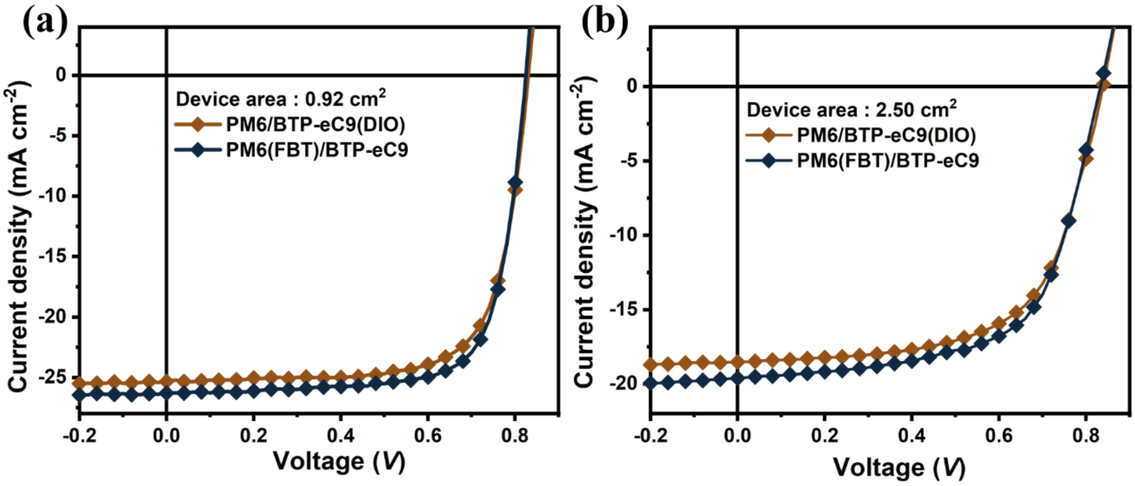

Figure 3.3.25. *J-V* curves of the PM6/BTP-eC9 LBL devices at (a) 0.92 cm^2 and (b) 2.50 cm^2.

3.3.8 References

1. D. Koo, S. Jung, J. Seo, G. Jeong, Y. Choi, J. Lee, S. M. Lee, Y. Cho, M. Jeong, J. Lee, J. Oh, C. Yang and H. Park, *Joule*, 2020, **4**, 1021-1034.
2. S. Chen, S. Jung, H. J. Cho, N.-H. Kim, S. Jung, J. Xu, J. Oh, Y. Cho, H. Kim, B. Lee, Y. An, C. Zhang, M. Xiao, H. Ki, Z.-G. Zhang, J.-Y. Kim, Y. Li, H. Park and C. Yang, *Angewandte Chemie International Edition*, 2018, **57**, 13277-13282.
3. M. Kaltenbrunner, M. S. White, E. D. Głowacki, T. Sekitani, T. Someya, N. S. Sariciftci and S. Bauer, *Nature Communications*, 2012, **3**, 770.
4. Y. Cui, H. Yao, J. Zhang, K. Xian, T. Zhang, L. Hong, Y. Wang, Y. Xu, K. Ma, C. An, C. He, Z. Wei, F. Gao and J. Hou, *Advanced Materials*, 2020, **32**, 1908205.
5. J. Yuan, Y. Zhang, L. Zhou, G. Zhang, H.-L. Yip, T.-K. Lau, X. Lu, C. Zhu, H. Peng, P. A. Johnson, M. Leclerc, Y. Cao, J. Ulanski, Y. Li and Y. Zou, *Joule*, 2019, **3**, 1140-1151.
6. M. Jeong, J. Oh, Y. Cho, B. Lee, S. Jeong, S. M. Lee, S.-H. Kang and C. Yang, *Advanced Functional Materials*, 2021, **31**, 2102371.
7. Y. Lin, A. Magomedov, Y. Firdaus, D. Kaltsas, A. El-Labban, H. Faber, D. R. Naphade, E. Yengel, X. Zheng, E. Yarali, N. Chaturvedi, K. Loganathan, D. Gkeka, S. H. AlShammari, O. M. Bakr, F. Laquai, L. Tsetseris, V. Getautis and T. D. Anthopoulos, *ChemSusChem*, 2021, **14**, 3569-3578.
8. F. Liu, L. Zhou, W. Liu, Z. Zhou, Q. Yue, W. Zheng, R. Sun, W. Liu, S. Xu, H. Fan, L. Feng, Y. Yi, W. Zhang and X. Zhu, *Advanced Materials*, 2021, **33**, 2100830.
9. Y. Lin, Y. Firdaus, F. H. Isikgor, M. I. Nugraha, E. Yengel, G. T. Harrison, R. Hallani, A. El-Labban, H. Faber, C. Ma, X. Zheng, A. Subbiah, C. T. Howells, O. M. Bakr, I. McCulloch, S. D. Wolf, L. Tsetseris and T. D. Anthopoulos, *ACS Energy Letters*, 2020, **5**, 2935-2944.
10. M. Zhang, L. Zhu, G. Zhou, T. Hao, C. Qiu, Z. Zhao, Q. Hu, B. W. Larson, H. Zhu, Z. Ma, Z. Tang, W. Feng, Y. Zhang, T. P. Russell and F. Liu, *Nature Communications*, 2021, **12**, 309.
11. S. Bao, H. Yang, H. Fan, J. Zhang, Z. Wei, C. Cui and Y. Li, *Advanced Materials*, 2021, **33**, 2105301.
12. C. J. Brabec, M. Heeney, I. McCulloch and J. Nelson, *Chemical Society Reviews*, 2011, **40**, 1185-1199.
13. Y. Wang and X. Zhan, *Advanced Energy Materials*, 2016, **6**, 1600414.
14. J. Zhang, H. S. Tan, X. Guo, A. Facchetti and H. Yan, *Nature Energy*, 2018, **3**, 720-731.
15. S. Li, C.-Z. Li, M. Shi and H. Chen, *ACS Energy Letters*, 2020, **5**, 1554-1567.
16. D. H. Kim, J. Mei, A. L. Ayzner, K. Schmidt, G. Giri, A. L. Appleton, M. F. Toney and Z. Bao, *Energy & Environmental Science*, 2014, **7**, 1103-1109.
17. M. Hiramoto, H. Fukusumi and M. Yokoyama, *Applied Physics Letters*, 1992, **61**, 2580-2582.

18. D. Wöhrle and D. Meissner, *Advanced Materials*, 1991, **3**, 129-138.

19. M. Hiramoto, H. Fujiwara and M. Yokoyama, *Applied Physics Letters*, 1991, **58**, 1062-1064.

20. M. Granström, K. Petritsch, A. C. Arias, A. Lux, M. R. Andersson and R. H. Friend, *Nature*, 1998, **395**, 257-260.

21. C. W. Tang, *Applied Physics Letters*, 1986, **48**, 183-185.

22. R. Yu, X. Wei, G. Wu and Z. a. Tan, *Aggregate*, 2022, **3**, e107.

23. Y. Zhang, K. Liu, J. Huang, X. Xia, J. Cao, G. Zhao, P. W. K. Fong, Y. Zhu, F. Yan, Y. Yang, X. Lu and G. Li, *Nature Communications*, 2021, **12**, 4815.

24. L. Zhan, S. Li, X. Xia, Y. Li, X. Lu, L. Zuo, M. Shi and H. Chen, *Advanced Materials*, 2021, **33**, 2007231.

25. K. Weng, L. Ye, L. Zhu, J. Xu, J. Zhou, X. Feng, G. Lu, S. Tan, F. Liu and Y. Sun, *Nature Communications*, 2020, **11**, 2855.

26. K. Jiang, J. Zhang, Z. Peng, F. Lin, S. Wu, Z. Li, Y. Chen, H. Yan, H. Ade, Z. Zhu and A. K. Y. Jen, *Nature Communications*, 2021, **12**, 468.

27. R. Sun, J. Guo, C. Sun, T. Wang, Z. Luo, Z. Zhang, X. Jiao, W. Tang, C. Yang, Y. Li and J. Min, *Energy & Environmental Science*, 2019, **12**, 384-395.

28. X. Xie, J. Liao, J. Liu, Y. Meng, W. Huang, X. Zhan, L.-M. Wang, Q. Li, T. Zhu, S. Liu and Y.-P. Cai, *Physica Status Solidi - Rapid Research Letters*, 2021, **15**, 2100386.

29. P. Cheng, C. Yan, Y. Wu, S. Dai, W. Ma and X. Zhan, *J. Mater. Chem. C*, 2016, **4**, 8086-8093.

30. X. Li, X. Du, J. Zhao, H. Lin, C. Zheng and S. Tao, *Solar RRL*, 2021, **5**, 2000592.

31. L. Ye, Y. Xiong, Z. Chen, Q. Zhang, Z. Fei, R. Henry, M. Heeney, B. T. O'Connor, W. You and H. Ade, *Advanced Materials*, 2019, **31**, 1808153.

32. H. Fan, H. Yang, Y. Wu, O. Yildiz, X. Zhu, T. Marszalek, P. W. M. Blom, C. Cui and Y. Li, *Advanced Functional Materials*, 2021, **31**, 2103944.

33. J. Oh, S. M. Lee, S. Jung, J. Lee, G. Park, S.-H. Kang, Y. Cho, M. Jeong, B. Lee, S. Kim and C. Yang, *Solar RRL*, 2021, **5**, 2000812.

34. R. Yu, H. Yao, L. Hong, Y. Qin, J. Zhu, Y. Cui, S. Li and J. Hou, *Nature Communications*, 2018, **9**, 4645.

35. L. Ye, Y. Cai, C. Li, L. Zhu, J. Xu, K. Weng, K. Zhang, M. Huang, M. Zeng, T. Li, E. Zhou, S. Tan, X. Hao, Y. Yi, F. Liu, Z. Wang, X. Zhan and Y. Sun, *Energy & Environmental Science*, 2020, **13**, 5117-5125.

36. X. Wang, L. Zhang, L. Hu, Z. Xie, H. Mao, L. Tan, Y. Zhang and Y. Chen, *Advanced Functional Materials*, 2021, **31**, 2102291.

37. R. Yu, G. Wu, Y. Cui, X. Wei, L. Hong, T. Zhang, C. Zou, S. Hu, J. Hou and Z. a. Tan, *Small*, 2021, **17**, 2103497.

38. S.-H. Kang, J. Lee, D. Yoo, B. H. Lee and C. Yang, *Journal of Materials Chemistry C*, 2019, **7**,

8522-8526.

39. J. Yuan, Y. Zhang, L. Zhou, C. Zhang, T.-K. Lau, G. Zhang, X. Lu, H.-L. Yip, S. K. So, S. Beaupré, M. Mainville, P. A. Johnson, M. Leclerc, H. Chen, H. Peng, Y. Li and Y. Zou, *Advanced Materials*, 2019, **31**, 1807577.
40. Y. Cui, H. Yao, J. Zhang, T. Zhang, Y. Wang, L. Hong, K. Xian, B. Xu, S. Zhang, J. Peng, Z. Wei, F. Gao and J. Hou, *Nature Communications*, 2019, **10**, 2515.
41. J. Lee, S.-H. Kang, S. M. Lee, K. C. Lee, H. Yang, Y. Cho, D. Han, Y. Li, B. H. Lee and C. Yang, *Angewandte Chemie International Edition*, 2018, **57**, 13629-13634.
42. Y. Wang and T. Michinobu, *Journal of Materials Chemistry C*, 2016, **4**, 6200-6214.
43. Q. Nie, A. Tang, Q. Guo and E. Zhou, *Nano Energy*, 2021, **87**, 106174.
44. R. Yu, H. Yao, Y. Xu, J. Li, L. Hong, T. Zhang, Y. Cui, Z. Peng, M. Gao, L. Ye, Z. a. Tan and J. Hou, *Advanced Functional Materials*, 2021, **31**, 2010535.
45. X. Zhang, Y. Li, D. Zhang, G. Wu, H. Zhang, J. Zhou, X. Li, Z. Saud uz, J. Zhang, Z. Wei, H. Zhou and Y. Zhang, *Science China Chemistry*, 2021, **64**, 116-126.
46. C. N. R. Rao, R. Venkataraghavan and T. R. Kasturi, *Canadian Journal of Chemistry*, 1964, **42**, 36-42.
47. Q. Li, L.-M. Wang, S. Liu, L. Guo, S. Dong, G. Ma, Z. Cao, X. Zhan, X. Gu, T. Zhu, Y.-P. Cai and F. Huang, *ACS Energy Letters*, 2020, **5**, 3637-3646.
48. A. Armin, G. Juska, M. Ullah, M. Velusamy, P. L. Burn, P. Meredith and A. Pivrikas, *Advanced Energy Materials*, 2014, **4**, 1300954.
49. T. Jia, W. Zhou, Y. Chen, J. Han, L. Wang, F. Li and Y. Wang, *Journal of Materials Chemistry A*, 2015, **3**, 4547-4554.
50. A. K. K. Kyaw, D. H. Wang, V. Gupta, W. L. Leong, L. Ke, G. C. Bazan and A. J. Heeger, *ACS Nano*, 2013, **7**, 4569-4577.
51. Y. Terao, H. Sasabe and C. Adachi, *Applied Physics Letters*, 2007, **90**, 103515.
52. M. D. M. Faure and B. H. Lessard, *Journal of Materials Chemistry C*, 2021, **9**, 14-40.
53. Z. Ding, J. Kettle, M. Horie, S. W. Chang, G. C. Smith, A. I. Shames and E. A. Katz, *Journal of Materials Chemistry A*, 2016, **4**, 7274-7280.
54. S. Samson, J. Rech, L. Perdigón-Toro, Z. Peng, S. Shoaee, H. Ade, D. Neher, M. Stolterfoht and W. You, *ACS Applied Polymer Materials*, 2020, **2**, 5300-5308.
55. B. Lee, S. Kim, H.-W. Nho, J. Oh, G. Park, M. Jeong, Y. Cho, S. M. Lee, O.-H. Kwon and C. Yang, *Advanced Energy Materials*, 2021, **11**, 2102594.
56. R. Sun, Q. Wu, J. Guo, T. Wang, Y. Wu, B. Qiu, Z. Luo, W. Yang, Z. Hu, J. Guo, M. Shi, C. Yang, F. Huang, Y. Li and J. Min, *Joule*, 2020, **4**, 407-419.

57 R. Sun, J. Guo, C. Sun, T. Wang, Z. Luo, Z. Zhang, X. Jiao, W. Tang, C. Yang, Y. Li, J. Min, *Energy & Environmental Science,* 2019, **12**, 384.

58 R. Sun, Q. Wu, J. Guo, T. Wang, Y. Wu, B. Qiu, Z. Luo, W. Yang, Z. Hu, J. Guo, M. Shi, C. Yang, F. Huang, Y. Li, J. Min, *Joule*, 2020, **4**, 407.

59 K. Weng, L. Ye, L. Zhu, J. Xu, J. Zhou, X. Feng, G. Lu, S. Tan, F. Liu, Y. Sun, *Nature Communications,* 2020, **11**, 2855.

60 X. Xie, J. Liao, J. Liu, Y. Meng, W. Huang, X. Zhan, L.-M. Wang, Q. Li, T. Zhu, S. Liu, Y.-P. *Physica Status Solidi – Rapid Research Letters,* 2021, **15**, 2100386.

61 K. Jiang, J. Zhang, Z. Peng, F. Lin, S. Wu, Z. Li, Y. Chen, H. Yan, H. Ade, Z. Zhu, A. K. Y. Jen, *Nature Commun*ications, 2021, **12**, 468.

62 Y. Zhang, K. Liu, J. Huang, X. Xia, J. Cao, G. Zhao, P. W. K. Fong, Y. Zhu, F. Yan, Y. Yang, X. Lu, G. Li, *Nature Communications*, 2021, **12**, 4815.

63 L. Zhan, S. Li, X. Xia, Y. Li, X. Lu, L. Zuo, M. Shi, H. Chen, *Advanced Materials*, 2021, **33**, 2007231.

64 J. Chen, J. Cao, L. Liu, L. Xie, H. Zhou, J. Zhang, K. Zhang, M. Xiao, F. Huang, *Advanced Functional Materials*, 2200629.

65 L. Ye, Y. Cai, C. Li, L. Zhu, J. Xu, K. Weng, K. Zhang, M. Huang, M. Zeng, T. Li, E. Zhou, S. Tan, X. Hao, Y. Yi, F. Liu, Z. Wang, X. Zhan, Y. Sun, *Energy & Environmental Science*, 2020, **13**, 5117.

66 J. Cai, H. Wang, X. Zhang, W. Li, D. Li, Y. Mao, B. Du, M. Chen, Y. Zhuang, D. Liu, H.-L. Qin, Y. Zhao, J. A. Smith, R. C. Kilbride, A. J. Parnell, R. A. L. Jones, D. G. Lidzey, T. Wang, *Journal of Materials Chemistry A*, 2020, **8**, 4230.

67 Y. Zhang, Y. Cho, J. Lee, J. Oh, S.-H. Kang, S. M. Lee, B. Lee, L. Zhong, B. Huang, S. Lee, J.-W. Lee, B. J. Kim, Y. Li, C. Yang, *Journal of Materials Chemistry A,* 2020, **8**, 13049.

68 R. Yu, H. Yao, Y. Xu, J. Li, L. Hong, T. Zhang, Y. Cui, Z. Peng, M. Gao, L. Ye, Z. a. Tan, J. Hou, *Advanced Functional Materials*, 2021, **31**, 2010535.

69 H. Fan, H. Yang, Y. Wu, O. Yildiz, X. Zhu, T. Marszalek, P. W. M. Blom, C. Cui, Y. Li, *Advanced Functional Materials*, 2021, **31**, 2103944.

70 J. Fu, S. Chen, K. Yang, S. Jung, J. Lv, L. Lan, H. Chen, D. Hu, Q. Yang, T. Duan, Z. Kan, C. Yang, K. Sun, S. Lu, Z. Xiao, Y. Li, *iScience* 2020, **23**, 100965.

71 X. Wang, L. Zhang, L. Hu, Z. Xie, H. Mao, L. Tan, Y. Zhang, Y. Chen, *Advanced Functional Materials*, 2021, **31**, 2102291.

72 R. Yu, G. Wu, Y. Cui, X. Wei, L. Hong, T. Zhang, C. Zou, S. Hu, J. Hou, Z. a. Tan, *Small*, 2021, **17**, 2103497.

CHAPTER 4 Experimental Section

4.1 General Material Characterization Methods

On a Varian VNRS 400 MHz spectrometer, ^{1}H and ^{13}C NMR spectra were acquired using $CDCl_3$ as the solvent and tetramethylsilane as the internal standard. Ultraflex III was used to get MALDI-MS spectra. CV measurements were performed on an Iviumstat.h 3 with a three-electrode cell system in a nitrogen bubbled 0.1 M n-Bu_4NPF_6 solution in acetonitrile at a scan rate of 100 mV s^{-1} at room temperature. An Ag/Ag^+ electrode, platinum wire, and platinum were used as the reference electrode, counter electrode, and working electrode, respectively. The Ag/Ag^+ reference electrode was calibrated using a ferrocene/ferrocenium redox couple as an external standard, whose oxidation potential is set at –4.8 eV with respect to a zero-vacuum level. The HOMO energy levels were obtained from the equation HOMO (eV) = $-(E_{\mathrm{ox}}^{\mathrm{onset}} - E_{1/2}^{\mathrm{ferrocene}} + 4.8)$. The LUMO levels were obtained from the equation LUMO (eV)= $-4.8 - (E_{\mathrm{red}}^{\mathrm{onset}} - E_{1/2}^{\mathrm{ferrocene}})$. The M_{n} and M_{w} molecular weights, and the PDI of the polymer were determined by HT-GPC with Agilent 1200 HPLC and mini DAWN TREOS using polystyrene as the standard in 1,2,4-trichlorobenzene at 100 °C (HPLC grade). UV-vis spectra were recorded with a UV-1800 instrument (SHIMADZU). PL spectra was obtained by a Varian Cary Eclipse fluorescence spectrometer. DSC and TGA were conducted with a differential scanning calorimeter (TA instruments, USA) with a scan rate of 10 °C per minute. The FT-IR absorption spectra were measured on a Varian 670 infrared spectrometer with wavenumber ranging from 1000 to 4000 cm^{-1}.

4.2 Material Synthetic Procedures and Characterizations

Without additional purification, all chemicals and reagents were acquired from Sigma-Aldrich, Alfa Aesar chemical bsiness, and Tokyo Chemical Industry Co., Ltd. Unless otherwise specified, all solvents were ACS grade.

Chapter 2.1

*Synthesis of triisopropyl(thiophen-2-yl)silane (**3**)*: To a two-neck round-bottom flask, thiophene was dissolved in anhydrous THF and purged with argon for 20 min. The solution was then cooled to −78 °C and n-BuLi was added dropwise. After 1 h at this temperature, triisopropylsilyl chloride was added to the reaction mixture, warmed to room temperature, and stirred overnight. The reaction was quenched with water, then the mixture was extracted with diethyl ether, dried with $MgSO_4$, and solvent was removed under reduced pressure. The crude products were purified via silica gel column chromatography using hexane as an eluent to afford a product as a transparent liquid (5.12 g, 89.6% yield). ^{1}H NMR (400 MHz, $CDCl_3$), δ (ppm): 7.62 (d, 1H), 7.29 (d, 1H), 7.22 (dd, 2H), 1.34 (m, 3H), 1.10 (d, 18H).

Synthesis of iBDD-Si (4): To a mixture solution of compound **1** in anhydrous dichloromethane, oxalyl chloride and catalytic amount of DMF was added. The resulting solution was stirred for 12 h at room temperature, and volatiles were removed under reduced pressure to obtain crude 2,5-dibromothiophene-3,4-dicarbonyl dichloride (**2**) which was used for next step directly. To a stirred solution of the compound **2** in anhydrous dichloromethane, $AlCl_3$ was added in small portions at 0 °C. The mixture was stirred for 3 h at this temperature, then compound **3** was added dropwise. The mixture was stirred at room temperature for 3 h, poured into ice water to quench the reaction, and extracted with dichloromethane. The combined organic layer was dried with $MgSO_4$ and solvent was removed using rotary evaporator. The crude products were purified by a silica gel column chromatography eluting with hexane/dichloromethane (2:1, v/v) to obtain compound 4 as a light yellow solid (1.04 g, 64.2% yield). ^{1}H NMR (400 MHz, $CDCl_3$), δ (ppm): 7.78 (s, 1H), 1.39 (m, 3H), 1.12 (d, 18H).

Synthesis of iBDDTh-Si (5): To a two-neck round-bottom flask, compound **4** and tributyl(thiophen-2-yl)stannane were dissolved in toluene, and purged with argon for 15 min. Subsequently, $Pd(PPh_3)_4$ was added, purged again with argon for 15 min, and the mixture heated to reflux overnight. After removing solvent under reduced pressure, the crude product was purified by a silica gel column chromatography eluting with hexane/dichloromethane (2:1, v/v) to obtain compound **5** as a reddish solid. ^{1}H NMR (400 MHz, $CDCl_3$), δ (ppm): 7.86 (m, 2H), 7.81 (s, 1H), 7.55 (m, 2H), 7.15 (m, 2H), 1.39 (m, 3H), 1.13 (d, 18H).

Synthesis of iBDDTh-Si-Br: In a two-neck round-bottom flask, compound **5** was dissolved in THF, and NBS was added in one portion. The reaction mixture was stirred 3 h in the absence of light. Water was added, and the mixture was extracted with dichloromethane, dried over $MgSO_4$, and concentrated under reduced pressure. Further purification via silica gel column chromatography using hexane/dichloromethane (3:1, v/v) to afford *i*BDDTh-Si-Br_2 as a reddish solid (979.2 mg, 94.7% yield). ^{1}H NMR (400 MHz, $CDCl_3$), δ (ppm): 7.82 (s, 1H), 7.55 (m, 2H), 7.11 (m, 2H), 1.39 (m, 3H), 1.13 (d, 18H). ^{13}C NMR (100 MHz, $CDCl_3$), δ (ppm): 176.33, 174.34, 151.32, 148.07, 144.55, 143.09, 134.55, 134.11, 131.23, 130.14, 119.17, 18.54, 11.71. EA: anal. calcd C, 46.42; H, 3.75; S, 18.36; Found: C, 46.43; H, 3.74; S, 18.38. HRMS (ESI) m/z 697.90 ($C_{27}H_{26}Br_2O_2S_4Si$ calcd. for m/z 697.89).

General procedure for polymerization and purification of copolymers: To a long Schlenk flask, BDT(2F)-Sn_2 (1.0 eq.), *i*BDDTh-Si-Br_2 (x eq.), and BDDTh-Br_2 (1−x eq.) were dissolved in freshly distilled toluene (5 mL), and purged with argon for 20 min. Then, $Pd(PPh_3)_4$ (0.02 eq. of BDT(2F)-Sn_2)

was added and purged again with argon for 20 min. The reaction mixture was stirred at 120 °C for 48 h, and precipitated to methanol. Crude copolymer was washed via sequential Soxhlet extraction with methanol, acetone, hexane to remove low molecular weight fractions. The residue was extracted with CF, concentrated, precipitated to methanol, and filtered. Filtrates were dried in high vacuum oven to afford the purified copolymer as a dark solid.

Synthesis of PM6: Using the procedure described above, BDT(2F)-Sn_2 and BDDTh-Br_2 was used to synthesize PM6. Isolated yield = 95.7%, ^{1}H NMR (600 MHz, TCE-d_2, 70 °C), δ (ppm): 7.99–6.49 (br), 3.53–2.63 (br), 2.17–1.26 (br), 1.23–0.69 (br). EA: anal. calcd C, 66.85; H, 6.43; S, 20.99; Found: C, 66.91; H, 6.42; S, 20.95.

Synthesis of PM6-5Si: Using the procedure described above, BDT(2F)-Sn_2, *i*BDDTh-Si-Br_2, and BDDTh-Br_2 was used to synthesize PM6-5Si. Isolated yield = 96.1%, ^{1}H NMR (600 MHz, TCE-d_2, 70 °C), δ (ppm): 7.99–6.49 (br), 3.53–2.63 (br), 2.17–1.26 (br), 1.23–0.69 (br). EA: anal. calcd C, 66.68; H, 6.40; S, 21.05; Found: C, 66.70; H, 6.41; S, 21.07.

Synthesis of PM6-10Si: Using the procedure described above, BDT(2F)-Sn_2, *i*BDDTh-Si-Br_2, and BDDTh-Br_2 was used to synthesize PM6-10Si. Isolated yield = 93.8%, ^{1}H NMR (600 MHz, TCE-d_2, 70 °C), δ (ppm): 7.99–6.49 (br), 3.53–2.63 (br), 2.17–1.26 (br), 1.23–0.69 (br). EA: anal. calcd C, 66.51; H, 6.36; S, 21.11; Found: C, 66.56; H, 6.35; S, 21.15.

Synthesis of PM6-15Si: Using the procedure described above, BDT(2F)-Sn_2, *i*BDDTh-Si-Br_2, and BDDTh-Br_2 was used to synthesize PM6-15Si. Isolated yield = 91.7%, ^{1}H NMR (600 MHz, TCE-d_2, 70 °C), δ (ppm): δ (ppm): 7.99–6.49 (br), 3.53–2.63 (br), 2.17–1.26 (br), 1.23–0.69 (br). EA: anal. calcd C, 66.35; H, 6.33; S, 21.18; Found: C, 66.31; H, 6.34; S, 21.20.

Chapter 3.1

Synthesis of PS macroinitiator: In a round flask, 1-bromoethyl benzene (0.1 g, 0.54 mmol) was dissolved completely in *p*-xylene (7 mL), and styrene (5 mL, 4.36 mmol) was shortly passed through an aluminum oxide column to remove the inhibitor before use. Then, CuBr (0.0775 g, 0.54 mmol), PMDETA (0.22 mL, 1.02 mmol) were added to the solution at room temperature under argon. Then, the reaction mixture was stirred at 110 °C for 4 h. After the reaction had completed, the polymer solution was precipitated into methanol and filtered off. Finally, the PS polymer was obtained under a *vacuum*. M_n = 8.6 kDa, PDI = 1.29. ^{1}H NMR (400 MHz, $CDCl_3$, δ): 7.20 to 6.30 (br, Ar-*H*), 4.60 to 4.35 (br, -CH_2Br), 2.10 to 1.60 (br, -CH_2-), 1.50 to 1.30 (br, -C*H*-), 1.30 to 1.25 (br, -CH_3)

Synthesis of PS-b-PPFS: In a round flask, the PS macroinitiator (0.1 g) was dissolved completely in *p*-xylene (7 mL), and PFS monomer (6.02 mL, 4.36 mmol), CuBr (0.0775 g, 0.54 mmol), PMDETA (0.22 mL, 1.02 mmol) were added to the solution at room temperature under argon. Then, the reaction mixture was stirred at 110 °C for 4 h. After the reaction had completed, the polymer solution was precipitated into methanol and filtered off. Finally, the PS-*b*-PPFS block copolymer was obtained under a *vacuum*. M_n = 40.7 kDa, PDI = 1.39. ^{1}H NMR (400 MHz, $CDCl_3$), δ (ppm): 7.20 to 6.30 (br, Ar-*H*), 2.25 to 1.70 (br, -CH_2-), 1.50 to 1.20 (br, -C*H*-)

Synthesis of PPFS: In a round flask, PFS monomer (3 mL, 2.17 mmol) passed through an aluminum oxide column to remove the inhibitor before use and was dissolved completely in *p*-xylene (5 mL). AIBN (0.089 g, 0.05 mmol) was added to the solution at room temperature under argon. Then, the reaction mixture was stirred at 110 °C for 4 h. After the reaction had completed, the polymer solution was precipitated into methanol and filtered off. Finally, the PPFS homopolymer was obtained under a *vacuum*. M_n = 5.2 kDa, PDI = 1.33. ^{1}H NMR (400 MHz, $CDCl_3$), δ (ppm): 2.75 to 2.15 (br, -CH_2-), 2.10 to 1.70 (br, -C*H*-)

Chapter 3.2

According to the previously disclosed procedures, PM6, J71, IT4F, ITIC, and Y6 were synthesized.[1-4]

Synthesis of 12-bromododecyl 3-(3,5-di-tert-butyl-4-hydroxyphenyl)propionate (1): In methylene chloride, 3-(3,5-*di-tert*-butyl-4-hydroxyphenyl)propionic acid, 12-bromo-1-dodecanol, and 4-(dimethylamino)pyridine were dissolved. After cooling the solution to 0°C, *N,N'*-dicyclohexylcarbodiimide was added, followed by a return to room temperature. After five hours of vigorous stirring, the precipitate was filtered and purified by silica gel column chromatography. White powder, yield = 91.2% (1.7 g). ^{13}C NMR ($CDCl_3$, 100 MHz) δ ppm 173.41, 152.18, 135.92, 131.20, 124.82, 64.67, 36.58, 34.36, 34.12, 32.89, 31.10, 30.36, 29.56, 29.55, 29.54, 29.48, 29.30, 28.82, 28.71, 28.22, 25.97; ^{1}H NMR ($CDCl_3$, 400 MHz) δ ppm 7.00 (s, 2H), 5.06 (s, 1H), 4.08 (t, *J* = 6.8 Hz, 2H), 3.40 (t, *J* = 6.8 Hz, 2H), 2.89 – 2.84 (m, 2H), 2.66 – 2.44 (m, 2H), 1.93 – 1.79 (m, 2H), 1.65 – 1.57 (m, 2H), 1.41 (s, 18H), 1.33 – 1.19 (m, 12H); MALDI-TOF MS (*m/z*) 524.171 (M^+).

Synthesis of 12-cyanododecyl 3-(3,5-di-tert-butyl-4-hydroxyphenyl)propionate (BHT-CN): Compound 1 was dissolved with sodium cyanide in dimethylformamide. After 6 hours of heating at 70 °C, the mixture was cooled to room temperature, water was added, and the organic layer was separated using ethyl ether. The precipitate was filtered out after drying with magnesium sulfate, and the filtrate was purified using silica gel column chromatography. Pale yellow powder, yield = 83.7%. ^{13}C NMR ($CDCl_3$, 100 MHz) δ ppm 173.41, 152.18, 135.93, 131.20, 124.82, 119.91, 64.65, 36.58, 34.36, 31.08, 30.36, 29.54, 29.51, 29.33, 29.30, 28.81, 28.72, 28.70, 25.95, 25.43, 17.19; ^{1}H NMR ($CDCl_3$, 400 MHz) δ ppm 7.00 (s, 2H), 5.08 (s, 1H), 4.07 (t, *J* = 6.8 Hz, 2H), 2.86 (t, *J* = 6.8 Hz, 1H), 2.63 – 2.55 (m, 2H), 2.33

(t, *J* = 7.1 Hz, 2H), 1.71 – 1.58 (m, 2H), 1.43 (s, 18H), 1.35 – 1.22 (m, 12H); MALDI-TOF MS (*m/z*) 471.552 (M^+).

Synthesis of 12-bromododecyl tricosafluorododecyl 3-(3,5-di-tert-butyl-4-hydroxyphenyl)propanoate (BHT-PF): Methylene chloride was used to dissolve 3-(3,5-*di*-*tert*-butyl-4-hydroxyphenyl)propionic acid, 1*H*,1*H*-perfluoro-1-dodecanol), and 4-(dimethylamino)pyridine. The solution was cooled to 0 °C, *N, N'*-dicyclohexylcarbodiimide was added, and then the temperature was brought back to room temperature. After 5 hours of vigorous stirring, the precipitate was filtered out and the filtrate was purified by silica gel column chromatography. White powder, yield = 86.4% (2.67 g). ^{13}C NMR ($CDCl_3$, 100 MHz) δ ppm 171.58, 152s.36, 136.06, 130.40, 124.77, 35.86, 34.33, 30.66, 30.30; ^{1}H NMR ($CDCl_3$, 400 MHz) δ ppm 6.97 (s, 2H), 5.09 (s, 1H), 4.58 (t, *J* = 13.7 Hz, 2H), 2.89 (t, *J* = 6.9 Hz, 2H), 2.76 – 2.65 (m, 2H), 1.42 (s, 18H); MALDI-TOF MS (m/z) 860.443 (M^+).

Chapter 3.3

BT (2,1,3-Benzothiadiazole) was purchased from Combi-Blocks. FBT and 2FBT were synthesized according to previously reported literature.[5] PM6, *L*-PM6, *H*-PM6, and *H*-PTQ10 were synthesized according to the previously reported methods.[6,7] PTQ10 was purchased from Brilliant Matters (M_n: 19.1 kDa, M_w: 40.9 kDa, PDI: 2.14). Y6 and BTP-eC9 were purchased from eflexPV. The molecular weights of the PM6 and PTQ10 were characterized with HR-GPC at 100 °C using polystyrene as the standard in 1,2,4-trichlorobenzene (HPLC grade). The solutions for FT-IR absorption spectra were prepared by PM6 films with BT solid additives of optimized weight ratio in chloroform with same concentration of 8mg mL^{-1}.

Synthesis of PM6: Diorganobromide (500 mg, 0.532 mmol) and diorganostanne (407.6 mg, 0.532 mmol) compounds were dissolved in toluene (22.5 ml) in a two-neck round flask and then purged with argon for 30 min. A solution of $Pd(PPh_3)_4$ (24.6 mg, 0.021 mmol) in anhydrous toluene (2.5 ml) was added to the mixture in one portion in an argon state. Then the mixture was heated at 120 °C in a pre-heated oil bath for 12 h. The resulting polymers were precipitated in methanol, followed by Soxhlet extraction in sequence of methanol, acetone, and n-hexane. Finally, the chloroform fraction was extracted and reprecipitated in methanol to get the target product (M_n: 41.3 kDa, M_w: 109.7 kDa, PDI: 2.66).

Synthesis of L-PM6: According to the procedure described above, the mixture was heated at 120 °C in a pre-heated oil bath for 9 h to synthesize L-PM6 (M_n: 30.4 kDa, M_w: 106.9 kDa, PDI: 3.51).

Synthesis of H-PM6: According to the procedure described above, the mixture was heated at 120 °C in a pre-heated oil bath for 36 h to synthesize H-PM6 (M_n: 49.3 kDa, M_w: 144.7 kDa, PDI: 2.93).

Synthesis of H-PTQ10: 2,5-bis(trimethylstannyl)thiophene (82.0 mg, 0.2 mmol) and 5,8-dibromo-6,7-difluoro-2-((2-hexyldecyl)oxy)quinoxaline (112.9 mg, 0.2 mmol) were dissolved in anhydrous toluene (6 mL) in a long Schlenk flask, and purged with argon for 20 min. Then, of tetrakis(triphenylphosphine)palladium(0) (6.9 mg, 0.006 mmol) was added and purged again with argon for 20 min. The reaction mixture was stirred at 110 °C for 36 h. After cooling down, the crude mixture was poured into methanol, then transferred to thimble filter. Sequential Soxhlet extraction with methanol, acetone, and hexane was performed to remove low molecular weight fractions. The residue was extracted with chloroform, concentrated, and precipitated to methanol. The purified polymer was collected by filtration and dried in high vacuum oven (M_n: 46.7 kDa, M_w: 111.8 kDa, PDI: 2.39).

4.3 Solar Cell Device Fabrication and Characterization Methods

Chapter 2.1

The patterned ITO-coated glass substrates were rinsed using detergent, acetone and isopropanol and were subsequently dried overnight in an oven. The OSCs were fabricated with a configuration of ITO/PEDOT:PSS/active layer/PDINO/Al. PEDOT:PSS (Bayer Baytron AI4083) was spin- coated at 4000 rpm onto an ITO substrate, followed by annealing at 140 °C for 10 min in air. The active layers were spin-coated from CF solution and 0.5 vol% CN as a solvent additive with total concentration of 17.6 mg mL^{-1} (PM6:N3 dissolved at RT) followed by thermal annealing 80 °C for 5 min. In the case of PM6-xSi polymers, the active layers were spin-coated from CF solution and 0.5 vol% CN with total concentration of 15 mg mL^{-1} (PM6-5/10Si:N3 dissolved at RT and PM6-15Si:N3 dissolved at 40 °C) followed by thermal annealing 100 °C for 5 min. Then, a methanol solution of PDINO (1.0 mg mL^{-1}) was spin-coated onto the active layer with a spin rate of 3000 rpm for 30 s. Finally, a 100 nm Al cathode was thermally evaporated on top of the substrates under vacuum ($<3.0 \times 10^{-6}$ Pa). The area of fabricated OSC devices is 4.77 mm^2. The *J*–*V* characteristics were measured on a Keithley 2400 source under the illumination of an AM 1.5G solar simulator with an intensity of 100 mW cm^{-2}.

Chapter 3.1

The NF-OSCs were fabricated with a configuration of ITO/PEDOT:PSS/active layer/PDINO/Al. PEDOT:PSS was spin-coated at 4000 rpm onto ITO substrate, followed by annealing at 140 ˚C for 15 min in air. The active layer was spin-coated from chlorobenzene solution with a D:A weight ratio of 1:1 *w/w*% and heated at 45 ˚C for overnight under stirring. In each polymer additives case (1 to 5) *w/w*% of the total active layer concentration while in DIO case (0.5, 1, 2, and 3) *v/v*% of the solvent volume was used in the preparation of additive based active layer solution, followed by a thermal annealing treatment at 150 ˚C for 10 min. Then, methanol solution of PDINO was spin-coated on the active layer with spin rate of 3000 rpm for 30 s. Finally, 100 nm Al cathode was thermally evaporated on top of the substrates under vacuum ($< 3.0 \times 10^{-6}$ Pa).

Chapter 3.2

The OSCs were fabricated with a configuration of ITO/PEDOT:PSS/active layer/PDINO/Al. PEDOT:PSS (Bayer Baytron 4083) and spin-coated at 4000 rpm onto an ITO substrate, followed by annealing at 140 °C for 10 min in air. The active layer was spin-coated from chlorobenzene solution with a D : A weight ratio of 1 : 1 and heated at 45 °C overnight under stirring. For each BHT-based additive case, 1 to 5 w/w% of the total active layer concentration (while in DIO case, 0.5 v/v% of the solvent volume) was used in the preparation of the active layer solution, followed by thermal annealing treatment at 100 °C for 10 min. Then, a methanol solution of PDINO (1.0 mg mL^{-1}) was spin-coated onto the active layer with a spin rate of 3000 rpm for 30 s. Finally, a 100 nm Al cathode was thermally evaporated on top of the substrates under vacuum (<3.0 x 10^{-6} Pa).

Chapter 3.3

PM6/Y6 based LBL device was fabricated with a configuration of ITO/PEDOT:PSS/PM6/Y6/PDINO/Al. PEDOT:PSS (Bayer Baytron 4083) was spin-coated at 4000 rpm onto an ITO substrate, followed by annealing at 140 °C for 10 min in air. As for the LBL OSCs, PM6 solution was prepared in chloroform at 8 mg mL^{-1} with 10 to 40% (w/w) BT solid additives of the PM6 concentration. Y6 solution was prepared in chloroform at 9 mg mL^{-1} with 0.5% CN of the solvent volume. The PM6 solution was spin-coated on the PEDOT:PSS film at 2200 rpm for 60 s, and then annealed at 100 °C for 5 min. Y6 is deposited on the PM6 film at 2300 rpm for 60 s with annealing at 100 °C for 5 min. In case of PTQ10/Y6 based device, PTQ10 and Y6 were prepared at 7 mg mL^{-1} and 9 mg mL^{-1} respectively. For PM6/BTP-eC9 based device, the device structure of ITO/PEDOT:PSS/PM6/BTP-eC9/PFN-Br/Ag. PM6 was prepared at 7 mg mL^{-1} and BTP-eC9 with concentration of 9 mg mL^{-1}. The donor polymer film with FBT additive was treated with thermal annealing at 100 °C for 5 min, and then the acceptor film is processed with annealing at 100 °C for 5 min. Then, a methanol solution of PDINO (1.0 mg mL^{-1}) or PFN-Br (0.5 mg mL^{-1}) was spin-coated onto the active layer with a spin rate of 3000 rpm for 30 s. Finally, a 100 nm Al or Ag cathode was thermally evaporated on top of the substrates under vacuum (<3.0 x 10^{-6} Pa).

Characterization Methods

The *J*–*V* characteristics were measured on a Keithley 2400 source under the illumination of an AM 1.5G solar simulator with an intensity of 100 mW cm^{-2}. The EQE was measured in ambient air using the QE-R3011 (Enli Technology) model. The electron and hole mobilities were measured using the SCLC technique. For hole-only devices, the device architectures are ITO/PEDOT:PSS/active layer/Au and ITO/ZnO/active layer/PDINO/Al, respectively. The SCLC mobilities were calculated using the Mott–Gurney equation, SCLC = $(9/8)\varepsilon_0\varepsilon_r\mu((V_2)/(L_3))$, where ε_r is the relative dielectric constant of the organic semiconductor, ε_0 is the permittivity oy space, μ is the mobility of zero-field, L is the thickness of the active layer, and *V* is apphas appliedge across the device. Thin-film AFM images were acquired with a multimode V microscope (Veeco, USA) with a nanoscope controller and Si tips (Bruker). A JEOL USA JEM-2100F (Cs corrector) transmission electron microscope was utilized for TEM examination. At the PLS-II 6D U-SAXS beamline of the Pohang Accelerator Laboratory in Korea, GIWAXS was conducted. The scattering signal was recorded with a two-dimensional CCD detector (Rayonix SX165). The X-ray light had an 11,24 KeV energy. Adjusting the incidence angle of X-rays to 0.12 to maximize the signal-to-background ratio. XPS was measured using K-alpha.

4.4 References

1. W. Zhao, S. Li, H. Yao, S. Zhang, Y. Zhang, B. Yang, J. Hou, *Journal of the American Chemical Society,* 2017, **139**, 7148.
2. J. Yuan, Y. Zhang, L. Zhou, G. Zhang, H.-L. Yip, T.-K. Lau, X. Lu, C. Zhu, H. Peng, P. A. Johnson, M. Leclerc, Y. Cao, J. Ulanski, Y. Li, Y. Zou, *Joule,* 2019, **3**, 1140;
3. M. Zhang, X. Guo, W. Ma, H. Ade, J. Hou, *Advanced Materials*, 2015, **27**, 4655;
4. H. Bin, L. Gao, Z.-G. Zhang, Y. Yang, Y. Zhang, C. Zhang, S. Chen, L. Xue, C. Yang, M. Xiao, Y. Li, *Nature Communications*, 2016, **7**, 13651.
5. N. Cho, K. Song, J. K. Lee, J. Ko, *Chemistry – A European Journal*, 2012, **18**, 11433.
6. L. Ye, S. Li, X. Liu, S. Zhang, M. Ghasemi, Y. Xiong, J. Hou, H. Ade, *Joule*, 2019, **3**, 443
7. C. Sun, F. Pan, H. Bin, J. Zhang, L. Xue, B. Qiu, Z. Wei, Z.-G. Zhang, Y. Li, *Nature Communications*, 2018, **9**, 743.

CHAPTER 5 Acknowledgement

2017 년 설레는 마음을 안고 들어온 대학원에서 이제 2022 년, 졸업을 앞두고 있습니다. 6 년이라는 짧지 않는 시간 동안 하나하나 세세히 생각에 잠겨보면 여러 실험을 통해 해냈다는 성취감과 실패의 좌절감을 느끼면서 한 해 한 해 성장할 수 있었던 것 같습니다. 그 기간 동안 저의 도전을 지지해 주시고 도움을 주셨던 분들에게 감사를 표하고자 합니다.

먼저 대학원 면접 보기 직전 갑작스런 컨택에도 저를 받아주시고 6 년간 아낌없이 지도해 주신 양창덕 교수님께 감사 말씀 드립니다. 교수님의 연구에 대한 열정과 아낌없는 지도는 저에게 있어 좋은 연구자의 자세와 목표를 가르쳐주셨습니다. 교수님의 진심 어린 조언과 말씀을 깊이 새기며 앞으로도 발전하는 연구자가 되고자 합니다.

또한 박사 자격 심사과정에서 많은 가르침을 주신 권태혁 교수님, 김진영 교수님, 박혜성 교수님, 장지욱 교수님께도 감사드립니다. 교수님들께서 해주신 조언들을 잊지 않고 더욱 연구에 정진할 수 있는 능동적인 연구자가 되도록 하겠습니다. 공동연구를 진행하고 있는 백정민 교수님, 권태혁 교수님, 장지욱 교수님께도 다시 한번 감사 말씀 드립니다. 교수님들께서 해주신 조언을 가지고 더욱 발전된 연구자가 되도록 하겠습니다.

박사학위 기간 동안 함께 생활했던 연구실 선배님들에게도 깊은 감사드립니다. 연구실에 처음 들어왔을 때 많은 가르침을 주셨던 이규철 교수님, 소자로 넘어오면서 이상한 질문에도 친절하게 알려준 정호오빠, 신출내기였던 저에게 하나하나 친절하게 설명해 줬던 Chen 과 Tanya, 언제나 잘되고 있냐고 조언들과 함께 저의 안부를 물어봐 준 상면오빠, 항상 제가 무언가를 물어보면 친절하게 말해주고 조언도 아낌없이 해줬던 소희언니, 모든 것이 어색했던 저에게 먼저 말을 걸어준 대희오빠와 유진언니, 항상 밝게 대해주셨던 혜진언니, 함께 디바이스 실을 꾸려나가면서 항상 궂은일을 마다하지 않고 든든한 지원이 됐던 병규오빠, 같이 연구를 진행하면서 많은 것을 배운 민규오빠, 그리고 정말 배울 점이 많았던 용준이까지 모든 선배님들에게 감사드리며 앞으로의 선배님들의 미래를 응원하겠습니다.

같이 생활해온 후배들에게도 감사 말씀 전합니다. 어느덧 4 년 차가 끝나가는 든든한 지원군이 됐던 성훈이와 서영이, 항상 실험실에 활력을 불어넣어 준 승록이, 처음 소자 막내로 들어와 많은 일들을 도와줬던 근형이, 소자 팀에 들어와 궂은일도 마다하지 않고 본인 연구에도 열정이 많은 zhe 와 지원이, 합성과 소자를 같이 진행하는 대단하고 멋진 Huyen 과 동후, 합성을 진행하면서 모르는 것을 탐구하며 점점 멋진 연구자가 되어 가고 있는 원준이와 상진이, 실험실 막내로서 항상 웃음을 잃지 않고 열심히 하는 재영이과 하영이까지 모두 연구실 생활 잘 마무리하길 바라고 원하는 목표 이루길 항상 응원하겠습니다.

합성 학생들에게 든든한 버팀목이 되어주시는 윤성준 박사님, 서로 고민들을 나누고 조언도 해주고 서로에게 응원을 해줬던 Lian 박사님, 최근에 교환학생으로 들어온 Xuexiang, 또 몇 년간 언제나 친절하게 행정 일에 도움을 주신 소은 선생님까지 모두에게 감사드리고 행복하셨으면 좋겠습니다.

그리고 저의 학위과정을 응원해 줬던 친구들에게도 감사드립니다. 나의 소꿉친구, 고등학교에서부터 벌써 14 년 동안 응원해 주고 다독여준 친구들, 10 년이 되는 기간 동안 소중한 인연을 이어가는 대학 동기들, 각자의 목표를 가진 연구자라는 접점을 통해 맺은 인연들 모두가 저에게 힘을 주셨고 앞으로의 행복한 미래를 응원하겠습니다.

또한 지난 6 년 동안 서로의 행복과 슬픔을 나누며 같이 성장해간 나의 동기이자 연인인 성우, 너는 나에게 성공하겠다는 결심과 목표를 주었고 학위과정을 무사히 끝낼 수 있게 원동력이 되어줬어. 앞으로의 길도 서로 응원하며 나아가 서로에게 큰 힘이 되어주는 그런 관계가 되자.

마지막으로 살아온 날들 동안 저의 결정에 언제나 동의해 주며 아낌없이 지원해 주셨던 우리 부모님에게도 감사를 전합니다. 엄마, 아빠의 무한한 사랑으로 인해 이렇게 성장할 수 있는 사람이 될 수 있었습니다. 항상 존경하고 사랑합니다. 어딜 가서도 부끄럽지 않을 딸이 될게요. 그리고 나의 남동생, 언제나 고맙고 너의 꿈을 위해 응원한다. 지금 집에서 잠자고 있을 나의 버팀목 쿠르에게도 고마움을 전합니다.

저의 학위기간 동안 응원해 주시고 아낌없는 찬사를 보내주신 모든 분들께 다시 한번 감사드립니다.

CHAPTER 6 Appendix

Chapter 2.1

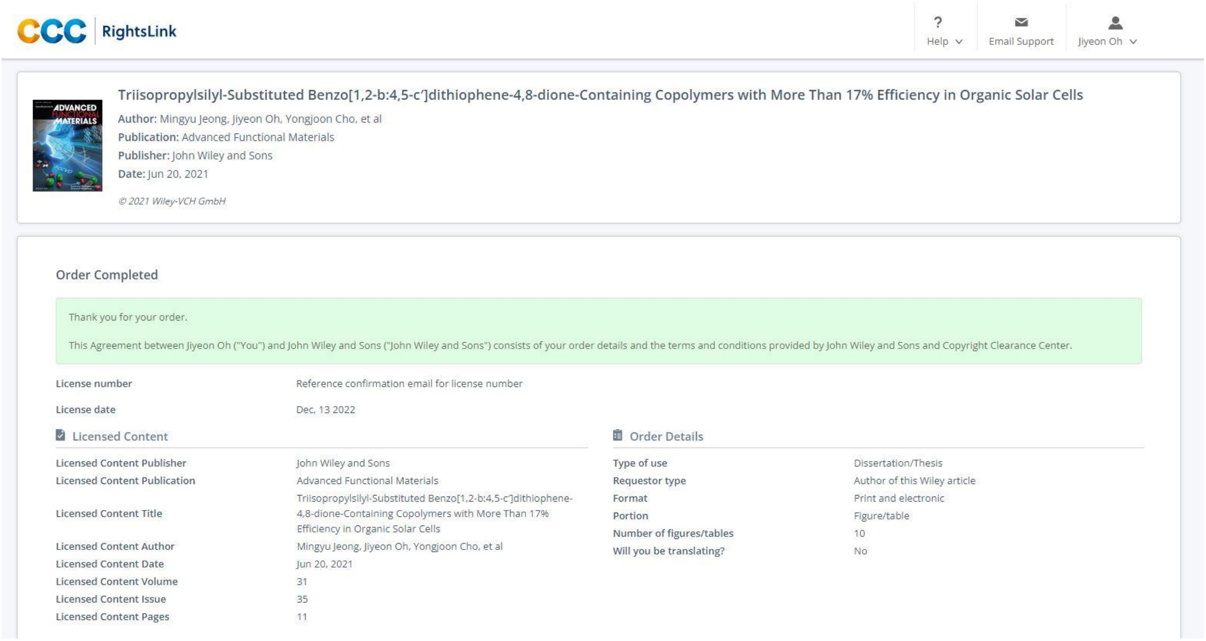

Triisopropylsilyl-Substituted Benzo[1,2-b:4,5-c′]dithiophene-4,8-dione-Containing Copolymers with More Than 17% Efficiency in Organic Solar Cells

Author: Mingyu Jeong, Jiyeon Oh, Yongjoon Cho, et al
Publication: Advanced Functional Materials
Publisher: John Wiley and Sons
Date: Jun 20, 2021

© 2021 Wiley-VCH GmbH

Order Completed

Thank you for your order.

This Agreement between Jiyeon Oh ("You") and John Wiley and Sons ("John Wiley and Sons") consists of your order details and the terms and conditions provided by John Wiley and Sons and Copyright Clearance Center.

License number	Reference confirmation email for license number
License date	Dec, 13 2022

Licensed Content

Licensed Content Publisher	John Wiley and Sons
Licensed Content Publication	Advanced Functional Materials
Licensed Content Title	Triisopropylsilyl-Substituted Benzo[1,2-b:4,5-c′]dithiophene-4,8-dione-Containing Copolymers with More Than 17% Efficiency in Organic Solar Cells
Licensed Content Author	Mingyu Jeong, Jiyeon Oh, Yongjoon Cho, et al
Licensed Content Date	Jun 20, 2021
Licensed Content Volume	31
Licensed Content Issue	35
Licensed Content Pages	11

Order Details

Type of use	Dissertation/Thesis
Requestor type	Author of this Wiley article
Format	Print and electronic
Portion	Figure/table
Number of figures/tables	10
Will you be translating?	No

Chapter 3.1

Reproduced in part with permission from J. Oh et al *J. Mater. Chem. C*, 2019, **7**, 4716. Copyright 2019 The Royal Society of chemistry.

If you are the author of this article, you do not need to request permission to reproduce figures and diagrams provided correct acknowledgement is given.

Chapter 3.2

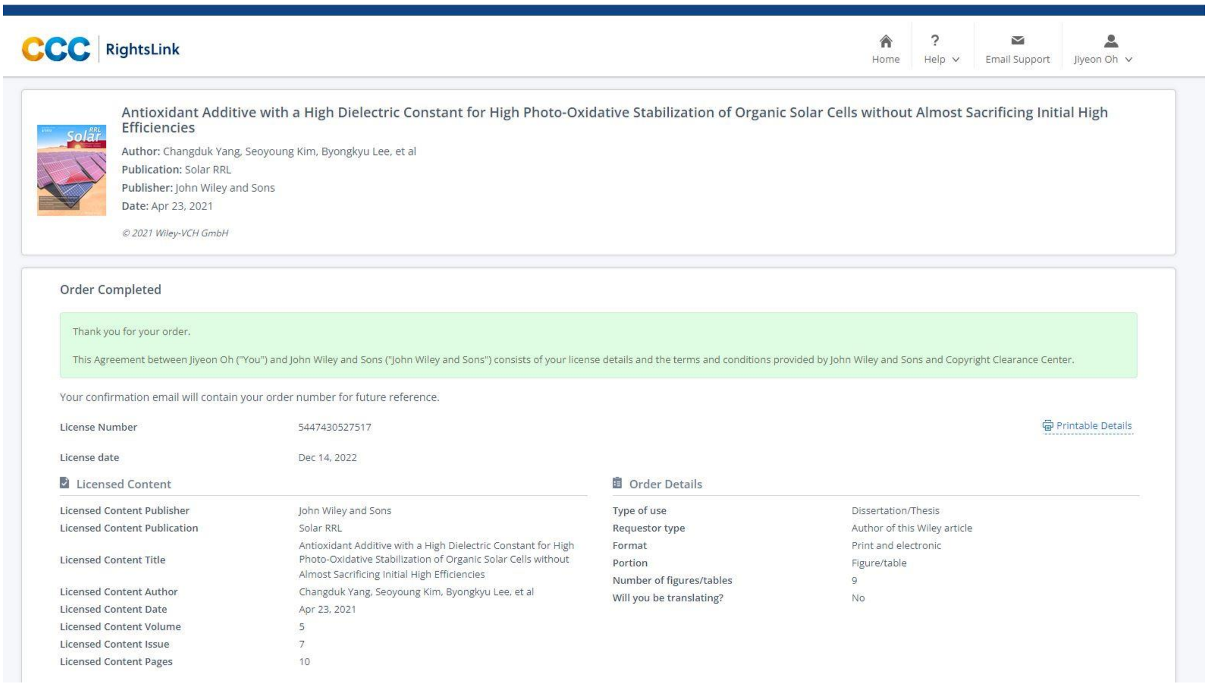

Antioxidant Additive with a High Dielectric Constant for High Photo-Oxidative Stabilization of Organic Solar Cells without Almost Sacrificing Initial High Efficiencies

Author: Changduk Yang, Seoyoung Kim, Byongkyu Lee, et al
Publication: Solar RRL
Publisher: John Wiley and Sons
Date: Apr 23, 2021

© 2021 Wiley-VCH GmbH

Order Completed

Thank you for your order.

This Agreement between Jiyeon Oh ("You") and John Wiley and Sons ("John Wiley and Sons") consists of your license details and the terms and conditions provided by John Wiley and Sons and Copyright Clearance Center.

Your confirmation email will contain your order number for future reference.

License Number	5447430527517
License date	Dec 14, 2022

Printable Details

Licensed Content

Licensed Content Publisher	John Wiley and Sons
Licensed Content Publication	Solar RRL
Licensed Content Title	Antioxidant Additive with a High Dielectric Constant for High Photo-Oxidative Stabilization of Organic Solar Cells without Almost Sacrificing Initial High Efficiencies
Licensed Content Author	Changduk Yang, Seoyoung Kim, Byongkyu Lee, et al
Licensed Content Date	Apr 23, 2021
Licensed Content Volume	5
Licensed Content Issue	7
Licensed Content Pages	10

Order Details

Type of use	Dissertation/Thesis
Requestor type	Author of this Wiley article
Format	Print and electronic
Portion	Figure/table
Number of figures/tables	9
Will you be translating?	No

Chapter 3.3

Reproduced in part with permission from J. Oh et al *J. Mater. Chem. A*, 2022, **10**, 20606. Copyright 2022 The Royal Society of chemistry.

If you are the author of this article, you do not need to request permission to reproduce figures and diagrams provided correct acknowledgement is given.

Curriculum Vitae

Jiyeon Oh

M.S.-Ph.D. Combined Course **(2017.03 ~)**
Department of Energy Engineering
Ulsan National Institute of Science and Technology (UNIST)
50, UNIST-gil, Ulsan 44919, South Korea

Birth: 1993.07.10 / Sex: Female
E-mail: delayoh@unist.ac.kr / absthe12@gmail.com

✓ EDUCATION QUALIFICATION

Ulsan National Institute of Science and Technology, Ulsan, South Korea
M.S.-Ph.D. Combined Course, Department of Energy Engineering,
Advisor: Prof. Changduk Yang

2017 –

Korea University, Sejong, South Korea
B.S., Department of Advanced Material Chemistry

2012 – 2016

✓ RESEARCH EXPERIENCE

Ulsan National Institute of Science and Technology, Ulsan, South Korea
Graduate Student (M.S.-Ph.D. Combined Course), Department of Energy Engineering
Advisor: Prof. Changduk Yang
Project: Multipurpose Solid Additives for Efficient and Stable Organic Solar Cells

2017 –

✓ AREA OF RESEARCH INTEREST

Design and Characterizations of Organic Optoelectronic Devices
Quantum Efficiencies and Optical Properties

Fabrication of Organic Materials: Water Splitting System
High-Performing Photoanode Devices

Synthesis and Application of Organic-Inorganic Hybrid Materials
Molecular Design and Analysis for Triboelectric Nanogenerator

✓ WORK EXPERIENCES WITH INSTRUMENT

2D-Grazing incidence X-ray diffraction (2D-GIXD) in Pohang Accelerator Laboratory in Korea and analysis by using **Igor-Pro** software package

FT-IR with Varian 670 at attenuated total reflectance (ATR) mode

UV-Vis-NIR absorption spectra with UV-1800 (SHIMADZU) spectrophotometer

Atomic Force Microscopy (AFM) measurement with Multimode V microscope

PV-external quantum efficiency with Boulder QEX7

FTPS external quantum efficiency

Electroluminescence external quantum efficiency with Enlitech ELCT-300

TPV, TPC, and Photo-CELIV with T4000 (McScience) organic semiconductor parameter test system

✓ HONORS AND AWARDS

Academic Next Generation Cultivation Program in the Field of Science and Technology
National Research Foundation (NRF)
Project Title: Development of Organic Photocatalyst Materials for Highly-Efficient and -Stable STH (Solar-To-Hydrogen) Production
2021 – 2023

Outstanding Graduate Student Award for Excellence
Ulsan National Institute of Science and Technology (UNIST)
2022

Outstanding Graduate Student Award
Ulsan National Institute of Science and Technology (UNIST)
2021

The National Scholarship for Science and Engineering,
Korea Student Aid Foundation (KOSAF)
2017 – 2022

✓ SELECTED PUBLICATIONS

1. Highly Efficient Layer-by-Layer Large-Scale Manufacturing Polymer Solar Cells with Minimized Device-to-Device Variations by Employing Benzothiadiazole-Based Solid Additives
   – **Jiyeon Oh**,† Sungwoo Jung,† So-Huei Kang, Geunhyung Park, Mingyu Jeong, Seoyoung Kim, Seunglok Lee, Wonjun Kim, Byongkyu Lee, Sang Myeon Lee, and Changduk Yang*
   – ***Journal Materials Chemistry A*****, 2022, 10, 20606** †equally contributed

2. Selective, Stable, Bias-Free, and Efficient Solar Hydrogen Peroxide Production on Inorganic Layered Materials [Selected as the Back Cover]
   – Jaejung Song,† Je Min Yu,† Jang Hyuk Ahn,† Hyeonjin Cho,† **Jiyeon Oh**,† Yoon Seo Kim, Jieun Kim, Myohwa Ko, Seong-hun Lee, Tae Joo Shin,* Hu Young Jeong,* Changduk Yang,* Jun Hee Lee,* Ji-Wook Jang,* and Seungho Cho*
   – ***Advanced Functional Materials*** **2022,** 2110412 †equally contributed

3. Halogen-free Donor Polymers Based on Dicyanobenzotriazole for Additive-free Organic Solar Cells
   – Lei Wang,† Tingting Wang,† **Jiyeon Oh**,† Zhongyi Yuan,* Changduk Yang,* Yu Hu, Xiaohong Zhao,* and Yiwang Chen
   – ***Chemical Engineering Journal*** **2022,** 442, 136068 †equally contributed

4. Novel Narrow Bandgap Terpolymer Donors Enables Record Performance for Semitransparent Organic Solar Cells Based on All-Narrow Bandgap Semiconductors
   – Xuexiang Huang,† Lifu Zhang,† Yujun Cheng,† **Jiyeon Oh**,† Chunquan Li, Bin Huang, Lin Zhao, Jiawei Deng, Youhui Zhang, Zuoji Liu, Feiyan Wu, Xiaotian Hu, Changduk Yang, Lie Chen,* and Yiwang Chen*
   – ***Advanced Functional Materials*** **2022**, 32, 5, 2108634 †equally contributed

5. Triisopropylsilyl-Substituted Benzo[1,2-b:4,5-c′]dithiophene-4,8-dione-Containing Copolymers with More Than 17% Efficiency in Organic Solar Cells
   – Mingyu Jeong,† **Jiyeon Oh**,† Yongjoon Cho, Byongkyu Lee, Seonghun Jeong, Sang Myeon Lee, So-Huei Kang, and Changduk Yang*

– ***Advanced Functional Materials*** **2021**, 31, 35, 2102371 †equally contributed

6. Novel High-Efficiency Polymer Acceptors via Random Ternary Copolymerization Engineering Enables All-Polymer Solar Cells with Excellent Performance and Stability
   – Dong Chen,† Siqi Liu,† **Jiyeon Oh**,† Bin Huang, Ruizhi Lv, Jiabin Liu, Changduk Yang*, and Lie Chen*
   – ***ACS Applied Materials & Interfaces*** **2021**, 13, 15, 17892–17901 †equally contributed

7. Antioxidant Additive with a High Dielectric Constant for High Photo-Oxidative Stabilization of Organic Solar Cells without Almost Sacrificing Initial High Efficiencies
   – **Jiyeon Oh**,† Sang Myeon Lee,† Sungwoo Jung, Jungho Lee, Geunhyung Park, So-Huei Kang, Yongjoon Cho, Mingyu Jeong, Byongkyu Lee, Seoyoung Kim, and Changduk Yang*
   – ***Solar RRL*** **2021**, 5, 7, 200812 †equally contributed

8. Over 13.8% Efficiency of Organic Solar Cells Fabricated by Air-processable Spontaneously Spreading Process Through Water Temperature Control
   – Tanya Kumari,† **Jiyeon Oh**,† Sang Myeon Lee, Mingyu Jeong, Jungho Lee, Byongkyu Lee, So-Huei Kang, and Changduk Yang*
   – ***Nano Energy*** **2021**, 85, 105982 †equally contributed

9. Narrow Band-gap Materials with Overlapping Absorption Simultaneously Increase The Open Circuit Voltage and Average Visible Transmittance of Semitransparent Organic Solar Cells
   – Xuexiang Huang,† **Jiyeon Oh**,† Yujun Cheng,† Bin Huang,* Shanshan Ding, Qiannan He, FeiYan Wu, Changduk Yang,* Lie Chen* and Yiwang Chen
   – ***Journal Materials Chemistry A*** **2021**, **9**, 5711 †equally contributed

10. Structural Similarity Induced Improvement in the Performance of Organic Solar Cells Based on Novel Terpolymer Donors
    – Yujun Cheng,† Hui Jin,† **Jiyeon Oh**,† Xuexiang Huang,† Ruizhi Lv, Bin Huang,* Zaifei Ma,* Changduk Yang,* Lie Chen* and Yiwang Chen,
    – ***Journal Materials Chemistry A*** **2021**, **9**, 9238 †equally contributed

11. 3D Cu Ball-based Hybrid Triboelectric Nanogenerator with Non-fullerene Organic Photovoltaic Cells for Self-powering Indoor Electronics
    – Sungwoo Jung,† **Jiyeon Oh**,† U. Jeong Yang,† Sang Myeon Lee, Jungho Lee, Mingyu Jeong, Yongjoon Cho, Seoyoung Kim, Jeong Min Baik,* and Changduk Yang*
    – ***Nano Energy*** **2020**, 77, 105271 †equally contributed

12. Ring-perfluorinated Non-volatile Additives with A High Dielectric Constant Lead to Highly Efficient and Stable Organic Solar Cells
    – **Jiyeon Oh**,† Sungwoo Jung,† Mingyu Jeong, Byongkyu Lee, Jungho Lee, Yongjoon Cho, Sang Myeon Lee, Shanshan Chen, Zhi-Guo Zhang, Yongfang Li, and Changduk Yang*
    Journal of Materials Chemistry C **2019**, **7**, 4716 †equally contributed

13. Effects of Incorporating Different Chalcogenophene Comonomers into Random Acceptor Terpolymers on the Morphology and Performance of All-polymer Solar Cells
    – Yujin An,† **Jiyeon Oh**,† Shanshan Chen, Byongkyu Lee, Sang Myeon Lee, Daehee Han and Changduk Yang*
    – ***Polymer Chemistry*** **2018** 9, 593-602 †equally contributed

✓ OTHER PUBLICATIONS

1. High-level Periodic Conjugated Terpolymers through AA/BB Monomer Pair-type Terpolymerization Improve Performance of Polymer Solar Cells
   – Sungwoo Jung, Yongjoon Cho, Yutong Ji, Jiyeon Oh, Geunhyung Park, Wonjun Kim, Seonghun Jeong, Sang Myeon Lee, Shanshan Chen, Youdi Zhang*, and Changduk Yang*
   – *Nano Energy* **2022**, 108059

2. Self-assembly Enables Simple Structure Organic Photovoltaics via Green-solvent and Open-air-Printing: Closing the Lab-to-fab Gap
   – Hua Tang, Jie Lv, Kuan Liu, Zhiwei Ren, Hrisheekesh Thachoth Chandran, Jiaming Huang, Ying Zhang, Hao Xia, Jafar I. Khan, Dingqin Hu, Cenqi Yan, **Jiyeon Oh**, Shanshan Chen, Shenglong Chu, Patrick W.K. Fong, Haiyan Chen, Zhengguo Xiao, Changduk Yang, Zhipeng Kan, Frédéric Laquai, Shirong Lu,* and Gang Li*
   – ***Materialstoday*** **2022**, 4, 5

3. Rational Regulation of the Molecular Aggregation Enables A Facile Blade-Coating Process of Large-area All-Polymer Solar Cells with Record Efficiency
   – Dong Chen, Siqi Liu, Bin Huang, **Jiyeon Oh**, Feiyan Wu, Jiabin Liu, Changduk Yang, Lie Chen,* and Yiwang Chen*
   – ***Small*** **2022**, 18, 20, 2200734

4. Non-conjugated Terpolymer Acceptors for Highly Efficient and Stable Lager-area All-polymer Solar Cells
   – Jiabin Liu, Jinliang Liu, Jiawei Deng, Bin Huang, **Jiyeon Oh**, Lin Zhao, Liang Liu, Changduk Yang, Dong Chen,* Feiyan Wu,* and Lie Chen*
   – ***Journal of Energy Chemistry*** **2022**, 71, 631

5. Non-Fused Polymerized Small Molecular Acceptors for Efficient All-Polymer Solar Cells
   – Baoqi Wu, Yue Zhang, Shizeng Tian, **Jiyeon Oh**, Mingqun Yang, Langheng Pan, Bingyan Yin, Changduk Yang, Chunhui Duan,* Fei Huang, and Yong Cao
   – ***Solar RRL*** **2022**, 2101034

6. Volatile Solid Additive-Assisted Sequential Deposition Enables 18.42% Efficiency in Organic Solar Cells
   – Jianqiang Qin, Qianguang Yang, **Jiyeon Oh**, Shanshan Chen,* George Omololu Odunmbaku, Nabonswendé Aïda Nadège Ouedraogo, Changduk Yang, Kuan Sun,* and Shirong Lu*
   – ***Advanced Science*** **2022**, 9, 9, 2105347

7. 16.3% Efficiency Binary All-polymer Solar Cells Enabled by A Novel Polymer Acceptor with An Asymmetrical Selenophene-fused Backbone
   – Huiting Fu, Qunping Fan, Wei Gao, **Jiyeon Oh**, Yuxiang Li, Francis Lin, Feng Qi, Changduk Yang, Tobin J. Marks, and Alex K.-Y. Jen*
   – ***Science China Chemistry*** **2022**, 65, 309

8. Near-infrared Absorbing Polymer Acceptors Enabled by Selenophene-fused Core and Halogenated End-group for Binary All-polymer Solar Cells with Efficiency Over 16%
   – Qunping Fan, Huiting Fu, Zhenghui Luo, **Jiyeon Oh**, Baobing Fan, Francis Lin, Changduk Yang, and Alex K.-Y.Jen*
   – ***Nano Energy*** **2022**, 92, 106718

9. Regio-Specific N-Alkyl Substitution Tuning the Molecular Packing of High-Performance Non-Fullerene Acceptors
   – Feng Qi, Leighton O. Jones, Kui Jiang, Sei-Hum Jang, Werner Kaminsky, **Jiyeon Oh**, Hongna Zhang, Zongwei Cai, Changduk Yang, Kevin L. Kohlstedt, George C. Schatz, Francis R. Lin,* Tobin J. Marks* and Alex K.-Y. Jen*
   – ***Materials Horizons*** **2022**, 9, 403

10. Sequentially Deposited Active Layer with Bulk-Heterojunction-like Morphology for Efficient Conventional and Inverted All-Polymer Solar Cells
    – Tao Zhan, Mingqun Yang, Ping Cai*, **Jiyeon Oh**, Xiyue Yuan, Baoqi Wu, Langheng Pan, Yanfei Zhao*, Changduk Yang, Chunhui Duan*, Fei Huang, and Yong Cao
    – ***ACS Applied Energy Materials*** **2021**, 4, 11, 13307

11. A Guest-assisted Molecular-organization Approach for >17% Efficiency Organic Solar Cells Using Environmentally Friendly Solvents
    – Haiyang Chen, Rui Zhang, Xiaobin Chen, Guang Zeng, Libor Kobera, Sabina Abbrent, Ben Zhang,

Weijie Chen, Guiying Xu, **Jiyeon Oh**, So-Huei Kang, Shanshan Chen, Changduk Yang, Jiri Brus, Jianhui Hou, Feng Gao,* Yaowen Li,* and Yongfang Li
– ***Nature Energy*** **2021**, 6, 1045

12. Viable Mixing Protocol Based on Formulated Equations for Achieving Desired Molecular Weight and Maximal Charge Separation of Photovoltaic Polymer
    – Byongkyu Lee,Seoyoung Kim, Hak-Won Nho, **Jiyeon Oh**, Geunhyung Park, Mingyu Jeong, Yongjoon Cho, Sang Myeon Lee, Oh-Hoon Kwon,* and Changduk Yang*
    – ***Advanced Energy Mateirals*** **2021**, 11, 46, 2102594 Advanced Energy Materials

13. Effects of the Polarity and Bulkiness of End-Functionalized Side Chains on the Charge Transport of Dicyanovinyl-End-Capped Diketopyrrolopyrrole-Based n-Type Small Molecules
    – So-Huei Kang, Doyoung Lee, Hyunwook Kim, Wonbin Choi, **Jiyeon Oh**, Joon Hak Oh*, and Changduk Yang*
    – ***Applied Materials & Interfaces*** **2021**, 13, 44, 52840

14. Efficiency Improvement of All-Small-Molecule Organic Solar Cells Through Fused-Aromatic-Ring Side-Chained Donors
    – Chao Hu,* Jingjing Xu, Songming Cai, Peihao Huang, **Jiyeon Oh**, Changduk Yang, Shanshan Chen, Kuan Sun, Ke Yang,* and Shirong Lu*
    – ***Solar RRL*** **2021**, 5, 12, 2100705

15. Thiophene with Oligoethylene Oxide Side Chain Enables Random Terpolymer Acceptor to Achieve Efficient All-Polymer Solar Cells
    – Feiyan Wu, Jinliang Liu, Jiabin Liu, **Jiyeon Oh**, Bin Huang, Dong Chen, Zuoji Liu, Qiannan He, Changduk Yang, and Lie Chen
    – ***ChemElectroChem*** **2021**, 8, 20, 3936

16. Enabling High Efficiency of Hydrocarbon-Solvent Processed Organic Solar Cells through Balanced Charge Generation and Non-Radiative Loss
    – Baobing Fan, Francis Lin, **Jiyeon Oh**, Huiting Fu, Wei Gao, Qunping Fan, Zonglong Zhu, Wen Jung Li, Ning Li, Lei Ying, Fei Huang, Changduk Yang,* and Alex K.-Y. Jen*
    – ***Advanced Energy Materials*** **2021**, 11, 41, 2101768

17. Significantly Enhanced Thermal Stability From A New Kind of N-type Organic Semiconductor DFA4: A Fully Fused F8IC
    – Tainan Duan,* Yangjiang Wu, Ke Yang, **Jiyeon Oh**, Changduk Yang, Shanshan Chen, Cheng Zhong, Donghong Yu, Yan Zhao* and Shirong Lu
    – ***Journal of Materials Chemistry C*** **2021**, 9, 13625

18. N-Type Quinoidal Polymers Based on Dipyrrolopyrazinedione for Application in All-Polymer Solar Cells
    – Langheng Pan, Tao Zhan, **Jiyeon Oh**, Yue Zhang, Haoran Tang, Mingqun Yang, Mengmeng Li,* Changduk Yang, Xi Liu,* Ping Cai,* Chunhui Duan,* Fei Huang, and Yong Cao
    – ***Chemistry A European Journal*** **2021**, 27, 54, 13527

19. A Donor Polymer Based on 3-cyanothiophene with Superior Batch-to-batch Reproducibility for High-efficiency Organic Solar Cells
    – Xiyue Yuan, Yunli Zhao, Tao Zhan, **Jiyeon Oh**, Jiadong Zhou, Junyu Li, Xiaojing Wang, Zhiqiang Wang, Shuting Pang, Ping Cai, Changduk Yang, Zhicai He, Zengqi Xie, Chunhui Duan,* Fei Huang, and Yong Cao
    – ***Energy & Environmental Science*** **2021**, 14, 5530

20. Modulating Chlorination Position on Polymer Donors for Highly Efficient Non-Fullerene Organic Solar Cells
    – Bin Huang,* Lin Hu,* Na Chen, Yujun Cheng, Xuexiang Huang, **Jiyeon Oh**, Changduk Yang, Shi-Yong Liu,* and Lie Chen*
    – ***Solar RRL*** **2021**, 5, 10, 2100510

21. Sustainable Highly Charged C_{60}-functionalized Polyimide in A Nnon-contact Mode Triboelectric Nanogenerator
    – Jae Won Lee, Sungwoo Jung, Jinhyeong Jo, Gi Hyeon Han, Dong-Min Lee, **Jiyeon Oh**, Hee Jae Hwang, Dukhyun Choi, Sang-Woo Kim, Jun Hee Lee,* Changduk Yang,* and Jeong Min Baik*
    – ***Energy & Environmental Science*** **2021**, 14, 1004

22. Molecular Ordering and Phase Segregation Induced by a Volatile Solid Additive for Highly Efficient All-Small-Molecular Organic Solar Cells
    – Shanshan Chen, Junfeng Ye, Qianguang Yang, **Jiyeon Oh**, Dingqin Hu, Ke Yang, George Omololu Odunmbaku, Feng Li, Qingqing Yu, Zhipeng Kan, Zeyun Xiao, Changduk Yang, Shirong Lu,* and Kuan Sun*
    – ***Journal of Materials Chemistry A*** **2020**, 9, 2857

23. Highly Efficient Organic Photovoltaics Enhanced Using Organic Passivation Layer Vacuum Deposition
    – Byongkyu Lee, Seonghun Jeong, Yongjoon Cho, Mingyu Jeong, Sang Myeon Lee, **Jiyeon Oh**, and Changduk Yang*
    – ***Advanced Functional Materials*** **2020**, 30, 51, 2005037

24. High-performance and Stable Photoelectrochemical Water Splitting Cell with Organic-photoactive-layer Based Photoanode
    – Je Min Yu, Jungho Lee, Yoon Seo Kim, Jaejung Song, **Jiyeon Oh**, Sang Myeon Lee, Mingyu Jeong, Yongseon Kim, Ja Hun Kwak, Seungho Cho,* Changduk Yang,* and Ji-Wook Jang*
    – ***Nature Communications*** **2020**, 11, 5509

25. Guest-oriented Non-fullerene Acceptors for Ternary Organic Solar Cells with Over 16.0% and 22.7% Efficiencies under One-sun and Indoor light
    – Yongjoon Cho, Tanya Kumar, Seonghun Jeong, Sang Myeon Lee, Mingyu Jeong, Byongkyu Lee, **Jiyeon Oh**, Youdi Zhang, Bin Huang, Lie Chen, and Changduk Yang*
    – ***Nano Energy*** **2020**, 75, 104896

26. Volatilizable and Cost-effective Quinone-based Solid Additives for Improving Photovoltaic Performance and Morphological Stability in Non-fullerene Polymer Solar Cells
    – Youdi Zhang, Yongjoon Cho, Jungho Lee, **Jiyeon Oh**, So-Huei Kang, Sang Myeon Lee, Byongkyu Lee, Lian Zhong, Bin Huang, Seungjin Lee, Jin-Woo Lee, Bumjoon J. Kim, Yongfang Li, and Changduk Yang*
    – ***Journal of Materials Chemistry A*** **2020**, 8, 13049

27. Horizontal-, Vertical-, and Cross-Conjugated Small Molecules: Conjugated Pathway-Performance Correlations along Operation Mechanisms in Ternary Non-Fullerene Organic Solar Cells
    – Sang Myeon Lee, Tanya Kumari, Byongkyu Lee, Yongjoon Cho, Jungho Lee, **Jiyeon Oh**, Mingyu Jeong, Sungwoo Jung, and Changduk Yang*
    – ***Small*** **2020**, 16, 5, 1905309

28. A Built-in Electric Field Induced by Ferroelectrics Increases Halogen-free Organic Solar Cell Efficiency in Various Device Types
    – Tanya Kumari, Sungwoo Jung, Yongjoon Cho, Hwang-Pill Kim, Jae Won Lee, **Jiyeon Oh**, Jungho Lee, Sang Myeon Lee, Mingyu Jeong, Jeong Min Baik, Wook Jo, and Changduk Yang*
    – ***Nano Energy*** **2020**, 68, 104327

29. Toxic Solvent- and Additive-Free Efficient All-Polymer Solar Cells via a Simple Random Sequence Strategy in Both Donor and Acceptor Copolymer Backbones
    – Mingyu Jeong, Byongkyu Lee, Yongjoon Cho, **Jiyeon Oh**, Sang Myeon Lee, Jungho Lee, and Changduk Yang*
    – ***Small Methods*** **2020**, 4, 1, 1900696

30. Flexible Organic Solar Cells Over 15% Efficiency with Polyimide-Integrated Graphene Electrodes
    – Donghwan Koo, Sungwoo Jung, Jihyung Seo, Gyujeong Jeong, Yunseong Choi, Junghyun Lee, Sang Myeon Lee, Yongjoon Cho, Mingyu Jeong, Jungho Lee, **Jiyeon Oh**, Changduk Yang,* and

HyesungPark*
– ***Joule*** **2020**, 4, 5, 1021

31. Insights into Constitutional Isomeric Effects on Donor–acceptor Intermolecular Arrangements in Non-fullerene Organic Solar Cells
– Jungho Lee, Eun Min Go, Satej Dharmapurikar, Jianqiu Xu, Sang Myeon Lee, Mingyu Jeong, Kyu Cheol Lee, **Jiyeon Oh**, Yongjoon Cho, Chunfeng Zhang, Min Xiao, Sang Kyu Kwak,* and Changduk Yang*
– ***Journal of Materials Chemistry A*** **2019**, 7, 18468

32. Thick-Film High-Performance Solar Cells with a C_{60}-Containing Polystyrene Additive
– Byongkyu Lee, Mingyu Jeong, Jungho Lee, **Jiyeon Oh**, Yongjoon Cho, Sungwoo Jung, Sang Myeon Lee, Shanshan Chen, and Changduk Yang*
– ***Solar RRL*** **2019**, 3, 6, 1900033

33. Highly Flexible and Efficient All-Polymer Solar Cells with High-Viscosity Processing Polymer Additive towad Potential of Stretchable Devices
– Shanshan Chen, Sungwoo Jung, Hye Jin Cho, Na-Hyang Kim, Seungon Jung, Jianqiu Xu, **Jiyeon Oh**, Yongjoon Cho, Hyeongwon Kim, Byongkyu Lee, Yujin An, Chunfeng Zhang, Min Xiao, Hyungson Ki, Zhi-Guo Zhang, Ju-Young Kim, Yongfang Li, Hyesung Park,* and Changduk Yang*
– ***Angewandte Chemie*** **2018**, 57, 40, 13277

34. Ultrafast Channel II Process Induced by a 3D Texture with Enhanced Acceptor Order Ranges for High-performance Non-fullerene Polymer Solar Cells
– Shanshan Chen, Sang Myeon Lee, Jianqiu Xu, Jungho Lee, Kyu Cheol Lee, Tianyu Hou, Yankang Yang, Mingyu Jeong, Byongkyu Lee, Yongjoon Cho, Sungwoo Jung, **Jiyeon Oh**, Zhi-Guo Zhang, Chunfeng Zhang, Min Xiao, Yongfang Li, and Changduk Yang*
– ***Energy & Environmental Science*** **2018**, 11, 2569

✓ CONFERENCES/WORKSHOP

1. Highly Efficient Layer-by-Layer Polymer Solar Cells with Minimized Device-to-Device Variations in Both Small- and Large-Scale Manufacturing by Employing Benzothiadiazole-Based Solid Additives
– **Jiyeon Oh**, Sungwoo Jung, and Changduk Yang*
– ***The Korean Institute of Electrical and Electronic Materials Engineers*** June 22-24, **2022**, Korea, Poster Presentation

2. Additive Effect of Polypentafluorostyrene for High-Performance Non-Fullerene Organic Solar cells
– **Jiyeon Oh** and Changduk Yang*
– ***International Conference on Science and Technology of Synthetic Metals 2018*** July 01-06, **2018**, Korea, Poster Presentation

3. Polypentafluorostyrene Processing Additive for High-Performance Non-Fullerene Organic Solar Cells
– **Jiyeon Oh** and Changduk Yang*
– ***The Polymer Society of Korea*** April 04-06, **2018**, Korea, Poster Presentation

4. Workshop on “Polymer New Technologies Course 2018”
– ***The Polymer Society of Korea*** April 04, **2018**, Korea